Enabling the Selective Conversion of Biomass-Derived Oxygenates to C4-C5 dienes

A DISSERTATION
SUBMITTED TO THE FACULTY OF THE
UNIVERSITY OF MINNESOTA
BY

Gaurav Kumar

IN PARTIAL FULFILLMENT OF THE REQUIREMENTS
FOR THE DEGREE OF
DOCTOR OF PHILOSOPHY

Advised by Professor Paul Dauenhauer and Professor Michael Tsapatsis

May 2021

Acknowledgement

I express deep gratitude to my advisors Prof. Paul Dauenhauer and Prof. Michael Tsapatsis for their research guidance during my PhD. Paul has given me a lot of creative independence which has greatly impacted my growth as a scientist. His optimistic outlook in the face of research failures is truly unique, and has helped me stay motivated and keep striving. I greatly admire him putting his graduate students' well-being above all else and rejecting the pervasive culture of 'good science only happens when you are miserable'. As a scientist, Michael is my role-model and someone who I continue to look up-to everyday. I have learnt from him the values of rigor, reproducibility, doing things the right way, and asking the right questions. His calm demeanor, directed guidance, and objectivity in conducting and discussing science have shaped how I approach new problems. I especially thank him for being patient and believing in me during some difficult times at the start of my PhD. In Paul and Michael, I have been lucky to find allies who have always placed my ambitions and development as a priority, and have always acted in my best interest.

I am appreciative of Dr. Omar Abdelrahman, Dr. Anargyros Chatzimitriou, and Dr. Limin Ren for helping me kickstart (not without hiccups!) my PhD. I am grateful to my collaborators: Dr. Lisa Li (University of Delaware) for the DFT calculations presented in Chapter 2; Hannah Bossert (UMN) and Dan McDonald (UMN) for assisting in execution and analysis of research presented in Chapter 3 (UMN); Prof. Dongxia Liu (UMCP) and Dr. Dandan Xu (UMass Amherst) for their help in synthesizing some catalysts reported in Chapter 4; Yutong Pang (UMN) and Xinyu Li (UMN) for assisting in the work presented in Chapter 5; and Anatoliy Kuznetsov (CMU) for his efforts in the work briefly discussed in Chapter 6. Special thanks also to Dr. Matheus Dorneles Mello (BNL) and Dr. Tianyi Luo (JHU) for introducing me to the intriguing world of Metal Organic Frameworks. I thank Dr. Manish Shetty, and Dr. Alexander M. Ardagh, with whom I have had countless stimulating research conversations that positively impacted my work. I also thank both research groups, past, and present, for maintaining a healthy research environment where we revel in each other's success.

I thank my parents for their unwavering commitment to my education; their perseverance despite all odds stacked against them has ultimately shaped my journey as a first-generation college student. My sister, Nikita, continues to listen to my rants on any

number of topics related and unrelated to research, and I thank her for the open ears. I also thank my partner, Anupama, for her affection that continues to ground me to reality and keeps me going. I thank my friends, both here in the States, and back home in India, for sticking with me through thick and thin. Many thanks to Vineet, Chinmayee, Greg, Paridhi, Yutong, and ChoongSze, who have all been great friends, and collectively, a wonderful support-system. I cannot wait to see the great things they go on to accomplish in their respective professional careers.

Finally, I must thank all my teachers through school, and my undergraduate studies at IIT Roorkee – I am forever indebted to them for instilling in me the love of learning and staying curious.

Table of Contents

List of Figures

List of Tables

List of Schemes

Chapter 1

Introduction

1.1 Motivation

The depletion of fossil fuel reserves along with the growing concerns of carbon footprint and global warming have led to research efforts focused on deriving fuels and energy from lignocellulosic biomass.[1–3] This area has gained further momentum after the US Department of Energy released a report listing twelve potential biomass-based building block chemicals to be used for producing specialty chemicals in 2004.[4] While biomass is abundant and cheap, the conversion to value-added products remains challenging. Unlike petroleum, biomass-derived feedstock contains excess oxygen that must be removed to produce commodity chemicals.[3,5,6] The oxygen moieties are generally removed by the loss of CO_2/CO by decarboxylation/decarbonylation pathway,[7,8] or as H_2O by hydrodeoxygenation or dehydration pathways.[9–11]

Zeolites are microporous materials extensively used in petrochemical applications like catalytic cracking, olefin oligomerization, and reforming processes,[12] and are increasingly being employed in biomass conversion catalysis to derive platform chemicals. One such class of compounds are C4-C5 dienes – widely used monomers in adhesives, synthetic rubber, and plastics, and currently manufactured in the US as a byproduct of the cracking of naphtha and gas oil fraction of crude oil.[13] With a recent shift towards using shale-gas (primarily composed of light molecules like methane and ethane) as a cheap alternative to crude oil for ethylene production, refineries are decoupling production routes of ethylene and larger fractions including dienes. Consequently, butadiene production in the US has dropped by *ca.* 30% since 2007. As demands continue to rise and supplies fall, other on-purpose and possibly renewable routes that are not coupled to ethylene production are required.

One such chemical pathway utilizes the tandem-ring opening dehydration (hereinafter referred to as dehydra-decyclization) of biomass-derived saturated furanic species to produce these dienes (**Scheme 1.1**). For example, four-carbon tetrahydrofuran

(THF) reacts on the surface of a solid Brønsted acid catalyst to produce butadiene, while five-carbon methylated tetrahydrofuran (2-MTHF) yields linear pentadienes. Limited prior investigations of this chemistry had not rigorously tackled the three fundamental catalyst design challenges, namely assessing: rates (*how fast the reaction occurs per active site of the catalyst),* diene selectivities (*how much of fed-in carbon ends up in desirable product/s*), and lifetime (*catalyst stability under reaction conditions*). In addition, the origin of side products (propene, formaldehyde, and alkylated aromatics), as well as the identity of key reaction intermediates were unknown. The breadth of accessible dienes would be afforded by our ability to prepare numerous substituted THF precursors, and yet it remained unclear how these substituents tune the chemistry of diene formation. Similarly, catalyst deactivation occurred on all reported catalyst at timescales that were prohibitively low and would require frequent high temperature regeneration cycles to restore activity. Due to this lack of detailed mechanistic knowledge, the maximum diene selectivities attainable in the chemistry had remained low (< 60%) **(Figure 1.1)**; increasing these selectivities would drive down energy-intensive downstream separation costs, and potentially lead to economic feasibility of the overall process.

1.2 Background

1.2.1 Feedstock: how are biomass-derived cyclic ethers produced?

The feedstocks used in this work are five-membered saturated cyclic ethers called (methyl)tetrahydrofurans (M)THF's, which can be derived directly or indirectly from glucose. 3-MTHF can be obtained from a three-step process which involves fermentation of glucose to itaconic acid[14,15] or mesaconic acid;[16] a two-step hydrogenation to 2-methyl-1,4-butanediol (MBDO);[17] and a dehydration step leading to cyclization (**Scheme 1.1**).[18] 2-MTHF has shown promise as a drop-in gasoline additive,[19] and is produced from biomass-derived intermediates like levulinic acid and furfural,[20] both of which are derived from sugars in acid hydrolysis. Levulinic acid can be hydrogenated to 4-hydroxypentanoic acid (HPA) followed by dehydration to γ-valerolactone (GVL). GVL is further hydrogenated to 1,4-pentanediol which dehydrates to form 2-MTHF.[2,21] One-pot synthesis of 2-MTHF from levulinic acid or esters of levulinic acid has been reported on many metal catalysts, including Ni-Cu/Al_2O_3,[22] Ru-N-triphos complexes,[23] Pt-Mo/H-BEA,[24] and

alumina-doped Cu/SiO_2.[25] Alternatively, furfural can undergo hydrogenation to produce 2-methylfuran, which can further be hydrogenated on metallic sites, forming 2-MTHF. Some of the recent works on the one-pot conversion of furfural to 2-MTHF have used metal catalysts like $Cu/Pd/SiO_2$,[26] Pt/Co,[27] Ni/SiO_2,[28] $Ni\text{-}Sn/TiO_2$.[29] THF can similarly be derived from acid hydrolysis of xylose to furfural, followed by decarbonylation and hydrogenation steps.[3,30] These chemical transformations are frequently carried out on metal surfaces like Pd,[31] $Mn/Cd/Al_2O_3$,[32] and Pt/SiO_2.[33]

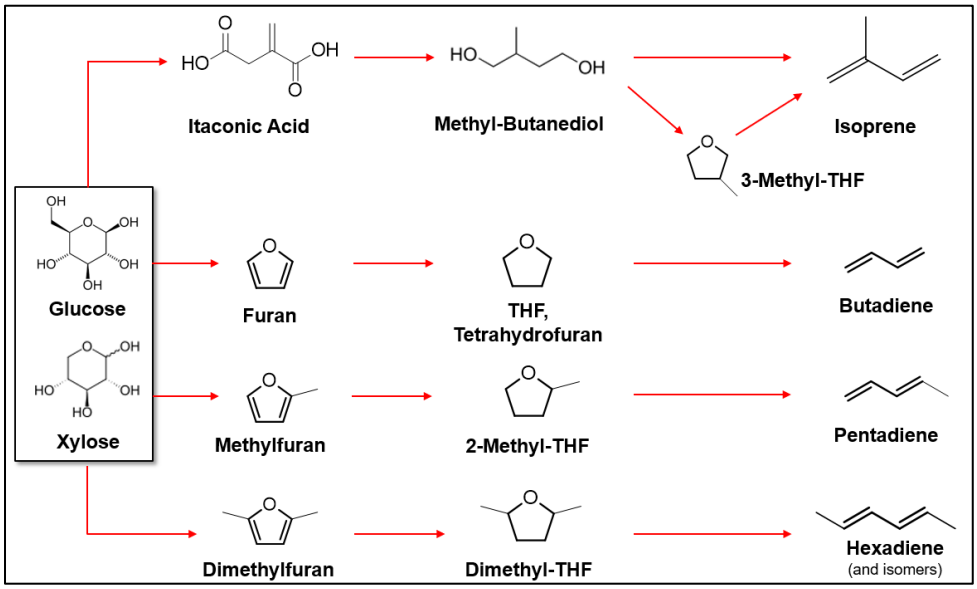

Scheme 1.1 *Conversion of monosaccharide sugars into dienes and involved key intermediates*

1.2.2 Dehydration of cyclic ethers to dienes. There is limited work in the literature on the catalytic dehydration of cyclic ethers. Traditional Brønsted acidic aluminosilicate zeolites are active to dehydration, but they also catalyze competing reaction pathways leading to low selectivities to the products of interest. Dauenhauer and co-workers recently reported the efficacy of phosphorus-containing siliceous zeolitic frameworks in the catalytic dehydration of 3-MTHF to isoprene,[34] and THF to butadiene.[18] The catalyst with highest reported selectivities in these articles was the hierarchical material P-SPP. The observed isoprene selectivity was ~70% at 20-25% 3-MTHF conversion, while the butadiene selectivity was 85%-99% at both low (9%) and high (89%) THF conversion. Furthermore, the researchers reported high selectivities (>95%) to pentadienes from 2-

MTHF, and to hexadienes (~85%) from 2,5- dimethyl tetrahydrofuran (DMTHF), particularly at low conversions (<10%) of the corresponding cyclic ethers. While P-zeolites are very selective to the formation of dienes in this chemistry, little work exists highlighting the role of phosphorus and the active site structure of these materials. Fan *et al.* have reported characterization results for phosphorus-containing zeolites P-BEA and P-SPP by

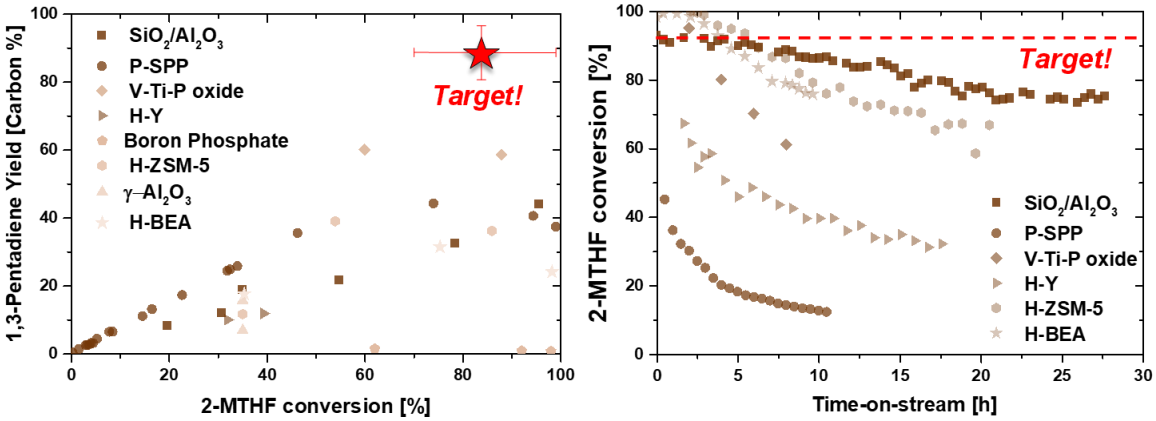

Figure 1.1 *Compilation of (left) piperylene yield as a function of 2-methyltetrahydrofuran (2-MTHF) conversion measured over variety of catalysts, and (right) 2-MTHF conversion as a function of time-on-stream, reported in open literature.*[18,20,35]

^{31}P solid-state MAS NMR, 2-propanamine TPD and Pyridine FTIR experiments.[36] 2-Propanamine doesn't undergo Hofmann elimination on these materials. Furthermore, a strong Pyridinium ion peak is absent in Pyridine-FTIR experiments. Both results suggest that the active sites in these materials are likely weakly acidic.

Dumesic and co-workers recently reported ~68% 1,3-pentadiene yield in the dehydration of 2-MTHF over silica/alumina.[20] 3-MTHF was excluded in this study due to low activity of this catalyst towards 3-MTHF ring opening. The researchers used contact-time experiments to identify the nature of major intermediates and products. While penten-ol and pentanal were found to be primary products, butene and formaldehyde were secondary products. In addition, the dienes were found to be produced from two separate pathways involving pentanal and penten-ol respectively.[20] In another study on the hydrodeoxygenation of 2-MTHF over WP/SiO_2 by Oyama *et al.*, a slightly different dehydration mechanism leading to the formation of dienes has been proposed.[37] However, these researchers also report that dienes and aldehyde come from same initial intermediates. Another separate study on the hydrodeoxygenation of 2-tetrahydropyran

over Ni_2P/SiO_2 supports this result, where the final dehydration product (2-hexene) was argued to be produced by two different pathways, both involving secondary oxygenated species (Hex-4-en-1-ol and hex-4-enal).[38] While these studies are indicative of possible mechanisms for (M)THF dehydration, the lack of an effective catalyst for this chemistry have hampered detailed kinetic studies.

1.3 Thesis Scope and Objectives

The background provides the basis for three specific research directions we explored with an overarching goal of achieving high diene yields. The prerequisite for designing right catalysts was a detailed understanding of the origin of selectivity, which necessitated a fundamental study of the chemistry on a well-defined model system. Based on this understanding, we synthesized and characterized multiple possible 'right' candidates. The course of discovering new materials inevitably involves labor-intensive methods of catalyst screening, so engineering low-cost automated methods for preliminary catalyst evaluation becomes important in order to direct time and resources away from routine repetitive tasks involved in setting up reactions. To this end, we fabricated an adapted gas-chromatograph which could be operated as a plug flow reactor to quickly screen our synthesized materials. These two steps of synthesizing a host of presumably selective catalysts along with screening multiple such catalysts led to the discovery of well-known weakly Brønsted acidic boron-containing zeolites as highly selective catalysts for 2-MTHF-to-pentadiene chemistry, and we then spent time and effort in trying to understand the effects of acid-site strength and diffusional hurdles in the chemistry. Lastly, we turned our attention to the previously reported aluminum free P-zeosils with the intention of gaining an understanding of their active sites and assess the applicability of standard acid site counting techniques for these materials. As such, this thesis is organized as follows:

In Chapter 2, we combine the first-principle DFT calculations and microkinetic modeling from the Vlachos Group (University of Delaware) along with our own experimental efforts to deep-dive into the mechanisms and reaction pathways of THF dehydra-decyclization to butadiene, and Retro-Prins condensation to propene and formaldehyde on a site-isolated H-ZSM-5 (Si/Al 140). This collaborative effort allowed us

to understand the kinetic bottleneck of this chemistry along with the nature of diene-forming intermediate species. Importantly, this work led to the formulation of relative C-O/C-C scission rates as the selectivity descriptor and guided our subsequent catalyst design strategies (discussed in Chapter 4).

In Chapter 3, we discuss our efforts in engineering a common Gas-Chromatograph as an automated packed bed flow reactor for evaluating the many catalysts synthesized to screen for the (M)THF dehydra-decyclization. This adapted GC enabled the control of reaction parameters for vapor-phase catalytic flow chemistries directly from the GC circuitry. After carrying out reactor validation tests (e.g., residence time distributions, isothermal operation, absence of heat and mass-transfer limitations), it was found that typical reaction parameters could be obtained with reasonable accuracy with nearly no manual intervention on this low-cost setup. This automated reactor setup has since helped in the successful screening of promising catalysts for not just (M)THF dehydra-decyclization, but other chemistries of interest to the Dauenhauer Group.[39]

Chapter 4 discusses our strategies to tune 2-MTHF dehydra-decyclization to favor conjugated 1,3-Pentadiene. This was accomplished by a two-fold approach - catalytic evaluation of weakly Brønsted acidic boron-containing zeolites in different surrounding framework environments consistently exhibited higher C-O/C-C scission rates than aluminosilicate zeolites. A second 'lever' circumvented the production of non-conjugate isomer of 1,3-Pentadiene, namely 1,4-Pentadiene. Operating in diffusion-controlled regime allowed for the facile isomerization of 1,4-Pentadiene to the thermodynamically stable 1,3-Pentadiene to near-equilibrium ratios of 1,3-PD/1,4-PD. This was accomplished at promoting these isomerization events on three distinct length scales, namely reactor bed lengths (cm), acidic domains in zeolite crystallites (μm), as well as the extent of confinement (Å).

In Chapter 5, we come back for a closer look at the phosphorus-containing aluminum-free materials which were discovered as selective dehydra-decyclization in work preceding this dissertation. Particularly, we employ a combination of solid acid characterization, and kinetic interrogations during two distinct Bronsted acid catalyzed chemistries (isopropanol dehydration, and Hofmann elimination of alkylamines) establishing the catalytic consequences of weakly Brønsted acidic character of the active

sites in these materials. In the process, we also shed light on the limitations of extending commonly employed techniques for acid catalysis turnover frequency (TOF) measurements to weaker solid acids.

Finally, Chapter 6 discusses some concluding remarks, particularly with respect to the feasibility of implementing the process technology at the core of this dissertation (saturated furans to C4-C5 dienes) on an industrial scale. It then goes on to discuss the possible directions which can be pursued with respect to process improvements as well as gaining more fundamental insights into these chemical transformations on different metal-acid bifunctional surfaces to boost reaction rates, which remains the outstanding problem on the weakly acidic materials discussed in preceding chapters.

Chapter 2

Mechanisms and pathways of THF dehydra-decyclization on H-ZSM-5

Reproduced with permission from Li, S; Abdelrahman O.A*; Kumar, G*; Tsapatsis, M; Vlachos, D; Caratzoulas, S; Dauenhauer, P.J. Dehydra-Decyclization of Tetrahydrofuran on H-ZSM5: Mechanisms, Pathways, and Transition State Entropy *ACS Catalysis* **2020**, *9(11)*, 10279–10293. *(* Equal contribution)* https://doi.org/10.1021/acscatal.9b03129

2.1 Conspectus

Being an important monomer for rubbery and hard polymeric materials, butadiene can be produced efficiently from biomass-derived tetrahydrofuran (THF) using solid-acid zeolite catalysts. In this work, electronic structure calculations, kinetic experiments, and microkinetic modeling were applied to investigate the THF dehydra-decyclization reaction to butadiene as well as its retro-Prins fragmentation to the side product propene on a Brønsted acid site within H-ZSM5. A comprehensive reaction network consisting of fifteen elementary surface reactions was investigated, and a microkinetic model was parameterized using computed energetics to compare with experimental kinetic data. Among the proposed reaction pathways, THF dehydra-decyclization primarily proceeds via an alkenol intermediate species, 2-buten-1-ol, while retro-Prins fragmentation to propene occurs through a direct pathway. Two other alkenol species that could be involved in the reaction network, 3-buten-1-ol and 3-buten-2-ol, do not substantially contribute to THF conversion. While multiple elementary steps were found to be kinetically relevant, the Brønsted acid catalyzed ring opening of THF is the predominantly rate-limiting surface reaction. The apparent activation energies (ca. 30 kcal mol^{-1} for both butadiene and propene in the temperature range of 220-270 °C), reaction orders and selectivity as well as absolute rates predicted by the model are in agreement with experimental values, provided that the modeled entropy of activation is calculated to account for translational freedom for transition states that exhibit complete proton transfer from the solid acid site.

2.2 Introduction

Butadiene is a key monomer in the production of synthetic rubbers, such as *cis*-1,4-polybutadiene, a major component of automobile tires.[40] It also finds application in other important copolymers with unique properties, such as the abrasion-resistant styrene-butadiene rubber (SBR) and the ABS (acrylonitrile-butadiene-styrene) plastic used in

automotive trim components, Lego™ bricks, computer housing, and numerous other applications.[41] In the existing petrochemical approach, butadiene is recovered after separation of the C4 hydrocarbons from naphtha crackers, where ethylene is the main product. The recent shale gas revolution will see a reduction in the production of C3/C4 olefins and aromatics (benzene, toluene and xylene) as abundant shale-derived ethane is motivating a shift away from heavier feedstocks.[5] Butadiene production in the United States of America has dropped by *ca*. 30% since 2007,[42] and new on-purpose butadiene production routes that are not coupled to ethylene production are required to satisfy growing demand.[43]

In prior work,[44] we designed an alternative, renewable route to 1,3-butadiene from tetrahydrofuran (THF), which is the product of decarbonylation and hydrogenation of biomass-derived furfural. Catalysts for butadiene production from THF were screened using a microcatalytic method, including metal oxides (Nb_2O_5, ZrO_2), silica-alumina, phosphotungstic acid, sodium phosphate and several zeolitic materials. Among the zeolitic catalysts, the phosphorus-containing, all-silica materials (P-zeosils) were the most selective to butadiene. In particular, the phosphorus-containing self-pillared pentasils (P-SPP) and P-MFI zeolites exhibited >85% selectivity to butadiene even at conversion of THF as high as 90%. Similar high selectivity (90%) to pentadiene was also achieved on these P-modified materials when feeding alkyl-substituted THF, that is 2-methyl-tetrahydrofuran (2-MTHF) and 3-methyl-tetrahydrofuran (3-MTHF).[44,45]

Ring opening and dehydration (dehydra-decyclization) of THF has also been reported on mixed metal oxides and conventional solid acid catalysts. Norman[35] reported diene selectivity of *ca*. 70% from 2-MTHF over a V-Ti-P ternary mixed oxide catalyst (at conversions of 60%-88%), whereas only half the selectivity was achieved on boron phosphate catalyst under identical reaction conditions. It was also demonstrated that dehydration of 3-MTHF and tetrahydropyran (THP) was not as efficient as the corresponding reaction of 2-MTHF; and diene production was also much less selective. Pisano *et al.*[46] obtained 31% butadiene yield in gas-phase dehydra-decyclization of THF on sodium phosphate. Kumbhalkar *et al*.[20] investigated the dehydra-decyclization reaction of 2-MTHF on several solid acid catalysts and measured similar diene selectivities in the range of 60-70% for SiO_2/Al_2O_3, Al-Sn-BEA, H-ZSM5 and H-BEA catalysts at ~35%

conversion. The predominantly Lewis acid catalyst, γ-Al_2O_3, was less selective (less than 40%) for pentadiene, compensated by formation of byproducts, butenes and pentenols. The relatively high selectivity to butenes on γ-Al_2O_3 was attributed to Lewis-acid-catalyzed retro-Prins condensation of the allylic alcohol (2-penten-1-ol in this scenario) to alkene and aldehyde. The same authors also explored several other cyclic ether compounds and determined the reactivity order 2,5-dimethyltetrahydrofuran (2,5-DMTHF) > 2-MTHF > THP > THF. Possible reaction pathways were also discussed in that work, based on space-time studies on SiO_2/Al_2O_3, but the reaction mechanism was not determined. The co-existence of both Brønsted and Lewis acid sites (at a ratio of *ca*. 4) in SiO_2/Al_2O_3 made distinguishing the reaction mechanism on each type of acid site challenging.

The primary goal of this work is to elucidate the reaction mechanism of diene formation via dehydra-decyclization reactions of THF on well-characterized tetrahedral Al Brønsted acid sites of H-ZSM-5. We identified reaction intermediates, determined the dominant reaction pathways and rate-limiting reactions, and illustrated the promoting-effect of a methyl group at the α-position on the THF ring to explain reactivity differences in the dehydra-decyclization of 2-MTHF, 3-MTHF and THF.

2.3 Methods

2.3.1 Materials and experimental methods. Chemicals were purchased and used without further treatment: THF (≥99.9% with 250 ppm BHT as inhibitor, Sigma Aldrich), 2-MTHF (≥98%, BHT as stabilizer, TCI Chemicals), 3-MTHF (≥95%, BHT as stabilizer, TCI Chemicals), 2,5-DMTHF (≥96%, mixture of *cis*- and *trans*-, Sigma Aldrich), 1-butanol (≥ 99.4%, Sigma Aldrich), 2-buten-1-ol (mixture, *cis*- and *trans*-, 96%, Sigma Aldrich), 3-buten-1-ol (≥98%, Sigma Aldrich), Di-butyl ether (≥98%, TCI Chemicals), 4-penten-1-ol (≥99%, Sigma Aldrich), 4-penten-2-ol (≥99%, Sigma Aldrich), 3-penten-1-ol (≥95%, Alfa Chemistry), 2-penten-1-ol (*trans*-, Sigma Aldrich), pyridine (99.8%, Sigma Aldrich), and silicon-dioxide (quartz chips, 4-20 mesh, Sigma Aldrich). Experiments to evaluate the kinetic isotope effect were performed using the same reaction methods with the feed substituted with tetrahydrofuran-D8 (≥99%, ≥99.5 atom % D, Sigma Aldrich). Ammonium-form ZSM5 was purchased from Zeolyst International (CBV28014,

Si/Al=140) and converted to its hydrogen form by calcination in a boat placed within a 1" quartz tube under air flow at 823 K using a ramp rate of 2 K min^{-1} for 10 hours.

All kinetic measurements were performed at atmospheric pressure in an up-flow fixed bed reactor. Catalysts (after the aforementioned calcination for converting the ammonium to hydrogen form) were pressed and sieved to particle sizes ranging from 500-1000 μm and placed between deactivated quartz wool (Restek 24324) plugs in a ¼" quartz U-tube. Pressure drop across the catalyst bed was maintained below 5% of total pressure. Void volume in the tube was minimized by loading quartz chips upstream of the catalyst bed. A 1/16" K-type thermocouple (Omega) was placed just above the reactor bed for temperature measurements. Isothermal conditions were maintained in the reactor furnace using a temperature PID controller (Omega CN 7800). Control experiments were performed to verify the absence of any catalytic activity by the thermocouple or the deactivated quartz wool under reaction conditions. The catalysts were then calcined *in situ* at 823 K in 40 sccm Air (99.997%, Minneapolis Oxygen) using a ramp rate of 3 K min^{-1}, then cooled to reaction temperature and purged with He (99.995%, Matheson) for at least 30 minutes before the introduction of reactant feed. Gas flow rates in the range of 60-120 sccm were adjusted using a mass flow controller (Brooks Instruments). All reactants were fed to a temperature-controlled vaporization section through a 1/16" PEEK capillary line (0.01" I.D.) using a syringe pump (Cole Parmer 74905 series). All transfer lines were resistively heated to avoid condensation of any species. On-line analysis of the reactor effluent was accomplished using a gas chromatograph (Agilent 7890) equipped with a quantitative carbon detector (Polyarc^{TM}, QCD[47]) and a flame ionization detector (FID). Separation was performed using an HP-PLOT Q column (Agilent, 19091P-QO4). All carbon balances closed to within ±10%. Unless otherwise specified, error bars represent 95% confidence intervals on independent replicate measurements.

The apparent activation barriers for the formation of butadiene and propene from THF were investigated in the temperature range of 493-543 K. The reaction rate order with respect to THF was obtained by varying its partial pressure from 2 to 100 torr. To analyze the reaction mechanism, we conducted a second set of experiments by feeding potential intermediate species, *viz.*, 2-buten-1-ol (2BOL), and 3-buten-1-ol (3BOL), which were considered as precursors of the products detected in the THF reaction based on electronic

structure calculations. Furthermore, to study the effect of substituents on the THF-ring, we conducted experiments for intermediate five carbon alkenol feeds expected from 2-MTHF ring-opening, namely, 4-penten-1-ol (4POL), 4-penten-2-ol (4P2OL), 3-penten-1-ol (3POL), and 2-penten-1-ol (2POL). All kinetic experiments for four and five-carbon alkenols were conducted in the temperature range of 373-413 K due to their high reactivity and rapid coking at THF reaction conditions. To deconvolute the effects of physical transients at early time-on-stream with rapid deactivation with the alkenols, all kinetic measurements were corrected to the state of the catalyst surface at steady-state 1-butanol dehydration. Briefly, 1-butanol dehydration was carried out until surface transients subsided, and an instantaneous switch to the alkenol feed was made. No measurable catalyst deactivation was observed for 1-butanol dehydration under the investigated temperatures, consistent with previous reports.[48,49] However, we observed rapid catalyst deactivation with all four and five-carbon alkenols, and no (<5% of initial) residual activity was detected after switching back to 1-butanol feed after ~ 4-5 hours on-stream with the alkenols.

Site time yields (STY) were calculated by normalizing the obtained rates with the number of Brønsted acid sites (BAS), quantified using *in situ* pyridine titration during the reference condition, i.e., steady state 1-butanol dehydration, to estimate the BAS count (Appendix **Figure A2.1**). STY is defined by **Eq. 2.1**

$$STY_i = \frac{F_i}{m_{cat} S_{\text{Brønsted}}} [=][\text{mol product } i/\text{mol } H^+/\text{h}] \quad (2.1)$$

where F_i is the molar flowrate of the product (mol/h), m_{cat} is the mass of the catalyst (g), and $S_{Brønsted}$ is the number of Brønsted acid site density (mol/g catalyst). The absence of both inter-, and intra-particle concentration gradients was ascertained by the Mears' criterion, and the Weisz-Prater criterion, respectively and the reported rates are in the kinetic regime.

2.3.2 Electronic structure calculations. All calculations were performed with Gaussian 09.[50] The H-ZSM5 model was constructed by substituting Al in the T12[51] position of the

MFI unit cell and incorporating a proton to an adjacent oxygen atom in the lowest-energy configuration. A cluster of 162 tetrahedral atoms (162T) was cut from the H-MFI crystal and all dangling bonds were saturated with H atoms. The HZSM-5 zeolite model is shown in **Figure 2.1**. Three ONIOM[52,53] layers were defined following the 'multicentered spherical cutoff' protocol[54] with cutoff radii of 3.5 Å, 6.0 Å and 8.2 Å for the high, intermediate, and real layers, respectively. The high-theory layer (25T plus adsorbed species) was allowed to relax and treated at the M06-2X/6-311G(2df,p) level of theory.[55] The intermediate layer (46T) was treated at the M06-2X/3-21G theory level and was frozen to maintain the zeolite pore structure integrity. The real layer (91T) was also frozen geometrically and modelled with the universal force field (UFF) molecular mechanics theory. Ground and transition states were confirmed by frequency analysis and intrinsic reaction coordinate (IRC) calculations.[56] Binding energies were corrected for the BSSE using the counterpoise method. The electronic energies have not been adjusted in any other way.

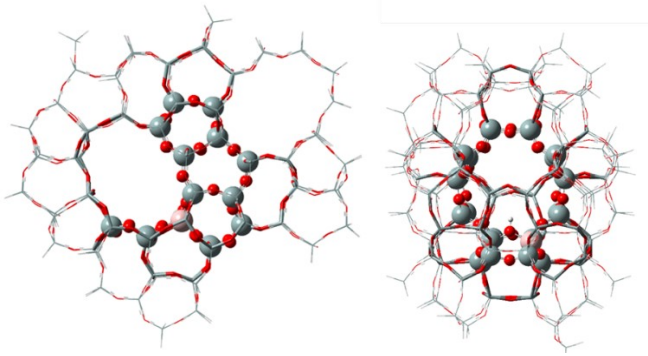

Figure 2.1. *Two views of the H-ZSM5 ONIOM model. High-theory layer shown in ball-and-stick representation, intermediate theory in tube representation and low-theory layer in wireframe representation. Color code: pink, Al; red, O; gray, Si; and white, H.*

Thermal corrections to the electronic energies were computed using the q-RRHO (quasi-rigid rotor harmonic oscillator) approximation proposed by Grimme[57] and by Head-Gordon.[58] In addition, we applied corrections to the entropies of intermediates and transition states according to the following scheme: Surface species (intermediates and transition states) stabilized by covalent or hydrogen bonds with the framework were assumed to be immobile, whereas the rest were allowed two-dimensional translational entropic freedom.[59–62] Critically, bond cleaving transition states activated by proton transfer from the active site were assumed to be 'unimolecular' in nature and thus

entropically mobile *if proton transfer in the transition state was completed*. Such species were identified visually (e.g., typical bond lengths and animation of the imaginary frequency vibrational mode) and confirmed by natural bond orbital (NBO) analysis. For example, in the transition state of the proton-catalyzed ring opening of THF, the proton of the active site is completely transferred to the oxygen atom of the ring and the corresponding imaginary mode involves only C-O vibration in the ring; the activated complex is not tethered to the active site and thus assumed free to explore configurations in the pore. The translational contribution to entropy and internal thermal energy were calculated from the translational partition function **Eq. (2.2)**, assuming a molecular surface area S_A of 200 pm × 600 pm, characteristic of the MFI framework pore size.[59]

$$q_{t,2D} = \frac{2\pi m k_B T}{h^2} S_A \tag{2.2}$$

where m is mass, k_B is the Boltzmann constant, h is Planck's constant and T is temperature.

Energetics calculated following this protocol were used to parameterize a microkinetic model denoted as the 'mobile' model throughout the text, while another 'immobile' model that ignores the translational freedom of surface species was also presented for comparison. Entropic effects on the predicted reaction rates are discussed in more detail in **Section 2.4.7**.

2.3.3 Microkinetic modelling. We have evaluated reaction network microkinetics in a plug flow reactor (PFR), modelled by the continuity equations for surface species j and gas-phase species k:

$$\frac{d\theta_j}{dt} = \sum_i \nu_{ij} r_i = 0 \tag{2.3}$$

$$\frac{dF_k}{dm_{cat}} = S_{\text{Brønsted}} \sum_i \nu_{ik} r_k \tag{2.4}$$

$$\theta_* + \sum_j \theta_j = 1 \tag{2.5}$$

where θ_* is the fractional coverage of the unoccupied vacant sites, F_k is the molar flow rate of gas-phase species k in mol/s, m_{cat} is the mass of the catalyst (g), $S_{\text{Brønsted}}$ is the acid

site concentration (mol/g) , and v_{ij} is the stoichiometric coefficient of component j in the elementary step i which proceeds at a rate

$$r_i = k_i \prod_{j \in R_i} c_j^{-v_{ij}} - k_{-i} \prod_{j \in P_i} c_j^{v_{ij}} \tag{2.6}$$

In the above, c_j represents either the fractional surface coverage θ_j, or the normalized pressure P_j/P_{tot} for gas-phase species, where P_j is partial pressure and P_{tot} is total pressure. The forward and reverse rate constants are related to each other through the equilibrium constant *K*:

$$K_i = \exp(-\frac{\Delta G_i}{RT}) = \frac{k_i}{k_{-i}} \tag{2.7}$$

where ΔG_i is the Gibbs free energy of reaction of step i. With the exception of adsorption from the gas phase, we use transition state theory to model the rate constants of all elementary surface reactions:

$$k = \frac{k_B T}{h} \exp\left(-\frac{\Delta G^{\ddagger}}{RT}\right) \tag{2.8}$$

where $\Delta G^{\ddagger}$ is the standard Gibbs free energy of activation. Gas-phase adsorption rates were obtained using collision theory[63] and the Hertz-Knudsen model,

$$r_A = f(\theta) \times \frac{P_A}{\sqrt{2\pi m_A k_B T}} \times \frac{1}{N_o} \tag{2.9}$$

where $f(\theta) = \theta_*$, the factor $\frac{P_A}{\sqrt{2\pi m_A k_B T}}$ is the flux of incident molecules of mass m_A and partial pressure P_A at temperature T, and N_o is the site density per unit area which was calculated to be ca. 1.5×10^{17} site/m^2 for the H-ZSM5 (Si/Al=140) catalyst used in our experiments. The corresponding rate constant of adsorption is:

$$k_A = \frac{P_{tot}}{\sqrt{2\pi m_A k_B T}} \times \frac{1}{N_o} \tag{2.10}$$

Desorption rate constants were then calculated from **Eq. (2.7)** using k_A and the equilibrium adsorption constant.

To identify the rate-limiting and selectivity-controlling elementary reactions, we computed the degree of rate control (X_{RC}) and selectivity control (X_{SC}), defined in **Eq. (2.11)**.[64,65] The $X_{RC,i}$ (or $X_{SC,i}$) of elementary reaction i is defined as the relative change of the overall reaction rate r_T (or reaction selectivity S) with respect to the relative change in the rate constant k_i at constant K_i:

$$X_{RC,i} = \frac{k_i}{r_T}\left(\frac{\partial r_T}{\partial k_i}\right)_{k_{j\neq i},K_i} \qquad X_{SC,i} = \frac{k_i}{S}\left(\frac{\partial S}{\partial k_i}\right)_{k_{j\neq i},K_i} \tag{2.11}$$

2.4 Results and Discussion.

The dehydra-decyclization of THF was investigated over a temperature range of 220-270 °C (493-543 K), over which butadiene, propene and butene(s) were observed as the major products. While the majority of kinetic investigations were performed over H-ZSM5 (Si/Al 140), Al content (Si/Al in the range of 11.5-140) and the extent of pore confinement (MFI, BEA, MCM-41, and amorphous silica alumina) of the solid acid catalyst were found to have insignificant effect on product distribution **(Appendix, Figure A2.2**).

Previously, we had reported the formation of these same three product groups over a variety of solid acid catalysts and wide range of operating conditions.[44,45] Across the various operating conditions in this study (**Table 2.1**), butadiene was the major product observed followed by propene. This is consistent with a recent investigation by Kumbhalkar *et al.*, where similar product distributions were observed for THF dehydra-decyclization over amorphous silica-alumina.[20] We additionally observed the formation of butanal, which was a minor contribution, but its selectivity increased with temperature. This observation is consistent with Chin and co-workers study of butanal conversion over solid Brønsted acids including H-ZSM5, where the formation of butadiene was experimentally observed.[66] This suggests a common chemical pathway through which butanal and the other major products in the current system can interconvert over solid Brønsted acid catalysts. Considering THF dehydra-decyclization under differential conditions, we measured the apparent kinetics of the two major product groups (dehydra-decyclization and retro-Prins, **Table 2.2**). The overall energetics of the two major pathways are similar (~30 kcal mol^{-1}). Additionally, the apparent reaction orders are also comparable, exhibiting a partial rate order of ~ 0.4 at 270 °C (543 K) over a range of 2 – 100 torr of THF. Consistent with this are the product selectivities presented in **Table 2.1**; a change in operating conditions does not strongly influence selectivity given the almost identical apparent kinetics.

2.4.1 Proposed reaction pathways and mechanisms. To understand the measured apparent kinetics of THF dehydra-decyclization, we considered the competing surface reactions leading to the observed vapor phase species. **Scheme 2.1** shows the proposed reaction network for dehydra-decyclization and retro-Prins fragmentation of THF evaluated by quantum chemical calculations. Dehydra-decyclization produces butadiene

Table 2.1. *Experimental kinetics of THF dehydra-decyclization over H-ZSM5 (Si/Al 140).*

T (°C)	P_{THF} (torr)	WHSV (hr^{-1})	Conversion (%)	$STY_{Butadiene}$ (s^{-1})	Fractional Selectivity		
					Butadiene	Propene	Butene
220	10.0	1.83	0.23	2.4×10^{-4}	0.50	0.32	0.18
230	10.0	1.83	1.53	4.8×10^{-4}	0.54	0.30	0.15
230	2.0	0.36	1.57	3.0×10^{-4}	0.53	0.28	0.19
230	40.0	7.59	0.15	5.8×10^{-4}	0.52	0.32	0.16
230	100.2	20.50	0.07	7.0×10^{-4}	0.52	0.31	0.16
240	10.0	1.83	0.66	8.9×10^{-4}	0.57	0.29	0.14
250	10.0	1.83	1.30	1.8×10^{-3}	0.58	0.28	0.14
260	10.0	1.83	2.17	2.9×10^{-3}	0.59	0.27	0.14
270	10.0	1.83	3.01	5.5×10^{-3}	0.60	0.27	0.13
270	2.0	0.36	6.72	2.5×10^{-3}	0.57	0.28	0.15
270	40.0	7.59	0.91	1.0×10^{-2}	0.60	0.27	0.13
270	101.9	20.90	0.44	1.2×10^{-2}	0.59	0.28	0.13

(desired product) and water; retro-Prins fragmentation forms propene and formaldehyde. In total, 15 surface reactions were investigated; the low-selectivity pathway to butene was not considered. In the current work, we did not experimentally observe the presence of alkenols. However, Kumbhalkar *et al.*[20] and Norman[35] both reported alkenol byproducts (e.g., pentenols in the case of 2-MTHF) in the effluent stream and suggested that these species are precursors to alkene formation via a retro-Prins mechanism. In particular, Kumbhalkar *et al.* have reported the primary nature of pentenols in the dehydra-decyclization of 2-MTHF, understandably at higher WHSVs (~7-67.2 g 2-MTHF/g cat./h) than that employed in this study (1.83-20.90 g THF/g cat./h).[20] Indeed, our quantum

chemical calculations predict the formation of the alkenol intermediates in the case of THF as well, including 3-buten-1-ol (3BOL), 2-buten-1-ol (2BOL) and 3-buten-2-ol (3B2OL).

Depicted in **Scheme 2.1** is the collection of catalytic pathways involved, where the primary cycle for butadiene production is identified within the black outline oval. Upon adsorption of THF to the Brønsted acid site of HZSM-5, the zeolite Oz-H bond is elongated by 0.11 Å and the proton is shared with the oxygen atom of THF at an O···H distance of 1.36 Å **(Appendix Figure A2.3)**. THF binds strongly to the zeolite, with a heat of adsorption of 30 kcal mol^{-1} at 250 °C (**Table 2.3**). Once adsorbed, THF protonation by the active site results in C-O bond breaking (TS1) and formation of a primary surface alkoxide, ALK1. The intermediate ALK1 undergoes an intramolecular 1,2-hydride shift (TS2) from C2 to C1, forming the secondary surface alkoxide ALK2. 2BOL is then formed from ALK2 via a C3-proton back-donation to the active site (TS9). 2BOL is coordinated to the acid site via its OH group and can undergo dehydration to butadiene via a concerted E2 mechanism (TS10). Alkenols bind through their OH groups more strongly (enthalpically) than their respective diene product, by more than 15 kcal mol^{-1} at 250°C (**Table 2.3**). Alternatively, the alkoxide intermediate ALK2 can also lead directly to butadiene by unimolecular dehydration (TS8), passing through the intermediate-transition state pair INT4-TS7; this is a minor pathway, however.

***Table 2.2**. Experiment and model-obtained apparent activation energies for dehydra-decyclization and retro-Prins condensation pathways, and reaction orders in THF on HZSM-5 (Si/Al 140).*

	Apparent activation energy (kcal mol^{-1})		**Reaction order in THF at 270 °C**	
	Experiments	Model[a]	Experiments	Model[a]
Dehydra-decyclization	33.1 ± 1.6	33.5 ± 1.8	0.41 ± 0.18	0.65 ± 0.08
Retro-Prins	29.6 ± 1.7	33.7 ± 2.0	0.41 ± 0.13	0.65 ± 0.08

[a] *Apparent activation energy, reaction order and their standard deviation were calculated using the energetics depicted in **Figure 2.2** and **2.3**, the fitting results are shown as the solid lines in **Figure 2.8** and **2.10**.*

Three additional secondary pathways to butadiene were also investigated, all involving the formation of the intermediate 3BOL, which can form from ALK2 by C1-proton back donation (TS3). Surface-bound 3BOL can react to butadiene via three potential

pathways: (a) E2 (concerted) dehydration via the transition state TS4; (b) E1 (stepwise) dehydration via the intermediate-transition state pair INT4*-TS7; and (c) isomerization to the 2° alkenol 3B2OL which further dehydrates to butadiene via TS6-INT4-TS7; 3B2OL dehydration follows the E1 mechanism via the carbenium INT4.

The primary side products (propene and formaldehyde) can form via three distinct retro-Prins fragmentation pathways. The first is directly from surface-bound THF, involving no surface intermediates and consists of the following sequence through TS11: proton transfer from the active site to the THF ring oxygen, C1-O bond scission, C2-to-C3 hydride shift, C3-C4 bond cleavage and proton back-donation to the active site — all in a single step, albeit not synchronously. The second pathway is similar to the direct one but proceeds through the primary surface alkoxide ALK1 that forms upon THF ring opening; it specifically entails a concerted 1,2-hydride shift from C2 to C3, C3-C4 bond cleavage, and proton back-donation to the active site (TS12). The third, more indirect, pathway proceeds through the intermediate 3BOL and involves the intermediate-transition state pair INT3-TS14.

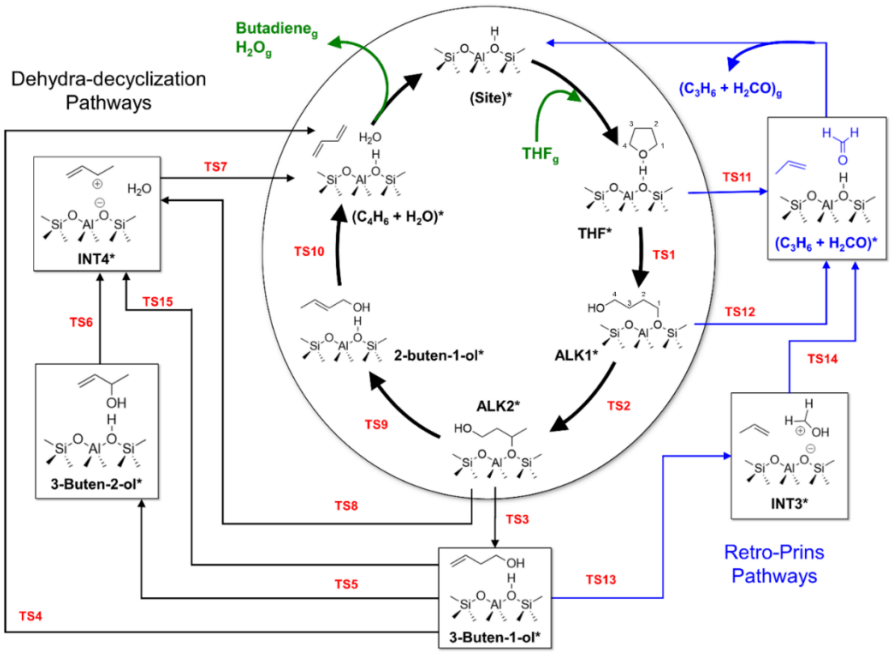

Scheme 2.1. *Proposed reaction network of THF dehydra-decyclization to butadiene (black arrows) and THF transformation to the retro-Prins (blue arrows) byproducts propene and formaldehyde. Fifteen transition states (TS) were investigated in this reaction network. Subscript 'g' denotes gas-phase species, while '*' marks surface species.*

2.4.2 Reaction energy profiles. Free energy profiles obtained following the 'mobile' assumption (to treat entropy) depicted in the methodology section are shown in **Figure 2.2** for THF dehydra-decyclization and **Figure 2.3** for retro-Prins fragmentation; the corresponding enthalpy profiles are provided in **Appendix Figure A2.4** and **A2.5,** respectively. Specifically, butadiene, propene, INT4, TS1, TS2, TS5, TS6, TS8, TS11 and TS12 were assumed to be mobile with two-dimensional translational freedom. In the dehydration transition states involving two fragments, the water fragment was also assumed to be mobile in TS4, TS7, TS10 and TS15, while the rest of the surface intermediates and transition states were assumed to be immobile. The computed activation enthalpies and transition states involving two fragments, the water fragment was also assumed to be mobile in TS4, TS7, TS10 and TS15, while the rest of the surface intermediates and transition states were assumed to be immobile. The computed activation enthalpies and entropies for all surface reactions are summarized in **Table 2.3** together with the calculated rate constants and equilibrium constants, and the transition state geometries are depicted in **Appendix Figure A2.6**.

It is clear from **Figure 2.2** that the 2BOL path to butadiene (red line) is energetically favored over the other three pathways since the latter are associated with high-energy transition states; that is, TS4 (3BOL dehydration), TS5 (isomerization to 3B2OL from 3BOL) and TS8 (unimolecular dehydration of ALK2 to INT4). While both E1 and E2 dehydration of 3BOL were considered, only the latter is shown in **Figure 2.2,** given their similar energetics; 3BOL transformation to INT4 (via TS15) is as difficult as its direct dehydration to butadiene (via TS4). In either case, the dehydration of 3BOL is energetically less favorable than that of 2BOL (TS10). THF dehydra-decyclization therefore likely proceeds through 2BOL. For the three retro-Prins pathways, it is difficult to infer the most favorable pathway based on free energy profiles; all three pathways have similar energy spans from the highest TS to the lowest intermediate state (**Figure 2.3**).[67] It is therefore not possible to predict the reaction selectivity solely based on energetics; a microkinetic model is required to determine the contribution of each pathway.

Table 2.3. *Enthalpy ($\Delta H_{reaction}$) and entropy ($\Delta S_{reaction}$) of reaction, activation enthalpy ($\Delta H_f^{\ddagger}$) and entropy ($\Delta S_f^{\ddagger}$ - mobile case) in the forward direction, forward rate constant (k_f) and equilibrium constant (K_{eq}) for all elementary reactions explored in the THF reaction network in H-ZSM-5*

	Elementary step	$\Delta H_{reaction}$ (kcal mol^{-1})	$\Delta S_{reaction}$ (cal mol^{-1} K^{-1})	$\Delta H_f^{\ddagger}$ (kcal mol^{-1})	$\Delta S_f^{\ddagger}$ (cal/mol/K)	k_f (s^{-1})	K_{eq}
	Surface reaction						
1)	THF* ↔ ALK1*	12.40	-0.06	49.14	19.70	6.50 x 10^{-4}	6.42 x 10^{-6}
2)	ALK1* ↔ ALK2*	2.34	2.42	32.65	18.55	2.82 x 10^{3}	0.356
3)	ALK2* ↔ 3BOL*	-3.52	3.27	20.19	1.94	1.07 x 10^{5}	1.53 x 10^{2}
4)	3BOL* ↔ (C_4H_6+H_2O)*	8.91	23.24	45.36	18.97	1.72 x 10^{-2}	22.8
5)	3BOL* ↔ 3B2OL*	-2.18	1.35	40.22	19.69	3.46	16.1
6)	3B2OL* ↔ INT4*	27.62	25.20	28.48	23.23	1.65 x 10^{6}	9.26 x 10^{-7}
7)	INT4* ↔ (C_4H_6 +H_2O)*	-16.54	-3.31	3.64	-4.75	3.01 x 10^{10}	1.53 x 10^{6}
8)	ALK2* ↔ INT4*	21.93	29.82	42.94	21.22	5.42 x 10^{-1}	2.27 x 10^{-3}
9)	ALK2* ↔ 2BOL*	-4.62	4.43	23.82	4.80	1.37 x 10^{4}	7.90 x 10^{2}
10)	2BOL* ↔ (C_4H_6 +H_2O)*	10.01	22.09	32.85	20.25	5.48 x 10^{3}	4.42
11)	THF* ↔ (H_2CO+C_3H_6)*	27.95	28.84	49.02	19.11	5.45 x 10^{-4}	4.23 x 10^{-6}
12)	ALK1* ↔ (H_2CO+C_3H_6)*	15.55	28.90	35.65	20.95	5.32 x 10^{2}	0.659
13)	3BOL* ↔ INT3*	24.10	18.24	30.47	-1.07	1.18	8.29 x 10^{-7}
14)	INT3* ↔ (H_2CO+C_3H_6)*	-7.37	4.96	0.42	1.20	1.34 x 10^{13}	1.46 x 10^{4}
15)	3BOL* ↔ INT4*	25.45	26.55	45.71	19.78	1.84 x 10^{-2}	1.49 x 10^{-5}
	Adsorption	$\Delta H_{reaction}$ (kcal mol^{-1})	$\Delta S_{reaction}$ (cal mol^{-1} K^{-1})			k_f (s^{-1})	K_{eq}
16)	$THF_{(g)}$ + * ↔ THF*	-30.29	-49.11			9.92 x 10^{9}	83.3
17)	$H_2O_{(g)}$ + * ↔ H_2O*	-16.44	-32.82			1.98 x 10^{10}	0.495
18)	$H_2CO_{(g)}$ + * ↔ H_2CO*	-14.99	-33.90			1.54 x 10^{10}	7.17 x 10^{-2}
19)	$3BOL_{(g)}$ + * ↔ 3BOL*	-30.54	-51.65			9.92 x 10^{9}	29.4
20)	$3B2OL_{(g)}$ + * ↔ 3B2OL*	-30.29	-49.44			9.92 x 10^{9}	70.4
21)	$2BOL_{(g)}$ + * ↔ 2BOL*	-31.03	-45.80			9.92 x 10^{9}	8.99 x 10^{2}
22)	$C_4H_{6(g)}$ + * ↔ C_4H_6*	-14.36	-27.91			1.15 x 10^{10}	0.79
23)	$C_3H_{6(g)}$ + * ↔ C_3H_6*	-10.81	-27.51			1.30 x 10^{10}	3.18 x 10^{-2}

2.4.3 Reaction pathway and sensitivity analysis. A microkinetic analysis of the reaction network was conducted using the computed energy profiles (**Table 2.3**) at 250°C and reactant partial pressures representative of experimental measurements. The dominant pathways, together with their contributions to the reaction flux, are shown in **Scheme 2.2**. THF dehydra-decyclization to butadiene proceeds mainly through 2BOL, contributing 96% of the reaction flux for butadiene formation, followed by the 3B2OL path at 4% of the reaction flux. The remaining two dehydra-decyclization pathways (3BOL path and the intramolecular dehydration path) are slower by several orders of magnitude and do not contribute significantly to butadiene formation. Propene forms predominantly through the transition states TS11 and TS12 at a reaction flux ratio of about 4:1; the indirect pathway through 3BOL is slower by two orders of magnitude and its contribution to propene formation is negligible. Among the fifteen proposed elementary reactions, only six contribute significantly to the reaction flux.

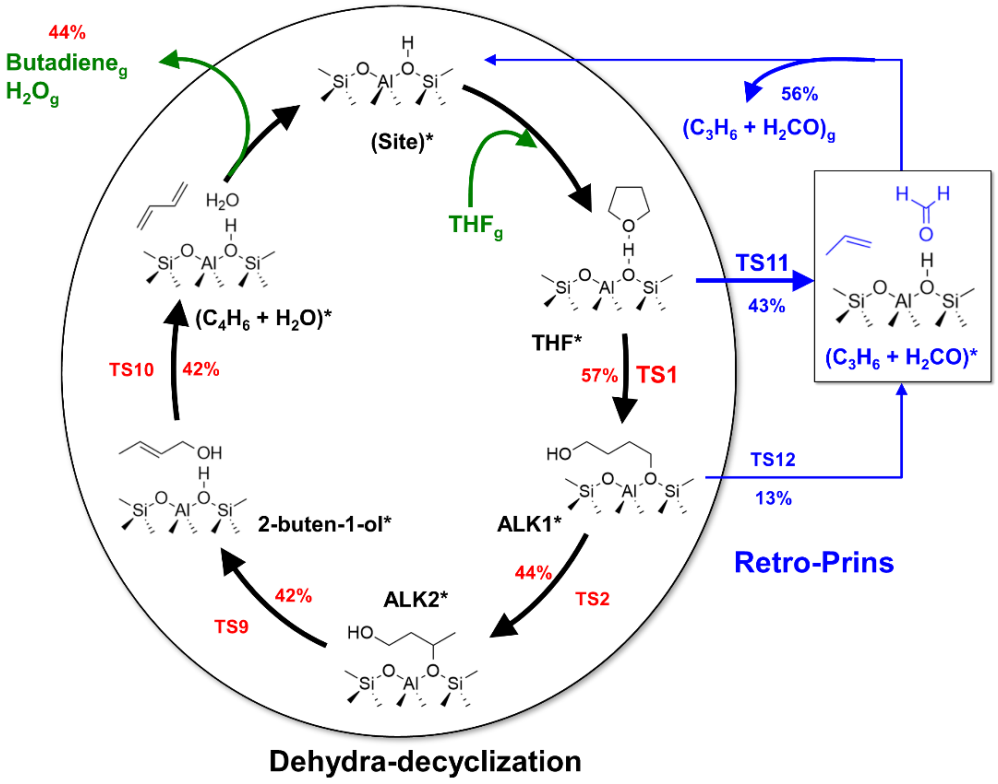

Scheme 2.2. *Reaction mechanism of THF transformation to the desired product butadiene and side product propene. Numbers show the 'mobile' model predicted contributions of each elementary step to the overall reaction at 250 °C, using energetics shown in* ***Table 2.3****.*

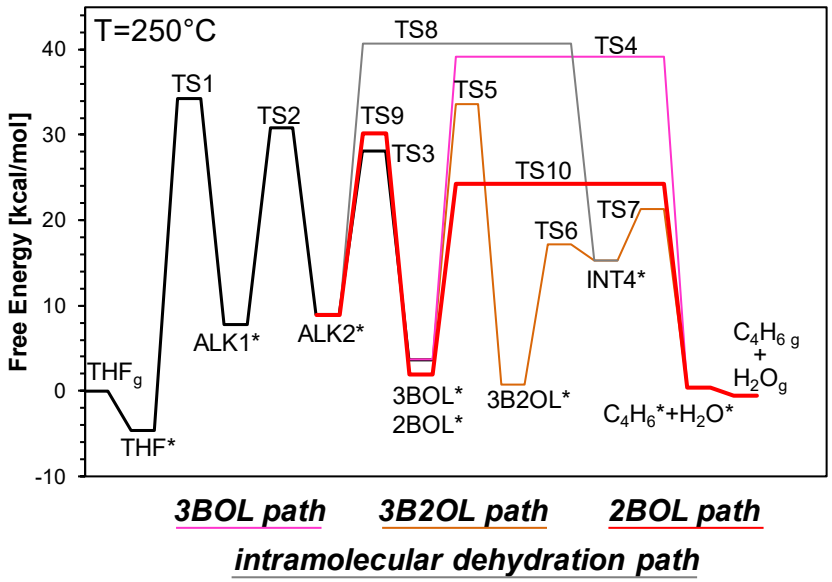

Figure 2.2. *Free energy profile of THF dehydra-decyclization to butadiene (C_4H_6) and water in H-ZSM5 at 250 °C. Subscript 'g' indicates gas-phase species, and '*' marks surface species. Pathways include the intramolecular dehydration path in black, the 3-butene-1-ol (3-BOL) path in pink, the 3-buten-2-ol (3B2OL) path in orange, and 2-buten-2-ol (2BOL) path in red.*

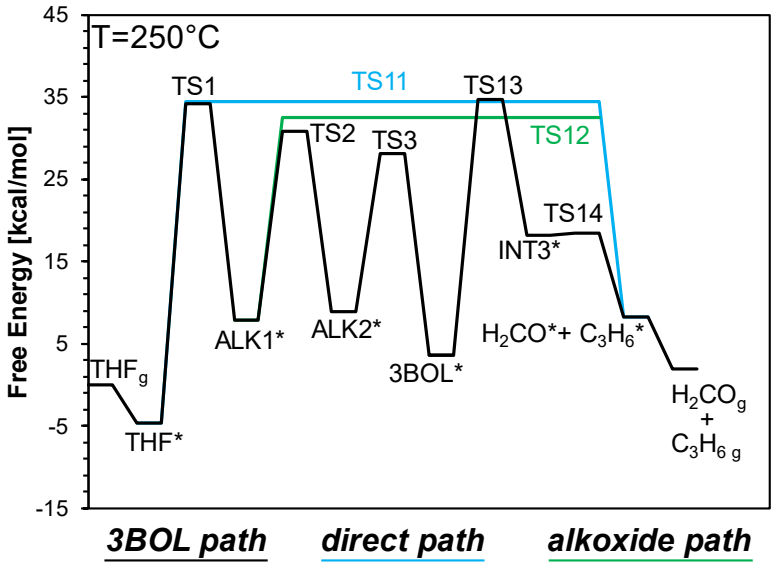

Figure 2.3. *Free energy profiles of the retro-Prins fragmentation of THF to propene (C_3H_6) and formaldehyde (H_2CO) in HZSM-5 at 250 °C. Subscript 'g' indicates gas-phase species, '*' marks surface species. Three pathways include the direct path from THF to formaldehyde and propene (teal), the alkoxide path in green, and the longest pathway through intermediate 3-buten-1-ol (3BOL).*

In the course of the reaction, THF undergoes ring opening in two probable ways: if the THF ring O abstracts a proton from the active site, the C-O bond breaks, and the surface alkoxide ALK1 forms (TS1); if a C2-to-C3 hydride shift occurs instead, then the C3-C4 bond will cleave and the retro-Prins products will form (TS11). The surface alkoxide, ALK1, undergoes two reactions: a C2-to-C3 hydride shift (TS2) to convert to the secondary surface alkoxide (ALK2), the precursor of 2BOL; or C2-to-C3 hydride shift coordinated with C3-C4 bond cleavage and proton back-donation to form propene and formaldehyde (TS12). The reaction flux through the second, concerted pathway to propene is less than a third of that through the secondary surface alkoxide (ALK2). Upon its formation, ALK2 undergoes deprotonation (from the C3 carbon) to yield the alkenol 2BOL (TS9), which subsequently dehydrates to butadiene (TS10).

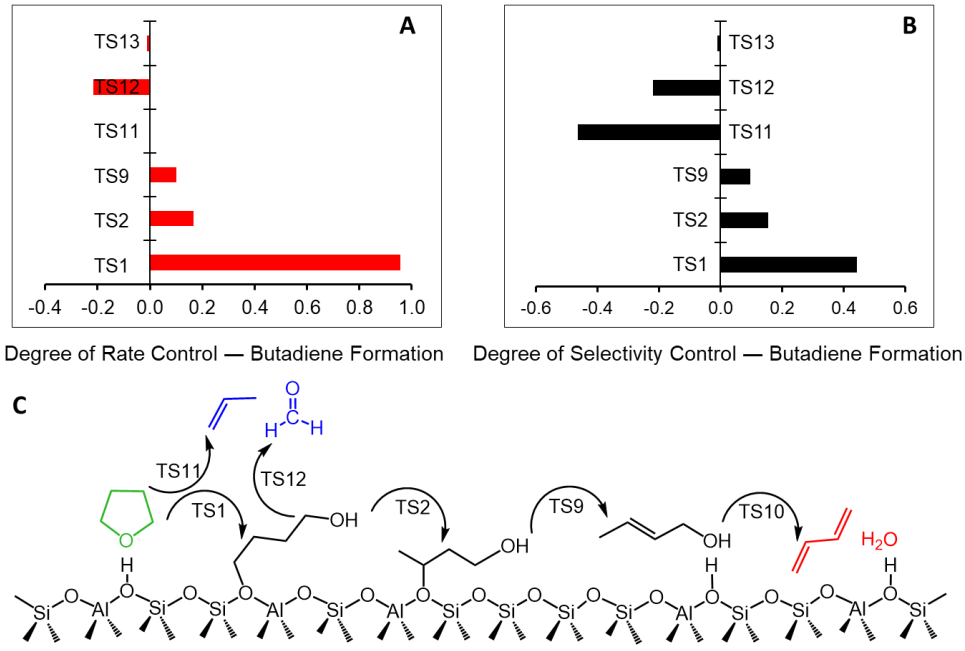

Figure 2.4. *Degree of rate control for butadiene production* ***(A)*** *and degree of selectivity control to butadiene* ***(B)*** *for the key reaction pathway transition states* ***(C).*** *All other transition states contributed negligibly; full details in the supporting info* ***Table A2.1***

To assess the kinetic contribution of the competing pathways and individual transition states, the degree of rate control associated with butadiene formation was calculated (**Figure 2.4A)**. Only four transition states are kinetically relevant to the overall rate of butadiene formation (TS1, 2, 9, and 12). The rate of butadiene formation is predominantly controlled by the transition state involving THF ring opening (TS1), with

an X_{RC} value of 0.96. The selectivity to butadiene is also quite sensitive to the energy of TS1 and can vary substantially with the energy of the transition state TS1 (**Figure 2.4B**); for example, stabilizing TS1 by a mere 2 kcal mol^{-1} (within the error of the quantum chemical calculations) increases the selectivity to butadiene by ca. 40% relative to the experimental value. This is consistent with the other two key transition states being TS11 and TS12 (**Figure 2.4C**); the relative rates of this reaction triangle (TS1-TS11-TS12) primarily dictate the overall rate of reaction and selectivity to butadiene or propene products. The predominant propene formation pathway ('direct' pathway) is rate-controlled by the transition state TS11, with an X_{RC} value of 0.79 (**Table A2.1**).

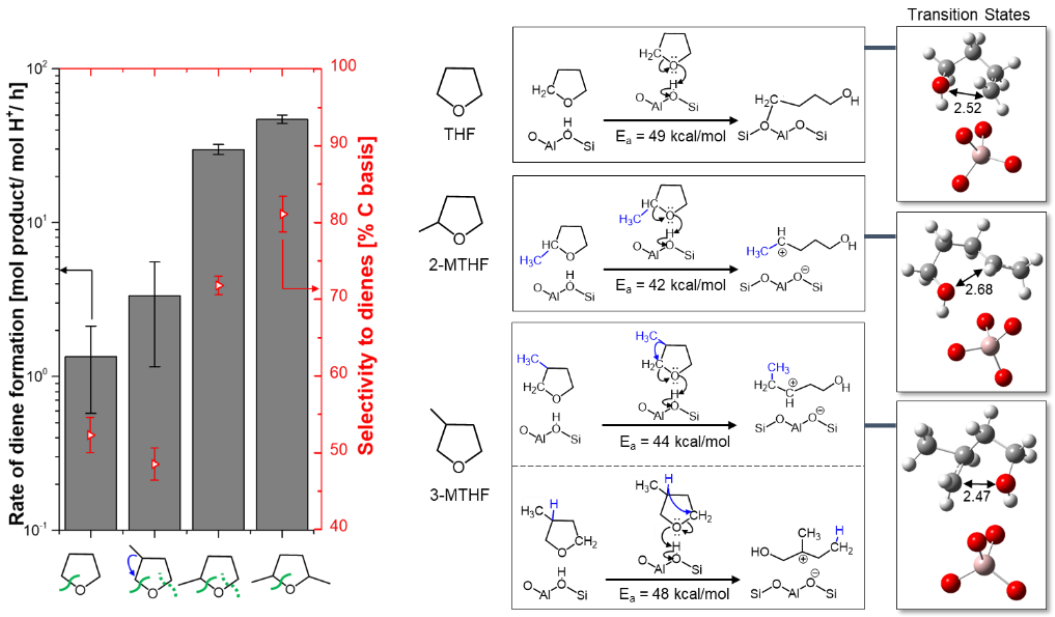

Figure 2.5*. (Left) (primary axis) Site time yields of diene formation, and (secondary axis) selectivity to dienes, from THF, 2-MTHF, 3-MTHF and 2,5-DMTHF (Reaction conditions: T =503 K, WHSV=2.9-3 h^{-1}, $p_{reactant}$=10.5 torr, all conversions <10%). (Right) Mechanism of ring-opening of THF and derivatives, 2-MTHF, and 3-MTHF, and the corresponding potential energy barriers. Insets show the transition state structures with bond lengths in Å.*

2.4.4 Substituent effect on THF ring-opening. With the degree of rate control analysis indicating ring opening to be the most kinetically relevant step, it is expected that methyl substitution on the furan ring leads to increased rates of reaction. We additionally expect methyl substitution to lead to a higher diene selectivity, given the large positive degree of selectivity control calculated for ring opening (TS1). To this end, we investigated the dehydra-decyclization of 2-MTHF, 3-MTHF and 2,5-DMTHF. We follow the same carbon

numbering nomenclature as in the case of THF, and therefore the positions on which the methyl group is attached is C1, C2, and C1/C4 in cases of 2-, 3-, and 2,5-DMTHF, respectively. Considering the case of 2-MTHF, ring opening on the C1-O side proceeds via a secondary carbenium, as opposed to the less stable primary carbenium encountered with THF ring opening. While the 2-MTHF ring opens in a manner analogous to THF, ring opening in 3-MTHF follows a different mechanism: it is accompanied by either a methyl or hydride shift (**Figure 2.5**). If the 3-MTHF ring opens on the C1-O side, then the methyl shift from the C2 to the C1 position will take place and a secondary carbenium will form. If the C4-O bond opens instead, then a hydride shift from the C2 to the C4 position will occur, leading to a tertiary carbenium intermediate. The methyl shift pathway is more favorable. In the methyl shift transition state calculated in **Figure 2.5**, the breaking C-C bond is stretched by 0.11 Å while the forming C-C bond has a length of 2.02 Å. The calculated ring-opening potential energy barriers for THF, 2-MTHF and 3-MTHF are 49, 42 and 44 kcal mol^{-1}, respectively.

Kinetic experiments comparing the ring-opening of the four cyclic ethers shows that the rate of ring-opening decreases in the order 2,5-DMTHF > 2-MTHF >> 3-MTHF ~ THF, which is in good agreement with the calculated ring-opening barriers (**Figure 2.5**). In addition, the diene selectivities are higher upon the stabilization of TS1 by the addition of a methyl group on the C1/C4 location. This shows that methyl substitution has a promoting effect on ring-opening, consistent with the degree of rate and selectivity control analysis described in the previous section **(Figure 2.4)**. This promoting effect has also been observed by Kumbhalkar *et al.*, who proposed a different ring-opening mechanism for 2-MTHF that involves 1,3-hydride shift from the C4 to the C1 position along with C1-O bond scission.[20] We were not able to locate such a transition state for 2-MTHF in our quantum chemical calculations. Additionally, in a study highlighting the hydrogenolysis of saturated cyclic ethers on ReO_x modified Rh/C, the same group has elucidated the effect of electron-donating substituents on the rate of C-O bond rupture.[68] They note a higher reactivity for the ring-opening of tetrahydrofurfuryl alcohol and 2-MTHF, compared to THF and THP. Other recent reports have also elucidated C-O bond rupture as the rate-limiting step in the hydrogenolysis of 2-MTHF and THP on different metal phosphides.[38,69–72] While the reaction pathways, product identity and distribution for hydrogenolysis are different from

dehydra-decyclization, the first step for both chemistries involves C-O bond activation and, to that extent, it is expected that the trends involving molecular substitution and this reaction step are similar.

2.4.5 Reaction kinetics of alkenols. Subsequent to ring opening, is alkenol dehydration on the surface to the respective diene. While the increased rates of reaction due to methyl substitution are consistent with more facile ring opening, which acts as the dominant surface reaction, it is possible that the increased rates observed are due to the formation of more readily dehydrated alkenols. Initially formed from THF as an alkoxide (**Scheme 2.1**), alkenols can rearrange (essentially desorb and re-adsorb through the hydroxyl group) before dehydrating to diene products. The dehydration activity of an alkenol may depend on the stability of carbenium formed upon its protonation; a more substituted carbenium may lead to a more facile rate of dehydration. 2-MTHF ring-opening from the C4-side re-

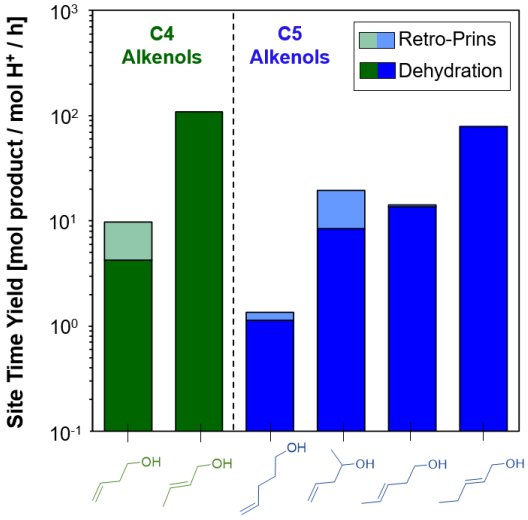

Figure 2.6. *Comparison of retro-Prins and dehydration Site-time yields (STY's) obtained for the various intermediate alkenols expected from the ring-opening of THF and 2-MTHF at 413 K. All experimental conditions are the same as in* ***Figure 2.7****.*

-sults in the formation of a more-substituted secondary alkenol (4-penten-2-ol), while only primary alkenols are obtained as a result of THF ring opening. It then follows that the experimentally observed higher reactivity of 2-MTHF may be due to the more facile dehydration of a secondary alkenol, as opposed to a more facile ring opening. It is therefore necessary to understand the dehydration of the relevant alkenol species, so as to experimentally verify whether or not ring opening truly exhibits a large degree of rate

control. To this end, we investigated the kinetics of alkenol dehydration through a second set of experiments feeding them directly as reactants.

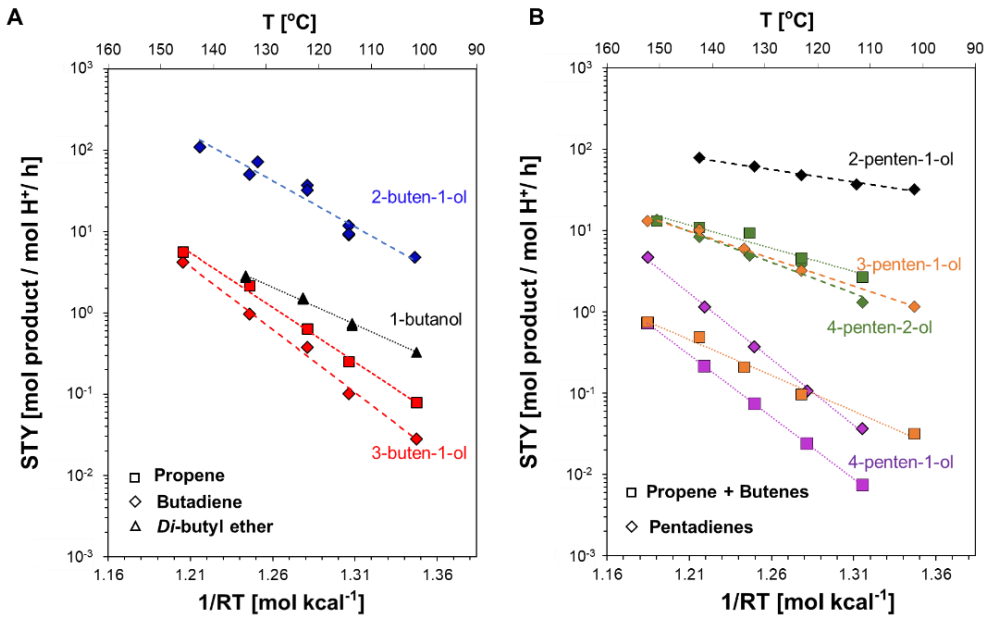

Figure 2.7(A) *Arrhenius plots for the rate of formation of propene, and butadiene from 2-buten-1-ol and 3-buten-1-ol respectively, and di-butyl ether from 1-butanol.* ***(B)*** *Arrhenius plots for the rate of formation of all C5 dehydration products (i.e., 1,3-pentadiene1,4-pentadiene, and isoprene) and butenes from 2-penten-1-ol, 3-penten-1-ol, 4-penten-2-ol, and 4-penten-1-ol, respectively. Partial pressure of both alkenols was 10.5 torr, whereas the partial pressure of 1-butanol was 5 torr. WHSV was maintained in the range 3.2-6.5 h^{-1}. All conversions were kept <10% for all species except 2-buten-1-ol, and 2-penten-1-ol; and <25% for 2-buten-1-ol and 2-penten-1-ol.*

Initial attempts to measure alkenol dehydration kinetics at reaction conditions relevant to THF dehydra-decyclization revealed facile alkenol dehydration; therefore, kinetic measurements were performed at lower temperatures (373-423 K) to maintain differential conditions. As shown in **Figure 2.6**, two four-carbon alkenols (3-buten-1-ol (3BOL) & 2-buten-1-ol (2BOL)) exhibit butadiene production rates differing by an order of magnitude; 2BOL with the alkene functional group closer to the hydroxyl group dehydrates faster than 3BOL and does not exhibit a retro-Prins pathway. Similar behavior was found for the dehydration of 2BOL and 3BOL on different solid acid catalysts like γ-Al_2O_3 and SiO_2-Al_2O_3 at 533 K; 2BOL is completely selective to butadiene while 3BOL leads to significant formation of propene through a retro-prins pathway.[73] Comparing the four and five-carbon alkenols, the overall rate of dehydration and retro-Prins condensation was comparable in both cases (**Figure 2.6**), where 2BOL and 2-penten-1-ol (2POL)

exhibited the highest rates of dehydration. Similarly, the rate of pentadiene formation from five carbon alkenols decreased as the alkene functionality moved further away from the C1 hydroxyl group. This behavior was observed over a range of temperatures as shown in **Figure 2.7**; the apparent activation barriers measured for all the five carbon alkenols in the temperature range 373-423 K are tabulated in **Table 2.4.** This suggests that alkenol intermediates obtained from the ring opening of THF or 2-MTHF will dehydrate at comparable rates. This in sharp contrast with the trend in the overall rate of furan conversion, where 2-MTHF undergoes dehydra-decyclization an order of magnitude faster than THF does **(Figure 2.5)**. We therefore conclude that the increased rate of furan dehydra-decyclization as a result of methyl substitution is in fact due to more facile ring opening since the kinetics of the subsequent alkenol dehydration does not appear to be affected.

Table 2.4 *Apparent activation barriers and Site time yields for the formation of Dehydration and retro-Prins condensation products from four and five-carbon alkenol feeds on HZSM-5 (Si/Al=140)* [a]

Reactant	Apparent activation energy (kcal mol^{-1})		Site Time Yield at 413 K (h^{-1})	
	Retro-Prins	Dehydration	Retro-Prins	Dehydration
3-buten-1-ol	30.9 ± 1.1	35.6 ± 1.5	3.83	5.58
2-buten-1-ol	-	26.5 ± 2.5	-	108.30
1-butanol	-	21 ± 0.8	-	5.21
3-penten-1-ol	20.3 ± 1.9	14.5 ± 1.0	0.50	8.39
4-penten-1-ol	35.2 ± 1.4	37.4 ± 1.2	0.22	1.14
4-penten-2-ol	13.3 ± 1.3	17.5 ± 1.1	10.5	8.38
2-penten-1-ol	-	7.1 ± 0.5	-	78.9

[a] *Experimental conditions are the same as indicated in* ***Figure 2.7****.*

The experimentally observed selectivity to both butadiene and propene using alkenol feeds (**Table A2.2** and **Table A2.3 in the Appendix**) are different than the corresponding values with THF as feed; 2BOL and 3BOL exhibit a higher and lower selectivity to butadiene, respectively. To understand this apparent discrepancy in alkenol

reactivity when fed directly versus when produced as intermediates through THF ring-opening, the rate of 3BOL dehydration was measured in the presence of a THF-cofeed at 413 K. It is important to note that THF does not react at these temperatures but will readily adsorb on Brønsted acid sites, competing with the alkenols for active sites as indicated by the comparable heats of adsorption (**Table 2.3**). While the overall rate of alkenol conversion decreased with increasing THF partial pressures, the suppression in the rate of propene production was greater than that of butadiene production, suggesting that 3BOL favors the dehydration pathway over retro-Prins chemistry at higher THF coverages **(Figure A2.7)**. This is consistent with the lower selectivity to butadiene observed with a pure THF feed, where the coverage of alkenol is expected to be significantly lower. Furthermore, it is improbable that the nature of active sites catalyzing dehydration and retro-Prins condensation of 3BOL are different. Rather, this observation likely reflects the difference in surface coverage effects on the respective elementary-steps for retro-Prins condensation and dehydration for 3BOL, limiting direct comparison of product distributions observed with alkenol and THF feeds. This finding does not contradict the earlier observation made in the absence of THF where 3BOL is favoring the retro-Prins pathway; rather, it highlights the dependence of 3BOL conversion on operating conditions.

2.4.6 Apparent kinetics of THF dehydra-decyclization. The apparent activation energies were calculated in the temperature range of 493-543 K (220-270°C) from the microkinetic model (**Scheme 2.1**, **Tables 2.2** and **2.3**). The model predicted values of 33.5 $\pm$ 1.8 kcal mol^{-1} for THF dehydra-decyclization and 33.7 $\pm$ 2.0 kcal mol^{-1} for retro-Prins fragmentation, which are in reasonable agreement with the experimental values of 33.1 $\pm$ 1.6 and 29.6 $\pm$ 1.7 kcal mol^{-1} , respectively (**Figure 2.8)**. It is instructive to comment on the similar activation energy values for the two pathways. The dehydra-decyclization to butadiene is controlled by a late transition state (TS1, in **Scheme 2.1**) in which the proton of the active site is fully transferred to THF, which undergoes ring opening at the C-O bond. In addition to these nuclear motions, the dominant (in terms of reactive flux) retro-Prins pathway, through TS11 (**Scheme 2.1**), involves concerted 1,2-hydride shift and C3-C4 bond breaking. The similar activation energies obtained from the calculations are primarily due to the fact that, although the 1,2-H-shift is rather spontaneous because it converts a primary carbocation to a more stable secondary one, the resulting carbenium is

not in turn stabilized by the conjugate base of the active site. As a result, the carbenium remains highly unstable and can access the C3-C4 bond breaking channel to propene (retro-Prins). Although it is difficult to ascertain which specific nuclear motion is responsible for the activation energy in this complex retro-Prins transition state (TS11), we believe that the energetically most demanding nuclear motion is the C-O bond vibration that leads to ring opening, which would explain why the butadiene and retro-Prins paths have so similar activation energies.

Under the reaction conditions investigated, the active sites are predominantly occupied by THF (**Figure 2.9**), decreasing from a 0.76 monolayer (ML) to 0.25 ML coverage as the reaction temperature is increased from 493 K to 543 K. The surface coverages of all other intermediates are negligibly small (< 0.01 percent, see **Figure 2.9**). The relatively low coverage of alkenol intermediates together with their absence in the product stream implies facile alkenol dehydration, consistent with the experimental kinetics of alkenol dehydration. Extrapolating rates of alkenol dehydration to 503 K, the rate of 3BOL dehydration proceeds four orders of magnitude faster than THF dehydra-decyclization.

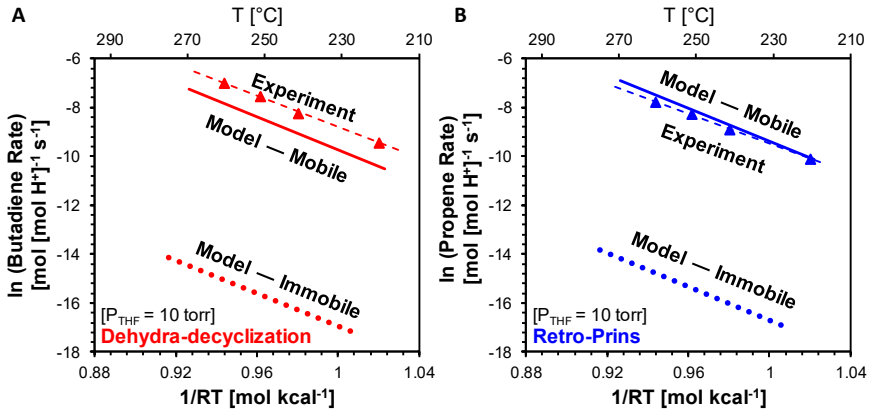

Figure 2.8. *Arrhenius plots in the temperature range of 220-270 °C from model and experiments for* ***(A)*** *the dehydra-decyclization to butadiene and* ***(B)*** *the retro-Prins to propene reactions of THF with H-ZSM5. WHSV = 1.83 h^{-1}. Dotted lines show the model fit by taking into account the translational entropic corrections listed in* ***Sec 2.4.2*** *and corresponding free energy profiles are shown in* ***Figure 2.2*** *and* ***2.3***.

THF reaction orders were determined by varying its partial pressure from 2 to 100 torr (**Figure 2.10** and **Table 2.2**). For both the dehydra-decyclization and the retro-Prins fragmentation reactions, the model predicted the same reaction order of 0.65, in satisfactory agreement with the experimental value of 0.41 (for both reactions) at 543 K. At this temperature, the THF coverages varies in the range of 0.06-0.77 ML as the THF partial

pressure varies from 2 to 100 torr. As expected, the THF reaction order decreases with decreasing temperature on account of the higher THF coverage at low temperatures. For example, at 503 K, the THF coverage increases from 0.38 ML to 0.97 ML in response to the THF partial pressure change from 2 to 100 torr, accordingly the THF reaction order is reduced to 0.22 for both reactions. We should note that the two pathways have similar reaction orders on account of the fact that the corresponding rate-limiting steps *immediately follow* THF adsorption.

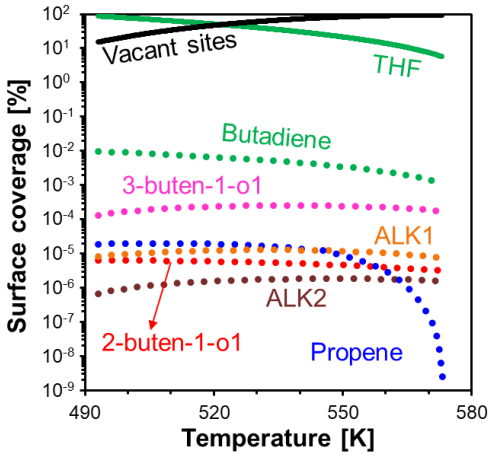

Figure 2.9. *Surface coverage (at 5% of THF conversion) as a function of temperature predicted from the microkinetic model. Only the four most abundant surface species are shown here. Reaction conditions: P_{THF} = 10 torr, WHSV was adjusted to achieve 5% conversion at all temperatures.*

Through steady state switches between THF and deuterated THF (THF-D8, **Figure 2.11**), we observed the presence of what appears to be a primary kinetic isotope effect for both the rate of butadiene and propene formation (KIE = 1.6-1.8). However, careful examination of the vibrational modes of the ring-opening transition state reveals compounded secondary kinetic isotope effects. Specifically, the ring-opening transition state involves more than just proton transfer from the active site (fully completed in the transition state) and C-O bond cleavage.

The most salient nuclear motion that contributes to the compounded secondary KIE is the out-of-plane C1-H bend as the C1 carbon undergoes sp^3 to sp^2 re-hybridization upon ring opening (formation of primary carbocation). Furthermore, deuteration of THF affects numerous other vibrational frequencies in the reactant and transition states, mainly in the 1400-1550 cm^{-1} range; for example, H-C-H scissoring at the C1, C2 and C4 positions.

Ultimately, these various compounding effects result in a calculated KIE of 1.57, in agreement with the experimentally measured value.

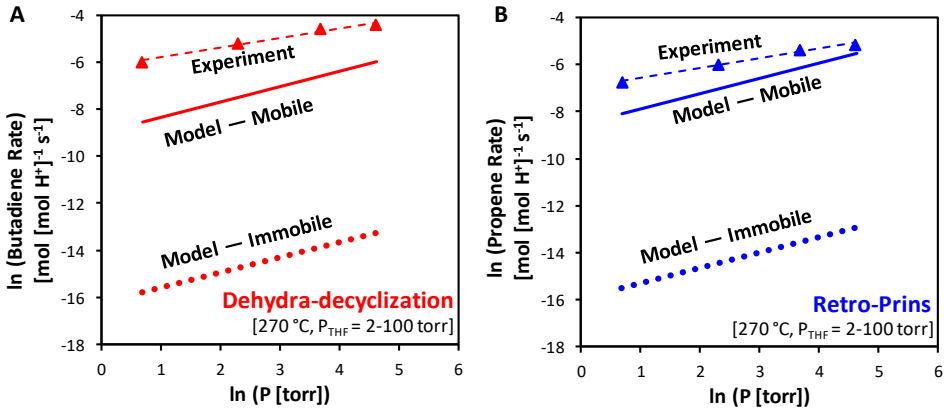

Figure 2.10 *Reaction rate as function of partial pressure of THF at 270°C for* ***(A)*** *the dehydra-decyclization to butadiene and* ***(B)*** *the retro-Prins to propylene reactions in HZSM-5. Dotted lines show the model fit assuming all adsorbates and transition states are immobile; the corresponding energy profiles are shown in* ***Figure 2.12 and 2.13*** *by the dotted lines. Solid lines show the model fit by taking into account the translational entropic effects on surface species following the scheme described in Section 2.3.2; the corresponding free energy profiles are shown in* ***Figure 2.2 and 2.3****.*

2.4.7 Entropy of surface species. The agreement between experimental and model apparent barriers and reaction orders does not extend to the absolute predicted rates of butadiene and propene if the translational freedom of the intermediates/TSs is restricted. As shown in **Figures 2.8** and **2.10**, the 'immobile' model differs in absolute rate from the experimental data by orders of magnitude. It is quite typical in mechanistic studies to assume that species (intermediates and especially transition states) under confinement are immobile and to compute their Gibbs free energies by considering only their vibrational entropy. As noted in the **Section 2.2** and also demonstrated elsewhere,[59–62] this simplifying assumption is justified for surface species that are stabilized by covalent (e.g., surface alkoxides) or strong hydrogen bonds with the framework. However, visual inspection of transition states TS1, TS2 and TS11 and verification by formal means (vibrational frequency and NBO analyses) reveals that the proton-activated bond-cleaving transformations are 'unimolecular' in nature. The associated activated complexes are therefore not tethered to the active site and are mobile within the confines of the pore, on account of the active site proton being completely transferred to THF. In a comparison 'mobile' model (**Figures 2.8** and **2.10**), these transition states are therefore further

stabilized by accounting for their additional entropic freedom in two dimensions. This 'mobile' interpretation of the transition states brings the predicted rates of reaction within error of the experimentally measured absolute rates for both butadiene and propene production.

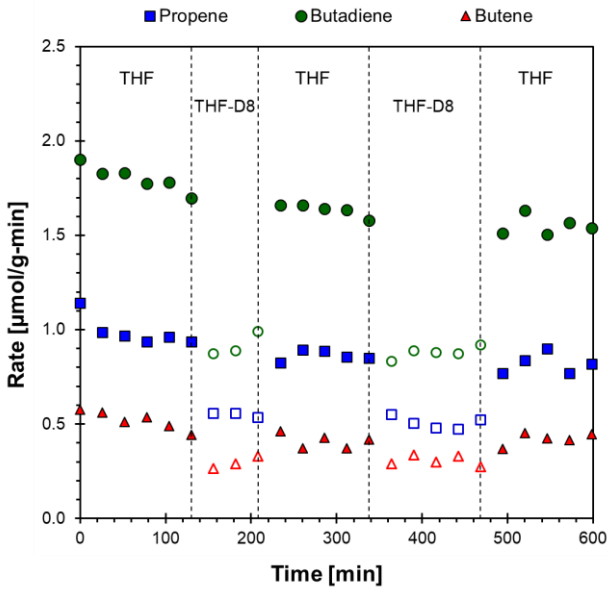

Figure 2.11 *Mass-normalized rates of formation of butadiene (green, ●), propene (blue, ■), and butenes (red, ▲) as a function of time-on-stream. The feedstock was periodically switched from tetrahydrofuran to deuterated D-8 tetrahydrofuran, resulting in a reduction in the formation rates of all three products. Filled symbols indicate rates measured using THF as a reactant, with open symbols indicating rates with THF-D8 feed under identical conditions. (Reaction conditions: T =503 K, P_{feed}=10.3 torr (balance He) and <1% conversion over HZSM-5 (Si/Al 140)).*

The impact of the 'mobile' model assumption of increased entropic freedom of the surface species also alters the reaction energy diagrams. In **Figures 2.12** and **2.13,** we compare the free energy profiles for the dominant dehydra-decyclization and retro-Prins fragmentation pathways with and without translational mobility in the pore. Two-dimensional translational mobility leads to further stabilization of transition states TS1, TS2, TS10 and TS11 by *ca*. 7-8 kcal mol^{-1}. This reduction in the intrinsic free energy barriers does not alter the apparent activation energy, but increases the pre-exponential factor by three orders of magnitude, reflecting the translational entropy contribution (within the 'mobile' assumption) to the reaction rate. In both 'mobile' and 'immobile' assumptions, THF ring opening remains the highest energy transition state and most rate limiting reaction for butadiene formation. In **Figure 2.14**, the entropy changes along the

main dehydra-decyclization pathway are depicted to convert tetrahydrofuran to butadiene and water. The 'immobile' model depicted in black indicates substantial reduction in entropy upon adsorption within the MFI micropore (i.e., loss in translational degrees of motion). Each intermediate and transition state then remains at low entropy before desorption as two species (butadiene and water) and a significant increase in overall entropy. The entropy reaction profile (red in **Figure 2.14**) of the 'mobile' model has complexity arising from the differences in transition state structure. Again, entropy decreases significantly upon adsorption of THF on the Brønsted acid site of HZSM-5. However, transition states TS1 and TS2 exhibit complete proton transfer from the acid site; they regain two degrees of translational entropy. In the dehydration transition state TS10, while the proton back-donation from the substrate is incomplete, complete proton transfer

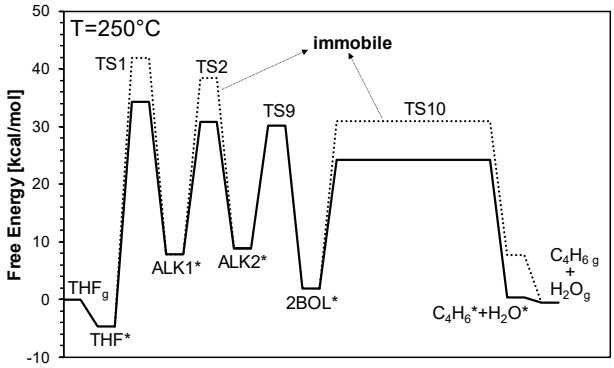

Figure 2.12 *Free energy profile of dominant dehydra-decyclization pathway (the 2BOL path in* ***Figure 2.2****) to butadiene from THF in HZSM-5. Dotted line indicates the corresponding energy profile without considering translational entropic effects (or equivalently assuming all adsorbates are immobile). Subscript 'g' indicates gas-phase species, and '*' marks surface species.*

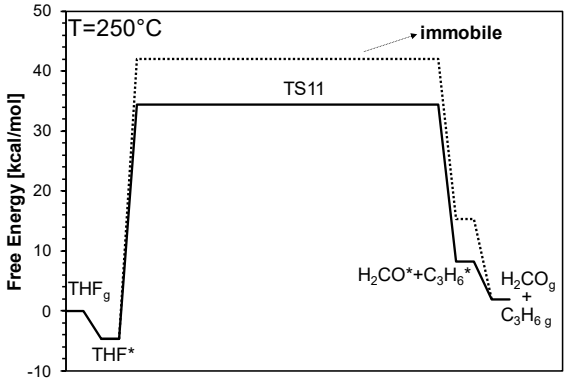

Figure 2.13 *Free energy profile of dominant retro-Prins fragmentation (the 'direct' path in* ***Figure 2.3****) to propene from THF in H-ZSM5. Dotted line indicates the corresponding energy profile*

without considering translational entropic effects (or equivalently assuming all adsorbates are immobile). Subscript 'g' indicates gas-phase species, and '' marks surface species.*

from the acid site is also observed with formation a water molecule that gains two degrees of translational entropy. These three transition states exhibit an increase in entropy and rate enhancement due to the increased mobility of their short-lived reaction transition states.

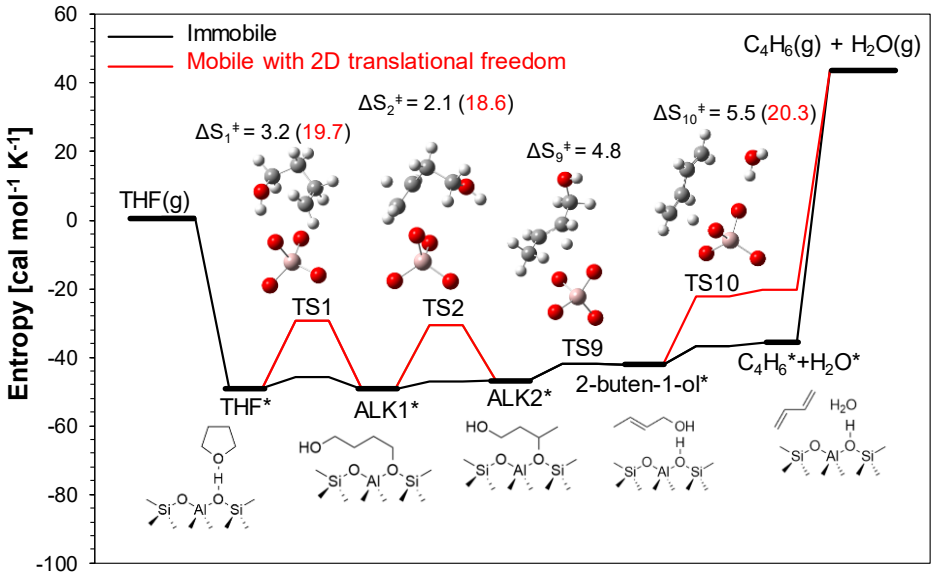

Figure 2.14 *Entropic states of intermediates and transition states along the main pathway for tetrahydrofuran dehydra-decyclization to butadiene for immobile (black) and mobile (red). The corresponding states under the mobile assumption used in this work is shown in red line. Entropy of activation of each step is provided in cal mol^{-1} K^{-1}.*

2.5 Conclusions. In this work, the dehydra-decyclization reaction and retro-Prins fragmentation of THF was examined in H-ZSM5 to butadiene and propene, respectively, using a combined approach of electronic structure calculations, reaction kinetics experiments and microkinetic modelling. A reaction network consisting of fifteen elementary surface reactions was proposed and the calculated energetics were used to parameterize a microkinetic model. Reaction path analysis revealed that only six elementary steps are kinetically relevant to the conversion of THF. Dehydra-decyclization proceeds sequentially through ring-opening to a primary surface alkoxide, 1,2-hydride shift to a secondary alkoxide, deprotonation to 2-buten-1-ol, which finally dehydrates to butadiene via an E2 mechanism. Two other alkenols proposed in the reaction network, *viz.* 3-buten-1-ol and 3-buten-2-ol, do not seem to be involved substantially. The much faster

dehydration rate of 2-buten-1-ol compared with 3-buten-1-ol as well as the absence of retro-Prins condensation when feeding 2-buten-1-ol in experiments further corroborates the dominant role of 2-buten-1-ol in butadiene production from THF in H-ZSM5. The side product propene can be formed directly from THF in a single step or from the primary surface alkoxide. A degree of control analysis suggests that the ring-opening step is both rate-limiting for butadiene production and selectivity-controlling. The rate-limiting nature of C-O bond rupture was experimentally validated by comparing the rates of decomposition of intermediate four and five-carbon alkenols expected from THF and 2-MTHF, respectively. The model predictions are in good agreement with the experimental measurements for the apparent activation energy, reaction order and selectivity. It is important to allow some translational freedom for the weakly bound intermediates in order to quantitatively describe the rate of reaction.

Chapter 3

Adapted Gas Chromatograph for Automated Catalytic Evaluation for Vapor-Phase Flow Chemistries

* Reproduced with permission from Kumar, G.*; Bossert, H.*; McDonald, D.; Chatzidimitriou, A; Ardagh M.A.; Pang, Y; Lee, C; Tsapatsis, M; Abdelrahman O.A.; Dauenhauer, P.J. Catalysis-in-a-Box: Robotic Screening of Catalytic Materials in the Time of COVID-19 and Beyond. *Matter* **2020**, *3(3)*, 805-823. (* *Equal Contribution*) https://doi.org/10.1016/j.matt.2020.06.025

3.1 Conspectus

There has been a gradual transition away from traditional, labor-intensive materials testing techniques to new automated approaches without compromising on data quality and at costs viable for academic laboratories. Reported here is the design and implementation of an automated micro-flow reactor for catalyst evaluation condensing conventional laboratory-scale analogues within a single gas chromatograph (GC), enabling the control of relevant parameters including reactor temperature and reactant partial pressures directly from the GC. Inquiries into the hydrodynamic behavior, temperature control, and heat/mass transfer were sought to evaluate the efficacy of the micro-flow reactor for kinetic measurements. As a catalyst material screening example, a combination of four Brønsted acid catalyzed probe reactions, namely the dehydration of ethanol, 2-propanol, 1-butanol, and the dehydra-decyclization of 2-methyltetrahydrofuran on a solid acid HZSM-5 (Si/Al 140), were carried out in the temperature range 403-543 K for the measurement of apparent reaction kinetics. Product selectivities, proton-normalized reaction rates, and apparent activation barriers were in agreement with measurements performed on conventional packed bed flow reactors. Furthermore, the developed micro-flow reactor was demonstrated to be about ten-fold cheaper to fabricate than commercial automated laboratory-scale reactor setups and is intended to be used for kinetic investigations in vapor-phase catalytic chemistries, with the key benefits including automation, low cost, and limited experimental equipment instrumentation.

3.2 Introduction

While the past two decades have produced a wave of new catalyst materials including hierarchical zeolites,[74] MOFs,[75] single-atom surfaces,[76] intermetallic structures,[77] and other low-dimensional materials[78], testing these catalysts to determine structure-performance relationships has traditionally remained reliant on labor-intensive

catalytic evaluation based methods. Such in-person material evaluation tends to be a multi-step process, where the traditional approaches have involved qualitative screening techniques[79–83] in search for the 'best' catalyst for the envisioned application, followed by kinetic interrogations of the shortlisted catalysts to establish reactivity, selectivity, and stability trends and subsequent detailed mechanistic inquiries into reaction pathways.[80,83] To continue this effective general approach to assessing materials performance, laboratory operations must transition to more automated methods requiring only minimal manual intervention.

The challenge of transitioning laboratories to more robotic operations arises from the complexity of catalytic materials testing. In particular, kinetic studies frequently utilize differential reactors to measure either initial or steady state rates of reaction over a wide range of operating conditions. For reactions occurring on gas-solid interfaces, such measurements are typically performed on packed bed flow reactors (PBRs),[83–88] which remain the workhorse of any heterogeneous catalysis laboratory. Importantly, laboratory-scale cost-effective PBRs are often custom-fabricated, and they require constant human monitoring owing to multiple independent process control elements, and separate, often non-coupled, reaction and separation/quantification components.[80,83] The manual interventions on these equipment typically involve operations like switching valves, and/or precisely altering reaction conditions at determined intervals. Furthermore, data analysis from common analytical instruments on these PBRs (like gas chromatography units (GCs)) remains largely manual. Together, these factors lead to cumbersome experimentation and analysis, especially in scenarios requiring kinetic measurements for many catalysts or assessing catalyst stability on-stream for prolonged periods.

The ability to perform high fidelity kinetic studies with minimal human oversight would greatly reduce the labor and costs associated with catalyst development and discovery, and recent research efforts reflect this interest.[89] Flow reactors[90–92] as well as control algorithms[51,93–95] are increasingly integrated with online analytical tools to collect and analyze kinetic data without user supervision. However, these experimental systems are almost always fabricated for a specific targeted application, and important heat and mass transfer considerations are often not explicitly reported, dissuading other research groups to invest time and resources to fabricate them. One straightforward implementation

of low-cost automated microreactors with broad applicability among previously reported approaches is the *pulsed*-flow technique, which involves dosing a pulse of reactant over a catalytic material to study product distribution trends. This approach is readily integrated within a commercial gas chromatograph (GC),[18,45,96–100] but the transient nature of the technique limits kinetic parameter estimation. In addition, the product distributions under such transient conditions may vary from corresponding steady-state values.[87] Extending this approach to modify existing GCs, enabling reliable but largely automated kinetics measurements in a continuous flow method while also facilitating safe laboratory operation has been the focus of this report.

Here, the automated vapor-phase *continuous* micro-flow reactor is described as integrated within a gas chromatograph (GC) unit capable of measuring the reaction kinetics of vapor-phase catalytic chemistries with volatile feeds (either gases or vaporizable liquids). The design and implementation of the setup is first presented. This is followed by detailed investigation of heat and mass transfer characteristics under cold-flow as well as reaction conditions by a recently developed online toolbox (GradientCheck) reported by Ribeiro and co-workers.[101] Thereafter, kinetic parameters (namely turnover rates, apparent activation barriers, and product distributions) for acid-catalysed vapor-phase dehydration of three alcohols (ethanol, 2-propanol, 1-butanol) and a cyclic ether (2-methyltetrahydrofuran) on a solid acid catalyst (HZSM-5, Si/Al 140) are measured and compared with previously reported values under similar conditions. To address the labor-intensive nature of chromatogram data handling, a chromatogram analysis tool is developed in-house and integrated to the experimentation workflow for automatic GC peak detection and peak area quantification.

The fabricated setup as well as the reported data analysis tool are primarily intended for materials researchers to obtain kinetic data of vapor-phase chemistries with minimal user-supervision and safe working conditions. The provided information along with the detailed analysis of the performance of the device enable simple implementation in any laboratory that is testing catalytic materials. Extensive supporting information provides detailed parts lists and instructions for implementation with both hardware and software modifications **(Appendix, Section A3.1)**. Additionally, the provided analysis means that immediate transition of a laboratory to safer, more robotic catalyst materials testing can be

conducted with the justification that resulting data achieves the quality obtained using conventional methods.

3.3 Methods

This section discusses a detailed design and implementation of the reactor, independent temperature measurements to investigate axial variations under non-reaction conditions, and residence time distribution studies within the micro-flow reactor. The methodology used in the apparent kinetic measurements for all the example reactions are also discussed. Detailed heat and mass-transfer characteristics specific to each of the probe reactions are discussed in the **Appendix (Section A3.4).**

3.3.1 Design and Implementation. The following modifications were performed on an Agilent 7890 GC unit to convert it to the micro-flow reactor **(Scheme 3.1)**. The automatic liquid sampler (ALS) was uninstalled, and the front inlet of the GC was installed as an auxiliary heater. The flow control to this front inlet (housing the catalyst bed) was achieved using upstream referenced mass flow controllers (MFC, Vici Valco Model 100) in conjunction with an auxiliary electronic pressure controller (EPC, Agilent G3452) (gas delivery details can be found in **Section A3.1, and Figure A3.4**). Given the upstream reference configuration of the MFC, a fixed and repeatable gas flow rate could be delivered for a particular supply pressure set by the EPC. Gas flowrates delivered by the MFC were therefore calibrated as a function of the auxiliary EPC pressure set point, which could be directly controlled through the GC **(Figure A3.4)**.

A splitless inlet liner (Agilent, 5190-2293) was utilized as the reactor tube (I.D.= 4 mm) **(Figure A3.2)**. The split vent for the front inlet was blocked using a capping nut (Swagelok SS-200-P); doing so forced gas flows exiting the reactor through one single outlet **(Figure A3.1 and A3.3)**. The back inlet was used for chromatography, where analyte separation was performed by an HP-PLOTQ column (Agilent, 19091P-QO4), connected to a quantitative carbon detector (QCD, Polyarc^{TM})[47] in conjunction with a flame ionization detector (FID).

Two six-port valves (Vici Valco, DC6UWE) (shown in **Scheme 3.1**; identified as V-1 and V-2 in **Scheme 3.2**) housed within a heated valve box (Agilent G1581A) were

used to route gas flows and perform gas-phase injections on the back inlet utilized for chromatography. Valve V-1 was installed as a gas-sampling valve; V-2 was installed as a

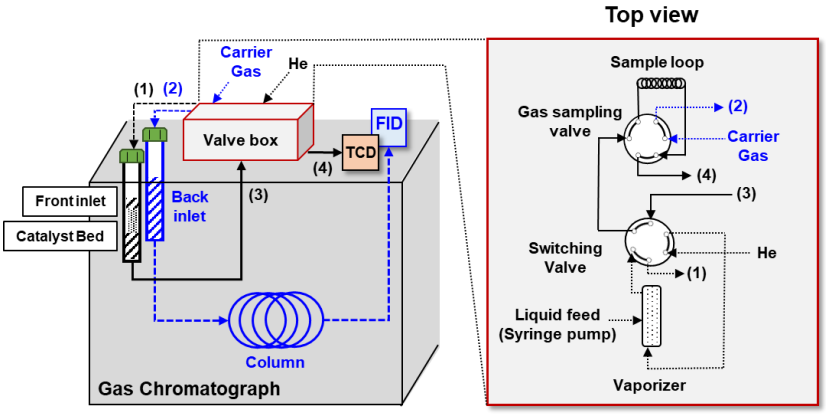

Scheme 3.1 A schematic for the vapor-phase micro-flow reactor integrated within a gas chromatograph (GC). *The instrumentation of the setup consists solely of a typical gas chromatograph, where the* ***front inlet*** *is used as a packed bed reactor. The gas flows are routed to either bypass or contact the catalyst bed by using a combination of two* ***six-port valves*** *housed within a* ***heated valve box unit****, and a thermal conductivity detector* ***(TCD)*** *is used for online reactor effluent monitoring. The* ***back inlet*** *is utilized for effluent quantification and consequently rate measurements through periodic gas-sampling followed by separation by a GC column and quantification through a flame ionization detector* ***(FID)****.*

switching valve **(Scheme 3.2 and Figure A3.1)**. A pressure gauge upstream of the reactor was used to monitor the pressure drops across the catalyst bed, by comparing to a reference pressure measured in absence of a catalyst bed (indicative of pressure drop due to process tubing and fittings). A vaporization section was housed within the heated valve box, and consisted of a ¼" tube (316 SS) filled with deactivated quartz chips (SiO_2, 4-20 mesh, Sigma Aldrich) to facilitate static mixing and effective vaporization of the injected liquid **(Figure A3.1)**. A thermal conductivity detector (TCD) placed in-line with the flow exiting the reactor stream was used as an online detector **(Scheme 3.2)**. Both front and back inlets were insulated with fiberglass insulation sheet (McMaster) to ensure that bed temperatures were close to the inlet wall temperature controlled by the auxiliary heater; this was later confirmed by secondary measurements on an empty bed.

Scheme 3.2 depicts the overall experimental methodology for performing kinetic measurements using the setup in three different configurations which are discussed below. The different valve positions to operate the setup for these specific configurations are also discussed, and listed in **Table 3.1**.

(a) Catalyst pre-treatment mode (Configuration 1; No reactant feed): Catalyst powders were pressed and sieved into aggregates of 500-1000 μm and placed between deactivated quartz wool (Restek 24324) to keep the catalyst bed in place. Typically, ~25-30 mg catalyst was used for the kinetic measurements. Catalyst masses were restricted to keep the bed located in the normalized height h/H (h is the height for packing the bed; H is total height of the liner) range of 0.15-0.35, where differences between actual and GC indicated temperature were found to be negligible; this is discussed in more detail in **Section 3.5.1**. Following the placement of the reactor in the front inlet, catalysts were pre-treated in air (99.997%, Minneapolis Oxygen) at 673 K for five hours at a ramp rate of 3 K min^{-1} **(Scheme 3.2a)**. After pre-treatment, the catalyst was cooled down to reaction temperature, and the gas supply was switched to He (99.995%, Matheson). The catalyst was kept at reaction temperature and purged with He for at least 30 minutes prior to reactant introduction.

(b) Reactor bypass mode (Configuration 1; reactant feed on): In the same configuration, liquid reactants were then pumped into the vaporization section through a 1/16" PEEK capillary line (0.01" ID) using a syringe pump (74905-04, Cole Parmer) and swept by the He stream exiting the reactor. In this way, the reactant stream bypassed the reactor by placing the vaporization section downstream of the reactor **(configuration 1, Scheme 3.2a)**. The valve box temperature was maintained at 473 K to ensure that all species were retained in the vapor phase. The vaporized reactant stream was swept through the vaporization section to V-2 **(Scheme 3.2b)** and routed to the TCD after filling the sampling loop located on V-1. Prior to introducing the reactant stream to the reactor, a steady reactant stream was ensured by observing a stable TCD signal for at least 15 minutes. Periodic gas sampling injections in this bypass configuration allowed for the total carbon quantification to gauge carbon balances during reaction.

(c) Reactant introduction and product quantification mode (Combination of Configurations 2 and 3): Once a stable vapor stream of reactant was established, V-2 was switched to direct the flow of He through the vaporizer section first (i.e., after the V-2 switch, the vaporizer becomes upstream of the reactor). The vaporized stream of reactants thus passed through the reactor and contacted the catalyst bed **(configuration 2, Scheme 3.2b)**. Effluent from the reactor continued to fill the sample loop attached to V-1 and

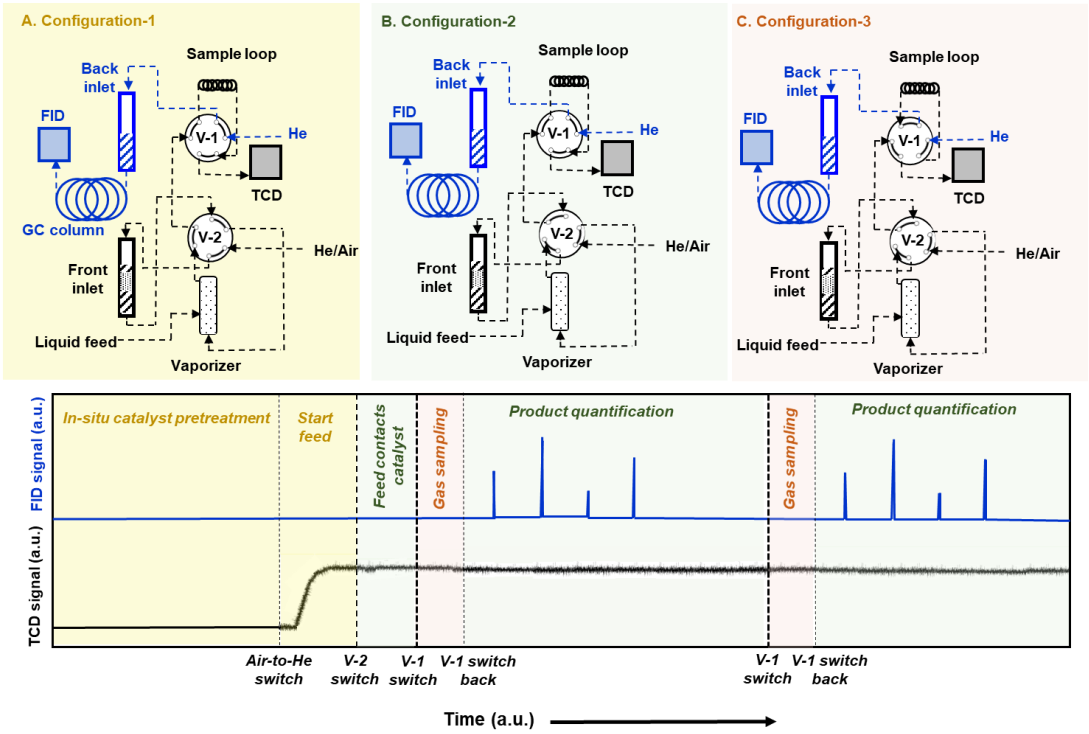

Scheme 3.2 Methodology for vapor-phase micro-flow reactor integrated within a gas chromatograph (GC). *Catalyst samples are loaded into the front inlet liner of a GC and reaction kinetics are studied by operating the setup in three configurations i)* ***in-situ catalyst pre-treatment mode (Configuration 1; No feed (A)):*** *Catalysts are calcined in-situ in flowing air at 673 K and then cooled down to reaction temperature and the carrier gas is switched from Air to He; ii)* ***Reactant dosing in bypass mode (Configuration 1; Feed on (A)):*** *A syringe pump delivers a steady flow of liquid reactant to the vaporizer, bypassing the reactor, and is routed directly to the online detector (TCD) till a stable signal is observed; and iii)* ***Reactant introduction and product quantification mode (Combination of Configurations 2 and 3 (B & C)):*** *The vaporized reactant stream is contacted with the catalyst bed in* ***configuration 2****, followed by periodic gas sampling* ***(configuration 3)*** *leading to the separation and quantification of products through QCD/FID.*

subsequently passed through the online TCD. Quantitative analysis of the reactor effluent was achieved by periodically switching the gas-sampling valve (V-1) at the start of every chromatography analysis **(configuration-3, Scheme 3.2c)**. This effectively allowed for the quantitative transfer of information from the reactive front inlet portion of the GC to the analytical chromatography back inlet portion. Helium carrier gas carried the contents of the sampling loop through the GC column to the QCD/FID for separation and quantification, and V-1 switched back after the sample injection was complete (0.5 min).

Configured this way, all kinetic measurements were performed in downflow mode. Notably, the setup could be operated in either of the three configurations without any

manual intervention. This ease of operation was due to the integration of all control elements within the GC circuitry and software without the use of any programmable logic controllers (PLCs) and/or customized LabView programs. These benefits are specifically listed below (see **Section A3.1.2 in the Appendix** for details on method development in (ChemStation ver 8.2.1) to allow control of all reactor parameters directly from method files):

(i) Reaction temperatures could be varied by adjusting the front inlet temperature (installed as an auxiliary heater) in the corresponding method files.

(ii) V-2 switching from bypass-to-reactor mode, as well as V-1 injection to the back inlet for product separation/quantification were also controlled directly through ChemStation method files.

(iii) Gas flows were set by calibrating the MFCs on auxiliary EPC (set in method files) with the final flowrates at the TCD outlet.

We note that the methodology described here is for the specific application reported, and can be easily tuned to other applications. For example, the choice of online detector (TCD in this work) is up to the user, and even the absence of an online detector and a methanizer (a quantitative carbon detector, POLYARC in this work) does not compromise the performance of the setup. Secondary detectors such as a mass spectrometer can be added to augment the quantitative information with real-time product identification. Similarly, for the reactant delivery, if reactants need to be introduced only for a short period of time (< 5-10 mins), an automated liquid sampler (ALS) can be used for a continuous pumping of reactants and can essentially act as a syringe pump. Indeed, if preliminary product distributions on a variety of different materials is the only intended application, a much simpler version of this setup with pulsed dosing of reactants followed immediately by separation and detection of products can be utilized, as highlighted by our earlier works.[18,45] While we use syringe pumps for liquid delivery, gaseous reactants can also be dosed using a separate gas line/s equipped with MFC/s. Total reaction pressures in excess of atmospheric levels can be achieved by using back-pressure regulator, and we have been to achieve pressures as high as ~100 psi with this simple modification, possibly allowing for moderately high-pressure chemistries to be probed (e.g. hydrodeoxygenation). In short,

there are many conceivable modifications using hardware that can be readily integrated with the GC depending on the specific application, rendering this approach versatile.

3.3.2 Temperature variations under non-reacting conditions. Temperature measurements were obtained on the front liner packed with deactivated quartz wool by inserting a 1/16" thermocouple (Omega). This 'empty reactor' was maintained at a particular set temperature as indicated by the GC for at least 20 minutes prior to every measurement, and the measurements were repeated in at least 10 different axial positions along the length of the liner.

3.3.3 Hydrodynamic behavior under non-reacting conditions. Residence time distributions (RTD) were measured to establish the range of flowrates under which flow in the setup was sufficiently plug-flow. All residence time studies were conducted by connecting the reactor effluent directly to the inlet of the TCD, so as to minimize the volume between the point of injection and detection. The reactor inlet was packed with deactivated quartz wool and maintained at 523 K; pulses of liquid ethanol were used as tracer. Liquid injections of ethanol pulses were manually performed with a 0.5 μL syringe (Agilent). Tracer identity is unlikely to change the hydrodynamic behavior under non-reacting conditions,[102] and the results obtained with ethanol are assumed to be broadly applicable. Typical injection volumes were 0.4 μL, and the experiments were conducted at low carrier flowrates (13-40 sccm) to capture the transition from axially dispersed to a non-dispersed regime.

3.3.4 Catalytic evaluation. Comparison of the turnover rates of reactions involves the calculation of site time yields (STYs) **(Eq. 3.1)**. For Brønsted acid catalysed chemistries, this calculation requires normalizing mass-based rates of reaction by the total Brønsted acid site density (BAS). The Brønsted acid site density (BAS, N_{H^+}) of the catalyst (HZSM-5) was measured by the quantification of butenes resulting from the Hofmann elimination of tert-butylamine using reactive gas chromatography (RGC) methodology described elsewhere,[103] and the results are discussed in the supporting information **(Section A3.2)**. These values (N_{H^+}) were used in the calculation of site-time yields **(Eq. 3.1)** in all probe reactions.

$$STY_i = \frac{F_i}{m_{cat.} N_{H^+}} = \frac{[mol\ product_i/h]}{[g][mol\ H^+/g]} \tag{3.1}$$

All kinetic experiments were performed under near-differential conversions (< ~15%) for a given feed by adjusting the weight-hourly space velocities (WHSVs). The reactions were investigated at ~25 torr partial pressure of reactant. Alcohol dehydration reactions were carried out in the temperature range 388 K - 483 K, whereas 2-methyltetrahydrofuran (2-MTHF) dehydra-decyclization was conducted in the temperature range 463-543 K. Due to an abundant literature on alcohol dehydration on solid acids, kinetic data obtained from the micro-flow reactor were compared with previously reported values. For the case of 2-MTHF dehydra-decyclization, however, the kinetic parameters obtained on the micro-flow reactor were directly compared with measurements performed on a traditional packed bed reactor as described in our earlier work.[104] Minimal catalyst deactivation was observed after initial transients for alcohol dehydration kinetics under the investigated conditions, and the rates reported here are steady-state values. Replicate experiments were carried out using randomized reactor temperature sequencing to minimize any systematic errors. Significant catalyst deactivation was observed during 2-MTHF dehydra-decyclization, and the methods to correct for deactivation to report initial rates are described in detail in **Appendix Section A3.3.**

All carbon balances closed to within ± 10%. Pressure drops across the reactor were maintained below 13-16% of total pressure for all kinetic experiments. Error bars represent the 95% confidence interval on at least three independent measurements, unless otherwise stated.

Table 3.1 *Possible valve positions and the corresponding configurations as highlighted in* ***Scheme 3.2****.*

Valve position		**Gas**	**Function**	**Configuration**
V1	**V2**			
Off	Off	Air	Calcination	1
Off	Off	He	Bypass	1
Off	On	He	Reaction	2
On	On	He	Reaction – Sample injection	3

3.4 Materials

Ethanol (200 Proof, ≥99.5%, Sigma Aldrich), 2-propanol (≥99.5%, Sigma Aldrich), 1-butanol (≥99.5%, Sigma Aldrich), and 2-methyltetrahydrofuran (2-MTHF, ≥98%, stabilized with BHT, TCI Chemicals) were used without further purification. Ammonium form of a high silica ZSM-5 (Si/Al=140) (Zeolyst CBV28014) was calcined ex-situ under airflow (~40 sccm) (zero grade, Minneapolis Oxygen) at 823 K for 10 hours at a ramp rate of 3 K min^{-1} (Lindberg Blue M tubular furnace). An exhaustive list of all major instrumentation parts as well as a manual guide for both hardware and software modifications on an existing GC to fabricate the setup is included in the SI **(Section A3.1, Table A3.1).**

3.5 Results and Discussion

3.5.1 Reactor temperature distribution - unreactive conditions. Laboratory-scale fixed-bed reactors conventionally involve heat transfer across a temperature-controlled wall, and gradients between the bulk phase in the reactor and the wall might lead to non-isothermal conditions inside the reactor. Similarly, a GC inlet is heated by a cartridge heater, and the controlled temperature is that of the inner inlet wall. To gauge the differences between the differences between the reactor set temperature and the actual temperature of the catalyst bed, independent measurements at different temperature set points as a function of axial positions inside the liner were conducted, and the results are shown in **Figure 3.1**. Notably, the axial region in the range $0.15 < h/H < 0.35$ showed <1% difference between measured and set temperature under non-reacting conditions. Furthermore, the deviation in temperature from the setpoint outside this region was significantly higher (> 10%) at higher temperatures (> 473 K). These results highlight that the axial location of the catalyst bed is sensitively linked to the temperature control attainable on this setup.

It is important to note that these measurements only probe the temperature distribution of the reactor under non-reacting conditions. Temperature gradients across the bed as well as within catalyst particles may also develop under reacting conditions, depending on reaction thermodynamics. As expected, highly endo-/exothermic reactions

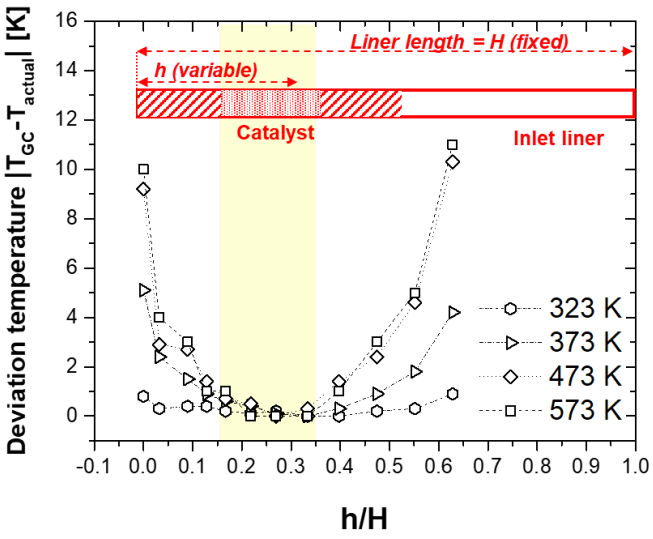

Figure 3.1 *The deviation in set and actual temperature as a function of the non-dimensionalized height of the splitless inlet liner used to hold the catalyst bed.*

are more likely to result in axial temperature gradients.[105] We have evaluated the temperature distribution of the catalyst bed under the reaction conditions for the probe reactions, and the results are discussed in **Section 3.5.3**.

3.5.2 Residence time distributions. Axial mass dispersion in packed bed reactors can limit the accurate determination of kinetic parameters. This manifests in the form of channelling and dead volumes, leading to back-mixing and non-plug flow hydrodynamics.[106] The extent of dispersion is described by, and inversely proportional to, the Peclet number **(Eq. 3.6)**, and packed beds can only be assumed to be free from axial dispersion effects for Pe >100.[106] The extent of axial dispersion is inversely proportional to the bed length, and RTD experiments were therefore performed on the reactor packed with quartz wool alone mimicking the limit $L \rightarrow 0$.[47]

Figure 3.2 depicts the experimental residence time distributions (RTDs) obtained at different gas flowrates. The obtained experimental data was fit to the RTD distribution of an axially dispersed plug flow reactor model with open boundary conditions **(Eq. 3.2)**. Using the average residence times **(Eq. 3.3)**, experimental variances **(Eq. 3.4)** were then compared with the corresponding values derived from the model **(Eq. 3.5)** to calculate Peclet numbers **(Eq. 3.6)**.

$$E(t) = \sqrt{\frac{u^3}{4\pi \boldsymbol{D} L}} exp\left[-\frac{(L-ut)^2}{4\boldsymbol{D}L/u}\right] \qquad (3.2)$$

$$\bar{t} = \int_0^\infty tE(t)dt \quad (3.3)$$

$$\sigma_{exp}^2 = \int_0^\infty (t - \bar{t})^2 \, E(t).\, dt \quad (3.4)$$

$$\sigma_{model}^2 = \frac{2\boldsymbol{D}L}{u^3} \quad (3.5)$$

$$Pe_a = \frac{uL}{\boldsymbol{D}} \quad (3.6)$$

Gas flowrates ≤ 25 sccm led to Peclet numbers in the range ~50-90, indicating non-negligible degree of back-mixing under these flowrates. However, the RTD curve at a slightly higher flowrate (40 sccm) exhibited significantly lower variance, leading to Pe ~ 280. It is therefore possible to operate the setup with plug flow hydrodynamics at moderately low flowrates (> 40 sccm).

3.5.3 Reaction kinetics measurements. Any new reactor needs to be characterized and benchmarked against traditional designs; this can be accomplished by measuring and comparing reaction kinetics for relatively simple and well understood probe chemistries. To this extent, we utilized C2-C4 alcohol dehydration, and the dehydra-decyclization of a five-membered saturated ether 2-MTHF. Alcohol dehydration on Brønsted acid sites proceeds by two mechanisms: a unimolecular pathway to the corresponding olefin, and a bimolecular pathway to a di-alkyl ether **(Scheme 3.3)**.[107–110] Alternatively, 2-methyltetrahydrofuran (2-MTHF) can either undergo dehydra-decyclization to linear pentadienes, namely 1,3-pentadiene and 1,4-pentadiene, or fragment to butenes and formaldehyde by a competing retro-Prins condensation pathway **(Scheme 3.3)**. Other typical side products are propene and large aromatics (C6+ fraction).[111]

In the case of alcohol dehydration, the kinetic preference to unimolecular/biomolecular dehydration pathways was found to be temperature dependent. Increasing temperature consistently led to unimolecular dehydration being favored over the bimolecular pathway for all three alcohols. Taking ethanol as a representative case, this observation is highlighted in **Figure 3.3a**. While di-ethyl ether was the only observed dehydration product at low temperatures (≤ 413 K), ethylene selectivities exhibited a monotonic rise with increase in temperature for the range investigated (388 K-483 K). Corresponding product distributions from previous reports are also shown for the same chemistry in **Figure 3.3a**, and direct comparisons reveal good agreement between the

product distributions obtained on the micro-flow reactor setup and previously reported values. It has been widely reported that the 10-membered ring (MR) channels in the MFI framework (for ZSM-5) enthalpically stabilize the bulkier bimolecular pathway transition state (TS) for light alcohol (C1-C4) dehydration at low temperatures due to tighter pore confinement.[107,108,110,112] Increasing temperature increases the contribution of entropy, thereby favoring looser transition state fits, and leading to higher unimolecular product selectivities at higher temperatures. Consistent with this discussion, the same behavior was indeed observed for the other two alcohols (namely, 2-propanol and 1-butanol) employed in this study, and the results can be found in **Table A3.3 and Section A3.4 in the Appendix**.

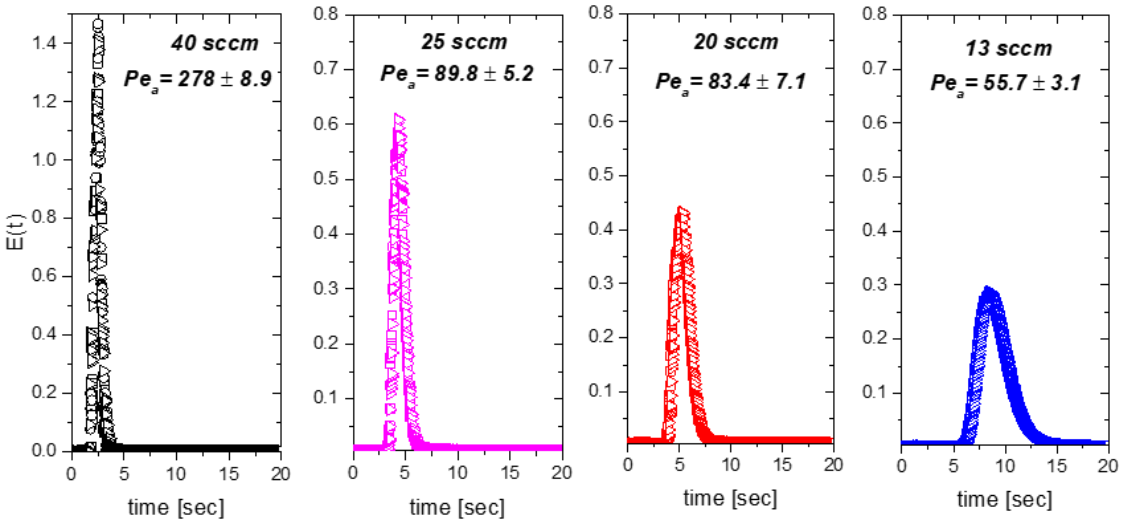

Figure 3.2 *The residence time distribution obtained from the inlet liner packed with deactivated quartz wool at four different carrier gas flowrates. The experiments were performed with ethanol pulses and the inlet was maintained at 523 K. Different symbols* (□, ▷, and ○) *represent replicate runs under identical conditions. Corresponding Peclet numbers given by* ***Eq.3.6*** *are also indicated on the insets. Errors indicate the 95% CI on the Peclet numbers resulting from independent experimental runs.*

For 2-MTHF dehydra-decyclization, linear pentadienes were found to be the dominant product with selectivities of ~70-75% under low conversions (2.9-8.0 %) in the temperature range investigated (483-523 K) **(Figure 3.3b)**. The obtained product distributions were again found to be in reasonable agreement with the values obtained from the traditional packed bed reactor setup, as well as previously reported values under similar reaction conditions.[20]

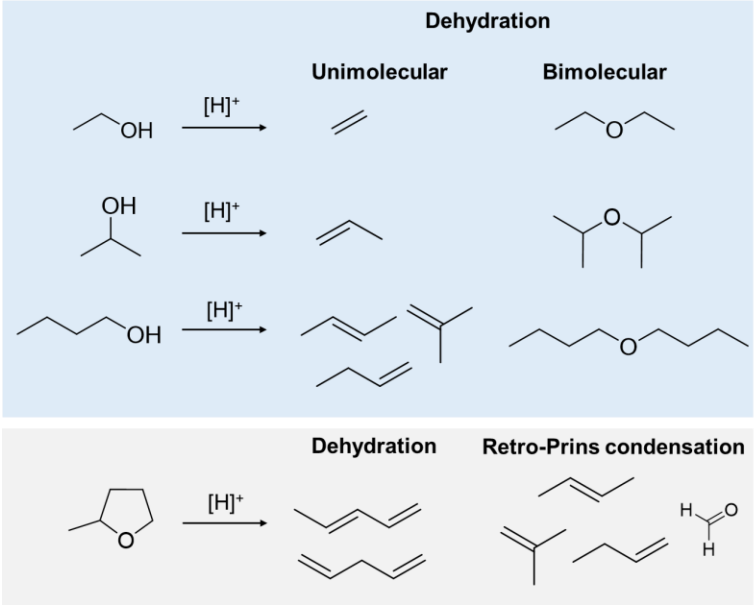

Scheme 3.3 *Known reaction pathways for the Brønsted acid catalyzed dehydration of ethanol, 2-propanol, 1-butanol, and dehydra-decyclization of 2-methyltetrahydrofuran (2-MTHF).*

The Arrhenius dependence of proton-normalized rates of the most dominant reaction products for all the test reactions are plotted in **Figure 3.4.** The corresponding values of STYs previously reported under similar experimental conditions are also plotted to directly compare them against the values obtained from the micro-flow reactor setup. The STYs for all the probe reactions obtained from our setup are typically within a factor of ~2x of the corresponding values reported in literature. The calculation of STYs inherently has considerable errors associated with it, in part due to the different measurement methods for estimating the Brønsted acid site count. Furthermore, the absolute value of STYs depend on the experimental variables like the space velocities and consequently the conversions at which the product formation rates are calculated, and hence it is safe to conclude that the micro-flow reactor reported here is capable of accurate STY measurements provided the conversions are near differential (<15%). The apparent activation barriers extracted from the Arrhenius plots measured in this work are listed in **Table 3.2** along with previously reported values. Considering the apparent nature of our measurements (which are likely a convolution of intrinsic kinetics and thermodynamics), the agreement with previously reported values is also reasonable, especially given that some of these referenced values are intrinsic zero-order rate-constants, and are expected to

be higher than apparent (nearly first order) rate constants due to adsorption enthalpy contributions.

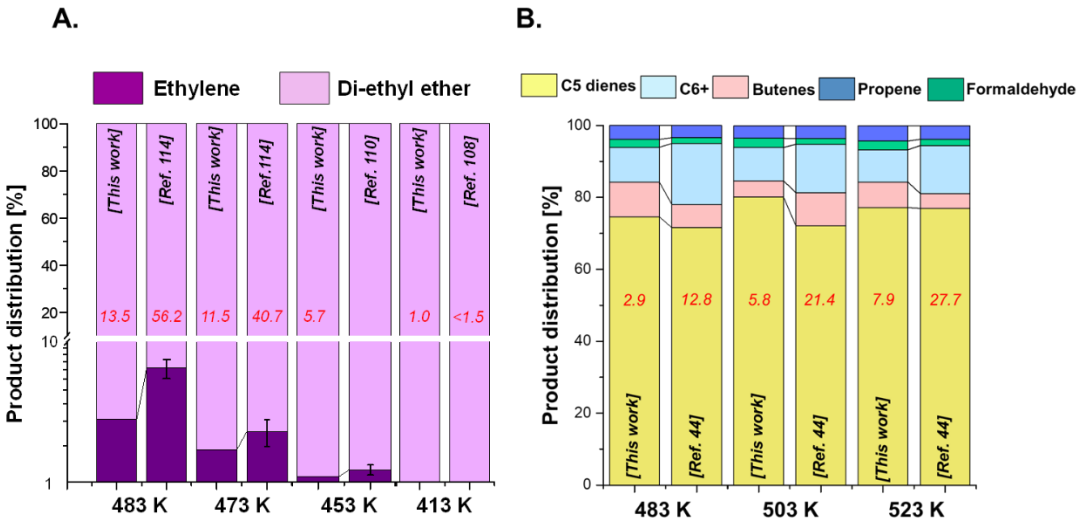

Figure 3.3 (A) *The product distribution obtained from ethanol dehydration at different reaction temperatures compared with previously reported values on HZSM-5. The conversions are indicated on the chart in red; the values for Ref.110 were not explicitly reported but differential. WHSV for the data from the micro-flow reactor is 7.35 g EtOH/g cat./h;* ***(B)*** *The product distribution obtained from 2-MTHF dehydra-decyclization at different reaction temperatures compared with measurements carried out on HZSM-5 (Zeolyst CBV8014, Si/Al=40) under similar experimental conditions on a traditional packed bed reactor (PBR) as described in Ref. 104. The conversions are indicated on the chart in red. WHSV for the data from the micro-flow reactor is 5.5 g 2-MTHF/g cat./h, while WHSV for the data from the PBR is in the range 3.2-7.5 g 2-MTHF/g cat./h). Carbon balances for both sets of data are within ±7%.*

Another application of a laboratory-scale PBR is the estimation of rate orders by varying reactant partial pressures. We highlight the applicability of the micro-flow reactor setup by considering ethanol dehydration at low temperatures (388-409 K); under these conditions, di-ethyl ether (DEE) is the only reaction product. As expected, DEE production rates were sensitive to the ethanol partial pressures in the low partial pressure regime (<10 torr) **(Figure 3.5)**. At high ethanol partial pressures (>30 torr), DEE production rates were less sensitive to ethanol partial pressures, but did not achieve zero-order kinetics indicative of a surface saturated with ethanol. However, this behavior is not due to the setup's inability to measure rates accurately under these conditions but rather that higher ethanol pressures are required to achieve a zero-order kinetic regime. Notably, the absolute DEE STY values as well as ethanol partial pressure dependence showed reasonably good agreement with values previously reported under similar reaction conditions on ZSM-5 by Bhan and co-

workers.[108] Along with all the applications highlighted so far, long-term stability analysis of a catalyst can also be performed on this setup, provided that the reaction conditions ensure complete bed utilization.[113] An example case for a test chemistry suffering from deactivation (2-MTHF dehydra-decyclization) carried out on HZSM-5 is included in the **Appendix (Section A3.5 and Figure A3.8)** to illustrate the efficacy of this setup to perform automated long-term stability investigations**.**

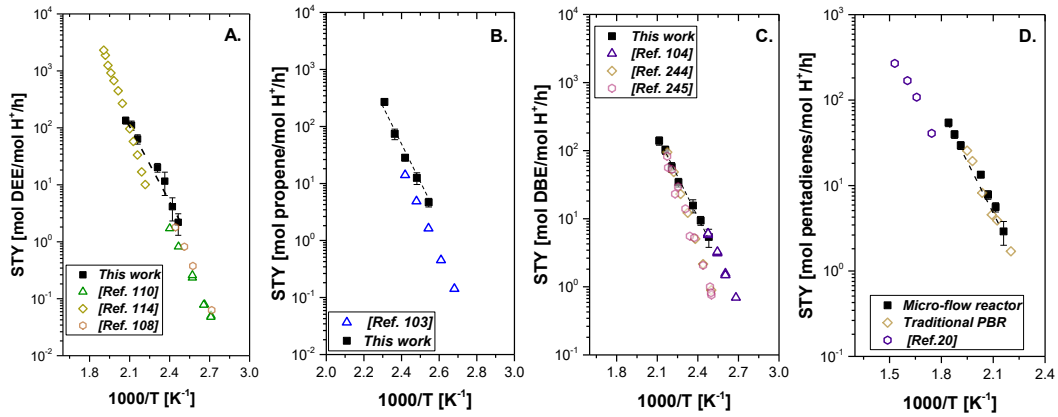

Figure 3.4 *Site-time yields of major products plotted as a function of inverse temperature for (left to right)* ***(A)*** *ethanol,* ***(B)*** *2-propanol,* ***(C)*** *1-butanol, and* ***(D)*** *2-MTHF (Reaction conditions:* $p_{reactant}$ *~ 25 torr, He flowrate = 60 sccm, WHSVs in the range 5.0-7.6 g reactant/g cat./ h; all conversions kept below 15%). Error bars indicate in* ***A-C*** *represent the 95% CI on multiple injections from the same experimental run to measure steady state rates, while the error bars in* ***D*** *represent 95% CI on replicate independent measurements on fresh/recalcined catalyst beds. The references indicated on the insets are also listed in the last column of* ***Table 3.2****.*

As previously noted, calculations to probe the temperature distribution of the reactor under reaction conditions were carried out by: (i) the measurement of axial bed temperature gradients, combined with (ii) calculation of inter-, and intra-particle temperature gradients **(Section A3.4 in the Appendix)**. For the reported kinetics collected under strictly differential conversions, both external and internal particle gradients were found to be negligible **(Section A3.4 in the Appendix)**. At the highest temperature of kinetic measurements, the axial temperature change across the catalyst bed were estimated to be ~0.6 K, ~ -2.4 K, ~0.7 K, and ~-0.4 K for dehydration of ethanol, 2-propanol, 1-butanol, and 2-MTHF, respectively **(see Section A3.4 in the Appendix)**. With the exception of 2.4 K, these temperature drops are all within the resolution limits of a

thermocouple and indicate the nearly isothermal operation of the reactor, at least under these low conversion conditions.

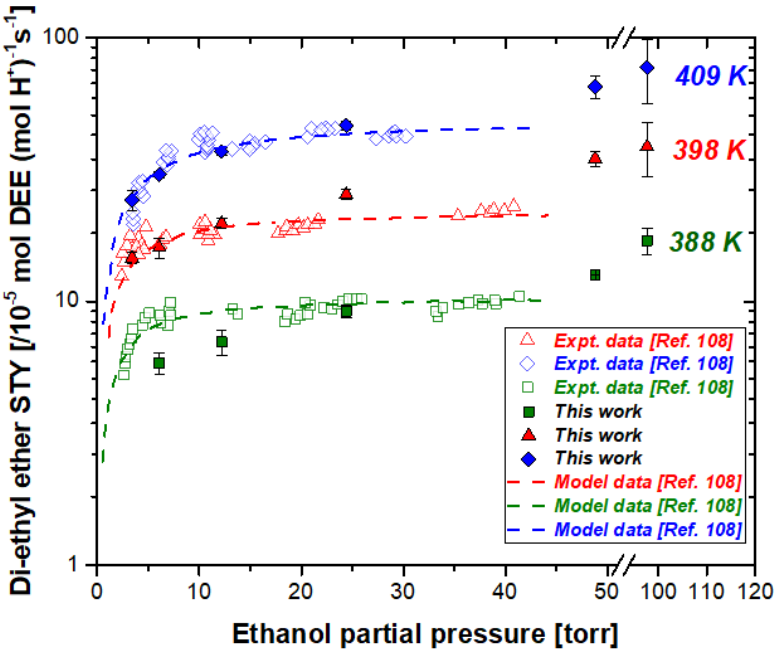

Figure 3.5 *Di-ethyl ether site-time yields measured as a function of ethanol partial pressure on HZSM-5 (Si/Al 140) at 388 K, 398 K, and 409 K, respectively, on the micro-flow reactor setup. The error bars represent a 95% CI in the steady state rate measurements on one catalyst bed (Reaction conditions: WHSVs in the range 0.81-28.6 g EtOH/g cat/h, carrier gas flowrate = 60 sccm, all conversions were kept below 1.2 %). The reported data is compared with experimental and modeled data from Chiang et al.*[108] *where the rates were reported at conversions <1.5% on HZSM-5 (Si/Al 42.5).*

Table 3.2 *Apparent activation energies for the major dehydration product of ethanol, 2-propanol, 1-butanol, and 2-MTHF under reaction conditions measured on HZSM-5 (Si/Al 140) compared with previously reported values*

Reactant	Product(s)	Apparent activation barrier [kcal/mol]	
		This work	Literature
Ethanol	di-ethyl ether	19.7 ± 1.5	21.9[114],23.2[110],24.5[108]
2-propanol	propene	34.5 ± 1.9	34.9 ±1.6[103]
1-butanol	di-butyl ether	17.6 ± 0.7	18 ± 2[49], 21.0 ± 0.8[104]
2-methyltetrahydrofuran	(1,3 + 1,4)-Pentadienes	17.4 ± 1.9	21.5 ± 1.5*, 17.7±1.7[20]**

** These measurements were performed on a traditional packed bed reactor as described in Li et al.*[104] *,*
***These measurements were performed on amorphous silica-alumina (13.7 wt % alumina content)*

These results, taken together, highlight that the product distributions, absolute values of STYs along with their partial pressure dependencies, and the apparent activation barriers measured using this setup are under nearly isothermal reaction conditions, and hence in good agreement with previous studies reported on more traditional packed bed reactors. Comparable reactor performance underpins the utility of this automated setup to obtain kinetic parameters.

3.5.4 Benefits and limitations of the reported micro-flow reactor setup. As highlighted through the earlier discussions, the micro-flow reactor affords automated operation without requiring constant human intervention. In addition, the fabrication of the setup is fairly straightforward and requires minimal added instrumentation over and above typical GC operation. Many catalysis laboratories across the world are indeed equipped with fully automated state-of-the-art setups operating in a 24/7 mode, but the key benefit of using the reported approach vs. these high-end commercial reactor systems lies the significant cost savings in implementing this approach. As shown in **Figure 3.6**, depending on the desired level of instrumentation (e.g., new/refurbished GC, or the presence/absence of online detectors), the cost benefit of fabricating the micro-flow reactor setup can range anywhere from ~2-10x over these commercial systems, which amount to cost savings of $20,000-80,000. Therefore, this approach can potentially enable significantly more kinetic data per unit cost without compromising its quality. With the ease of operation, relatively simple fabrication, and low cost, we view this approach as a tool for standardized experimental reaction systems which can be readily utilized by materials synthesis researchers.

One can reasonably argue that only one catalyst can be tested at any given time, limiting the reactor throughput, while also requiring manual intervention for catalyst changeover. However, a typical mid-size heterogeneous catalysis laboratory in the US employs anywhere between two-to-10 gas chromatograph units, some of which can be converted to these automated micro-flow reactors given the minimal additional fabrication costs **(Figure 3.6)**. Therefore, the possible shortcomings arising from the testing capability being limited to one catalyst at any given time can be solved by added investment enabling operation of multiple units in parallel. With the reduced-workforce regulations where

staggered work hours in laboratories is going to be the norm for the foreseeable future (due to the pandemic), these low-cost automated setups offer another key advantage; to the extent that a laboratory has multiple such units, one researcher can operate ~2-5 systems (potentially being used on different research projects/chemistries/researchers) at a given time depending on familiarity and know-how, meaning that multiple researchers do not need to be present for 'their' systems to operate in 24/7 mode.

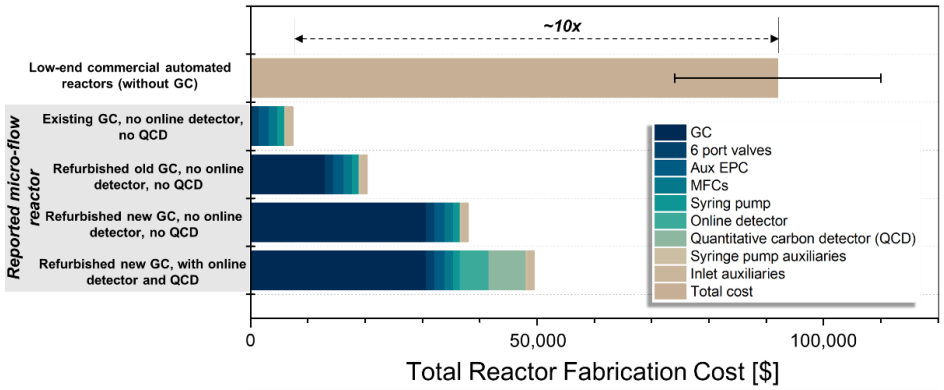

Figure 3.6 *Comparison of the fabrication cost for the reported micro-flow reactor under different considered scenarios (e.g., choice of GC, presence/absence of an online detector and a methanizer (quantitative carbon detector, QCD) compared with typical prices of commercial low-end automated lab-scale flow reactors.*

What about the gas cylinder changeovers and setting up feed-stream dosing (which are not controlled by a GC)? With the increasing global shortage of helium, researchers are moving to low cost alternatives like hydrogen for carrier gases for their gas chromatography needs,[115] which can be generated in-house using hydrogen generators. Even in cases where helium gas cylinders are used, it is possible to set up helium cylinder multipacks in conjunction with manifolds for these equipment, enabling continuous operation for weeks without requiring replacement. Setting up liquid feed dosing using syringe pump/HPLC pumps remains manual but is usually quick; as pointed out before, for applications only requiring an initial estimation of product distributions, a significantly simpler version of this setup as a transient pulsed microreactor from our earlier works[18,45] can be utilized, which would barely require any manual intervention in setting up feeds as the dosing is through the GC autosampler itself. Similarly, for chemistries utilizing light gases as feeds (viz. methane activation, carbon dioxide valorisation), it is possible to set up

individual lines with separate mass flow controllers (MFCs), and such systems can run practically indefinitely for a given catalyst bed.

The ease of fabricating does lead to some limitations of using the proposed system, one of which is the feasible conditions of catalyst temperature control. While a small range of h/H ratios ensures minimal deviation temperature, one should be mindful that temperature deviations can be as high as > 10% even without considering the reaction thermodynamics, if the catalyst bed packing extends outside the range of $0.15 < h/H < 0.35$. This criterion limits the total mass of catalyst that can be packed in this setup to ~30-45 mg, meaning that highly exothermic reactions requiring bed-dilutions may not be suited for this setup. Furthermore, the maximum operating temperature for the setup is limited by the maximum allowable temperature of the GC inlet (673 K, Agilent 7890). Therefore, *in-situ* catalyst pre-treatments requiring higher temperatures cannot be achieved. Lastly, the unit is not intended to be used for multiphase mixtures; if liquids with low vapor pressures are used, separate heat tracing of individual transfer lines may be required, which compromises the simplicity of fabricating the setup.

3.6 Conclusions. We provide a detailed design and implementation strategy of an automated micro-flow reactor integrated within a typical gas-chromatograph unit, enabling kinetic data acquisition without manual intervention for vapor-phase chemistries carried out at near ambient pressures. Temperature control inside the reactor depends on the axial position of the catalyst bed, where deviations are negligible in the region $0.15 < h/H < 0.35$. Residence time distribution analysis reveals near plug flow hydrodynamics at relatively small gas flowrates (>40 sccm). A combination of four Brønsted acid catalysed reactions further highlight the absence of heat and mass transport limitations under strictly differential conversions (≤ 5%), and the axial temperature change remains < 2% for the investigated chemistries. Furthermore, typical kinetic parameters are in reasonable agreement with previous reports. Lastly, a chromatogram analysis tool developed in-house integrated with the experimental workflow enables the handling of raw chromatography files for automated evaluation of peak areas. The setup has significant cost savings compared to commercial automated lab-scale reactors, and coupled with its automated

implementation affords an opportunity to carry out catalytic evaluation of materials in a reliable manner without compromising data quality.

Chapter 4

Catalytic consequences of acid-site strength and diffusional hurdles in the dehydra-decyclization of 2-methyltetrahydrofuran to pentadienes

*Reproduced with permission from Kumar, G; Liu, D; Xu, D.; Ren, L; Tsapatsis, M; Dauenhauer, P.J. Dehydra-decyclization of 2-methyltetrahydrofuran on boron-containing zeolites. Green Chemistry **2020**, *22*, 4147-4160. https://doi.org/10.1039/D0GC00136H

4.1 Conspectus

Biomass-derived 2-methyltetrahydrofuran (2-MTHF) undergoes tandem ring-opening and dehydration (dehydra-decyclization) to linear pentadienes, namely 1,3-pentadiene and 1,4-pentadiene. It can also fragment to butenes and formaldehyde through a competing retro-Prins condensation pathway. Using detailed kinetic measurements of 2-MTHF dehydra-decyclization on zeolites with disparate acidities (boro-, and alumino-silicates) and micropore environments (MFI, MWW, and BEA), weakly acidic borosilicates were shown to exhibit ca. 10-30% higher selectivity to dienes at about five-to-sixty times lower proton-normalized rates than aluminosilicates (453-573 K). Dehydra-decyclization site time yields (STYs) were invariant for aluminosilicates within the investigated frameworks, indicating the absence of pore-confinement influence. However, individual site-normalized reaction rates varied by almost an order of magnitude on borosilicates in the order MWW > MFI > BEA at a given temperature (523 K), indicating the unidentical nature of active sites in these weak solid acids. The diene distribution remained far from equilibrium and was tuned towards the desirable conjugated diene (1,3-pentadiene) by facile isomerization of 1,4-pentadiene. This tuning capability was facilitated by high bed residence times, as well as the smaller micropore sizes among the zeolite frameworks considered. The suppression of competing pathways, and promotion of 1,4-pentadiene isomerization events lead to a hitherto unreported ~86% 1,3-pentadiene yield and an overall ~ 89% combined linear C5 dienes' yield at near quantitative (~98%) 2-MTHF conversion on the borosilicate B-MWW, without a significant reduction in diene selectivities for at least 80 hours time-on-stream under low space velocity (0.85 g reactant/g cat./h) and high temperature (658 K) conditions. Finally, starting with iso-conversion levels (ca. 21-26%) and using total turnover numbers (TONs) accrued over the entire catalyst lifetime as the stability criterion, borosilicates were demonstrated to be significantly more stable than aluminosilicates under reaction conditions (~3-6x higher TONs).

4.2 Introduction

Conjugated C4-C5 dienes, currently manufactured as a byproduct of the cracking of naphtha and gas oil fraction of crude oil, are vital bulk chemicals for the elastomer industry.[13,116] Due to a recent surge in the supply of shale-gas ethane, refineries are finding ways to decouple the production of ethylene and C4-C5 fractions including isoprene, butadiene, and piperylene (1,3-pentadiene), accentuating the need to produce these chemicals from alternative on-purpose routes possibly utilizing renewable feedstocks such as lignocellulosic biomass.[5,117–119] While isoprene is understandably the most valuable C5 diene isomer, 1,3-pentadiene has recently attracted attention as a high potential feedstock for fine chemical synthesis using transition metal catalysis.[120–123]

We previously reported a thermochemical route to 1,3-butadiene, 1,3-pentadiene, and isoprene, from the vapor-phase dehydra-decyclization of biomass-derived saturated five-membered cyclic ethers tetrahydrofuran (THF), 2-methyltetrahydrofuran (2-MTHF), and 3-methyltetrahydrofuran (3-MTHF), respectively.[44,45] These studies reported high selectivity to corresponding dienes on phosphorus-containing all-silica zeolites. However, the nature of active sites and the surrounding silica framework in these materials remains nebulous.[36,124] Cho *et al.* reported the inability of these sites to catalyze 2-propylamine Hoffman elimination, and to protonate pyridine.[36] Most recently, Gorte and co-workers have reported the onset temperature of H-D exchange of toluene on phosphorus self-pillared pentasil (P-SPP) to be ≥100 K higher than aluminosilicates, highlighting the weakly acidic nature of these materials.[125] It is also important to note that these phosphorous active sites are distinctly different from the well-studied Brønsted acidic sites in silicoaluminophosphates (commonly known as SAPO zeotypes);[126–128] the P-OH functionalities on aluminum-free all-silica support in P-zeosils are significantly weaker. Based on these observations, the role of acid site strength on dehydra-decyclization was considered on solid Brønsted acids with relatively well-understood active sites weaker than bridged hydroxyls in aluminosilicates.

The tuning of Brønsted acidic site strength has been implemented in zeolites by incorporating different trivalent atoms in the framework.[129–132] Iglesia and co-workers have reported deprotonation energy (DPE) determined from periodic density functional theory calculations as a measure of the acidic strength of microporous solid acids.[133] Furthermore,

the same group has shown the effect of heteroatoms like Al^{3+}, B^{3+}, and Ga^{3+} in MFI framework on DPE values, indicating that the acid site strength among heteroatom-substituted zeolites increases as H-Al-MFI > H-Ga-MFI >> H-B-MFI.[134] Notably, borosilicates exhibit ~80-100 kJ/mol higher DPE values than aluminosilicates, making them weakly acidic.[134,135] It is therefore unsurprising that purely borosilicate zeolites are rarely used for acid catalysis and have been traditionally used either as precursor to the synthesis of Lewis acid catalysts,[136–138] or more recently to modify the textural or acidic properties of aluminosilicates.[139–142] Among other examples, Chen *et al.* have reported that incorporation of the appropriate amount of boron concentrates the aluminum more selectively in the sinusoidal channels of MWW;[139] others have been able to tune aluminum siting by competitive boron incorporation in other frameworks including MFI[142,143] and BEA.[144] Furthermore, Gounder and co-workers have recently shown that boron incorporation can be used to regulate crystallite sizes in MFI independent of total aluminum content.[140]

We have recently highlighted the mechanisms and pathways for THF dehydra-decyclization on ZSM-5.[145] These cyclic ethers undergo rate-limiting ring-opening on Brønsted acid sites to an alkoxide, which rearranges and dehydrates to form unsaturated alcohols as intermediates, followed by their dehydration to form dienes. The key competing pathway is retro-Prins condensation, which results from the fragmentation of the adsorbed C_n ether/alkoxide to C_{n-1} olefin and formaldehyde. 2-MTHF is more reactive than THF and 3-MTHF towards C-O bond rupture due to a kinetically relevant carbenium transition state ion pair formed upon ring opening,[20,68] and is extensively studied for hydrodeoxygenation to pentanols, and consequently pentane, on metal-phosphide catalysts.[37,146–148] Due to its high reactivity, 2-MTHF can act as a surrogate cyclic ether to probe weakly acidic materials in more detail for dehydra-decyclization.[20]

In this study, we consider aluminum- and boron-containing zeolites in three frameworks (MWW, MFI, and BEA) to evince the role of heteroatom identity and confining environments in the dehydra-decyclization of 2-MTHF-to-1,3-pentadiene. Using apparent kinetic measurements, B-sites are shown to exhibit higher diene selectivities, albeit at significantly lower rates than aluminosilicates (as normalized by total Brønsted acid site counts). Moreover, borosilicates are shown to have *ca.* 3-6 times more total

turnovers than aluminosilicates under investigated reaction conditions (T=573 K, $p_{2\text{–MTHF}}$ =25-26 torr, initial 2-MTHF conversion in the range 21-26%). The diene distribution remains far from equilibrium, and higher bed residence times predictably lead to increments in 1,3-pentadiene (1,3-PD) formation rates, consistent with its favorable thermodynamic conformation compared to 1,4-pentadiene (1,4-PD). The diene distribution is also framework-dependent; 10-MR channels in MFI and MWW show higher preference to 1,3-PD over 1,4-PD than 12-MR channels in BEA. These findings are then utilized to achieve a stable ~86% 1,3-PD yield on boron-containing MWW framework.

4.3 Materials and Methods

4.3.1 Material synthesis and characterization. The following were purchased and used without any further treatment: 2-methyltetrahydrofuran (2-MTHF, ≥98% with BHT as stabilizer, TCI Chemicals), pyridine (99.8 %, Sigma Aldrich), tert-butylamine (≥98%, Sigma Aldrich), 1,4-pentadiene (≥98%, TCI chemicals), 1,3- pentadiene (cis- and trans- mixture, ≥98%, TCI Chemicals), 4-penten- 1-ol (≥99%, Sigma Aldrich), 4-penten-2-ol (≥ 99%, Sigma Aldrich), 3-penten-1-ol (≥95%, Alfa Chemistry), 2-penten-1-ol (≥95%, trans- , Sigma Aldrich) 2,6-di-tert-butyl pyridine (DTBP, ≥97 %, Sigma Aldrich), silicon-dioxide (quartz chips, 4-20 mesh, Sigma Aldrich), tetrapropylammonium hydroxide solution (TPAOH, 40 wt% in water, Sigma Aldrich), NaOH (Macron Chemicals), fumed silica (Cab-o-sil M5, scintillation grade, Acros Organics), ammonium nitrate (≥98 %, Sigma Aldrich), boric acid (≥97 %, Macron Chemicals), anhydrous borax ($Na_2B_4O_7$, ≥99 %, Sigma Aldrich), tetrapropylammonium hydroxide (TPAOH 40 wt% in water, Alfa Aesar), piperidine (99 %, Sigma Aldrich), tetraethylammonium hydroxide solution (TEAOH, 40 wt % in water, Sigma Aldrich), hexamethyleneimine (≥99 %, Sigma Aldrich), tetraethyl orthosilicate (TEOS, ≥99 %, Sigma Aldrich), cetyltrimethylammonium chloride (CTAB, Sigma-Aldrich, 99% purity), sodium aluminate (MP Biomedicals) .

NH_4^+ form of ZSM-5 (CBV8014, Si/Al=40), and Al-BEA (CP814C, Si/Al=12.5) were purchased from Zeolyst International. MCM-22 (Si/Al=24) was synthesized using

hexamethyleneimine as the structure-directing agent using the same procedure reported by Corma and co-workers,[149] (detailed procedure is included in **Section A4.1.1** in the **Appendix**). MCM-36 was prepared by swelling and pillaring of MCM-22 as reported by Maheshwari *et al.*[150] (detailed procedure is included in **Section A4.1.1** in the **Appendix**). Boron-containing zeolites in three different frameworks MWW,[136] BEA,[151,152] and MFI[134] were synthesized modifying existing hydrothermal synthesis procedures, and detailed steps are included in **Section A4.1.1** in the **Appendix**. All catalysts were calcined in a boat placed within a 1" quartz tube under air flow at 823 K using a ramp rate of 2 K min^{-1} for 10 hours prior to any catalytic testing. We employed aluminosilicates with relatively low Si/Al (in the range of 12.5 to 40) to keep them comparable to bulk boron loadings in the borosilicate analogues.

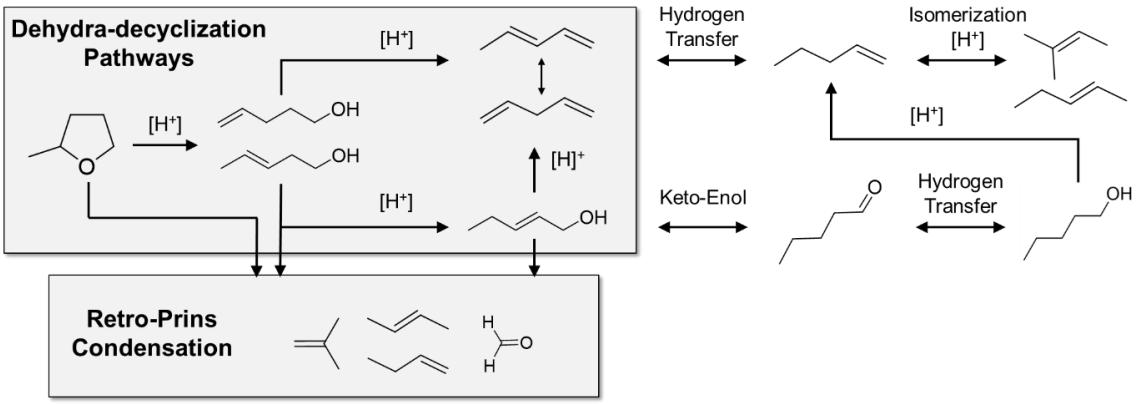

Scheme 4.1 *Known reaction pathways for the conversion of 2-MTHF over solid Brønsted acids.*[20,44,45,66,153,154]

Powder X-ray diffraction (XRD) patterns were collected on a Bruker AXS D5005 diffractometer using Cu K_α radiation (=1.5418 Å) with a step size of 0.02° and a step time of four seconds. Inductively Coupled Plasma Optical Emission Spectrometry (ICP-OES) was used for elemental analysis. Textural information of all synthesized samples was characterized through Ar physisorption in an Autosorb iQ2 porosimetry instrument (Quantachrom). Prior to analysis, catalysts were outgassed at 573 K for six hours and subsequently cooled down to room temperature under vacuum. BET specific surface area measurements were used to represent the total surface area of the catalyst materials; total pore volume was determined using a single point measurement at P/P_0 = 0.95. SEM was performed on a JEOL JSM-6500F scanning microscope operated at 2.0 kV.

All TEM images were obtained with a FEI Tecnai G2 F30 TEM operating at 300 kV using a charge-coupled device (CCD) camera. MAS NMR experiments were performed using a Bruker DSX-500 and a Bruker 4.0 mm MAS probe. The spectral frequencies were 500.2, 160.5, and 99.4 MHz for ^{1}H, ^{11}B, and ^{29}Si nuclei, respectively. Samples were spun at 13 kHz for ^{1}H and ^{11}B detections, and 8 kHz for ^{29}Si. For ^{11}B MAS NMR, 0.5 sec $\pi/12$ pulse was used. The chemical shifts were calibrated to external references of TMS for ^{1}H and ^{29}Si, and $BF_3(OEt)_2$ for ^{11}B.

4.3.2 Catalytic Experiments. All kinetic measurements were performed in the temperature range of 430-550 K at total pressures of 1.00-1.05 bar in an upflow fixed bed reactor. Catalyst samples were pressed and sieved to particle sizes ranging from 250-500 μm and placed between deactivated quartz wool plugs in a 1/4" quartz U-tube. Void volume in the tube was minimized by loading quartz chips upstream of the catalyst bed. A 1/16" K-type thermocouple (Omega) was placed just above the catalyst bed for temperature measurements. The furnace temperature was regulated by using a temperature PID controller (Omega CN 7800). All catalyst samples were calcined in situ at 823 K in 40 sccm air (99.997%, Minneapolis Oxygen) using a ramp rate of 3.0 K min^{-1}. The reactor was thereafter cooled to reaction temperature and purged with He (99.995 %, Matheson) for at least 30 minutes prior to introducing the reactant feed to eliminate temperature gradients across the bed. Reactant partial pressures were varied using a combination of carrier gas flowrates (10-150 sccm) by a mass flow controller (Brooks Instruments 5850E), and volumetric flowrate of the reactant using a syringe pump (Cole Parmer 74905 series). All transfer lines were maintained at temperatures ≥ 400 K to avoid condensation of any species. Online analysis of the reactor effluent was performed using a gas chromatograph (Agilent 6890) equipped with a quantitative carbon detector (QCD, Polyarc™)[47] and a flame ionization detector (FID). Separation was performed using an HP-PLOT Q column (Agilent, 19091P-QO4). All carbon mass balances closed to within ± 10%. Unless otherwise specified, error bars represent 95% confidence intervals on independent replicate measurements on fresh catalyst beds from the same batch. As noted earlier, retro-Prins condensation of 2-MTHF produces butenes and formaldehyde in equimolar ratio, and the amount of formaldehyde was indirectly calculated by the quantification of butenes.

A combination of Mears' and Weisz-Prater criterion was used to investigate the external and internal mass transfer limitations, respectively **(Section A4.2 in the Appendix)**.[155] Under near differential conditions ($X_{2\text{-MTHF}}$ <13%), while the rates for BEA and MFI (with both heteroatoms) were found to be free from any diffusional limitations, such a conclusion could not be reached for B-MWW and MCM-22, and the reported rates on these materials likely reflect a complex interplay of reaction and intra-crystalline diffusion. All aluminosilicates deactivated under reaction conditions over time scales of a few hours, and all reported rates were corrected to a bare catalyst surface by using a first-order deactivation model and extrapolating obtained rates to time zero. Kinetic experiments at different temperatures were conducted using fresh catalyst beds to minimize systematic errors. Alternatively, borosilicates deactivated at much longer time scales than aluminosilicates, and reported rates on these materials were all corrected to a reference condition of 523 K to account for any small intervening deactivation during kinetic measurements. Brønsted acid site densities of all aluminosilicates were measured using the Hoffman-elimination of tert-butylamine. The Reactive Gas Chromatography (RGC)[103] technique was used to quantify all butene isomers resulting from Hoffman elimination of tert-butylamine on a Brønsted acid site (BAS), assuming each butene molecule was produced on a unique BAS.

Previous works by Gorte and co-workers shows that alkylamines can desorb without undergoing Hoffman elimination on the acid sites in borosilicates due to their low reactivity.[156] Moreover, the nature of these sites as well as boron coordination changes with the extent of hydration,[157] and it is likely that part of tetrahedral boron in solid state ^{11}B MAS NMR is actually trigonally coordinated under reaction conditions. To account for these factors, the BAS count for borosilicates was estimated by *in situ* pyridine titration experiments during 2-MTHF dehydra-decyclization in the temperature range 453-477K. 2-MTHF dehydra-decyclization was carried out until initial transients subsided, and an instantaneous switch was made to the 2-MTHF/pyridine mixture (molar ratio∼310:1) at identical volumetric flowrate. Total 2-MTHF consumption rate was monitored with titrant uptake and linearly extrapolated to zero rates to quantify the total number of catalytically relevant acid sites in borosilicates. Experiments with selective DTBP titrations to deconvolute the catalytic role of different pore systems in aluminum-containing MWW

(namely MCM-22, and MCM-36) were conducted at 453 K, sufficiently lower than temperatures corresponding to the onset of DTBP desorption on aluminosilicates.[158,159] Similar to *in situ* pyridine titration on borosilicates, 2-MTHF dehydra-decyclization was carried out for a fixed time (*ca.*175 minutes), and an instantaneous switch was made to 2-MTHF/DTBP mixture (molar ratio∼650:1) at identical volumetric flowrate. Separation of compounds for these measurements were performed with a Restek RTx-5 column.

Experiments to evaluate the stability of all catalysts were performed at 573 K and $p_{2\text{-MTHF}}$ ∼25 torr; bed residence times and carrier gas flowrates were adjusted on different catalysts to achieve an initial conversion of ∼21-26%. To provide a quantitative description of stability, we used total turnovers during catalyst lifetime **(Eq.4.3)**, which is a measure for the total moles of 2-MTHF converted to carbonaceous products per proton over the entire lifetime of catalyst.[160] Total TONs were calculated until the conversions for all catalysts decreased to ≤3%. The time scales to achieve this criterion for borosilicates was 300-470 h on stream, while aluminosilicates completely deactivated within 24-75 hours. Furthermore, by calculating the fraction of total turnovers **(Eq.4.4)**, product selectivities **(Eq.4.2)** were compared as a function of reaction progress allowing us to compare selectivities on catalysts with non-identical total turnovers.

$$STY_i = \frac{F_i}{m_{cat.}.N_{H^+}} \tag{4.1}$$

$$Selectivity_i(\%\text{C basis}) = \frac{\text{Total carbon present in the product}_i}{\text{Total carbon from the reactanct converted to products}} \times 100 \tag{4.2}$$

$$TON(t) = \frac{1}{N_{H^+}} \int_0^t \sum_n n.F_{C_n}(t')dt' = \int_0^t \sum_n n.STY_{C_n}(t')dt' \tag{4.3}$$

$$f_{total-turovers}(t) = \frac{TON(t)}{TON(t_{X_{2MTHF} \leq 3\%})} \tag{4.4}$$

where F_i is the molar flow-rate of product i, N_{H^+} is the Brønsted acid site (BAS) density, STY_i is the site time yield for product i, $m_{cat.}$ is mass loading of the catalyst, and n_i is the number of carbon atoms in product i.

4.4 Results and Discussion.

4.4.1 Characterization of synthesized materials. Powder X-ray diffraction patterns (PXRD), scanning and/or transmission electron microscopy images (SEM/TEM), and Ar-porosimetry measurements of MCM-22/MCM-36/B-MWW, ZSM-5/B-MFI, Al-BEA/B-BEA are reported in **Figures A4.1, A4.2, and A4.3,** respectively, of the **Appendix (Section A4.1.2-1.4)**. A detailed discussion of the boron environments and the corresponding results of ^{11}B and ^{29}Si MAS NMR are included in the **SI** (**Section A4.1.5 and Figure A4.4);** these data were found consistent with previous reports on borosilicate zeolites with three-, and four- coordinated boron **(details in Section A4.1.5)**. Elemental analyses, textural properties, Brønsted acid site densities, and crystallite sizes of all catalysts are listed in **Table 4.1.**

Table 4.1 *Structural, textural, and acidic properties of all zeolites*

Catalyst	Si/T[a]	BET Surface area (m^2/g)[b]	Total pore volume (cm^3/g)[c]	BAS (μmol/g)	H^+/T	R_{SEM}(μm)[g]
MCM-22	24.1	562	0.28	447.6	0.68[d]	1.8 ± 0.6
MCM-36	32.3	645	0.41	233.8	0.47[d]	6.3 ± 1.2
B-MWW	13.2	506	0.30	149.6	0.13[e]	15.3 ± 0.7
ZSM-5	40.0[f]	405	0.26	345.3	0.81[d]	0.44 ± 0.09
B-MFI	38.3	510	0.29	49.5	0.11[e]	0.32 ± 0.11
Al-BEA	12.5[f]	439	0.29	624.6	0.46[d]	0.58 ± 0.12
B-BEA	23.8	474	0.28	61.1	0.09[e]	3.7 ± 0.4

[a] (T=Al/B) Determined by ICP-OES (Galbraith Laboratories); [b] Determined from Ar adsorption-desorption isotherms; [c] Determined from Ar adsorption-desorption isotherms at P/P_0=0.95; [d] Obtained by the quantification of butenes formed from the Hoffman elimination of tert-butylamine; [e] Obtained during in-situ pyridine titration during 2-MTHF dehydra-decyclization in the temperature range 453-477 K; [f] From the manufacturer; [g] Calculated from at least 50 crystallites from their respective SEM micrographs, with the errors indicating a 95% CI on measurements.

Trace aluminum impurities in borosilicates have frequently lead to misinterpretation of their catalytic properties,[140] and the catalytic rates with

boroaluminosilicate materials have been shown to scale with aluminum contents as low as ~100 ppm.[161,162] To avoid these artifacts in this work, high-purity silica source Cab-o-Sil M5 with aluminum content <1.73 ppm (ICP-MS, Galbraith laboratories) was used instead of Ludox colloidal silica for all borosilicate synthesis to eliminate the presence of aluminum, and ICP-OES (Galbraith laboratories) showed Si/Al ≥ 11,000 in synthesized borosilicates, leading to ≤ 1.5 μmol/g BAS density from trace aluminum, indicating that the synthesized borosilicates are sufficiently free from aluminum impurities. While deboronation of the borosilicates can occur under less severe conditions than aluminosilicates **(Section A4.1.5 in the Appendix),** we have not carried out varying extents of deboronation to rigorously study its effect on activity trends in this work.

The acid site density in borosilicates was measured using in-situ pyridine titration during 2-MTHF dehydra-decyclization in the temperature range 453-477 K. The mole fraction of pyridine was kept low (~1.9×10^{-5}) so the partial pressure of 2-MTHF before and after its introduction could be assumed the same. The reduction in mass-normalized total 2-MTHF conversion rates were monitored with the uptake of the titrant, and the total number of B-sites were calculated by the cumulative pyridine uptake to completely suppress the rates **(Figure 4.1).**

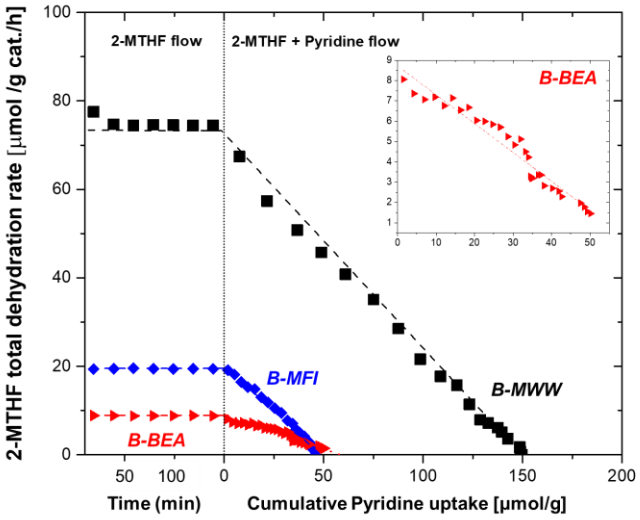

Figure 4.1 *Total consumption rate of 2-MTHF as a function of pyridine uptake over B-MWW(■), B-MFI (blue ◆), B-BEA (red ▶); Inset shows the corresponding data for B-BEA on a magnified scale. Titrant flow is an equivalent volumetric flowrate of 2-MTHF/Pyridine with 2-MTHF: Pyridine ~ 310. Inset shows the data for B-BEA on a magnified scale. (Reaction conditions: T = 453 K for B-MWW, 473 K for B-MFI, and 477 K for B-BEA;* p_{2MTHF} *= 10.5 torr for B-MWW, 4.5*

torr for B-BEA and B-MFI; WHSV = 0.60-4.50 g 2-MTHF/g cat./h; Carrier gas (He) flowrate = 60 sccm for B-MWW, 40 sccm for B-MFI and B-BEA; $X_{2MTHF} \leq 1\%$)

While the titration for B-MWW was carried out at 453 K, the corresponding experiments for B-MFI and B-BEA were carried out at 473 K and 477 K, respectively, due to their significantly lower reactivity than B-MWW **(also discussed in Section 3.4.2).**

Pyridine was found to titrate all the B-sites relevant in 2-MTHF dehydra-decyclization on B-MWW, as shown by the complete suppression of rates **(Figure 4.1).** For B-BEA and B-MFI, the rates dropped to ~85-90% of their initial values. Pyridine saturation was ascertained by monitoring pyridine breakthrough from the catalyst bed, and multiple gas-sampling injections with constant pyridine peak areas (with values sufficiently close to 2-MTHF:pyridine molar ratio of ~300) were observed to ensure pyridine saturation. Furthermore, upon switching back the feed to 2-MTHF after pyridine saturation, we did not observe the recovery of rates even at 477 K for over two hours, which indicates that pyridine remains a reversible yet strongly bound titrant for B-sites initially titrated in the temperature range investigated. The irreversible nature of pyridine adsorption has previously been shown at slightly lower temperature (433 K) during methanol dehydration on B-MFI.[134] The results **(Figure 4.1)** confirm the presence of acid sites which can protonate pyridine in these materials, the quantification of which allows for the calculation of site time yields (STYs) for the dehydra-decyclization pathway. Notably, the number of protons per heteroatom for boron-containing zeolites remains significantly lower than corresponding values for aluminosilicates **(Table 4.1),** as has been reported by Jones *et al.* previously for B-MFI.[134] Unlike aluminosilicates, the site homogeneity indicated by framework-independent DPE values has not been established for borosilicates, and it is possible that a majority of boron in the borosilicates is either not associated with a proton, or a fraction of protons associated with B lack the acidic strength to protonate pyridine irreversibly under the reaction conditions. However, it is reasonable to assume that the fraction of B sites unable to protonate pyridine (proton affinity = 930 kJ/mol)[163] cannot protonate 2-MTHF (proton affinity = 851 kJ/mol) either.[164] Therefore, the reported STYs on these materials are likely accurate even if this method does not titrate all acid sites in borosilicates.

As shown in **Figure 4.1**, the mass-normalized 2-MTHF consumption rates for B-MFI were almost twice the corresponding value for B-BEA, even though total boron content in B-BEA was ~1.5x higher than B-MFI. Moreover, B-MFI and B-BEA had similar total BAS counts (~50 and ~60 μmol/g, respectively) **(Table 4.1).** Thus, the dehydra-decyclization site time yields for B-MFI were ~2.4x higher than B-BEA, even at 5 K lower temperature. Since the rates don't scale linearly with bulk boron content, these results indicate that the relative distribution of active boron species is different in the three borosilicates investigated. Furthermore, these results underpin the necessity to probe the acidity of borosilicates strictly under reaction conditions due to their complex speciation behavior and changes in coordination upon contacting basic molecules including oxygenates.

An accurate explanation for this framework-dependent catalytic behavior of borosilicates would involve the estimation of Brønsted acid site strength of boron sites in these three frameworks. However, the different possible boron environments **(Figure A4.4 in the Appendix)** as well as the presence of crystallographically distinct T-sites which may differ in their DPE values, makes the estimation of a single representative DPE value difficult without also having apriori knowledge of relative distributions of these sites under reaction conditions. The distinct behavior of boron sites in SOD, and FER frameworks has been highlighted before by Fois *et al.*, who probed these sites by first principles calculations to study the non-identical nature of ammonia adsorption on these materials.[165]

4.4.2 Effect of heteroatom identity in dehydra-decyclization selectivity. The application of borosilicates and boron-modified aluminosilicates to selectively suppress the production of side reactions has been previously implemented for several chemistries. Some examples where boron-modified zeolites were utilized for this purpose include: dehydration of 2,3-butanediol to butanone over boric acid impregnated on ZSM-5;[166] Beckmann rearrangement of cyclohexanone oxime to caprolactam on B-MFI,[167,168] and B-ZSM-5;[169] catalytic cracking of MTBE to isobutene and methanol on B-MFI;[170] intramolecular Prins-cyclisation of citronellal on B-TUD-1;[171] isomerization of 1-hexene on B-MCM-41,[172] dehydrative aromatization of 2,5-dimethylfuran (DMF) to p-xylene on B-BEA,[135] and dehydration of 2-methylbutanal to isoprene.[173]

The known reaction pathways during the conversion of 2-MTHF over Brønsted acid sites are shown in **Scheme 4.1.** Consistent with this scheme, major products observed in our reactor effluent included 1,3-,and 1,4-pentadiene (dehydra-decyclization products), butenes and formaldehyde (retro-Prins condensation products), propene, pentenes, and large organics (identified as aromatic C_{6+} fraction). We conducted apparent kinetic rate measurements in the temperature range 453-573 K to assess the relative rates and selectivities to dehydra-decyclization and retro-Prins condensation, and the results are shown in **Figure 4.2**.

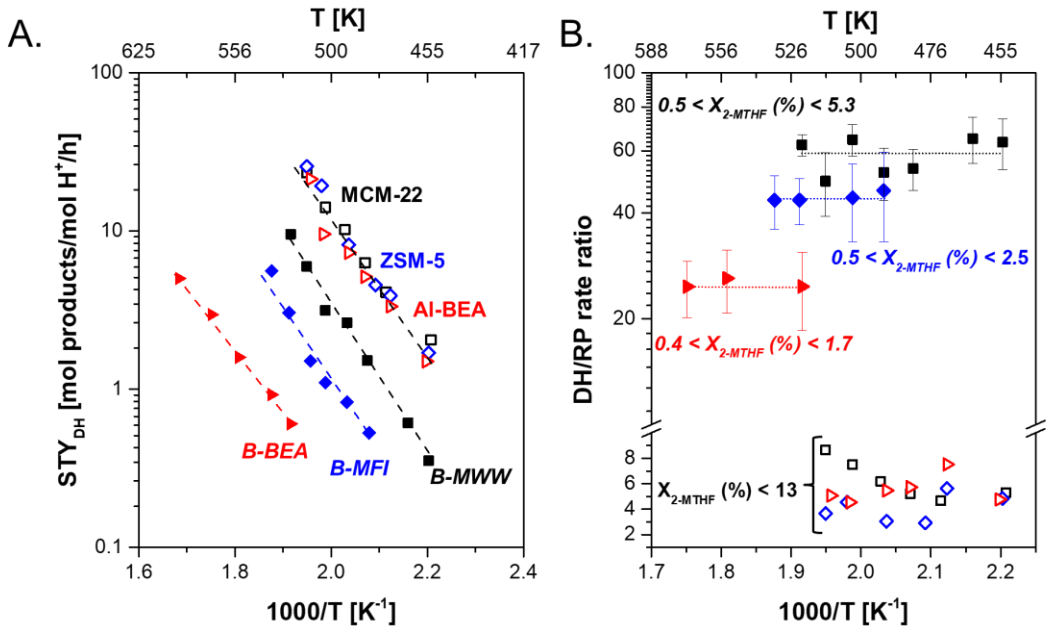

Figure 4.2 *(a) Arrhenius plots of apparent kinetics for the dehydra-decyclization of 2-MTHF and b) temperature dependence of dehydra-decyclization (DH) to Retro-Prins condensation (RP) rate ratios over B-MWW(■), MCM-22 (□), B-MFI (blue ◆), ZSM5 (blue ◇), B-BEA (red ▶), and Al-BEA (red ▷); X_{2MTHF} denotes the conversion of 2-MTHF. (Reaction conditions: p_{2MTHF} = 10.5 torr, Space velocity = 1.10-10.35 molec. 2-MTHF/H^+/min, Carrier gas (He) flowrate =60 sccm, X_{2MTHF} ≤13%). Dashed lines in (a) are fits to Arrhenius equation, and dashed lines in b) are to guide the eye. Brønsted acid site counts (mol H^+) for aluminosilicates and borosilicates are quantified using the Hoffman elimination of tert-butylamine, and in-situ pyridine titrations during 2-MTHF dehydra-decyclization, respectively. Error bars in b) are standard errors originating from uncertainty in the estimation of Retro-Prins condensation (RP) rates for borosilicates due to their low activity coupled with low selectivity to this pathway.*

The dehydra-decyclization rates were found invariant across the three frameworks in aluminosilicates **(Table 4.2)**, indicating that kinetically relevant ring-opening transition-state (TS) ion-pair[145] is likely stabilized to the same extent in MWW, MFI and BEA.

Table 4.2 *Measured apparent kinetic parameters of 2-MTHF dehydra-decyclization*

	$E_{app,DH}$ (kcal/mol)[a]	STY_{DH} ($\times 10^{-3}\ s^{-1}$)	STY_{RP} ($\times 10^{-3}\ s^{-1}$)	DH/RP ratio
ZSM-5	21.5 ± 1.5	7.11[b]	1.94[b]	3.7
Al-BEA	19.9 ± 1.4	5.92[b]	1.17[b]	5.1
MCM-22	-	6.50[b]	0.75[b]	8.7
B-MWW	-	1.65[b]	0.038[b]	49.2 ± 10.1
B-MFI	22.5 ± 2.3	0.42[b]	0.013[b]	31.9 ±12.6
B-BEA	18.2 ± 0.8	0.17[c]	0.007[c]	24.6 ±6.4

[a] *Determined by apparent kinetic measurements under conditions described in* ***Figure 4.2****, where the errors are 95% CI on the slope. The STYs on MWW materials were not under strict kinetic control under reaction conditions and therefore* $E_{app,DH}$ *is not reported on these materials;* [b] *Reported at T=512 K;* [c] *Reported at T=522 K. Errors in the calculations of Retro-Prins condensation STYs for borosilicates are reflected in the standard errors of the corresponding DH/RP rate ratios*

Consequently, the apparent activation energies for the dehydra-decyclization pathway on aluminosilicates (BEA, and MFI) are ~20 kcal/mol **(Table 4.2)**. These results are consistent with Kumbhalkar *et al*., who have also reported identical proton-normalized site-time yields for pentadienes' production over aluminosilicates having different micropore environments and extra-framework aluminum (ZSM-5 (Si/Al = 11.5), Al-BEA (Si/Al = 12.5), and Al-MOR (Si/Al = 10)).[20] The apparent dehydra-decyclization barrier of 17.7 kcal/mol on amorphous silica alumina in the temperature range 570-660 K is also qualitatively close to the values obtained by us, and small differences are likely caused by changes in apparent kinetics resulting from the differences in surface coverages at high temperature conditions employed in their study. Notably, these activation barriers are ~10-12 kcal/mol lower than four-carbon THF-dehydra-decyclization on ZSM-5 reported in our earlier work under similar reaction conditions,[145] providing further corroboration of the promoting-effect of a methyl substituent on the stabilization of the kinetically relevant transition state. Borosilicates catalyze the dehydra-decyclization pathway at STYs which are at-least ~5x lower than aluminosilicates **(Figure 4.2a)**. Furthermore, they exhibit different dehydra- decyclization STYs depending on framework.

Remarkably, there is approximately an order-of-magnitude difference in the dehydra-decyclization STY between the most active (B-MWW) and least active (B-BEA) borosilicate at given temperature (523 K). These results indicate that the speciation behavior of active sites in these materials is catalytically different depending on B siting and/or the micropore environments around the B-site. Furthermore, the nature of apparent kinetics for the dehydra-decyclization pathway remains similar on borosilicates as indicated by similar apparent barriers as on aluminosilicates **(Table 4.2).** The suppression of the retro-Prins (RP) condensation pathway on borosilicates is much greater (~ 30-50x) than the suppression of dehydra-decyclization (DH) pathway, leading to higher diene selectivities **(Figure 4.2b and Table 4.2)**. Consequently, these materials show ~ 6x-30x higher DH/RP rate ratios than aluminosilicates under near-differential conditions ($X_{2\text{-MTHF}}$ < 13%) **(Figure 4.2b).** This likely results from the inability of weakly acidic B-sites to fragment a C-C bond (the rate-determining step for retro-Prins condensation[145]). Furthermore, this behavior is not 2-MTHF conversion-dependent, and borosilicates show ~90% selectivity to dienes across all conversions, which is *ca.* 10-30% higher than aluminosilicates under similar reaction conditions **(Table A4.2 in Appendix)**. Furthermore, different extents of boron content, albeit in different micropore environments, do not seem to affect total diene selectivities (which remain >87% as shown in **Table A4.2**). These results, taken together, provide experimental evidence that weakly acidic borosilicates limit the kinetic branching to competing retro-Prins pathway in this chemistry.

4.4.3 Distribution of diene products. Besides the production of butenes and formaldehyde in the competing retro-Prins reaction pathway, another challenge to selectively produce the conjugated 1,3-pentadiene (1,3-PD) is the concurrent production of the non-conjugated 1,4-pentadiene (1,4-PD) during 2-MTHF dehydra-decyclization. This is illustrated in **Scheme 4.2**; 2-MTHF can ring-open from the more substituted 'C-2 side' or the less substituted 'C-5 side'. Ring opening from the 'C-2 side' is likely more favorable, given the carbenium character of the kinetically relevant transition state associated with ether ring opening, and leads to the formation of primary alkenols, namely, 3-penten-1-ol (E2 type elimination of $H_{\beta 1}$) or 4-penten-1-ol (E2 type elimination of $H_{\beta 2}$). While the dehydration of 3-penten-1-ol leads to 1,3-pentadiene, 4-penten-1-ol dehydration leads to 1,4-

pentadiene. Alternatively, the alkoxide formed upon ring-opening from the 'C-5' side can only form a secondary alkenol, namely, 4-penten-2-ol. This alkenol can further undergo dehydration to form 1,3-pentadiene (E2 type elimination of $H_{\beta 1}$) or 1,4-pentadiene (E2 type elimination of $H_{\beta 2}$).

To assess the validity of **Scheme 4.2**, we conducted experiments by feeding pure C5 alkenols, namely, 4-penten-1-ol, 3-penten-1-ol, 4-penten-2-ol, and 2-penten-1-ol, over ZSM-5 at lower temperature (413 K) than 2-MTHF reaction temperatures, primarily to maintain differential conditions given the facile dehydration of these alkenols. It was found that the preference to produce 1,3-pentadiene from different alkenols follows 2-penten-1-

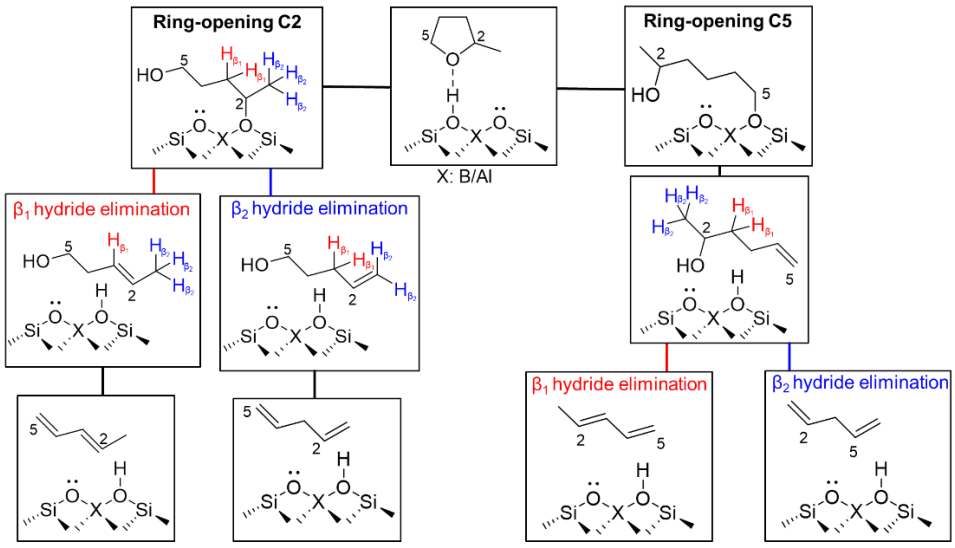

Scheme 4.2 *Proposed pathways for the production of 1,3-Pentadiene and 1,4-Pentadiene from 2-MTHF over Brønsted acid sites*

ol >> 4-penten-2-ol > 3-penten-1-ol ~ 4-penten-1-ol (**Figure A4.9 in the Appendix**). Neither 3-penten-1-ol nor 4-penten-1-ol was purely selective to 1,3-pentadiene and 1,4-pentadiene, respectively. Moreover, the most active and selective intermediate to 1,3-pentadiene, namely 2-penten-1-ol, does not result directly from a simple E2 elimination of the adsorbed alkoxides indicated in **Scheme 4.2**. Previous reports have highlighted that the migration of a double bond on a carbon chain is a low barrier step,[174,175] and consistent with this, these results indicate that both the intermediate primary alkenols as well as the produced dienes can inter-convert on a Brønsted acid site, which limits mechanistic interpretations about the origin of diene distribution directly from 2-MTHF.

4.4.3.1 Tuning selectivity to 1,3-pentadiene. 1,3-PD is thermodynamically more stable than 1,4-PD.[20,176] Using gas-phase thermochemistry data from NIST, it was found that all diene distributions were far from equilibrium under the reaction conditions in this study; selectivity to 1,3-PD was not equilibrium-limited **(Section A4.4 in Appendix).** 1,3-PD was formed as a favored diene with both borosilicates and aluminosilicates, and there was no obvious correlation between the 1,3-PD/1,4-PD selectivity ratio and heteroatom identity in the range of space times investigated **(Figure 4.3),** which is not surprising given this ratio would not only depend on the reactivity of protons, but also on their volume density, as well as the corresponding crystallite sizes. However, the preference towards 1,3-PD increased with reactor space times on all investigated zeolites irrespective of the heteroatom identity. For aluminosilicates, the total diene production rates were higher at low space times, and the increase in 1,3-PD production was only partly as a result of secondary enhancements due to 1,4-PD isomerization. However, on borosilicates, the increments in 1,3-PD formation rates was concommitant with the decrease in 1,4-PD production such that the overall diene selectivity remained nearly unchanged in the space times investigated (0.01-10 H^+.min/ molec. 2-MTHF). These results, taken together, indicate that the diene ratio can be tuned towards the conjugated 1,3-PD by operating under reaction conditions which facilitate the isomerization of the non-conjugated 1,4-PD. They also imply that the spatial gradients in diene concentrations are observable on the length scales of reactor bed lengths, and a fraction of 1,4-pentadiene formed at small bed length desorbs and reacts further down in the bed to form the thermodynamically favored 1,3-PD.

One would expect the more reactive protons in aluminosilicates to be more consequential in depleting unfavorable 1,4-pentadiene concentrations, and it was expected that the 1,3-PD/1,4-PD rate ratio would depend more sensitively on space time (or, equivalently, show higher slopes w.r.t. space time) on aluminosilicates than borosilicates. Interestingly, this was not found to be the case **(Figure 4.3).** While aluminosilicates are known to catalyze double bond isomerizations,[177–179] this observation suggested that even the weakly acidic borosilicates can isomerize 1,4-PD to 1,3-PD. This hypothesis was tested by feeding pure 1,4-pentadiene and 1,3-pentadiene over borosilicates, and the results are shown in **Figure A4.8 in the appendix**. 1,3-pentadiene did not show any conversion to 1,4-pentadiene on all borosilicates, consistent with its significantly higher thermodynamic

preference than 1,4-PD. Furthermore, the preference towards 1,3-pentadiene on borosilicates (B-MWW > B-MFI > B-BEA) **(Figure 4.3)** was directly correlated with their reactivity for 1,4-pentadiene isomerization confirming that the isomerization of 1,4-pentadiene remains facile, even on the weakly acidic borosilicates.

Interestingly, 12-MR BEA with both heteroatoms (B and Al) consistently exhibited a lower 1,3-PD/1,4-PD ratio than MWW and MFI frameworks across two decades of space times **(Figure 4.3)**. Furthermore, the preference to 1,3-PD was more pronounced when these differenes in diene kinetic preference between the investigated frameworks. For example, 10-MR channels in MFI impose more severe trasport restrictions facilitataing 1,4-PD isomerization than 12-MR channels in BEA, leading to higher 1,3-PD production

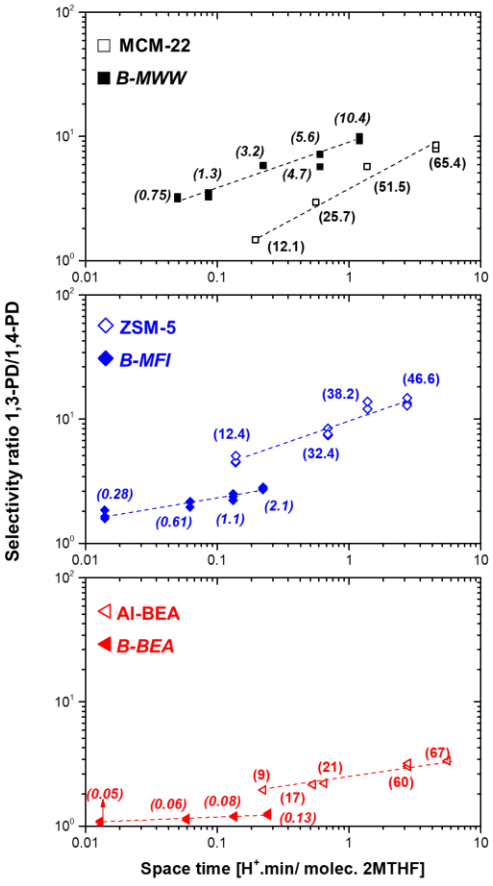

Figure 4.3 *Measured selectivity ratios of 1,3-Pentadiene/1,4-Pentadiene as a function of reactor space-times over B-MWW(■), MCM-22 (□), B-MFI (blue ◆), ZSM5 (blue ◇), B-BEA (red ◀), and Al-BEA (red ◁) (Reaction conditions: T=503 K, $p_{2\text{-}MTHF}$ = 1.5-120 torr, Carrier gas (He) flowrate =60 sccm). The bracketed values are the corresponding conversion levels. Dashed lines are provided to guide the eye.*

rates in MFI. However, such direct interpretations could not be drawn for MWW materials due to the highly non-distinct pore systems in its topology **(discussed in Section 4.4.3.2)**. Deconvoluting the catalytic role of these distinct pore systems would therefore provide insights into the origin of diene distribution on solid acids. To test our hypothesis, we designed (DTBP) titration experiments on alumniumn-containing MWW materials to study the change in diene distributioin as the chemistry was restricted selectively to a pore system smaller than in MFI (intra-layer 10-MR sinusoidal channels).

4.4.3.2 Deconvoluting the pore systems of aluminum-containing MWW in catalysis. MWW is formed by calcination of a precursor layered material, and consists of two independent pore systems **(Figure 4.4a)**. The intra-layer pore network consists of two-

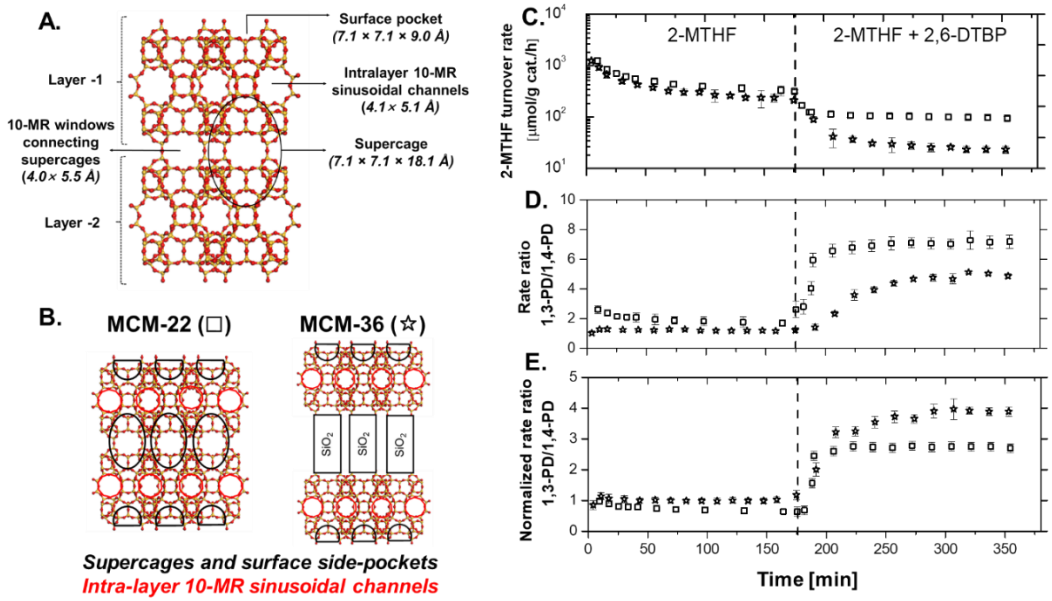

Figure 4.4 *(a) Detailed schematic of MWW framework indicating the location and relative sizes of all pore systems; b) Detailed schematic of MCM-22 and MCM-36 framework topology; c) Total rate of consumption of 2-MTHF; d) Absolute values of 1,3-PD/1,4-PD rate ratio; and e) Normalized rate ratio of 1,3-PD/1,4-PD (normalized to t = 0) as a function of time-on-stream after the introduction of DTBP titrant for MCM-22 (□), and MCM-36(☆). Titrant flow is an equivalent volumetric flowrate of 2-MTHF/DTBP with 2-MTHF: DTBP∼ 650:1 (Reaction conditions: T = 453K, p_{2MTHF} = 10.5 torr, WHSV= 3.97-5.05 g 2-MTHF/g cat./h, $X_{2MTHF} \leq 8\%$)*

dimensional sinusoidal 10-MR channels (4.1 × 5.1 Å). Perpendicular to these sinusoidal channels are larger supercages (7.1 × 7.1 × 18.1 Å) interconnected by elliptical 10-MR windows (4.0 × 5.5 Å). The transport between the two pore systems is restricted by 6-MR constrictions. The external surface of MWW crystals is terminated by supercages, which

leads to the formation of hourglass shaped surface side-pockets (7.1 × 7.1 × 9.0 Å). The MWW precursor can be swelled and pillared prior to calcination to preserve the intra-layer

Table 4.3 *Comparison of 2-MTHF dehydra-decyclization STYs before and after saturation by 2,6-DTBP as titrant on MCM-22, and MCM-36*

	STY_{DH} (h^{-1})	**Rate loss after DTBP saturation (%)**
MCM-22	2.9 ± 0.2	37.5 ± 1.4
MCM-36	5.3 ± 0.4	84.7 ± 2.1

[a] Reaction conditions: T=453K, p_{2MTHF} = 10.5 torr, X_{2MTHF} < 8%, Space velocities in the range of 0.37-1.25 molec.2-MTHF/H^+/min; [b] rate loss was calculated using the equation: 1-(residual rate after DTBP saturation/Rate immediately prior to titrant introduction) ×100 (%). All error bars represent a 95% CI from three independent measurements on fresh/recalcined beds.

crystallinity.[150,180] Given our previous results indicate the higher preference of 1,3-PD in medium-pore MFI than large-pore BEA, the presence of two different pore systems makes MWW a suitable topology to probe the effects of micropore environments in the production of 1,3-pentadiene.

Many recent reports have demonstrated the different catalytic performance of acid sites located in these distinct confining environments in MWW for various chemistries like methanol-to-hydrocarbons (MTH),[139,181] toluene disproportionation,[182] and methylcyclohexane[183]/n-heptane cracking.[184] While the sites in the side pockets are on the external surface and can be titrated with bulky bases that do not interact with intra-layer sinusoidal channels, the method cannot be used for titrating acid sites in the supercages due to their inter-connectivity through ellipsoidal 10-MR channels. On the other hand, smaller bases like pyridine have been shown to titrate all sites in MWW.[110] However, on swelling and pillaring the MWW precursor, the supercages don't collapse to form a 3-D structure after calcination, and this procedure leads to the preservation of long-range intra-layer crystallinity while creating inter-layer mesoporosity **(Figure 4.4b).** Upon successsful pillaring, a bulky base like DTBP can titrate not only the external surface side-pocket sites, but also the sites in the supercages which are now hourglass shaped surface side-pockets located in a mesoporous environment. This allows probing the catalytic role of different pore systems in determining the diene distribution by sequentailly restricting the chemistry to happen in the internal acid sites by DTBP tiration on MCM-22, and subsequently only in the 10-MR intra-layer sinusoidal channels by DTBP titration on MCM-36.

Prior reports have estimated that MCM-22 has ~ 8% sites in the external side-pockets, which can be titrated using DTBP during probe reactions like ethanol dehydration.[110,185] However, we observed a significantly higher (~ 38%) decrease in 2-MTHF consumption rates on MCM-22 upon DTBP saturation **(Table 4.3 and Figure 4.4c).** It has been shown that DTBP can access pore-mouth and channel-intersection sites in MWW,[185] and it is reasonable to expect that the accessibility of DTBP to these sites imposes more severe transport restrictions on 2-MTHF than ethanol, rendering some untitrated acid sites inaccessible to 2-MTHF. Besides, the ratio of external to internal sites in MWW depends on the particle size, and a higher drop in rates could also reflect more external specific surface area versus previous reports. Both the decrease in the rates **(Table 4.3 and Figure 4.4c)** and the timescales over which the rate dropped, were higher on MCM-36 than MCM-22, clearly indicating a higher number of sites being accessible to DTBP in MCM-36.

As seen in **Figure 4.4d,** the selectivity ratio of 1,3-PD/1,4-PD was in the range of ~2-3 prior to DTBP introduction on MCM-22, while it was ~1-1.2 for MCM-36, illustrating the role of pore environments on the diene distribution; mesopore environments in MCM-36 were detrimental to 1,3-PD production, consistent with our other findings. Upon the introduction of DTBP, the diene distribution shifted towards the conjugated diene on both catalysts. To study the relative changes in the diene distribution independent of absolute values, the formation rate ratio of 1,3-PD/1,4-PD was normalized by its initial value (at time zero). This also ensured that any product distribution changes due to catalyst deactivation did not affect the mechanistic interpretations. Concomitant with DTBP saturation, the normalized 1,3-/1,4-PD rate ratio on MCM-22 increased with the uptake of DTBP and stabilized at ~2.8 **(Figure 4.4e)**. As noted earlier, this diene distribution still has contribution of intra-layer sinusoidal channels and supercages. Nonetheless, this result indicates that the diene distribution shifts towards 1,3-PD when the catalytic contribution of external acid sites is completely suppressed. Most notably, the normalized 1,3-/1,4-PD rate ratio increased significantly upon DTBP introduction on MCM-36, and stabilized at ~4. As noted earlier, the sites in the super-cages are made accessible through pillaring of MCM-22. Hence, any residual rate after DTBP saturation on MCM-36 can be directly attributed to the intra-layer 10-MR sinusoidal channels. Indeed, when the chemistry was

restricted to occur only in these sinusoidal channels, the diene distribution became highly skewed in favor of the conjugated 1,3-pentadiene. Once again, we note that these measurements were not performed in strictly kinetic regime **(Section A4.2 in Appendix)**, thus supporting our other findings that impediment in diffusion facilitates 1,4-PD isomerization, thus leading to increments in 1,3-PD selectivity in medium-pore (10-MR) zeolitic channels.

4.4.4 Long-term stability of borosilicates. Catalytic evaluation of borosilicates or boron-modified aluminosilicates has been shown to increase time-on-stream stability for a variety of chemistries.[141,142,166,186–188] However, recent reports have highlighted the limitations of using time-on-stream (TOS) as a metric of catalyst stability, specially when comparing materials with varying reactivity,[160,189,190] as is the case with the two classes of zeolites in this study.

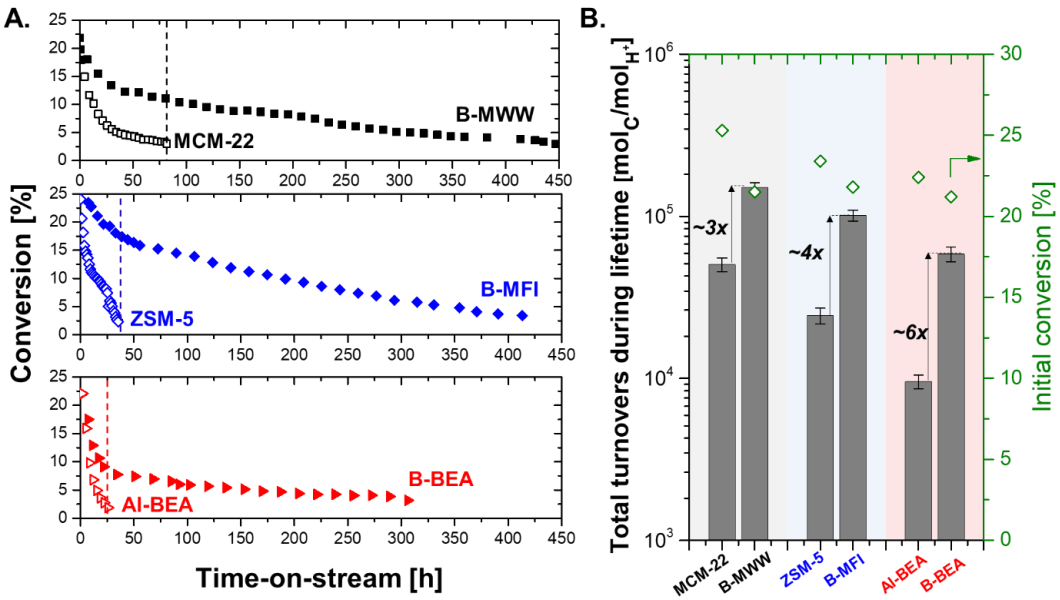

Figure 4.5 *a) 2-MTHF conversion as a function of time-on-stream on B-MWW(■), MCM-22 (□), B-MFI (blue ◆), ZSM5 (blue ◇), B-BEA (red ▶), and Al-BEA (red ▷); b) Total turnover numbers during catalyst lifetime (primary axis), and initial conversion (secondary axis) for all zeolites. (Reaction conditions: T= 573 K, p_{2MTHF} = 25-26 torr, Space velocity = 7.22-24.3 molec. 2-MTHF/H$^+$/min, Carrier gas (He) flowrate = 10-140 sccm). Error bars represent the standard errors in the calculation of total turnovers with the trapezoidal rule.*

We therefore use total turnover numbers per reactive proton (TON) during catalyst lifetime as the stability criteria **(Eq. 4.3)**.[160] As noted earlier, turnover number at time-on-stream *t*

is the cumulative moles of 2-MTHF-derived carbon converted to all products per mole of active site from time-on-stream 0 to time, *t*. The reactivity differences between boro-, and aluminosilicates manifest themselves in the different site-time yields (STYs) in **(Eq. 4.3).** This formalism further allows us to study changes in selectivity trends as a fraction of total turnovers, which is a more rigorous selectivity comparison for catalysts disparate in total TONs.[160]

Figure 4.5a shows the conversions on all zeolites as function of time-on-stream (TOS). In all the three investigated frameworks, borosilicates exhibited ~8-13x lifetimes, indicating their significantly higher stability under reaction conditions. To probe whether the relatively low Si/Al ratios in aluminosilicates were conducive to deactivation, we compared the time-on-stream data for two aluminosilicates with widely different Si/Al ratios (40, and 140, respectively) starting with iso-conversion levels (~25%) **(Figure A4.6)**. The detrimental effect of using high aluminum content aluminosilicates on catalyst lifetime

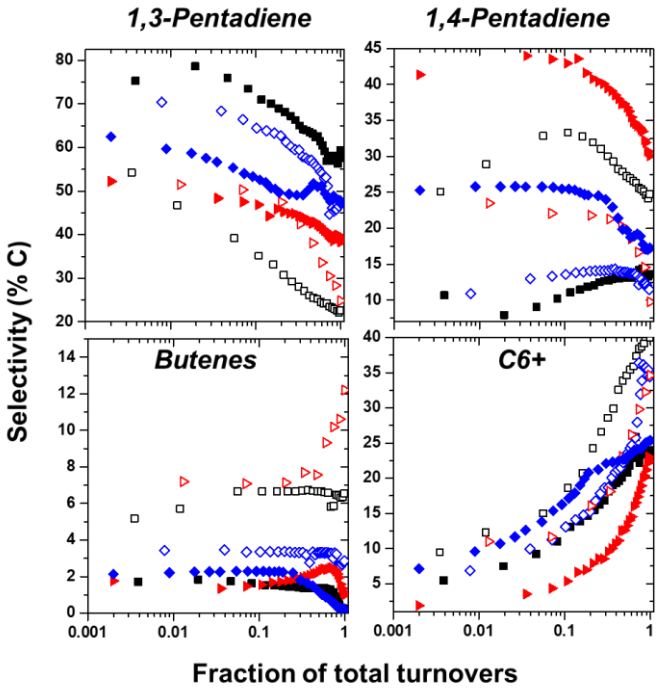

Figure 4.6 *Selectivity to (left to right and top to bottom) 1,3-Pentadiene, 1,4-Pentadiene, butenes, and C6+ compounds, as a function of the fraction of total turnovers B-MWW(■), MCM-22 (□), B-MFI (blue ◆), ZSM5 (blue ◇), B-BEA (red ▶), and Al-BEA (red ▷); Reaction conditions are same as* ***Figure 4.5****.*

(within a factor of 1.6x), was found to be much smaller than the effect of heteroatom identity (ie. Al/B) (~8-13x change). Interestingly, for both alumino-, and borosilicates, the

catalyst lifetime decreased in the order MWW > MFI > BEA. It is likely that C-C chain elongation steps terminate at shorter chain lengths in the 10-MR frameworks MFI and MWW. However, these condensation reactions leading to coking precursors occur more readily in the straight 12-MR channels of BEA, and are detrimental to total catalyst lifetime. **Figure 4.5 b** shows the total TONs for all zeolites employed in this study. As expected from the time-on-stream data, borosilicates showed ~3-6x higher total TONs than aluminosilicates starting from similar 2-MTHF conversions **(Figure 4.5 b)**. The product selectivities of all major products under reaction conditions were plotted as a function of total turnovers (**Eq. 4.4**) and are shown in **Figure 4.6**. As the catalysts deactivated, the selectivity to both 1,3-pentadiene and 1,4-pentadiene decreased for all zeolites; this reduction was mirrored by an increase in C6+ products (identified as alkylated aromatics), which are likely the coking precursors. Based on this observation, we conclude that linear pentadienes can further undergo condensation and/or cyclization reactions leading to these larger fractions. The product selectivity towards butenes was consistently lower on borosilicates than aluminosilicates at all stages of reaction progress, consistent with the inability of borosilicates to fragment C-C bonds. Notably, the selectivity to higher C6+ fraction was consistently lower in borosilicates (~15-22%) than aluminosilicates (25-40%), especially later in the reaction progress ($f_{total-turovers}(t) > 0.5$), when the catalysts had significantly deactivated. This is likely a result of weak-binding of these larger hydrocarbons, enabling desorption from boron-acid sites but irreversible adsorption and consequent condensation reactions on the aluminum acid sites, leading to coke formation. It is therefore likely that the higher stability of borosilicates is a direct consequence of reduced C6+ fraction formation.

4.5 Maximizing the yield of 1,3-pentadiene in the dehydra-decyclization chemistry. Recent reports of renewable catalytic pathways to piperylene production have utilized 2-MTHF as a feedstock. Other feeds have been less common, but a notable recent example includes a two-step deoxydehydration of xylitol leading to a 1,3-pentadiene yield of ~52%.[191] The hydrogenolysis of 2-MTHF is a frequently studied chemistry on metal phosphides, but the presence of high pressure of H_2 leads to the production of saturated species, and the overall yield to pentadienes is typically low; Oyama and co-workers have reported ~50% yield of pentadienes during the hydrodeoxygenation of 2-MTHF over

WP/SiO_2 at 548 K.[37] Other reports have reported negligible production of pentadienes in this chemistry.[146–148]

Dehydra-decyclization of 2-MTHF appears to be a promising chemistry to obtain high yields of 1,3-PD; Norman has recently reported that a ternary V-Ti-P oxide results in ~59% 1,3-PD yield during 2-MTHF dehydra-decyclization.[192] Dumesic and co-workers have reported 68% combined 1,3 + 1,4-pentadiene yield in the same chemistry on amorphous silica/alumina.[20] However, their reported yield dropped from 68% to 52% over 58 hours on-stream due to catalyst deactivation. Our previous studies on phosphorus-containing zeosils, while selective to dienes at low conversions, show a moderate dienes' yield of 60% at quantitative 2-MTHF conversions.[44]

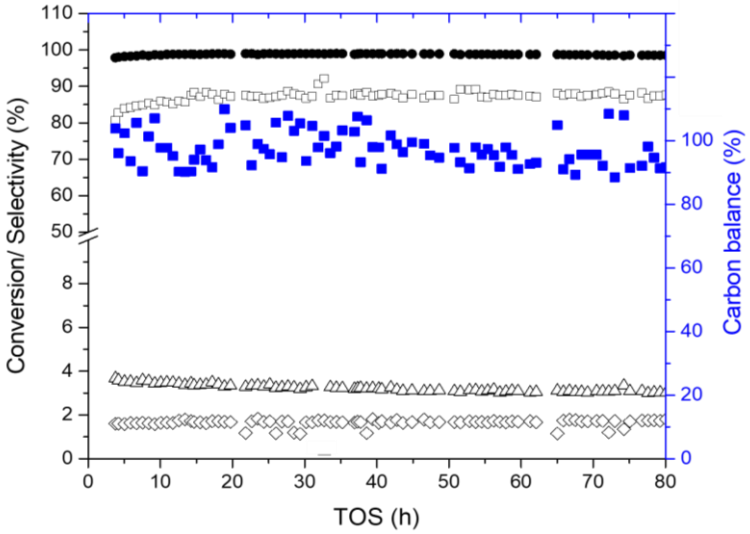

Figure 4.7 (primary axis) *2-MTHF conversion (●), and product selectivities towards 1,3-Pentadiene (□), 1,4-Pentadiene (◊), and butenes (Δ), and* ***(secondary axis)*** *Carbon mass balance (blue ■) (Reaction conditions: T= 658 K, p_{2MTHF} =3.6 torr, WHSV = 0.85 h^{-1}, Carrier gas flowrate= 35 sccm). Products with selectivity <2% are not shown.*

As noted before, borosilicates suppress both the competing retro-Prins pathway, as well as condensation reactions leading to C6+ fraction. Furthermore, these catalysts are significantly more stable under reaction conditions than aluminosilicates. Therefore, experiments were designed to probe borosilicates at near complete conversions to maximize the yield of dehydra-decyclization products in this chemistry, which predictably required high temperature and low space velocity conditions due to their instrinsic low reactivity. The obtained overall diene selectivities on borosilicates were consistently in the range of 86-92% independent of eperimental conditions and conversion levels. Most

notably, under these low space velocity (0.85 g 2-MTHF/g cat./h) and high temperature (658 K) conditions, a total diene yield of ~89% was observed on the borosilicate B-MWW. More importantly, the yield of conjugated 1,3-pentadiene was found to be ~86% **(Figure 4.7)**, and the corresponding diene selectivities were sustained for over 80 hours on-stream. Due to the lower activity of B-MFI and B-BEA, the yields obtained were limited by 2-MTHF conversions, and under similar experimental conditions, the 1,3-PD yield was found to be ~76% and ~24% on B-MFI, and B-BEA, respectively.

4.6 Conclusions. The systematic catalytic evaluation of boro-, and aluminosilicates in three zeolite topologies (MWW, MFI, and BEA) reveals that weakly acidic borosilicates suppress the competing retro-Prins pathway to butenes, as well as complex condensation pathways leading to coking precursors in the dehydra-decyclization of 2-methyltetrahydrofuran, thus leading to ~90% selectivity to dienes across different 2-MTHF conversions. The thermodynamic favorability of 1,3-pentadiene is shown by the increments in the diene distribution ratio of 1,3-/1,4-pentadiene by increasing reactor space-times and tighter micropore environments in MFI and MWW. Lastly, total catalyst lifetime in the chemistry is topology-dependent, with 12-MR BEA showing lower TONs for both heteroatoms, than MFI and MWW. Borosilicates exhibit a remarkable improvement in total catalyst lifetime in all three frameworks, ranging from ~3x in MWW to ~6x in BEA. These strategies are utilized to report a stable 1,3-pentadiene yield of ~86% on B-MWW.

Chapter 5

On the Acid Sites of Phosphorous Modified Zeosils

*Reproduced with permission from Kumar G., Ren L., Pang Y., Li X., Dauenhauer P.J., Tsapatsis M., Abdelrahman O.A., On the Acid Sites of Phosphorous Modified Zeosils, *Submitted* (Preprint available at https://doi.org/10.26434/chemrxiv.14225942.v1)

5.1 Conspectus

The acid sites of phosphorus-containing zeosils were probed through a combination of solid acid characterization, density functional theory calculations, and kinetic interrogations, establishing their weakly Brønsted acidic character. Due to the disparity in acid-site strength, P-zeosils catalyzed the probe chemistry of isopropanol dehydration slower than aluminosilicate zeolites by an order of magnitude on an active site basis. Propene selectivity during isopropanol dehydration remained 20-30% higher than that of aluminosilicates, illustrating the distinct nature of the weakly acidic phosphorus active sites that favored unimolecular dehydration routes. Regardless of the confining siliceous environment, the nature of phosphorous active sites was unchanged, indicated by identical apparent uni- and bi-molecular dehydration energy barriers. Kinetic isotope experiments with deuterated isopropanol feeds implicated an E2-type elimination propene formation mechanism on phosphorus-containing materials. Comparison of KIEs between phosphorus-containing zeosils and aluminosilicates pointed to an unchanged isopropanol dehydration mechanism, with changes in apparent energetic barriers attributed to weaker binding on phosphorous-active sites that lead to a relatively destabilized alcohol dimer adsorbate. Both ex-situ alkylamine Hofmann elimination and in-situ pyridine titration characterization methods exhibited phosphorous acid site counts dependent on probe molecules identity and/or concentration, underpinning the limitations of extending common characterization techniques for Brønsted-acid catalysis to weakly acidic materials.

5.2 Introduction

In the last decade, significant research has been devoted to harness the inexhaustible supply of renewable carbon in lignocellulosic biomass to derive fuels and bulk chemicals.[193,194] Biomass-derived intermediates are replete with multi-functional oxygen moieties (carbonyls, carboxylates, ethers) as well as organic impurities, both of which notoriously lead to coking.[193] Consequently, the use of aluminosilicate zeolites in catalytic

chemistries dealing with oxygenate dehydration frequently suffers from poor stability and the need for energy-intensive calcination cycles for regeneration.[194,195] Furthermore, activating these feeds selectively on 'strongly acidic' materials is often challenging, and designing new solid-acid catalysts may be required to efficiently process these alternative feedstock.[193,194,196]

One strategy to address these issues has involved the tuning of solid Brønsted site strength in zeolites to selectively promote desirable pathways, and has relied on the catalytic investigations of trivalent-atom-substituted ([Ga], [Fe], and [B]) zeolites.[197,198] Alternatively, our recent work on exploring selective dehydration catalysts has led to the development of phosphoric-acid supported on all-silica zeolites (with Si/P >10).[18,45,199] For example, phosphoric acid impregnated on self-pillared pentasil (P-SPP)[200] led to the suppression of undesired alkylation and oligomerization reaction products in the Diels-Alder cycloaddition of ethylene to dimethyl furan, leading to 97% p-xylene yield.[199] Compared to liquid phase phosphoric acid, reaction rates per phosphorus and selectivities in DMF-to-p-xylene chemistry were increased by using silica supports.[201] Using the same P-SPP catalyst, we demonstrated the selective conversion of tetrahydrofuran and methyltetrahydrofuran to butadiene and pentadienes, respectively.[18] Despite these investigations, phosphorous containing zeosils exhibit catalytic characteristics that have not yet been fully explored, and further advances require a fundamental understanding of their acidic active sites.

A related class of materials, solid phosphoric acid (SPA) catalysts, have been utilized for olefin oligomerization reactions for the better part of the last century.[202–205] However, there are notable differences between them and P-zeosils. For example, while Si-O-P linkages have not been detected on SPA catalyts,[206] their presence has been recently established in P-SPP.[207] Moreover, the support for SPA is either kieselguhr,[208] or pyrogenic/mesoporous silica,[209,210] while P-zeosils have been synthesized using both meso- and microporous supports.[18,45,199] Lastly, unlike SPA catalysts where only pyrophosphate phases are present, P-zeosils with low phosphorus loadings (Si/P >10) retain the crystallinity and specific surface area of the zeolitic phase.[199] It should be emphasized that P-zeosils are structurally distinct from silicoaluminophosphate (SAPO) zeotypes in that aluminum is not present in the framework,[18,45,199] and the origin of Brønsted acidity is not

a bridged hydroxyl between Si and P,[211,212] but rather terminal P-OH moieties. Despite the industrial prevalence of SPA catalysts, and unlike aluminosilicate analogues like H-ZSM-5, little in the way of fundamental catalytic information is known about P-zeosils. Limited characterization work has pointed to the presence of weak Brønsted acidic centers,[125,199] which is consistent with low reactivity observed in THF ring-opening dehydration reactions.[18]

Benchmarking the performance of P-zeosils using simple probe chemistries, and in doing so, investigating whether traditional acid site counting methods to calculate turnover frequencies can be extended to this class of materials, could contribute to improved understanding of their active sites. To that end, we used kinetic analysis of isopropanol (IPA) dehydration to comment on the identity and counts of active phosphorus species on a variety of all-silica microporous (MFI, BEA), mesoporous (MCM-41, SBA-15, SPP) and non-porous (Stöber) supports. Our goals are to (a) to compare and contrast the kinetic parameters (Rate-determining step/s (RDS's), site time yields (STY), uni-/bi-molecular dehydration selectivities, and activation barriers) on P-zeosils with aluminosilicate zeolites; (b) assess the implications of weak IPA binding on these sites in dehydration catalysis; and c) investigate changes in the nature of the catalytic P-site with the surrounding environments. More broadly, our results aim to address the challenges in studying catalytic surfaces with low affinity towards substrates, and the findings reported here can be extended to other acid-catalysis applications involving weak adsorbate-surface interactions.

5.3 Materials and Methods

5.3.1 Material synthesis and characterization. The following were purchased and used without any further treatment: Isopropanol (anhydrous, ≥99.5%, Sigma Aldrich), Isopropanol-d6 (99 atom%, Sigma Aldrich), Isopropanol-d8 (≥99.5 atom%, Sigma Aldrich), Isopropanol D(OH) (>98%, Sigma Aldrich), 1-propanol (anhydrous,≥99.7%, Sigma Aldrich), Ethanol (200 proof, ≥99.5%, Sigma Aldrich), Di-isopropyl ether (> 99% with BHT as stabilizer, Sigma Aldrich), Pyridine (99.8 %, Sigma Aldrich), n-Propylamine (≥99%, Sigma Aldrich), n-Butylamine (≥99.5%, Sigma Aldrich), Isopropylamine (≥99.5%, Sigma Aldrich), Cyclopentylamine (99%, Sigma Aldrich), Tert-butylamine

(≥99.5%, Sigma Aldrich), Tert-amylamine (≥98%, Sigma Aldrich), 2,6-di-tert-butyl pyridine (DTBP, ≥97 %, Sigma Aldrich), Phosphoric acid (85 wt%, Sigma Aldrich), Tetra(n-butyl)phosphonium hydroxide (TBPOH 40 wt%, TCI America), Tetraethyl orthosilicate (TEOS, 98%, Sigma-Aldrich), Hydrochloric acid (37 wt%, Sigma Aldrich), Cetyltrimethylammonium chloride (CTAB, ≥98%, Sigma-Aldrich,), Tetrapropylammonium bromide (TPABr, 98%, Sigma Aldrich), Hydrofluoric acid (48 wt% aqueous solution, Sigma Aldrich), Fumed silica (Cab-o-sil M5, scintillation grade, Acros Organics), PEO-PPO-PEO (P123, Sigma-Aldrich), Silicon-dioxide (quartz chips, 4-20 mesh, Sigma Aldrich), Tetrapropylammonium hydroxide (TPAOH 40 wt% in water, Alfa Aesar), Tetraethylammonium hydroxide solution (TEAOH, 40 wt % in water, Sigma Aldrich), Tetraethyl orthosilicate (TEOS, ≥99 %, Sigma Aldrich).

Ammonium form ZSM-5 (CBV 8014, Si/Al 40), ZSM-5 (CBV28014, Si/Al 140), and Al-BEA (CP814C, Si/Al 12.5) were obtained from Zeolyst International. Al-SPP (Si/Al 62) was the same sample previously characterized and reported by Xu *et al.*.[213] P-zeosils (P-SPP, P-BEA, P-MFI, P-SBA-15, P-MCM-41, P-Stöber) were synthesized by post-synthetic modification of all-silica analogues with an intended phosphorus loadings of Si/P molar ratio ~30, and detailed synthesis protocols can be found in the supporting information (**Section A5.1 in the Appendix)**. All catalysts were calcined in a boat placed within a 1" quartz tube under air flow at 823 K using a ramp rate of 2 K min^{-1} for 10 hours prior to any catalytic testing.

Powder X-ray diffraction (XRD) patterns were collected on a Bruker AXS D5005 diffractometer using Cu K_α radiation (=1.5418 Å) with a step size of 0.02° and a step time of four seconds. Inductively Coupled Plasma Optical Emission Spectrometry (ICP-OES) (Galbraith Laboratories) was used for elemental analysis of silicon and phosphorus for all reported catalysts. Textural characterization of all synthesized samples was performed with Ar physisorption in an Autosorb iQ2 porosimetry instrument (Quantachrom). Prior to analysis, crushed catalyst powders were outgassed at 573 K for six hours and subsequently cooled down to room temperature under vacuum. Brunauer–Emmett–Teller (BET) specific surface area measurements were used to represent the total surface area of the catalyst materials, and total pore volume was determined at $P/P_0 = 0.95$ for SPP, BEA, and MFI, and $P/P_0 = 0.99$ for SBA-15, Stöber, and MCM-41. Scanning

electron microscopy (SEM) was performed on a JEOL JSM-6500F scanning microscope operated at 5.0 kV.

Infrared (IR) spectra for pyridine were collected for P-SPP and Al-SPP on a Nicolet iS50 Fourier-transform infrared spectroscopy (FTIR) spectrometer with a Hg-Cd-Te (MCT, cooled to 77 K by liquid N_2) detector in the 4000 – 600 cm^{-1} range and were taken relative to an empty cell background reference collected under dynamic vacuum (< 0.01 Torr) at 423 K. Self-supporting wafers (10 -15 mg/cm^2) were sealed within an IR transmission cell (Harrick Scientific, ATK-024-3) with ZnSe windows. Wafer temperatures were measured within 2.0 mm of each side of the wafer by type K thermocouples (Omega). The IR cell was connected to a glass vacuum manifold, used for exposing the catalyst sample to controlled amounts of pyridine vapor. The catalyst sample was pretreated in-situ at 673 K for five hours with a ramp of 2.0 K min^{-1}, then cooled down to 423 K where pyridine was dosed until saturation. Finally, the temperature was raised to 623 K with a rate of 1.0 K min^{-1} while simultaneously collecting spectra every 3.0 min (Scan resolution of 4.0 cm^{-1}, total number of scans = 128).

5.3.2 Active-site quantification. Brønsted acid site (BAS) densities for all aluminosilicates reported in this work (Al-SPP, Al-MFI, and Al-BEA) were probed using the Hofmann elimination of tert-butylamine. To probe P-zeosils, Hofmann elimination of alkylamines with varying proton affinities (n-propylamine, n-butylamine, isopropyl amine, cyclopentylamine, tert-butylamine, tert-amylamine)[103] was performed and compared with analogous experiments with Al-MFI (Si/Al 140). All of these measurements were performed on a custom-made reactive gas chromatography (RGC) setup which essentially condenses a typical temperature-programmed desorption mass spectrometer (TPD-MS) within a gas chromatograph; the fabrication of the setup are detailed in Abdelrahman et al.[103].

Catalysts were pelletized and sieved to load ~ 20-30 mg of sample (500-1000 μm fraction), placed between plugs of deactivated quartz wool in a split inlet liner of the RGC setup. Samples were calcined *in-situ* in air at 673 K for one hour with a temperature ramp rate of 10 K min^{-1}. Thereafter, the gas was switched to helium (He), and the liner was cooled down to 423 K, where it was held for 30 min prior to amine dosing. The probe amine was dosed as pulses using an automated liquid sampler (ALS), and saturation of the

sample surface was ascertained by monitoring eluent amine breakthrough using a flame ionization detector (FID) directly downstream of the inlet. Once saturated, the bed was purged under a continuous stream of He (90 sccm) at the same temperature (423 K) for two hours to remove any physisorbed amine molecules. Thereafter, the temperature of the inlet liner was ramped from 423 K to 673 K at 10 K min^{-1} and held there for 30 min allowing for the adsorbed alkylamine to either desorb intact or undergo a Hofmann elimination to corresponding olefin and ammonia, while holding the GC oven at 303 K to trap all eluting alkenes. At the end of 30 minutes at 673 K, the temperature of the GC column, containing the trapped molecules, was raised from 303 K to 543 K at a ramp rate of 10 K min^{-1} and held there for 10 min to allow the olefin to elute from the column, and quantification was through the FID. A stoichiometry of 1:1 was assumed between the olefin and the BAS. These moles were normalized by the mass of sample loaded in the inlet liner to yield a Brønsted acid site mass density (μmol BAS/g cat.).

TPD curves for the tert-butylamine Hofmann elimination as well as molecular desorption were simulated using the Polanyi-Wigner equation using the kinetic parameters obtained from steady-state kinetic measurements. Two additional assumptions were made in this analysis: i) there is complete coverage of BAS by tBA at the start of the TPD for both set of materials, and ii) pre-exponential factor and activation energy is not a function of coverage. An open-access MATLAB code for the simulated TPD is available.[42]

5.3.3 Catalytic experiments. All kinetic measurements for isopropanol dehydration were performed for a range of partial pressure (3-100 torr) and temperatures (373 − 453 K) at ambient overall pressure in an upflow fixed bed reactor. While the majority of mechanistic studies were conducted on P-SPP, other P-zeosils were also probed to assess the support-dependence of active P-sites. Catalyst samples were pressed and sieved to particle aggregates of 106-250 μm and placed between deactivated quartz wool plugs in a 1/4" quartz U-tube; catalyst masses were in the range 25-70 mg. Void volume in the tube was minimized by loading quartz chips upstream of the catalyst bed. A 1/16" type-K thermocouple (Omega) was placed just above the catalyst bed for temperature measurements, and isothermal conditions were ensured by housing the reactor in a resistively heated furnace (MTI Corporation, GSL-1100X) with temperature control (PID

controller, Omega CN 7800). All catalyst samples were calcined *in situ* at 823 K in 40 sccm air (99.997%, Minneapolis Oxygen) using a temperature ramp rate of 5.0 K min^{-1}. They were then cooled to reaction temperature and purged with He (99.995 %, Minneapolis Oxygen) for at least 30 minutes prior to the introduction of reactant feed.

Reactant partial pressures were kept in the range ~2-100 torr by varying the volumetric flowrate of the reactants using a syringe pump (Cole Parmer 74905 series), and/or carrier gas flowrates (15-100 sccm) by a mass flow controller (Brooks Instruments 5850E). Pressure drops across the catalyst beds were maintained below 10% of total pressure. All transfer lines were maintained at temperatures ≥ 400 K to avoid condensation of any species. All carbon atom balances closed to within ~5%. Online analysis of the reactor effluent was performed with gas-sampling injections using a gas chromatograph (Agilent 7890A) equipped with a quantitative carbon detector (QCD, Polyarc^{TM})[47] and a flame ionization detector (FID), and separation was performed using an HP-PLOT Q column (Agilent, 19091P-QO4). To the extent possible, kinetic studies for a given synthesized catalyst were performed with the same batch for which all the characterization results are also reported (XRD, SEM, Ar-adsorption). In cases where kinetic data from multiple batches are reported, these batches were subjected to a reference catalytic condition (403 K, 30 torr IPA, WHSV of ~2.5 g IPA/ g cat./ h, 25 sccm diluent (He) flowrate) to assess any variations originating from synthesis procedures. All reported catalysis data are either from fully characterized batches or from batches that exhibit negligible variations (< 0.2% difference in conversions) in catalytic performance from the fully characterized batch at the reference condition specified above.

A combination of Mears' and Weisz-Prater criterion was used to ascertain the absence of external and internal mass transfer limitations, respectively **(Section A5.3.5 in the Appendix)**.[155] All reported rates are initial rates (t=0) under differential conversions (< 5% in all measurements for P-zeosils, and <10% for all measurements for aluminosilicates), which are obtained by correcting for intervening, albeit minor, catalyst deactivation under reaction conditions. For P-SPP catalyst, regeneration studies (re-calcining *in situ* at 823 K in 40 sccm air (99.997%, Minneapolis Oxygen) using a temperature ramp rate of 5.0 K min^{-1}) were carried out to find that deactivation was reversible **(Section A5.3.1 in the Appendix)**. For all *in-situ* pyridine titration experiments,

isopropanol dehydration was carried out until initial transients subsided, and an instantaneous switch was made to the IPA/titrant mixture (molar ratio~250-5500) at identical volumetric flowrate. Experiments with multiple pyridine partial pressures were performed by varying the molar ratio of IPA : pyridine in the feed mixture. An identical methodology of instantaneous switch to deuterated IPA feeds allowed for the measurement of kinetic isotope effect values. Unless otherwise mentioned, error bars are reported at a 95% confidence level.

5.3.4 Adsorption energy calculations using Density Functional Theory. Calculations of molecular adsorption on the active P-site was modeled as a Q_1^1 site with adjacent silanol **(Figure A5.7 in the Section A5.2)**. We note that there may be other possible Brønsted acidic -OH moieties in the wide variety of P-environments expected in these materials as noted in Jain et al.,[207] but we only consider the Q_1^1 site for these simulations. Analogous calculations on the bridging hydroxyl BAS in aluminosilicate MFI were also carried out for comparison. Calculations on the surface of the MFI framework were performed using periodic density functional theory (DFT) with the Vienna Ab Initio Simulation Package (VASP)[214] version 6.1.0 incorporated in the MedeA Environment. The generalized gradient corrected Perdew-Burke-Ernzerhof (GGA-PBE)[215] exchange correlation functional was employed in all calculations with a plane-wave basis set and the projector augmented wave (PAW) potentials, where Si (3s3p), O (2s2p), P (3s3p), Al (3s3p), H (1s), C (2s2p), and N (2s2p) were included explicitly in the valence.[216,217] A cutoff of the plane-wave basis of 500 eV along with the Γ-point sampling of reciprocal space was used. DFT-D3 with Beceke-Johnson (BJ) - damping was used to include van der Waals interactions between the adsorbate and zeolite.[218,219] A Gaussian smearing of 0.05 eV was applied at the Fermi level, and the total energies were extrapolated to zero smearing. Geometry optimizations were converged to an energy threshold of 10^{-5} eV and a force threshold of 0.02 eV $Å^{-1}$. Structure visualization was obtained using Avogadro[220,221] version 1.2.0.

An all-silicate MFI periodic unit cell ($20.090 \times 19.738 \times 13.142$ Å, $\alpha, \beta, \gamma = 90°$) was obtained from the International Zeolite Association (IZA) database. The T12-site is the most frequently chosen site for aluminum substitution due to its presence at the interception of the straight and sinusoidal channels of MFI[222–224] and the lowest energy

among all 12 T-sites,[225,226] T2-site is also located at the interception of channels[226,227] and is energetically comparable to T12-site for aluminum incorporation.[226] Additionally, the energetically most favorable T-site for the P-active site is unknown. As such, calculations were performed and compared on both T2 and T12-sites for both set of sites (Al-, and P-) to choose the most representative T-site for adsorption energy calculations.

To construct an internal BAS, one silicon on the T12-site or T2-site was substituted by an aluminum atom. The resulting negative charge from aluminum incorporation on the oxygen of the Si-O-Al linkage was balanced by a proton to form an internal BAS, followed by a geometry optimization (**See Figure A5..9 in Section A5.2 for details**). Internal BAS on the T12-site was calculated to be 13 kJ mol^{-1} more stable than BAS on the T2-site, and was therefore chosen for adsorption energy calculations on aluminum-containing MFI. In an analogous manner, an internal P-active site was constructed by breaking the Si-O-Si linkage of a T2-site or T12-site silicon **(Figure A5.7 in Section A5.2)**, where a phosphoric acid was attached to generate the internal P-active site, while the other silicon previously on the Si-O-Si linkage was terminated as a silanol group, as shown with the P-active site on a T2-position in **Figure A5.7A (Section A5.2 in the Appendix)**. As the T2-site is close to the boundary of the unit cell in the c direction, 1 × 1 × 2 supercells were constructed using the optimized structures for clear visualization of the internal acid sites and the interactions with adsorbent molecules after structure optimizations in the 1 × 1 × 1 unit cell. Notably, the internal P-active site was found to be ~74 kJ mol^{-1} more favorable on the T2-site compared to T12-site, indicating that while aluminum incorporation occurs on T12 position, P-active site is more likely to locate at the T2-site of MFI. Therefore, DFT calculations were performed on the T2-site for adsorption on P-active site.

Similarly, all adsorption energy calculations on the external surface of P-MFI were accomplished by constructing an external surface defined by a slab formed between two pentasil layers of MFI (**Figure A5.7B in Section A5.2 in the Appendix**).[228] The two pentasil layers were separated perpendicularly by a vacuum gap of 20 Å to prevent interactions between the two layers. Vacuum slabs of 10 Å were applied between the pentasil layers and the upper and bottom boundaries of the periodic unit cell to prevent interactions between pentasil layers in adjacent periodic cells. The dangling Si-O bonds were terminated as silanol groups at the top and bottom surfaces of the pentasil layers.[229]

An external P-active site was constructed by attaching a phosphoric acid on the T2-site with the same method used to construct the internal P-active site (**Figure A5.7B in Section A5.2 in Appendix**). A structural optimization was then performed on the structure containing an external P-active site at the T2 position.

Prior to adsorption calculations, probe molecules including tert-butylamine, IPA, and DIPE were optimized separately in a 25 × 25 × 25 Å cell. The energy-minimized molecules were then loaded to the zeolite unit cell with the oxygen of IPA and DIPE and the nitrogen of tert-butylamine facing the proton of Al- or P-active site. The initial N-H or O-H distances between the adsorbate nitrogen or oxygen and acid site proton were close to one bond length of the O-H bond in Al-, or P-active site. All atomic positions and lattice constants were relaxed to obtain adsorption structures. The adsorption energy (ΔE_{ads}) was calculated,

$$\Delta E_{ads} = E_{ZA} - E_Z - E_A \quad (5.1)$$

where E_Z and E_A are the minimized electronic energy of the zeolite framework and adsorbate, respectively, while E_{ZA} is the minimized electronic energy of the final adsorption structure.

5.4 Results and Discussion.

5.4.1 Synthesis and characterization of P-zeosils. Powder X-ray diffraction patterns (PXRD), scanning electron microscopy images (SEM), and Ar-porosimetry measurements of all synthesized P-zeosils (P-SPP, P-MFI, P-BEA, P-SBA-15, P-Stöber, P-MCM-41) are reported in the supporting information **(Section A5.1)**, and indicate that the crystallinity, morphology, as well as porosity for the all-silica zeosils is retained after P-loading on all-silica supports, consistent with previous reports on these materials.[18,199] Elemental analyses and textural properties of these synthesized samples are listed in **Table 5.1**. A detailed ^{31}P NMR study on the different P-environments on P-SPP has recently revealed a host of mono-, and oligomeric phosphorus environments which evolve with the extent of hydration.[207] We have assumed this to be more broadly applicable across different supports and not independently carried out ^{31}P solid state NMR characterization of P-zeosils

reported here. Since up to now only *ex-situ* NMR has been reported, extrapolating the obtained insights on P-environments to reaction conditions is challenging as accurately quantifying adventitious water (from liquid feeds, gas lines, and as reaction product) is non-trivial.

The reported samples vary from purely microporous (P-MFI and P-BEA), purely mesoporous (P-MCM-41), micro- and mesoporous (P-SBA-15 and P-SPP) to non-porous (P-Stöber); the bulk phosphorous content was held relatively constant across all materials (Si/P~30). Correponding data for the aluminosilicate zeolite samples has been previously reported in our prior works: ZSM-5 (Si/Al 40 and 140)),[197,230] Al-BEA (Si/Al 12.5),[197] and Al-SPP (Si/Al 62)[213] and not discussed here for brevity.

5.4.2 Brønsted Acidic Protons. Among techniques to probe solid acids, the Hofmann elimination of primary alkylamines to olefins and ammonia is particularly useful, as it occurs exclusively on Brønsted acidic centers.[103,231,232] An alkylamine stoichiometrically adsorbed on a BAS (1 mol alkylamine: 1 mol H^+) reactively desorbs via the Hofmann elimination in the course of a temperature ramp, forming its respective olefin, which is quantified and taken as a measure of the number of acessible BAS. We investigated the utility of this technique to measure the BAS density on P-SPP (Si/P 30) using six different primary alkylamines (n-propylamine (nPA), n-butylamine (nBA), isopropylamine (iPA), cyclopentylamine (cPA), tert-butylamine (tBA), and tert-amylamine (tAA), **Figure 5.1A)**. The alkylamines varied in proton affinity (918-940 kJ mol^{-1}) as well as the stability of the carbocation involved in the Hofmann elimination, where a more stable carbocation reacts and desorbs at lower temperatures (in terms of desoption temperatures: nPA~nBA < iPA~cPA<tBA~tAA).[103,231,232] Over a site-isolated Al-MFI (Si/Al 140), the BAS density remained constant at ~95 μmol H^+ g^{-1} within experimental error, independent of alkylamine proton affinity and/or carbocation stability **(Figure 5.1A)**. Conversely, over P-SPP, the measured BAS densities increased seven-fold across the range of alkylamines investigated. Considering pairs of alkylamines with similar carbocation stability (nPA/nBA, iPA/cPA, and tBA/tAA), differences in the measured BAS density revealed a dependence on the proton affinity of the alkylamine. Furthermore, these densities increased

with carbocation stability; tertiary alkylamines (tBA, and tAA) yielded significantly higher BAS densities than primary amines (nPA, and nBA).

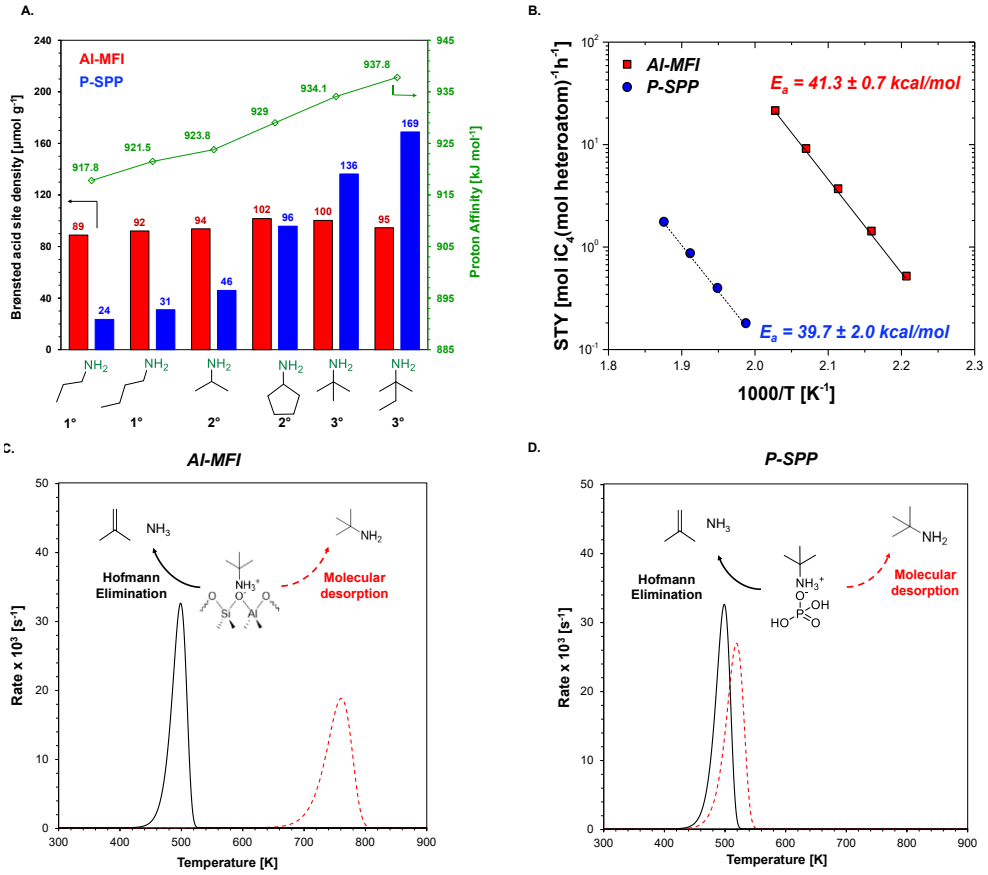

Figure 5.1 A. *(primary axis) The BAS count (μmol g_{cat}^{-1}) of (blue bars) P-SPP (Si/P=30) and (red bars) [H]-ZSM-5 (Si/Al=140) plotted for primary alkylamines; and (secondary axis) Proton affinity (kJ mol^{-1}) for all amines used for the measurement of BAS counts taken from NIST database. (left to right: n-propylamine, n-butylamine, isopropyl amine, cyclopentylamine, tert-butylamine, tert-amylamine);* ***B****. Arrhenius plot for tert-butylamine Hofmann elimination (isobutene formation rates) on P-SPP (●), and Al-MFI (Si/Al 140) (■) (Reaction conditions: P_{tBA} =10 torr; WHSV 2.7 g g cat^{-1} h^{-1} for P-SPP and 4.4 g g cat^{-1} h^{-1} for Al-MFI, He flowrate = 100 sccm, all conversions below 3.8% for P-SPP and 4.5 % for Al-MFI);* ***C.*** *TPD simulation of the tert-butylamine (tBA) Hofmann elimination and molecular desorption on Al-MFI and P-SPP. The solid black line is the calculated TPD based on measured kinetics of tBA Hofmann elimination reported in* ***B.,*** *while the dashed red line is the expected desorption TPD if tBA was to desorb intact. The simulations are based on the Polayni-Wigner equation (See methods for details).*

Measured BAS densities are only reliable if the adsorbed alkylamine reacts first and does not molecularly desorb.[19,20] While this assumption holds true for bridging hydroxyls in aluminosilicates,[233] challenges associated with extending it to weak acids have been previously illustrated on [B]-substituted zeolites.[156,234] Gorte and co-workers have shown that in the course of a TPD, isopropylamine can desorb without reacting on

the weakly Brønsted acidic centers of [B]-substituted MFI, leading to the undercounting of available BAS.[156] On weaker BAS where the barrier to molecular desorption is reduced, the assumption of negligible rates of molecular desorption may not hold true. In addition to the strength of the BAS, alkylamine proton affinity also determines the heat of adsorption and therefore the rate of molecular desorption.[156,233] Therefore, the probabililty of a pre-adsorbed alkylamine molecularly desorbing as opposed to reactively desorbing through Hofmann elimination will depend on the choice of alkylamine.

To quantitatively probe why these changes in desorption rates are only consequential for P-SPP and not Al-MFI, we compared the rate of reactive desorption via alkylamine Hofmann elimination relative to that of molecular desorption. Considering the Hofmann elimination of tert-butylamine as a representative case, the Arrhenius plots of isobutene formation rates are shown for Al-MFI (same data as reported by Chen et al.[235]) and P-SPP in **Figure 5.1B**; the apparent elimination activation energy remains within experimental error across the two materials. The observation of similar activation energies is consistent with previous studies suggesting that the kinetics of Hofmann elimination is independent of acid site strength (P-sites and aluminosilicates in this case).[236,237] Conversely, the rate of alkylamine molecular desorption is expected to be considerably larger over the weaker P-acid sites; the calculated tBA adsorption energy on P-MFI (-153 kJ mol^{-1}, **Table 5.3**) was significnatly less exothermic relative to Al-MFI (-229 kJ mol^{-1}, **Table 5.3**).

The combined effect of the insensitive energetics of Hofmann elimination relative to the varying molecular desorption can be visualized by comparing simulated TPD profiles for each, over Al-MFI and P-SPP. For Hofmann elimination, nearly identical TPD profiles are simulated for both P-SPP and Al-MFI due to identical reaction kinetics (black solid curve in **Figure 5.1C**). On the other hand, the simulated molecular desorption traces (dashed red curves in **Figure 5.1C**) show a sharp contrast; TPD profiles of molecular desorption and Hofmann elimination for tBA over Al-MFI are completely seperated by > 100 K **(Figure 5.1C)**. This means that on an aluminosilicate (Al-MFI), the rate of molecular desorption is significantly lower than the rate of Hofmann elimination such that any adsorbed alkylamine cannot desorb intact before it reacts, leading to all sites being 'counted'. However, this is not the case for the phosphorus active sites on P-zeosils;

significant overlap is expected on P-SPP on account of the accelerated rate of molecular desorption **(Figure 5.1C)**. The proton affinity and/or stability of resulting carbenium therefore influences whether or not the amine desorbs intact or reacts over P-SPP, with more stable (tertiary carbocation) and more basic (higher proton affinity) amines being able to carry out turnovers on a higher number of active sites. Whether the speciation of the additional sites counted with amines like tBA are identical to those counted with ones like nBA is unknown. Nontheless, these results, taken together, unambigiously identify P-zeosils as containing weak Brønsted acidic active sites.

5.4.3 Brønsted acidic protons probed by interaction with Pyridine. In addition to primary alkylamine Hofmann elimination, we investigated the interaction of pyridine with the weak P-sites of P-SPP using a combination of temperature-programmed desorption (TPD) and IR spectroscopy. Analogous experiments with Al-SPP were also carried out for comparison (**Figure 5.2A)**. The IR band at 1545 cm^{-1} is characteristic of pyridine adsorbed on Brønsted acid sites, forming a pyridinium ion via complete proton transfer. Despite their weaker acidity, P-zeosils were able to protonate pyridine, evidenced by the characteristic pyridinium ion band (**Figure 5.2B**). As the temperature was increased, the pyridinium band integrated area decreased on both Al- and P-SPP. While pyridine desorption from the surface of P-SPP was complete at a relatively mild temperature of ~523 K, a non-negligible fraction remained adsorbed on Al-SPP **(Figure 5.2C)**, consistent with the conclusion of weaker acidity of phosphorous based BAS relative to aluminosilicates based on Hofmann elimination (**Sec. 5.4.2**).

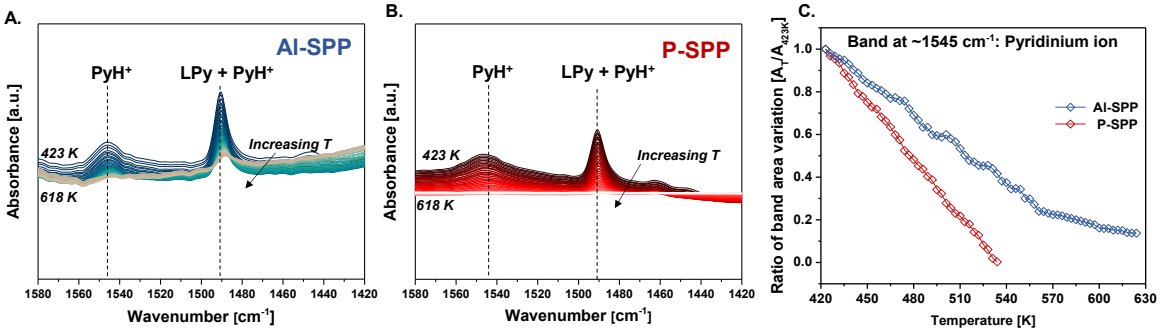

Figure 5.2 *IR spectra obtained during the temperature-programmed desorption of pyridine from* ***A.*** *Al-SPP (Si/Al 62) and* ***B.*** *P-SPP (Si/P 30);* ***C.*** *Pyridium peak band area (~1545 cm^{-1}) normalized to initial value (at 423 K) compared for Al-SPP and P-SPP.*

5.4.4 Isopropanol dehydration on P-zeosils. Alcohol dehydration has been extensively used as a probe reaction to characterize acidity in zeotype materials,[108,110,140,198,238] and recent computational as well as experimental studies have led to detailed understanding of

Table 5.1 *Structural and IPA dehydration related catalytic properties of all phosphorus-containing and aluminosilicate zeosils*

Catalyst	Si/X[a]	$E_{a,unimolecular}$[b] [kcal mol^{-1}]	$E_{a,bimolecular}$[c] [kcal mol^{-1}]	Temperature [K]	Sel_{uni} [%C][d]	$STY_{Dehyd.}$ [mol IPA (mol P h)$^{-1}$][d]
Phosphorous containing						
P-SPP	30.2	27.4 ± 0.6	18.5 ± 0.4	**403**	**83.1**	**0.21**
				423	89.1	0.91
				443	92.9	3.92
P-MFI	36.3	27.1 ± 0.9	18.0 ± 2.1	**403**	**87.5**	**0.29**
				423	92.8	1.31
				443	95.2	5.52
P-BEA	43.1	24.6 ± 0.8	16.9 ± 0.6	**403**	**71.5**	**0.03**
				423	77.3	0.11
				443	85.8	0.42
P-MCM-41	35.5	28.3 ± 1.0	19.4 ± 1.5	**403**	**80.1**	**0.03**
				423	86.3	0.13
				443	91.2	0.58
P-SBA-15	34.5	26.9 ± 2.1	17.8 ± 1.5	**403**	**64.2**	**0.05**
				413	66.7	0.09
				423	65.8	0.19
P-Stöber	32.0	24.6 ± 0.8	18.5 ± 1.5	**403**	**92.6**	**0.08**
				423	94.3	0.31
				443	96.1	1.16

Aluminosilicates						
				393	48.4	5.5
Al-MFI	40	35.7 ± 0.3	30.0 ± 2.7	**403**	**53.3**	**15.8**
				413	63.9	42.2
				373	17.2	1.4
Al-BEA	12.5	33.3 ± 2.8	24.3 ± 3.5	393	22.4	9.3
				403	**28.1**	**22.7**
				373	55.5	0.6
Al-SPP	62	36.8 ± 1.3	31.0 ± 1.7	393	64.1	7.6
				403	**63.6**	**17.6**

[a] ICP-OES (Galbraith Laboratories); [b] Calculated from the Arrhenius plots of propene formation rates at a fixed P_{IPA} = 30 torr in the temperature range 403-453 K and 373-413 K for aluminosilicates and for P-containing materials, respectively; [c] Calculated from the Arrhenius plots of di-isopropyl ether formation rates in the temperature range 373-453 K; [d] Selectivities and rates measured during IPA dehydration under following reaction conditions: P_{IPA} = 30 torr, WHSV in the range 2.0 – 60.4 g IPA^{-1} g.cat^{-1} h, all conversions < 8.5%. All values at 403 K have been bolded for easy comparison between P-zeosils and aluminosilicate zeolites at a common temperature.

underlying reaction mechanisms and pathways of light (C1-C4) alcohol dehydration on solid acid catalysts.[48,108,114,239–245] The ubiquitous themes tying these studies together are:
(i) the evidence for the coupling of unimolecular and bimolecular dehydration pathways, where adsorbed dimers that produce di-alkyl ethers (bimolecular dehydration product) can also contribute to olefin formation (unimolecular dehydration product),[114,243]
(ii) inhibition of olefin formation rates at high alcohol partial pressures (> 50 torr) due to the higher stability of adsorbed alcohol dimers relative to monomers,[108,239] and
(iii) an increased preference to unimolecular dehydration with increasing temperatures.[108,114,239,243]

The favorability of E1/E2 elimination pathways during alcohol dehydration on zeolites depends on the stability of carbenium formed during the reaction; previous reports have highlighted the prominence of E2 type pathways as the RDS for isopropanol (a secondary alcohol) dehydration in aluminosilicates MFI,[241,246] and FAU,[241] while primary alcohol dehydration primarily occurs through E1-type elimination pathways.[48,108,114,239,240,243–245] To better understand the active centers of P-zeosils, we

sought to compare the kinetics of isopropanol (IPA) dehydration over the two families of catalysts (aluminosilicates and P-zeosils).

5.4.4.1 Rate and selectivity towards propene. Across the various phosphorus-containing samples, propene was found to be the dominant product under reaction conditions **(Table 5.1)**. Active P-sites exhibited a preference to unimolecular dehydration relative to their aluminosilicate analogs (e.g., P-MFI versus Al-MFI in **Tables 5.1**), where selectivity to propene was ~ 30% higher. The differences in selectivity are in agreement with aqueous-phase secondary alcohol dehydration studied by Lercher and co-workers, in which bimolecular dehydration of cyclohexanol, 3-heptanol, and 2-methyl-3-hexanol was minimal using aqueous H_3PO_4 but prevalent over Al-BEA.[247,248] Within the family of phosphorous containing catalysts, SPP and MFI structures exhibited the largest activity per mol of bulk phosphorus content, suggesting that the zeolite structure may influence phosphorus active site speciation. However, despite the varying activities per bulk phosphorus content, the apparent energetics of dehydration across the various P-zeosils remain relatively unchanged within experimental error. Over P-SPP, propene formation faces an apparent activation energy of ~27 kcal mol^{-1}, with only minor differences among different silica supports **(Figure 5.3A)**. Similarly, apparent bimolecular dehydration barrier

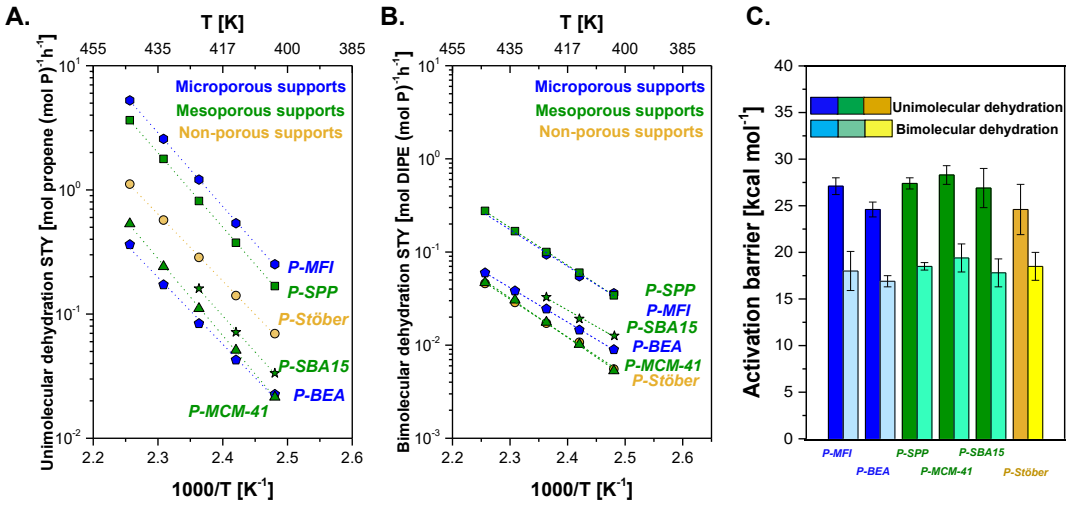

Figure 5.3 A. *Arrhenius plot for the unimolecular IPA dehydration rates (propene formation STYs) on all investigated P-zeosils;* ***B.*** *Arrhenius plot for the bimolecular IPA dehydration rates (DIPE formation STYs) on all investigated P-zeosils;* ***C.*** *Activation barriers of unimolecular and bimolecular dehydration compared for all investigated P-zeosils (Reaction conditions: T= 402 – 454 K; WHSV 2.0 – 5.9 g IPA g. cat^{-1} h^{-1}, diluent (He) flowrate 25 sccm, all conversions < 5%).*

to DIPE formation remained nearly constant at ~18 kcal mol^{-1} **(Figure 5.3B)**. The relative trend of the apparent barriers was also consistent with prior reports,[114,244,245] where the apparent barrier to unimolecular dehydration was found to be larger than that of bimolecular dehydration **(Figure 5.3C)**. Given that the activation energetics of alcohol dehydration are sensitive to the nature of the active site,[239] the identical activation energies signal that the nature of active P-sites is unchanged across the different phosphorus containing materials. The observed differences in the bulk-phosphorus normalized rates are likely due to differences in the relative amounts of available catalytic phosphorus sites.

Comparing the overall rate of dehydration across the two classes of materials, aluminosilicates were significantly more active on a heteroatom basis. At a fixed temperature of 403 K, the overall site time yield (STY) of isopropanol (IPA) dehydration over aluminosilicates and P-zeosils is ~20 mol C_3H_7OH (mol Al. h)$^{-1}$ and ~0.1 mol C_3H_7OH (mol P. h)$^{-1}$, respectively. Interestingly, despite the lower rate of dehydration, the phosphorous containing catalysts exhibited a smaller apparent activation energy; the apparent barrier to propene and di-isopropyl ether (DIPE) formation over P-zeosils are both lower by ~10 kcal mol^{-1} relative to their aluminosilicate counterparts (**Table 5.1**). To understand this seemingly contradictory result, it is necessary to consider the 'apparent'

Table 5.2 *DFT-calculated adsorption energies for surface species on active site in P-MFI and Al-MFI*

Molecule	**ΔE_{ads} [kJ mol^{-1}]**		**$\Delta\Delta E_{ads}$**
	P-active site	**BAS in Al-MFI**	**[kJ mol^{-1}]**
Tert-butylamine (tBA)	-153	-229	-76
Isopropanol (IPA)	-108	-121	-13
Di-isopropyl ether (DIPE)	-123	-182	-59

nature of the reported activation energies; macroscopically measurable apparent activation energies frequently include thermodynamic contributions like reactant adsorption energies ($E_{a,app} = f(\Delta H_{ads})$).[235,249,250] Computationally calculated adsorption energies of relevant surface species (IPA and DIPE) are significantly different on aluminosilicates and

phosphorous containing materials ($\Delta\Delta E_{ads,IPA}$ = 13 kJ mol^{-1} and $\Delta\Delta E_{ads,DIPE}$ = 59 kJ mol^{-1}, **Table 5.2**), making the direct comparison of measured activation energies across the two classes of materials non-trivial. Under identical reaction conditions, barriers over aluminosilicates are likely measured from an adsorbed state due to high surface monomer and dimer coverages (in black, **Figure 5.4A**), and from the gas-phase as reference on P-zeosils due to low coverages (in red, **Figure 5.4A**). As such, the apparent activation energies values for P-zeosils likely have larger contributions of IPA monomer and dimer adsorption enthalpies, which reduces the apparent activation energy relative to the intrinsic surface activation energy.

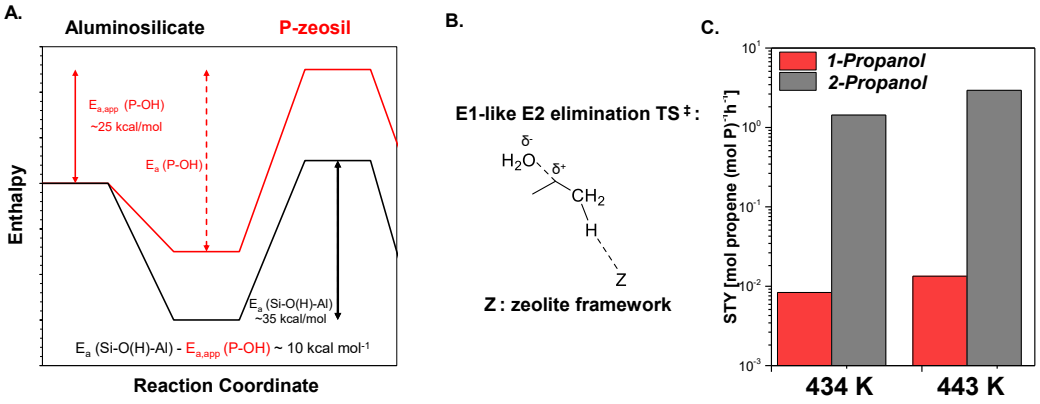

Figure 5.4 A. *Proposed reaction coordinate diagram for the barriers on aluminosilicates (in black) and P-zeosils (in red).* ***B.*** *Illustration of proposed kinetically relevant transition state for the elimination pathway during unimolecular dehydration of 2-propanol.* ***C.*** *Propene site time yield measured on P-SPP using 1-propanol and 2-propanol feed at two temperatures (434 K, and 443 K) (Reaction conditions: WHSV = 2.5 – 2.9 g reactant g cat^{-1} h^{-1}, carrier gas (He) flowrate 25 sccm, conversions below 5%).*

5.4.4.2 Nature of kinetically relevant transition state. The rationalization for the seemingly contradictory apparent barriers assumes that while adsorption and reaction energetics may differ across the phosphorus containing- and aluminosilicate materials, the dehydration mechanism is unchanged and faces similar rate limiting step(s). To verify whether this assumption is reasonable, we investigated the kinetically relevant IPA dehydration step(s) with kinetic isotope effect (KIE) experiments involving deuterated alcohol reactants ($C_3D_6(H)OH$, C_3D_7OD, and $C_3H_6(D)OH$)) (**Table 5.3**). Over P-SPP, C_3D_7OD exhibited a primary KIE of 1.87 ± 0.11 for propene formation (**Calculations included in Section A5.3.3 of Appendix**), implicating the direct involvement of a X-H bond scission event in a kinetically relevant step. The analogous value with C_3D_6OH (1.63 ± 0.05) was relatively

similar, suggesting that Cβ–H cleavage is the only kinetically relevant X-H cleavage to propene formation. The absence of a KIE with a deuterated Cα-H IPA feed ($C_3H_6(D)OH$, 1.07 ± 0.06) corroborates this conclusion, unambiguously identifying the Cβ–H cleavage as a kinetically relevant step for propene formation.

Table 5.3 *Kinetic isotope effect with isopropanol, isopropanol (d8), isopropanol (d6) and isopropanol-d-OH on P-SPP (Si/P 30) and Al-MFI (Si/Al 140)*

		Reactant		
Catalyst	**r_H/r_D**	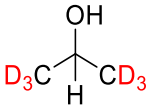	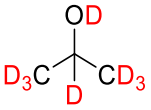	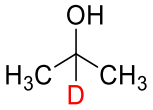
P-SPP	Propene	1.63 ± 0.05	1.87 ± 0.11	1.07 ± 0.06
	DIPE	1.25 ± 0.04	1.09 ± 0.10	1.03 ± 0.13
Al-MFI	Propene	1.71 ± 0.18	1.82 ± 0.07	0.43 ± 0.03
	DIPE	1.16 ± 0.15	1.13 ± 0.03	0.47 ± 0.02

(Reaction conditions for P-SPP: T= 403 K, P_{IPA}= 30 torr, WHSV= 4.37- 4.42 g IPA g cat.$^{-1}$ h^{-1}, Carrier gas (He) flowrate = 25 or 15 sccm; Conversions below 0.5%; Reactions for Al-MFI: T= 403 K, P_{IPA}= 30 torr, WHSV= 7.5- 9.50 g IPA g cat.$^{-1}$ h^{-1}, Carrier gas (He) flowrate = 60 sccm; conversions below 2.2 %).

These results are consistent with an E2-type elimination to propene, where Cβ-H is not fully severed **(in red, Figure 5.4B)**. Lercher and co-workers have reported similar KIE results in the case of secondary alcohols dehydration to olefins with aqueous-phase phosphoric acid.[247,248] While presence of solvent in these reports precludes a direct comparison, our results are in qualitative agreement in that the Cβ–H cleavage rate constant appears in the unimolecular dehydration kinetic expression.[247,248] It is important to note that 'true' E2 elimination (concerted single-step) does not result in the formation of a carbenium ion transition state, and it is reasonable to expect that the stability of the resulting carbenium would not affect unimolecular dehydration rates. However, a more than two order of magnitude increase in the rate of propene formation over P-SPP was observed using isopropanol compared to 1-propanol under identical reaction conditions **(Figure 5.4C),** suggesting that the mechanism is not truly a concerted E2 elimination. E2

elimination can often be complex, owing to possible asynchronous breaking combinations of C_α −O and C_β −H, and leading to multiple possible transition states with varying degree of bond dissociation.[245,246,251] While a pure E2 elimination involves simultaneous severance of C_α −O and C_β −H, an 'E1-like' E2 elimination in which breaking of the C−O bond is more pronounced than C-H, lends carbenium ion character to the unimolecular dehydration transition state: this would also corroborate an early transition state preserving the covalent C_β −H as evidenced by our KIE results.

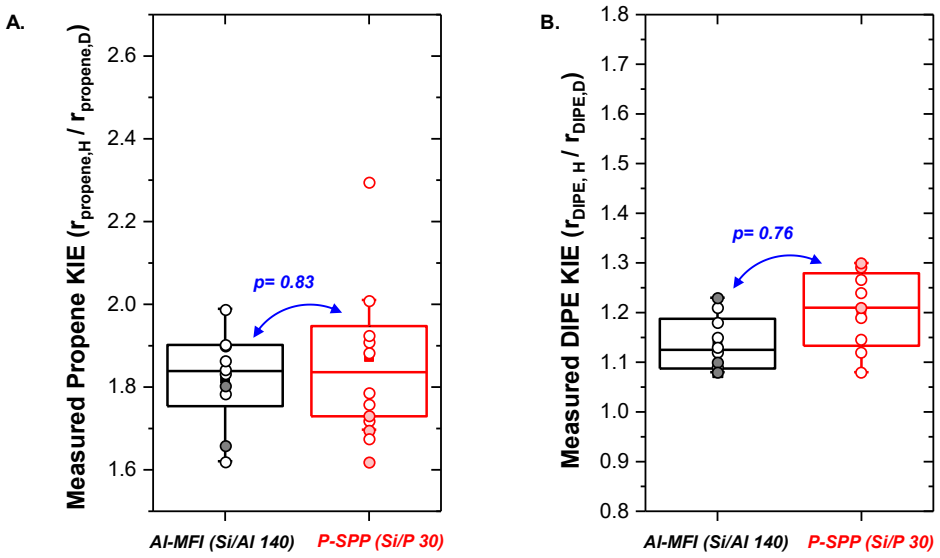

Figure 5.5 A. *Measured propene KIE on P-SPP compared with Al-MFI (Si/Al 140);* ***B.*** *Measured DIPE KIE on P-SPP compared with Al-MFI (Si/Al 140). The unfilled symbols correspond to IPA-d8, while the filled symbols are with IPA-d6. Analysis of variance was performed on the multiple replicates in each dataset and reported p-values (in blue) are reported at a 95% confidence interval. p-Values > 0.05 for both propene and DIPE indicate statistical insignificance between the KIE datasets reported on Al-MFI and the P-SPP.*

Alternatively, KIE values for DIPE formation with CD_6OH (1.25 ± 0.04) and CD_7OD (1.09 ± 0.10) were significantly lower than those for propene, while $C_3H_6(D)OH$ exhibited no KIE (1.03 ± 0.13) **(Table 5.3)**. These secondary KIEs (**Calculations included in Section A5.3.3 in Appendix)** implicate an E1 elimination (C_α-O scission) as the rate-limiting step for isopropanol (IPA) bimolecular dehydration. These results strongly suggest that unimolecular and bimolecular dehydration pathways proceed via distinct kinetically relevant activation events (C_β–H for uni-, and C_α–O for bi-molecular dehydration) on P-SPP, which also explains the distinct apparent activation barriers of these pathways measured on all phosphorous containing materials.

We next compared KIE results across the two classes of materials to gauge potential differences in surface dehydration mechanisms. Measured KIE values for CD_6OH (1.71 ± 0.18) and CD_7OD (1.82 ± 0.07) over Al-MFI were found to be within experimental error of those on P-SPP (**Figure 5.5**), signaling similar rate determining constraints over the bridging hydroxyls of aluminosilicate and Brønsted acid sites of phosphorous containing materials. Conversely, an inverse KIE was observed with C_α-H deuterated IPA ($C_3H_6(D)OH$), both for the rate of propene (0.43 ± 0.03) and DIPE formation (0.47 ± 0.02) **(Table 5.3)** on Al-MFI. This is an interesting result given we do not see any KIE with this C_α-H deuterated feed on P-SPP **(Table 5.3)**, suggesting that the coverage of a pre-equilibrated species is relevant, such that the measured KIE has significant thermodynamic contribution built into it. Specifically, we believe that deuterium substitution on the α-carbon of IPA stabilizes the intermediate participating in the kinetically relevant transition state, resulting in a thermodynamic effect that dominates the overall rate constants ($k_{TS}K_{ads}$) measured during KIE experiments. As to why inverse KIEs are observed on Al-MFI and not P-SPP, one needs to consider how the coverages at which these measurements are performed compare between the two materials. As noted before (**Sec. 5.4.4.1**), under identical conditions, surface coverages are significantly different on Al-MFI as compared with P-SPP; this is corroborated by lower apparent dehydration barriers observed on the P-zeosils on account of lower coverages. Mavrikakis and co-workers recently highlighted that thermodynamic isotope effect (TIE) values for H_2/D_2 dissociative adsorption on transition metals decrease in absolute value with increasing surface coverages as the lateral interactions between adsorbates are highly coverage-dependent.[252] Based on these results, we believe that the difference in KIEs observed with C_α-H deuterated IPA ($C_3H_6(D)OH$) between the two different materials once again captures coverage-related consequences to equilibrium constants.

Taken together, our KIE data highlight that the dehydration mechanism does not change between P-sites and Al-sites, and the differences noted in dehydration kinetics in this report reflect the implications of altered relative adsorption energetics rather than changes in dehydration mechanism.

5.4.4.3 Effects of P-active site in isopropanol dehydration kinetics. Olefin formation rates on aluminosilicate zeolites and polyoxometalates are typically inhibited at higher alcohol partial pressures irrespective of alcohol identity, due to the higher stability of adsorbed alcohol dimeric species relative to adsorbed monomers.[108,239] Macht et al. calculated this difference in the adsorption enthalpies to be ~84 kJ mol^{-1} for 2-butanol on H_3PW/SiO_2,[239] while Zhi et al. measured it to be ~66 kJ mol^{-1} for 1-propanol on Al-MFI.[253] While the expected inhibition of olefin formation at higher IPA partial pressure was observed over aluminosilicates **(Figure A5.13)**, it was absent over phosphorous containing materials; near zero-order behavior (0.17 ± 0.01) was observed on P-SPP and P-BEA across a similar range of IPA partial pressure **(Figure 5.6A)**. The lack of inhibition suggested a smaller difference between adsorption enthalpies of monomeric and dimeric IPA species on the active P-sites compared to aluminosilicates; surface-bound DIPE (DIPE*) is not significantly more stable than surface bound IPA (IPA*) on active P-sites. Indeed, adsorption energy calculations on P-SPP (**Figure 5.7**) revealed a marginal preference for DIPE adsorption over IPA (15 kJ mol^{-1}), in stark contrast with the 61 kJ mol^{-1} difference in the adsorption energy of DIPE and IPA on an aluminosilicate BAS (**Table 5.2**). Thus, a relatively destabilized DIPE* results in the absence of inhibition in propene formation rates at higher IPA partial pressures over P-zeosils.

It is instructive to note that zero-order propene formation routes on P-SPP is not at odds with the earlier discussion of reported apparent barriers being measured from gas-phase reference state. While numerous early studies on alcohol dehydration considered the dimeric species as inert, more recent reports have highlighted the prevalence of olefin formation routes from the decomposition of adsorbed dimer.[114,240,244] It follows that the formation routes of olefin and di-alkyl ether can be coupled, and near zero-order propene formation behavior on P-SPP and P-BEA cannot directly be interpreted as evidence for a saturated surface.

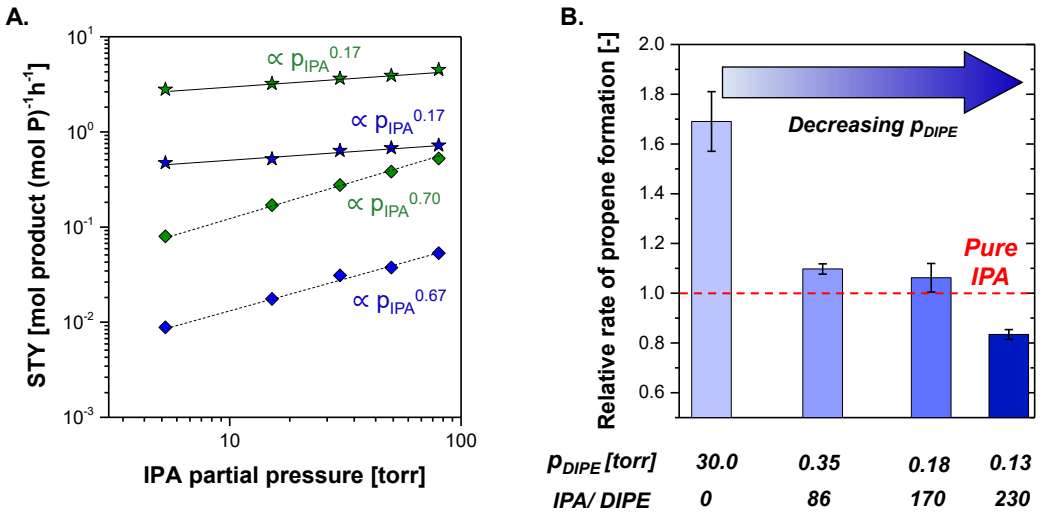

Figure 5.6 A. *Propylene (★) and di-isopropyl ether (◆) synthesis rates as a function of IPA partial pressures measured on P-SPP* ***(green)*** *and P-BEA* ***(blue)*** *(Reaction conditions: T= 443 K; WHSV=2.5 g reactant g cat^{-1} h^{-1}; Carrier gas (He) flowrate =25 sccm; Conversions below 1.5%). Solid and dashed black lines indicate fits to IPA power-law rate expression for propene, and DIPE, respectively. The resulting IPA rate orders for both products are indicated for P-SPP* ***(green)*** *and P-BEA* ***(blue)****;* ***B.*** *Relative rate of propene formation on P-SPP normalized to the corresponding value with IPA feed as a function of the molar ratio of IPA/DIPE during co-feed experiments (Reaction conditions: T = 403 K, P_{IPA} = 30 torr, WHSV = 3.1 – 5.3 g reactant g cat^{-1} h^{-1}, carrier gas (He) flowrate 25 sccm, conversions below 0.4 %).*

To probe whether the propene and DIPE formation routes are coupled, DIPE was fed to the reactor under identical conditions to IPA dehydration on P-SPP. Relative to the propene formation rates from IPA, propene rates from DIPE were ~1.7x higher on P-SPP. While this increase is significantly smaller than over Al-MFI (where we observed a ~ 37x increase), these results suggest that there exists a pathway from DIPE to propene on P-SPP.

To further probe the prevalence of this pathway, experiments were designed with IPA and DIPE cofeeds with molar IPA:DIPE ratios anticipated to mimic surface coverages during IPA dehydration **(Figure 5.6B)**. Notably, changing the DIPE surface coverages could be used to alter propene formation rates (relative rates in the range of ~ 0.8-1.2 depending on IPA: DIPE molar ratios), and these data provide no evidence to support the claim that propene formation only results from IPA on P-SPP, thus elucidating the apparent nature of kinetic measurements on P-zeosils despite near zero-order reaction orders; propene originating from DIPE* can mask the propene rate-order dependencies to appear close to zero-order even in a case where surface is relatively bare. Alternatively, DIPE formation rates were found to monotonically increase with IPA partial pressures on P-SPP

and P-BEA **(Figure 5.6A)** with rate orders close to unity (0.70 ± 0.01, and 0.67 ± 0.03 on P-SPP and P-BEA, respectively).

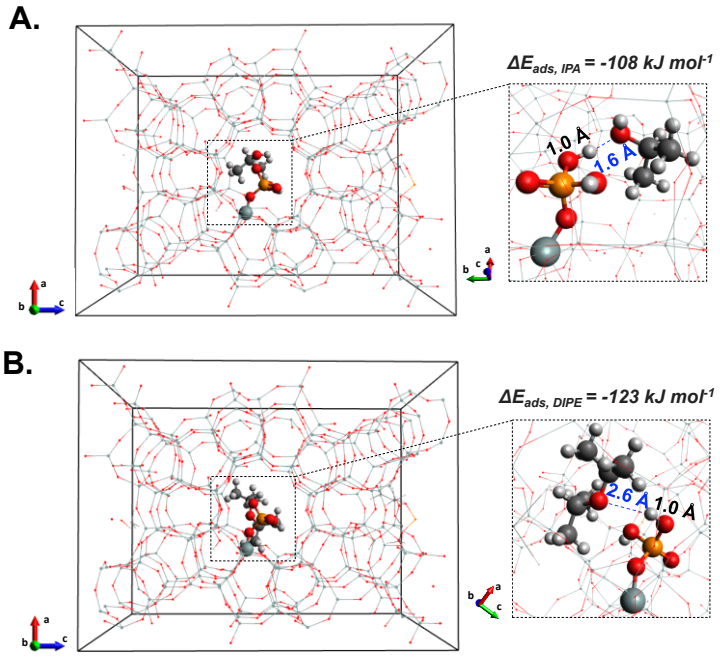

Figure 5.7 *The optimized structures of **A**. IPA and **B**. DIPE on a P-active site. Adsorption energies corresponding to each case is indicated on the inset. The O-H atomic distances between the oxygen of adsorbate and the proton of P-active site are shown in blue and the O-H distances between the oxygen and hydrogen of the P-active site are shown in black.*

The results of IPA dehydration, taken together, emphasize a recurring theme: the dehydration mechanism and the corresponding kinetically relevant steps remain unchanged across the two families of materials. Pathways for unimolecular and bimolecular dehydration are coupled on both materials, and the preference towards unimolecular dehydration increases with temperature on both. The key difference between the two materials is a consequence of the differences in adsorption energies on their surfaces; the comparable stability of DIPE* and IPA* on P-active sites leads to an increased selectivity to propene as a dehydration product. For the same reason, inhibition of propene formation at higher IPA partial pressures is not readily observed with P-zeosils as it is over aluminosilicates. Ultimately, these differences manifest in markedly lower apparent activation energies on P-zeosils, despite the lower absolute rates of dehydration.

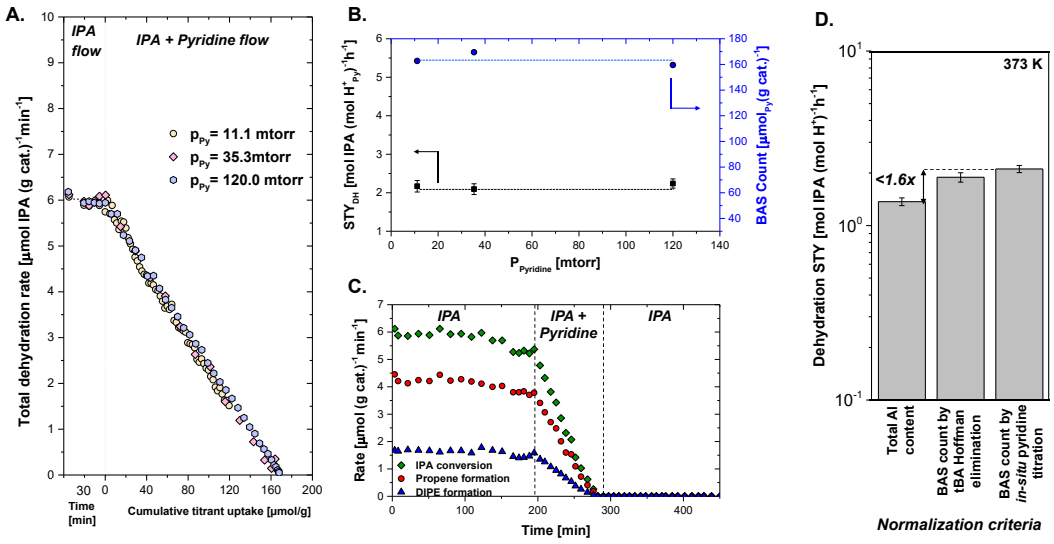

Figure 5.8 A. *Mass-normalized IPA conversion rates plotted as a function of pyridine uptake during in-situ pyridine titration on Al-SPP at different pyridine partial pressures (in the range 5.4-101.3 mtorr). (Reaction conditions: T= 373 K; P_{IPA}= 5.9 torr ; WHSV= 2.47 g reactant g cat^{-1} h^{-1}; Carrier gas (He) flowrate = 100 sccm; Conversions below 2%);* ***B. (primary axis)*** *IPA dehydration site time yields (STYs) as calculated by normalizing rates by cumulative pyridine uptake as a function of pyridine partial pressures, and* ***(secondary axis)*** *BAS count assuming a 1:1 stoichiometry between cumulative pyridine uptake and BAS;* ***C.*** *Mass-normalized rates of IPA conversion (◆), propene formation (●) and DIPE formation (▲) as a function of time-on-stream (TOS). (Reaction conditions: IPA: Pyridine 530:1, while other conditions are identical to (A) and (B));* ***D.*** *Site time yield of IPA dehydration calculated with different normalization criteria. Error bars are standard errors calculated by propagation of relative errors in mass-normalized rate and total acid site counts used for normalization.*

5.4.4.4 Probing the P-sites by in-situ pyridine titration during IPA dehydration. Given the *ex-situ* nature of the preceding measurements to probe P-zeosils discussed so far, we additionally evaluated the active sites of P-SPP and Al-SPP under isopropanol dehydration reaction conditions through *in-situ* titration methods. This allows us to more readily compare the intrinsic activity of aluminosilicates and P-active sites, accounting for sites actually involved in catalysis.[254] For acid catalysis (including alcohol dehydration[198,230,255]) on medium-pore microporous materials and larger, pyridine is the most commonly used in-situ titrant.[256,257] Assuming each pyridine molecule adsorbs on one acid site, the slope (rate vs mol pyridine uptake) and x-intercept (mol pyridine uptake) of the titration profile provide a measure of the STY and active site density under reaction conditions, respectively. Over a high silica Al-SPP (Si/Al 62), IPA dehydration mass-normalized rates

dropped to >96% of their initial value upon pyridine saturation at 373 K, indicating that virtually all catalytic sites relevant to IPA dehydration had been titrated **(Figure 5.8A)**. Pyridine partial pressures (11-120 mtorr) neither changed the measured STY nor BAS counts on Al-SPP **(Figure 5.8B)**, and these values remain ~ 2.1 mol mol $H^{+}{}_{Py}{}^{-1}$ h^{-1} and 165 µmol g^{-1} at 373 K, respectively. Once pyridine is removed the from feed stream, dehydration rates do not recover **(Figure 5.8C)**; pyridine remains irreversibly adsorbed on the active sites in Al-SPP. We then used three different IPA rate-normalization criteria: (i) BAS counts assuming all the aluminum present in Al-SPP is active (265 µmol g^{-1}), (ii) the BAS count measured during tBA Hofmann elimination of (190 µmol g^{-1}),[213] and (iii) BAS counts obtained from the *in-situ* pyridine titration data (165 ± 3 µmol g^{-1}), to estimate errors in STYs arising from using these different criteria (**Figure 5.8D**). Assuming that all aluminum in Al-SPP is active likely leads to an underestimation of the STY; not all aluminum will tetrahedrally coordinate within the SPP framework and form a BAS. Regardless, all STY values remain within a factor of ~1.5 of each other, meaning that the different rate-normalization criteria only result in the mild change in STY values for Al-SPP catalyst.

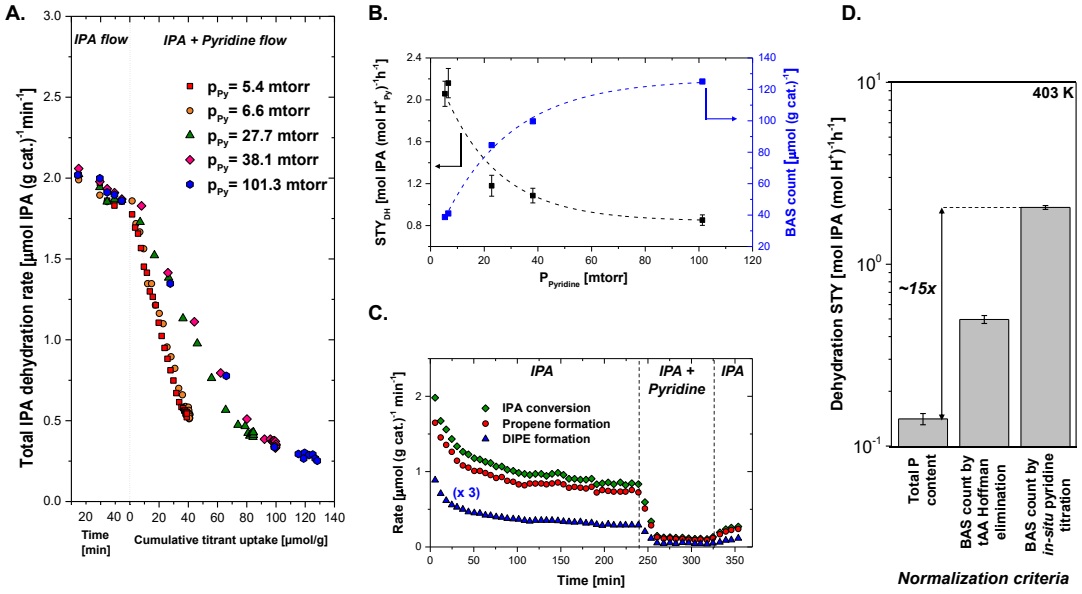

Figure 5.9 A. *Mass-normalized IPA conversion rates plotted as a function of pyridine uptake during in-situ pyridine titration on P-SPP at different pyridine partial pressures (in the range 5.4-101.3 mtorr). (Reaction conditions: T= 403 K; P_{IPA}= 30 torr ; WHSV= 2.59 g reactant g cat^{-1} h^{-1}; Carrier gas (He) flowrate = 25 sccm; Conversions below 0.5%);* ***B. (primary axis)*** *IPA dehydration site time yields (STYs) as calculated by normalizing rates by cumulative pyridine*

uptake as a function of pyridine partial pressures, and ***(secondary axis)*** *BAS count assuming a 1:1 stoichiometry between cumulative pyridine uptake and BAS;* ***C.*** *Mass-normalized rates of IPA conversion (◆), propene formation (●) and DIPE formation (▲) as a function of time-on-stream (TOS) (Reaction conditions: IPA: Pyridine 780:1, while other conditions are identical to (A) and (B));* ***D.*** *Site time yield of IPA dehydration calculated with different normalization criteria. Error bars are standard errors calculated by propagation of relative errors in mass-normalized rate and total acid site counts used for normalization.*

Over P-SPP, a more complex *in-situ* titration profile developed. As pyridine adsorbed on the active sites, IPA conversion rates dropped to ~75% of their initial value under low pyridine partial pressures (5.4-6.6 mtorr). Increased pyridine concentrations in the feed led to both an increased degree of rate quenching, as well as the number of acid sites counted. The rate suppression increased from ~75% to ~87% due to a twenty-fold increase in pyridine partial pressure (5.4 to 101.3 mtorr). Acid site counts, as obtained by extrapolation of the linear region of the rate versus cumulative uptake traces, also increased from 40 to 126 μmol g^{-1}. The non-zero rate of dehydration at pyridine saturation, combined with the effect of increasing pyridine partial pressure, present a possibility that P-sites capable of catalyzing isopropanol (IPA) conversions do not bind pyridine irreversibly. Given the catalytic site heterogeneity,[199,207] it is also plausible that higher concentrations of pyridine titrated 'less-reactive' sites, leading to higher acid site counts. However, we find this possibility unlikely given that propene and di-isopropyl ether (DIPE) selectivities remain nearly invariant with pyridine partial pressure after saturation **(Figure A5.12 in Section A5.3.2 in the Appendix)**. It is improbable that multiple inequivalent active sites would turnover IPA in a manner that preserves an identical unimolecular/dehydration pathway selectivity. It is more likely that the pyridine partial pressure dependence of acid site counts results from competitive adsorption between IPA and pyridine. From **Figure 5.9A and B**, we note that the slopes change with pyridine partial pressure and the quantification of a unique STY value is challenging. To further add to the complications involving STY measurements, although these active sites do bind pyridine, they do so reversibly; upon pyridine removal from the feed stream, both propene and DIPE rates start recovering on time-scales of minutes **(Figure 5.9C)**. Given that infinitely small pyridine uptakes are more representative of strict chemisorption on P-active sites, we believe that the most accurate turnover frequency is the value extrapolated to zero pyridine partial pressures, which results in a STY of 2.2 mol mol $H^{+}_{Py}{}^{-1}$ h^{-1} at 403 K **(Figure 5.9B)**. Similar

analysis for the cumulative pyridine uptakes further allows for an estimation of acid site counts as 40 μmol g^{-1}, which is generally in reasonable agreement with the BAS counts obtained during Hofmann elimination of isopropyl amine (46 μmol g^{-1}), albeit lower than more reactive alkylamines like tBA and tAA **(Figure 5.1A)**.

As shown in **Figure 5.9D**, STY values vary by ~15x depending on the normalization criteria used, which is a direct consequence of the low number of protons per heteroatom (H^+/P_{bulk} ~ 0.1-0.2) counted by the two site-counting methods employed (Hofmann elimination and *in-situ* pyridine titration). We note that similar proton/heteroatom values have been previously reported on other weakly Brønsted acidic materials (e.g. H^+/X_{bulk} in the range ~ 0.1-0.25 for B-MFI)[197,198] and it follows from the discussion that a majority of phosphorus in P-SPP is inactive for IPA dehydration/Hofmann elimination chemistries. However, within the limitations of this technique, this analysis allows for a reasonable comparison of phosphorous containing materials and aluminosilicate per active site. At 403 K, total dehydration STY for Al-SPP is 17.6 mol mol $H^+_{Py}{}^{-1}$ h^{-1} (**Table 5.1**), while it is almost an order of magnitude lower on P-SPP (2.2 mol mol $H^+_{Py}{}^{-1}$ h^{-1}) (**Table 5.1 and Figure 5.9D**).

5.5 Conclusions. This report probes the active sites in phosphorus-containing zeosils during Brønsted acid catalysis. Site-counts as obtained by Hofmann elimination of alkylamines demonstrate that more reactive tertiary alkylamine feeds (e.g., tert-amylamine) can carry out olefin formation turnovers on more active sites than primary alkylamines (e.g., n-propylamine) – a finding in sharp contrast to aluminosilicates where amine identity does not change the number of sites involved in olefin formation. During IPA dehydration, these P-zeosils exhibit > 80x lower heteroatom-normalized turnover rates than aluminosilicates, which is indicative of lower inherent activity of active sites and/or the presence of catalytically inactive P-species. Furthermore, these materials show a clear kinetic preference to unimolecular dehydration routes, yielding 20-30% higher propene selectivities than aluminosilicate analogs under identical reaction conditions. A diminished difference between adsorption energies of IPA and DPE allows propene rates to remain uninhibited at high IPA partial pressures. IPA dehydration to propene is found to proceed through an E2-elimination route with kinetically relevant C_β–H scission on P-SPP. More

importantly, the dehydration mechanism remains unaltered from the aluminosilicates, highlighting that differences in reaction performance are direct implications of weaker binding to active sites in P-zeosils. This weaker binding further affords an apparent lowering of lower uni-/bimolecular dehydration barriers by ~10 kcal mol^{-1} compared to aluminosilicates.

Chapter 6

Concluding remarks and proposed future directions

*Parts of this Chapter are reproduced with permission from Kuznetsov, A.; Kumar, G.; Ardagh, M.A.; Tsapatsis, M; Zhang, Q; Dauenhauer, P.J. On the Economics and Process Design of Renewable Butadiene from Biomass-Derived Furfural, *ACS Sustainable Chemistry & Engineering* **2020**, 8(8), 3273-3282. https://doi.org/10.1021/acssuschemeng.9b06881

6.1 Conspectus

This thesis has led to the discovery of weakly acidic heterogeneous catalysts as selective materials for the dehydra-decyclization of saturated furanic species, and has furthered the fundamental understanding of such active sites under catalytic conditions. However, on an applications-level, it is instructive to investigate the diene prices realistically achievable from this process under the choice of catalysts discussed in this dissertation. This Chapter briefly discusses our efforts in evaluating the technoeconomic analysis of a furfural-to-butadiene process technology on an industrial scale (100 kmol h^{-1} furfural feed). For furfural purchased at \$1.84 kg^{-1} (\$176 $kmol^{-1}$), a minimum sale price of butadiene of \$5.43 kg^{-1} is calculated, which is nearly four-times the existing butadiene prices afforded by petrochemical approaches. The key conclusion from this effort is clear: while these weakly acidic catalyst are diene-selective, the reaction rates per active site are still lower than the standards of typical industrial processes. The fundamental challenge in enhancing rates of desirable dehydra-decyclization pathways on Brønsted acidic materials alone is the inevitable loss in diene selectivities. Therefore, our proposed work aims to build on the mechanistic insights developed so far to improve the overall rates of reaction without altering diene selectivities by using bifunctional catalysts with metal-weak acid functionalities.

6.2 Renewable dienes: How far from industrial implementation?

The sustainability of the global economy depends on the affordability of sustainable polymeric materials,[258] which necessitates economically competitive sustainable monomer manufacturing.[259] The synthesis of industrially important monomers such as C5 olefins, *p*-xylene, and acrylonitrile from biomass-derived feedstocks has already been demonstrated.[199,260–264] 1,3-Butadiene is another monomer whose synthesis from biomass has attracted recent interest, owing to its applications in products such as tires and

sealants.[41,265] Traditionally, butadiene has been produced via the dehydrogenation of *n*-butane,[266] or as a byproduct of ethylene production during naphtha cracking.[5,118] To date, proposed biomass-based synthesis routes for butadiene have generally included either ethanol or C4 diols as starting materials.[18,118,267] Ipatieff and co-workers proposed the dehydrogenation of ethanol to acetaldehyde, followed by condensation and deoxygenation to butadiene,[118,268,269] and butadiene selectivities of 60-70% have been achieved with this approach at moderately high ethanol conversions (60-75%).[267] Lebedev developed a direct synthesis of butadiene from ethanol,[270] leading to a butadiene yield of ~65% at high ethanol conversions (~88%) on promoted tantalum-containing zeolites.[271] As already mentioned, the dehydration of C4 diols including 1,3-butanediol (1,3-BDO),[267,272,273] 2,3-butanediol (2,3-BDO),[267,274–277] and 1,4-butanediol (1,4-BDO),[46,267] to butadiene has also received attention since these alcohols can be derived from glucose via fermentation pathways.[278,279] Song *et al.* have recently reported the economic feasibility of butadiene production from 2,3-BDO using amorphous calcium phosphate (ACP)/ hydroxyapatite-alumina catalysts.[280–282] At the scale of 2500 kg/h feed (2,3-BDO) assumed to be purchased at $0.8/kg, the butadiene price was estimated to be $1.62/kg.[281] The price point for butadiene was found to be sensitive to 2,3-BDO prices, and payback times of less than five years were only possible for 2,3-BDO prices below $1.3/kg (>50% drop from current prices).[281]

While a stand-alone process utilizing furfural directly as a feedstock has not been utilized to the best of our knowledge, Athaley *et al.* have recently reported the production of butadiene from furfural as a byproduct in p-xylene. The proposed biorefinery utilizes biomass purchased at $0.06/kg at a process scale of ~400 kT feed/year to produce ~81 kT p-xylene/year and ~64 kT furfural/year to propose a butadiene minimum selling price (MSP) of $1.3 /kg.[283] Furan derivatives have been studied as a biomass-derived feedstock both for fuels and for commodity chemicals, and furfural yields of 72-87% from corn-derived feedstock including glucose and fructose have been achieved.[284–292] The promising nature of furfural as a biomass-derived value-added chemical has led to significant technological improvements in its manufacture,[293,294] and global production is projected to grow, particularly in China.[295] This market growth is primarily driven by a demand for furfuryl alcohol, which is used in foundry resins.[293]

The direct transformation of furfural to THF involves simultaneous decarbonylation and hydrogenation.[46,296–298] However, the highest selectivity achieved under continuous-flow conditions has remained low (< 40%), and the presence of side products (e.g. tetrahydrofurfuryl alcohol, furan, furfuryl alcohol, butanol, etc.) would likely lead to high downstream separations cost.[36–38] Instead, we considered a two-step process sequence from furfural to THF, with furan as an intermediate. The first step in the proposed process is the decarbonylation of furfural to furan, shown in **Scheme 6.1**. This reaction can take place in the gas or liquid phases, and supported Pd catalysts are usually used to achieve high yields.[299–302] Although the catalyst is prone to coking,[302] the co-feeding of hydrogen mitigates deactivation by hydrogenating and/or inhibiting the formation of coking precursors *in situ*,[295] and cumulative furan site-time yields as high as 100 kg per g Pd have been recently achieved.[302] While comparable furan yields have been reported on platinum,[303] the reaction is particularly sensitive to Pt particle size/shape,[33] and the choice of support.[304] For this work, we consider the gas-phase decarbonylation of furfural with a Pd/alumina catalyst treated with cesium carbonate, which has been reported to give >98% furan selectivity at >90% furfural conversion, being stable for ~383 hours on-stream before regeneration in examples 1-2 by Li and Ozer *et al*..[302]

The subsequent step to decarbonylation is the hydrogenation of furan to THF. Platinum,[305] ruthenium,[306] and palladium[307] have all been used as heterogeneous catalysts for this reaction. Hydrogen pressures of 7-35 atm and reaction temperatures of 80-150 °C are typically used.[308,309] While Raney nickel is often used,[309] palladium offers higher THF selectivity.[307] We consider a bubble-column reactor in which hydrogen at 22.5 bar is bubbled through liquid furan on a 5% Pd/carbon catalyst; these conditions have been shown to give nearly quantitative yields of THF at complete furan conversion.[307]

The third and final step is the dehydra-decyclization of THF to butadiene. The major side products in this reaction are propene and formaldehyde (Retro-Prins condensation products),[310] butenes, and heavy organics (C6+ fraction); while traditional solid acids like aluminosilicate zeolites are active, butadiene selectivities remain low (~50-60%) across all THF conversions.[44] We have previously reported that aluminum-free phosphorus-containing siliceous self-pillared pentasil (P-SPP) zeolite exhibits ~87%

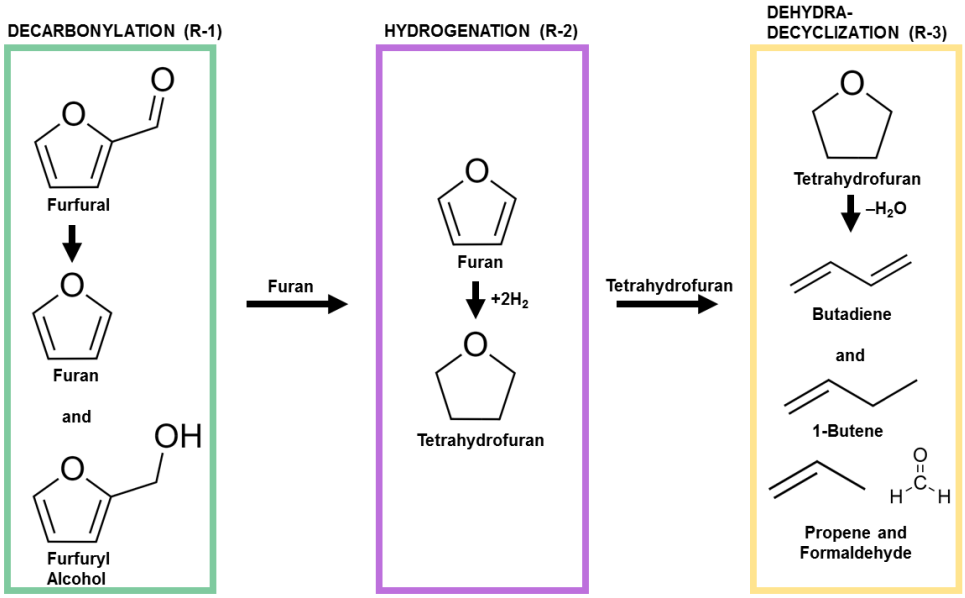

Scheme 6.1 *Process chemistry of three sequential reactors to convert furfural to butadiene: furfural decarbonylation (R-1), furan hydrogenation (R-2), and tetrahydrofuran dehydra-decyclization (R-3). The corresponding process flow diagram is included in Appendix (Figure A6.1)*

butadiene selectivity at ~83% THF conversion at 400 °C, albeit at a very low space velocity (0.04 g THF $gcat^{-1}$ hr^{-1}) owing to its low reactivity.[44] In the evaluation of process economics, we conducted experiments on P-SPP at 425 °C and used the obtained conversions and product selectivities in the simulation of this step. In total, our proposed process comprised the conversion of furfural to furan in a packed-bed reactor, the purification of furan using distillation, the hydrogenation of furan in a high-pressure bubble-column reactor to THF, the dehydra-decyclization of THF to butadiene in a packed-bed reactor, and the purification of butadiene using distillation followed by absorption **(Scheme 6.1).** While we direct the readers to our publication for details, we do wish to highlight the key conclusion from these efforts.

The minimum selling price (MSP) of butadiene that would yield a zero net present value for the entire project for the base case process (100 kmol hr^{-1} furfural feed) was calculated to be \$5.43 kg^{-1}. Although the selectivity improvements in reactors R-1 (decarbonylation) and R-3 (dehydra-decyclization) would result in a notable decrease in the MSP of butadiene, the change would still not be sufficient for the process to be profitable under current market conditions, as shown in **Figure 6.1**. Specifically, the MSP of butadiene calculated in the hypothetical scenario where both reactors exhibit 95%

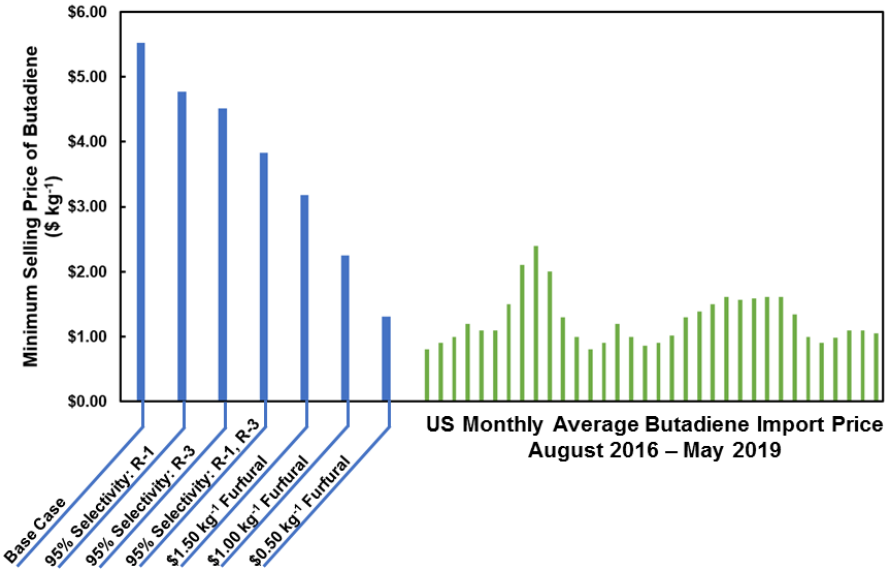

Figure 6.1. *Impact of potential selectivity improvements in R-1 (furfural decarbonylation) and R-3 (THF dehydra-decyclization) and furfural feedstock prices on the minimum selling price (MSP) of butadiene. The MSPs for cumulative process improvements are shown in blue. Monthly average import prices for the United States are presented in green for comparison.*[311–313]

selectivity at full conversion, \$3.80 kg^{-1}, is still 58% higher than the maximum observed butadiene price (\$2.40 kg^{-1}) in the last three years.[312] Therefore, the proposed process can only reach economic viability through a combination of technological and economic factors. We considered the cumulative process improvements described above combined with a decrease in the purchase price of furfural; the results are shown in **Figure 6.1**. The MSP of butadiene with the hypothetical improved process is only competitive with current prices at a furfural purchase price of \$0.5-1.0 kg^{-1} (also see **Figure A6.2** and **Figure A6.3** in the **Appendix**).

6.3 Proposed work

The technoeconomic analysis discussed above clearly demonstrated the roadblocks of using materials with inherently low reactivity; achieving quantitative feed conversions would require unreasonably large quantities of catalyst given the low space velocities (< 0.8 g (M)THF/g cat./h) under which these catalysts achieve complete conversions. Our proposed work addresses possible directions with an overarching goal of garnering industrial interest in this process technology.

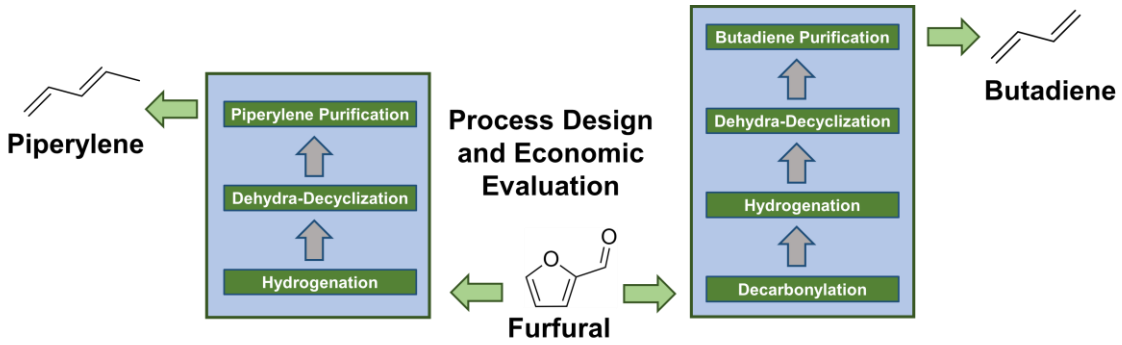

Figure 6.2 *Conceptual process design of two processes to derive butadiene/piperylene from furfural. Conversion to butadiene involves four-unit operations, while piperylene can potentially derived from furfural in only 3 steps.*

(1) Techno-economic evaluation of Furfural-to-piperylene chemistry on B-MWW Our process design and technoeconomic analysis made it clear that the yield loss of a carbon going from a five-carbon species (furfural) to a four-carbon species (butadiene) hurts the overall economic prospects of this process. Furthermore, this analysis still utilized P-zeosils to convert tetrahydrofuran to butadiene (the dehydra-decyclization step in **Figure 6.1**). While these catalysts are shown to be extremely diene selective at low conversions, overall butadiene yields have still remained low (< 65%) at high conversions. Furthermore, these catalysts deactivate rapidly when kept on-stream necessitating frequent high temperature regeneration cycles. All these factors contribute to driving butadiene prices which are too high under current economic climate. Given that B-MWW catalyst affords a significantly higher yield to piperylene while remaining exceptionally stable under reaction conditions, as well as the recognition that upgrading furfural to a C5 *(rather than a C4)*-diene is more likely to be cost-effective, an obvious next step is to evaluate the furfural-to-piperylene technology. As noted earlier and shown in **Figure 6.1**, this process contains one less unit operation *(no decarbonylation reactor)* compared to the butadiene process, which is expected to drive down capital equipment cost substantially while improving carbon yield of the process. Overall, the process economics for furfural-to-piperylene are expected to be substantially better than the furfural-to-butadiene technology with the existing weakly acidic catalysts.

The other fundamental idea to improve rates is the use of transition-metals in the chemistry; reduced metal surfaces are well-known C-O activation catalysts,[314] and can potentially be utilized to ring-open 2-MTHF (kinetic bottleneck of the process), while the

weak-acid functionality can then selectively catalyze the facile intermediate dehydration step, presumably preserving diene selectivities. Towards accomplishing this goal, we detail the following ideas that can be used to systematically investigate how metal-acid functionality can work in tandem to boost rates without altering diene selectivities.

(2) 2-MTHF ring-decomposition on pure metals. The working hypothesis of enhanced turnover frequencies (TOFs) and reduced activation barriers of (M)THF ring-opening step (C-O scission) should be first be tested by detailed kinetic investigations on supported-metals alone, both in presence and absence of reducing (H_2) atmosphere. These measurements will benefit from parallel density functional theory (DFT) calculations to map the decomposition pathways of (M)THF on standard metal surfaces (e.g., Pt(111)). While presence of hydrogen should lead to surface hydride-mediated reaction pathways akin to hydrodeoxygenation routes, previous work on furan decomposition on Pt(111) has shown that dehydrogenation mediated ring-opening pathways can also occur in which the metal surface extracts a hydride from the substrate (e.g., furan).[315] These two potentially distinct routes have direct implications in product distribution; presence of hydrogen is likely to favor alkanes over olefins and dienes. Therefore, it will be important to assess if the reaction can occur in absence of reducing atmosphere, and if not, optimize hydrogen partial pressures to retain unsaturated products in reactor effluent.

(3) Macroscopic investigation of metal-acid functional proximity. The degrees of freedom of surface adsorbates along with the proximity of the distinct functional active sites inevitably dictates the success of any multi-functional catalytic system. Furthermore, as noted above, the deleterious effect of hydrogen environment can potentially by minimized by restricting feed contact times on the metal site. These considerations should be assessed by systematically varying the macroscopic proximity of metal and acid-sites by either placing the supported metal bed upstream/downstream from the zeolite bed, or by preparing an intrapellet mixture of both **(Figure 6.3a).** The difference in rates along with the obtained product distributions will provide valuable insights on stable gas-phase intermediates which can be expected, and how these proximity effects alter the ring-opening rates. In particular, the first scenario (metal upstream) is a surrogate for desirable

sequence (ring-open on metal; dehydrate on B-site), and will be helpful to guide efforts listed in (4).

(4) Preparation and catalytic testing on metal -supported B-zeolites. Deposition of metals inside the micropores is challenging due to the atomic radii of transition metals, but they can be sited on both the external crystallite surface, as well in the mesoporous environments. To that end, swelling and pillaring of B-MWW should be performed to first create mesoporous environments adequate for depositing metals, leading to a host of multi-functional materials with different location, loadings, and microscopic proximity between the metal-acid sites. Characterization techniques (XRD, SEM, TEM, EXAFS, and CO chemisorption) should be carried out to identify and count catalytic metal sites. As shown in **Figure 6.3b**, it is expected that (M)THF binds to metal surface followed by hydride mediated formation of ring-opened intermediate, which can presumably interact with a nearby boron-site. Detailed catalytic investigation on these bifunctional boron-catalysts will not only answer fundamental questions about how the catalytic cycle turns over and whether or not diene selectivities can be preserved, but can potentially solve the long pertaining issue of sub-optimal reaction rates in the chemistry.

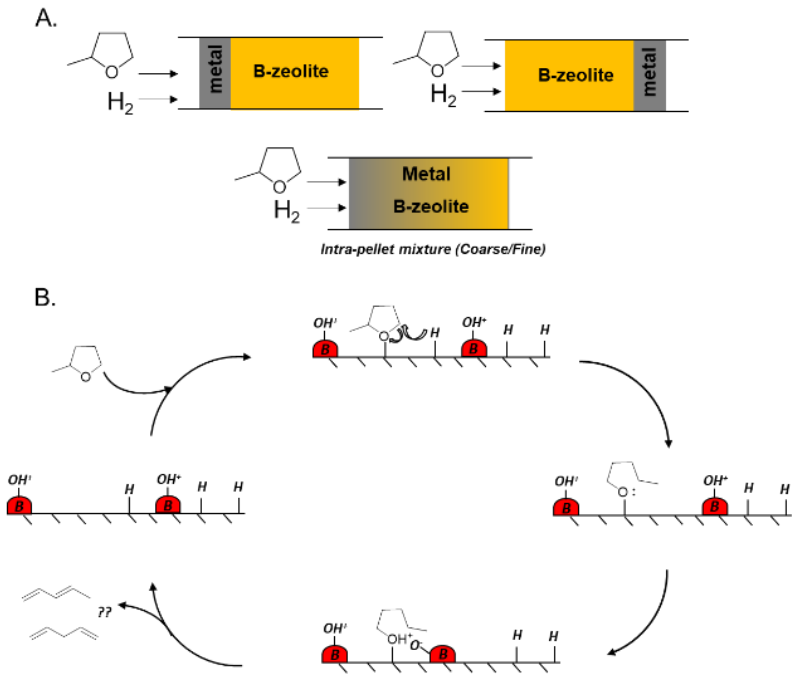

Figure 6.3*. (A) Possible packed bed configurations for varying metal/B-site proximity; (B) Proposed mechanism of 2-MTHF ring-opening on metal-supported B-zeolites.*

Bibliography

(1) Isikgor, F. H.; Becer, C. R. Lignocellulosic biomass: a sustainable platform for the production of bio-based chemicals and polymers. *Polym. Chem.* **2015**, *6* (25), 4497–4559.

(2) Mukherjee, A.; Dumont, M. J.; Raghavan, V. Review: Sustainable production of hydroxymethylfurfural and levulinic acid: Challenges and opportunities. *Biomass and Bioenergy* **2015**, *72*, 143–183.

(3) Li, X.; Jia, P.; Wang, T. Furfural: A Promising Platform Compound for Sustainable Production of C4and C5Chemicals. *ACS Catal.* **2016**, *6* (11), 7621–7640.

(4) Werpy, T.; Petersen, G. Top Value Added Chemicals from Biomass Volume I — Results of Screening for Potential Candidates from Sugars and Synthesis Gas Top Value Added Chemicals: Results of Screening for Potential Candidates. *Other Inf. PBD 1 Aug* **2004**,

(5) Bruijnincx, P. C. A.; Weckhuysen, B. M. Shale gas revolution: An opportunity for the production of biobased chemicals? *Angew. Chemie - Int. Ed.* **2013**, *52* (46), 11980–11987.

(6) Ennaert, T.; Schutyser, W.; Dijkmans, J.; Dusselier, M.; Sels, B. F. *Conversion of Biomass to Chemicals: The Catalytic Role of Zeolites*; Elsevier B.V., **2016**.

(7) Anderson, E. M.; Katahira, R.; Reed, M.; Resch, M. G.; Karp, E. M.; Beckham, G. T.; Román-Leshkov, Y. Reductive Catalytic Fractionation of Corn Stover Lignin. *ACS Sustain. Chem. Eng.* **2016**, *4* (12), 6940–6950.

(8) Meng, X.; Xiao, F. S. Green routes for synthesis of zeolites. *Chem. Rev.* **2014**, *114* (2), 1521–1543.

(9) Jacobs, P. A.; Dusselier, M.; Sels, B. F. Will zeolite-based catalysis be as relevant in future biorefineries as in crude oil refineries? *Angew. Chemie - Int. Ed.* **2014**, *53* (33), 8621–8626.

(10) Makshina, E. V; Dusselier, M.; Janssens, W.; Degrève, J.; Jacobs, P. A.; Sels, B. F. Review of old chemistry and new catalytic advances in the on-purpose synthesis of butadiene. *Chem. Soc. Rev.* **2014**, *43*, 7917–7953.

(11) Yang, Y.; Liu, Q.; Li, D.; Tan, J.; Zhang, Q.; Wang, C.; Ma, L. Selective hydrodeoxygenation of 5-hydroxymethylfurfural to 2,5-dimethylfuran on Ru–MoO_x/C catalysts. *RSC Adv.* **2017**, *7* (27), 16311–16318.

(12) Bellussi, G.; Carati, A.; Millini, R. *Industrial Potential of Zeolites*; 2010; Vol. 2.

(13) Sarkar, P.; Bhowmick, A. K. Sustainable rubbers and rubber additives. *J. Appl. Polym. Sci.* **2017**, *45701*, 45701.

(14) Boruta, T.; Bizukojc, M. Production of lovastatin and itaconic acid by Aspergillus terreus: a comparative perspective. *World J. Microbiol. Biotechnol.* **2017**, *33* (2), 1–

12.

(15) Medway, A. M.; Sperry, J. Heterocycle construction using the biomass-derived building block itaconic acid. *Green Chem.* **2014**, *16* (4), 2084–2101.

(16) Bai, W.; Tai, Y. S.; Wang, J.; Wang, J.; Jambunathan, P.; Fox, K. J.; Zhang, K. Engineering nonphosphorylative metabolism to synthesize mesaconate from lignocellulosic sugars in Escherichia coli. *Metab. Eng.* **2016**, *38* (June), 285–292.

(17) Spanjers, C. S.; Schneiderman, D. K.; Wang, J. Z.; Wang, J.; Hillmyer, M. A.; Zhang, K.; Dauenhauer, P. J. Branched Diol Monomers from the Sequential Hydrogenation of Renewable Carboxylic Acids. *ChemCatChem* **2016**, *8* (19), 3031–3035.

(18) Abdelrahman, O. A.; Park, D. S.; Vinter, K. P.; Spanjers, C. S.; Ren, L.; Cho, H. J.; Vlachos, D. G.; Fan, W.; Tsapatsis, M.; Dauenhauer, P. J. Biomass-Derived Butadiene by Dehydra-Decyclization of Tetrahydrofuran. *ACS Sustain. Chem. Eng.* **2017**, 5, 3732-3736..

(19) Pace, V.; Hoyos, P.; Castoldi, L.; Domínguez De María, P.; Alcántara, A. R. 2-Methyltetrahydrofuran (2-MeTHF): A biomass-derived solvent with broad application in organic chemistry. *ChemSusChem* **2012**, *5* (8), 1369–1379.

(20) Kumbhalkar, M. D.; Buchanan, J. S.; Huber, G. W.; Dumesic, J. A. Ring Opening of Biomass-derived Cyclic Ethers to Dienes over Silica/Alumina. *ACS Catal.* **2017**, 7, 5248-5256.

(21) Elliot, D. C.; Frye, J. G. Hydrogenated 5.carbon compounds and method of making. *United States Pat.* **1999**, *5,883.266* (4).

(22) Obregon, I.; Gandarias, I.; Miletic, N.; Ocio, A.; Arias, P. L. One-Pot 2-Methyltetrahydrofuran Production from Levulinic Acid in Green Solvents Using Ni-Cu/Al2O3 Catalysts. *ChemSusChem* **2015**, *8* (20), 3483–3488.

(23) Phanopoulos, A.; White, A. J. P.; Long, N. J.; Miller, P. W. Catalytic Transformation of Levulinic Acid to 2-Methyltetrahydrofuran Using Ruthenium - N-Triphos Complexes. *ACS Catal.* **2015**, *5* (4), 2500–2512.

(24) Mizugaki, T.; Togo, K.; Maeno, Z.; Mitsudome, T.; Jitsukawa, K.; Kaneda, K. One-Pot Transformation of Levulinic Acid to 2-Methyltetrahydrofuran Catalyzed by Pt-Mo/H-β in Water. *ACS Sustain. Chem. Eng.* **2016**, *4* (3), 682–685.

(25) Zheng, J.; Zhu, J.; Xu, X.; Wang, W.; Li, J.; Zhao, Y.; Tang, K.; Song, Q.; Qi, X.; Kong, D.; et al. Continuous hydrogenation of ethyl levulinate to γ-valerolactone and 2-methyl tetrahydrofuran over alumina doped Cu/SiO2catalyst: The potential of commercialization. *Sci. Rep.* **2016**, *6* (June), 2–10.

(26) Dong, F.; Zhu, Y.; Ding, G.; Cui, J.; Li, X.; Li, Y. One-step Conversion of Furfural into 2-Methyltetrahydrofuran under Mild Conditions. *ChemSusChem* **2015**, *8* (9), 1534–1537.

(27) Dohade, M. G.; Dhepe, P. L. One pot conversion of furfural to 2-methylfuran in the

presence of PtCo bimetallic catalyst. *Clean Technol. Environ. Policy* **2017**, 1–11.

(28) Ding, F.; Zhang, Y.; Yuan, G.; Wang, K.; Dragutan, I.; Dragutan, V.; Cui, Y.; Wu, J. Synthesis and Catalytic Performance of Ni / SiO 2 for Hydrogenation of 2-Methylfuran to 2-Methyltetrahydrofuran. *J. Nanomater.* **2015**, *2015*, 791529.

(29) Rodiansono; Khairi, S.; Hara, T.; Ichikuni, N.; Shimazu, S. Highly efficient and selective hydrogenation of unsaturated carbonyl compounds using Ni–Sn alloy catalysts. *Catal. Sci. Technol.* **2012**, *2* (10), 2139.

(30) Wang, S.; Vorotnikov, V.; Vlachos, D. G. Coverage-Induced Conformational Effects on Activity and Selectivity: Hydrogenation and Decarbonylation of Furfural on Pd(111). *ACS Catal.* **2015**, *5* (1), 104–112.

(31) Lejemble, P.; Gaset, A.; Kalck, P. From biomass to furan through decarbonylation of furfural under mild conditions. *Biomass* **1984**, *4* (4), 263–274.

(32) Coca, J.; Morrondo, E. S.; Sastre, H. Catalytic Decarbonylation of Furfural in a Fixed-Bed Reactor. *J. Chem. Technol. Biotechnol.* **1982**, *32* (9), 904–908.

(33) Pushkarev, V. V.; Musselwhite, N.; An, K.; Alayoglu, S.; Somorjai, G. A. High structure sensitivity of vapor-phase furfural decarbonylation/ hydrogenation reaction network as a function of size and shape of Pt nanoparticles. *Nano Lett.* **2012**, *12* (10), 5196–5201.

(34) Methyl-tetrahydrofuran, D.; Abdelrahman, O. A.; Park, D. S.; Vinter, K. P.; Spanjers, C. S.; Ren, L.; Cho, H. J.; Zhang, K.; Fan, W.; Tsapatsis, M.; et al. Renewable Isoprene by Sequential Hydrogenation of Itaconic Acid and Dehydra-Decyclization of 3 - Methyl-Tetrahydrofuran. **2017**, 5–8.

(35) Norman. catalytic dehydration of alcohols and ethers overaternary mixed oxide, D. W. Norman U.S. Patent , 8981172B2, 2015.

(36) Cho, H. J.; Ren, L.; Vattipalli, V.; Yeh, Y. H.; Gould, N.; Xu, B.; Gorte, R. J.; Lobo, R.; Dauenhauer, P. J.; Tsapatsis, M.; et al. Renewable p-Xylene from 2,5-Dimethylfuran and Ethylene Using Phosphorus-Containing Zeolite Catalysts. *ChemCatChem* **2017**, *9* (3), 398–402.

(37) Bui, P.; Cecilia, J. A.; Oyama, S. T.; Takagaki, A.; Infantes-Molina, A.; Zhao, H.; Li, D.; Rodríguez-Castellón, E.; Jiménez López, A. Studies of the synthesis of transition metal phosphides and their activity in the hydrodeoxygenation of a biofuel model compound. *J. Catal.* **2012**, *294*, 184–198.

(38) Bui, P. P.; Oyama, S. T.; Takagaki, A.; Carrow, B. P.; Nozaki, K. Reactions of 2-Methyltetrahydropyran on Silica-Supported Nickel Phosphide in Comparison with 2-Methyltetrahydrofuran. *ACS Catal.* **2016**, *6* (7), 4549–4558.

(39) Pang, Y.; Ardagh, M. A.; Shetty, M.; Chatzidimitriou, A.; Kumar, G.; Vlaisavljevich, B.; Dauenhauer, P. J. On the Spatial Design of Co-Fed Amines for Selective Dehydration of Methyl Lactate to Acrylates. ChemRxiv 2021. DOI: 10.26434/chemrxiv.13711168

(40) Axelsson, L.; Franzén, M.; Ostwald, M.; Berndes, G.; Lakshmi, G.; Ravindranath, N. H. Perspective: Jatropha cultivation in southern India: Assessing farmers' experiences. *Biofuels, Bioprod. Biorefining* **2012**, *6* (3), 246–256.

(41) Olivera, S.; Muralidhara, H. B.; Venkatesh, K.; Gopalakrishna, K.; Vivek, C. S. Plating on acrylonitrile–butadiene–styrene (ABS) plastic: a review. *J. Mater. Sci.* **2016**, *51* (8), 3657–3674.

(42) IEA Publications. IEA World Energy Outlook. Executive Summary;Nov. 2012. See the following: https://www.iea.org/publications/ freepublications/publication/English.pdf (accessed Sept. 30, 2019).

(43) Cespi, D.; Passarini, F.; Vassura, I.; Cavani, F. Butadiene from biomass, a life cycle perspective to address sustainability in the chemical industry. *Green Chem.* **2016**, *18* (6), 1625–1638.

(44) Abdelrahman, O. A.; Park, D. S.; Vinter, K. P.; Spanjers, C. S.; Ren, L.; Cho, H. J.; Vlachos, D. G.; Fan, W.; Tsapatsis, M.; Dauenhauer, P. J. Biomass-Derived Butadiene by Dehydra-Decyclization of Tetrahydrofuran. *ACS Sustain. Chem. Eng.* **2017**, *5* (5), 3732–3736.

(45) Abdelrahman, O. A.; Park, D. S.; Vinter, K. P.; Spanjers, C. S.; Ren, L.; Cho, H. J.; Zhang, K.; Fan, W.; Tsapatsis, M.; Dauenhauer, P. J. Renewable Isoprene by Sequential Hydrogenation of Itaconic Acid and Dehydra-Decyclization of 3-Methyl-Tetrahydrofuran. *ACS Catal.* **2017**, *7* (2), 1428–1431.

(46) Vecchini, N.; Galeotti, A.; Pisano, A. Process for the Production of 1, 3-butadiene from 1, 4-Butanediol via Tetrahydrofuran. Patent, WO 2016/092517, PCT/1B2015/059540, 2016.

(47) Maduskar, S.; Teixeira, A. R.; Paulsen, A. D.; Krumm, C.; Mountziaris; Fan, W.; Dauenhauer, P. J.; Mountziaris, T. J.; Fan, W.; Dauenhauer, P. J. Quantitative carbon detector (QCD) for calibration-free, high-resolution characterization of complex mixtures. *Lab Chip* **2015**, *15* (2), 440–447.

(48) Gunst, D.; Alexopoulos, K.; Van Der Borght, K.; John, M.; Galvita, V.; Reyniers, M. F.; Verberckmoes, A. Study of butanol conversion to butenes over H-ZSM-5: Effect of chemical structure on activity, selectivity and reaction pathways. *Appl. Catal. A Gen.* **2017**, *539*, 1–12.

(49) Makarova, M. A.; Paukshtis, E. A.; Thomas, J. M.; Williams, C.; Zamaraev, K. I. Dehydration of n-Butanol on Zeolite H-ZSM-5 and Amorphous Aluminosilicate - Detailed Mechanistic Study and the Effect of Pore Confinement. J. Catal. 1994, 149, 36−51.

(50) Frisch, M. J.; Trucks, G. W.; Schlegel, H. B.; Scuseria, G. E.; Robb, M. A.; Cheeseman, J. R.; Scalmani, G.; Barone, V.; Mennucci, B.; Petersson, G. A.; Nakatsuji, H.; Caricato, M.; Li, X.; Hratchian, H. P.; Izmaylov, A. F.; Bloino, J.; Zheng, G.; Sonnenberg, J. L.; Hada, M.; Ehara, M.; Toyota, K.; Fukuda, R.; Hasegawa, J.; Ishida, M.; Nakajima, T.; Honda, Y.; Kitao, O.; Nakai, H.; Vreven, T.; Montgomery, J. A., Jr.; Peralta, J. E.; Ogliaro, F.; Bearpark, M.; Heyd, J. J.;

Brothers, E.; Kudin, K. N.; Staroverov, V. N.; Keith, T.; Kobayashi, R.; Normand, J.; Raghavachari, K.; Rendell, A.; Burant, J. C.; Iyengar, S. S.; Tomasi, J.; Cossi, M.; Rega, N.; Millam, J. M.; Klene, M.; Knox, J. E.; Cross, J. B.; Bakken, V.; Adamo, C.; Jaramillo, J.; Gomperts, R.; Stratmann, R. E.; Yazyev, O.; Austin, A. J.; Cammi, R.; Pomelli, C.; Ochterski, J. W.; Martin, R. L.; Morokuma, K.; Zakrzewski, V. G.; Voth, G. A.; Salvador, P.; Dannenberg, J. J.; Dapprich, S.; Daniels, A. D.; Farkas, O.; Foresman, J. B.; Ortiz, J. V.; Cioslowski, J.; Fox, D. J. Gaussian 09, Revision D.01.; Gaussian, Inc., Wallingford CT, 2013. (15) Baerlocher, C.; McC

(51) Baerlocher, C.; McCusker, L. B. Database of Zeolite Structures. http://www.iza-structure.org/databases/.

(52) Dapprich, S.; Komáromi, I.; Byun, K. S.; Morokuma, K.; Frisch, M. J. A new ONIOM implementation in Gaussian98. Part I. The calculation of energies, gradients, vibrational frequencies and electric field derivatives. *J. Mol. Struct. THEOCHEM* **1999**, *461–462*, 1–21.

(53) Vreven, T.; Morokuma, K.; Farkas, Ö.; Schlegel, H. B.; Frisch, M. J. Geometry optimization with QM/MM, ONIOM, and other combined methods. I. Microiterations and constraints. *J. Comput. Chem.* **2003**, *24* (6), 760–769.

(54) Migues, A. N.; Muskat, A.; Auerbach, S. M.; Sherman, W.; Vaitheeswaran, S. On the rational design of zeolite clusters. *ACS Catal.* **2015**, *5* (5), 2859–2865.

(55) Zhao, Y.; Truhlar, D. G. The M06 suite of density functionals for main group thermochemistry, thermochemical kinetics, noncovalent interactions, excited states, and transition elements: Two new functionals and systematic testing of four M06-class functionals and 12 other function. *Theor. Chem. Acc.* **2008**, *120* (1–3), 215–241.

(56) Kenichi Fukui. The path of chemical reactions - the IRC approach. *Chem. Eng. News* **1968**, *46* (4), 5.

(57) Grimme, S. Supramolecular Binding Thermodynamics by Dispersion-Corrected Density Functional Theory. Chem. - Eur. J. 2012, 18, 9955−9964.

(58) Li, Y.; Gomes, J.; Sharada, S. M.; Bell, A. T.; Head-gordon, M. Improved Force-Field Parameters for QM/MM Simulations of the Energies of Adsorption for Molecules in Zeolites and a Free Rotor Correction to the Rigid Rotor Harmonic Oscillator Model for Adsorption Enthalpies. *J. Phys. Chem. C* 2015, 119, 1840−1850.

(59) Moor, B. A. De; Gobin, O. C.; Lercher, J. A.; Marin, G. B. Adsorption of C2 - C8 n-alkanes in zeolites. *J. Phys. Chem. C* **2011**, 1204–1219.

(60) Patet, R. E.; Caratzoulas, S.; Vlachos, D. G. Adsorption in zeolites using mechanically embedded ONIOM clusters. *Phys. Chem. Chem. Phys.* **2016**, *18* (37), 26094–26106.

(61) Patet, R. E.; Caratzoulas, S.; Vlachos, D. G. Tandem Aromatization of Oxygenated Furans by Framework Zinc In Zeolites . A Computational Study. *J. Phys. Chem. C*

2017, 121, 22178−22186.

(62) Patet, R. E.; Fan, W.; Vlachos, D. G.; Caratzoulas, S. Tandem Diels – Alder Reaction of Dimethylfuran and Ethylene and Dehydration to para -Xylene Catalyzed by Zeotypic Lewis Acids. *ChemCatChem* **2017**, 2523–2535.

(63) Motagamwala, A. H.; Ball, M. R.; Dumesic, J. A. Microkinetic Analysis and Scaling Relations for Catalyst Design. *Annu. Rev. Chem. Biomol. Eng.* **2018**, 9, 413−450.

(64) Campbell, C. T. The Degree of Rate Control: A Powerful Tool for Catalysis Research. *ACS Catal.* **2017**, *7* (4), 2770–2779.

(65) Stegelmann, C.; Andreasen, A.; Campbell, C. T. Degree of Rate Control : How Much the Energies of Intermediates and Transition States Control Rates. *J. Am. Chem. Soc.* **2009**, 131, 8077–8082.

(66) Yang, Y.; Lin, F.; Tran, H.; Chin, Y. H. C. Butanal Condensation Chemistry Catalyzed by Brønsted Acid Sites on Polyoxometalate Clusters. *ChemCatChem* **2017**, *9* (2), 287–299.

(67) Kozuch, S.; Shaik, S. How to Conceptualize Catalytic Cycles? The Energetic Span Model. *Acc. Chem. Res* **2011**, *44* (2), 101–110.

(68) Chia, M.; Pagán-Torres, Y. J.; Hibbitts, D.; Tan, Q.; Pham, H. N.; Datye, A. K.; Neurock, M.; Davis, R. J.; Dumesic, J. A. Selective hydrogenolysis of polyols and cyclic ethers over bifunctional surface sites on rhodium-rhenium catalysts. *J. Am. Chem. Soc.* **2011**, *133* (32), 12675–12689.

(69) Witzke, M. E.; Almithn, A.; Coonrod, C. L.; Hibbitts, D. D.; Flaherty, D. W. Mechanisms and Active Sites for C-O Bond Rupture within 2-Methyltetrahydrofuran over Ni, Ni12P5, and Ni2P Catalysts. *ACS Catal.* **2018**, *8* (8), 7141–7157.

(70) Iino, A.; Cho, A.; Takagaki, A.; Kikuchi, R.; Ted Oyama, S. Kinetic studies of hydrodeoxygenation of 2-methyltetrahydrofuran on a Ni2P/SiO2 catalyst at medium pressure. *J. Catal.* **2014**, *311*, 17–27.

(71) Cho, A.; Takagaki, A.; Kikuchi, R.; Ted Oyama, S. Active Sites in Ni2P/USY Catalysts for the Hydrodeoxygenation of 2-Methyltetrahydrofuran. *Top. Catal.* **2015**, *58* (4–6), 219–231.

(72) Bui, P.; Takagaki, A.; Kikuchi, R.; Oyama, S. T. Kinetic and infrared spectroscopy study of hydrodeoxygenation of 2-Methyltetrahydrofuran on a nickel phosphide catalyst at atmospheric pressure. *ACS Catal.* **2016**, *6* (11), 7701–7709.

(73) Sun, D.; Arai, S.; Duan, H.; Yamada, Y.; Sato, S. Vapor-phase dehydration of C4 unsaturated alcohols to 1,3-butadiene. *Appl. Catal. A Gen.* **2017**, *531*, 21–28.

(74) Hartmann, M. Hierarchical zeolites: A proven strategy to combine shape selectivity with efficient mass transport. *Angew. Chemie - Int. Ed.* **2004**, *43* (44), 5880–5882.

(75) Chughtai, A. H.; Ahmad, N.; Younus, H. A.; Laypkov, A.; Verpoort, F. Metal-

organic frameworks: Versatile heterogeneous catalysts for efficient catalytic organic transformations. *Chem. Soc. Rev.* **2015**, *44* (19), 6804–6849.

(76) Wang, A.; Li, J.; Zhang, T. Heterogeneous single-atom catalysis. *Nat. Rev. Chem.* **2018**, *2* (6), 65–81.

(77) Furukawa, S.; Komatsu, T. Intermetallic Compounds: Promising Inorganic Materials for Well-Structured and Electronically Modified Reaction Environments for Efficient Catalysis. *ACS Catal.* **2017**, *7* (1), 735–765.

(78) Voiry, D.; Shin, H. S.; Loh, K. P.; Chhowalla, M. Low-dimensional catalysts for hydrogen evolution and CO2 reduction. *Nat. Chem .Rev.* **2018,** 10.1038/s41570-017-0105.

(79) Holzwarth, A.; Schmidt, H. W.; Maier, W. F. Detection of catalytic activity in combinatorial libraries of heterogeneous catalysts by IR thermography. *Angew. Chemie - Int. Ed.* **1998**, *37* (19), 2644–2647.

(80) Cong, P.; Doolen, R. D.; Fan, Q.; Giaquinta, D. M.; Guan, S.; Mcfarland, E. W.; Poojary, D. M.; Self, K.; Turner, H. W.; Weinberg, W. H. High-throughput synthesis and screening of combinatorial heterogeneous catalyst libraries *Angew. Chem.* **1999**, No. 4, 483–488.

(81) Hendershot, R. J.; Snively, C. M.; Lauterbach, J. High-throughput heterogeneous catalytic science. *Chem. - A Eur. J.* **2005**, *11* (3), 806–814.

(82) Van Veen, A. C.; Farrusseng, D.; Rebeilleau, M.; Decamp, T.; Holzwarth, A.; Schuurman, Y.; Mirodatos, C. Acceleration in catalyst development by fast transient kinetic investigation. *J. Catal.* **2003**, *216* (1–2), 135–143.

(83) Corma, A.; Serra, J. M. Heterogeneous combinatorial catalysis applied to oil refining, petrochemistry and fine chemistry. *Catal. Today* **2005**, *107–108*, 3–11.

(84) Huybrechts, W.; Mijoin, J. érôme; Jacobs, P. A.; Martens, J. A. Development of a fixed-bed continuous-flow high-throughput reactor for long-chain n-alkane hydroconversion. *Appl. Catal. A Gen.* **2003**, *243* (1), 1–13.

(85) Hendershot, R. J.; Lasko, S. S.; Fellmann, M. F.; Oskarsdottir, G.; Nicholas Delgass, W.; Snively, C. M.; Lauterbach, J. A novel reactor system for high throughput catalyst testing under realistic conditions. *Appl. Catal. A Gen.* **2003**, *254* (1), 107–120.

(86) Hahndorf, I.; Buyevskaya, O.; Langpape, M.; Grubert, G.; Kolf, S.; Guillon, E.; Baerns, M. Experimental equipment for high-throughput synthesis and testing of catalytic materials. *Chem. Eng. J.* **2002**, *89* (1–3), 119–125.

(87) Pérez-Ramírez, J.; Berger, R. J.; Mul, G.; Kapteijn, F.; Moulijn, J. A. Six-flow reactor technology a review on fast catalyst screening and kinetic studies. *Catal. Today* **2000**, *60* (1), 93–109.

(88) Moulijn, J. A.; Pérez-Ramírez, J.; Berger, R. J.; Hamminga, G.; Mul, G.; Kapteijn, F. High-throughput experimentation in catalyst testing and in kinetic studies for

heterogeneous catalysis. *Catal. Today* **2003**, *81* (3), 457–471.

(89) Parrott, A. J.; Bourne, R. A.; Akien, G. R.; Irvine, D. J.; Poliakoff, M. Self-optimizing continuous reactions in supercritical carbon dioxide. *Angew. Chemie - Int. Ed.* **2011**, *50* (16), 3788–3792.

(90) Waldron, C.; Pankajakshan, A.; Quaglio, M.; Cao, E.; Galvanin, F.; Gavriilidis, A. An autonomous microreactor platform for the rapid identification of kinetic models. *React. Chem. Eng.* **2019,** 4, 1623-1636.

(91) Perera, D.; Tucker, J. W.; Brahmbhatt, S.; Helal, C. J.; Chong, A.; Farrell, W.; Richardson, P.; Sach, N. W. A platform for automated nanomole- scale reaction screening and micromole-scale synthesis in flow. *Science* **2018**, *434* (January), 429–434.

(92) Holmes, N.; Akien, G. R.; Blacker, A. J.; Woodward, R. L.; Meadows, R. E.; Bourne, R. A. Self-optimisation of the final stage in the synthesis of EGFR kinase inhibitor AZD9291 using an automated flow reactor. *React. Chem. Eng.* **2016**, *1* (4), 366–371.

(93) Cherkasov, N.; Bai, Y.; Expósito, A. J.; Rebrov, E. V. OpenFlowChem-a platform for quick, robust and flexible automation and self-optimisation of flow chemistry. *React. Chem. Eng.* **2018**, *3* (5), 769–780.

(94) Reizman, B. J.; Jensen, K. F. An automated continuous-flow platform for the estimation of multistep reaction kinetics. *Org. Process Res. Dev.* **2012**, *16* (11), 1770–1782.

(95) R. Watanabe, T. Komatsu, S. Sakamoto, Y. Uranoc, H. Noji High-throughput single-molecule bioassay using micro-reactor arrays with a concentration gradient of target molecules, *Lab Chip* **2018** (18) 2849-2853.

(96) https://github.com/richardingham/octopus (Accessed 22 July 2020).

(97) Deshpande, A.; Krishnaswamy, S.; Ponnani, K. Pulsed Micro-reactor: An alternative to estimating kinetic parameters of non-catalytic gas–solid reactions. *Chem. Eng. Res. Des.* **2017**, *117*, 382–393.

(98) Wang, H.; Zhao, P.; Jiang, B.; Liu, W. A pulse reactor-gas chromatographic investigation of the kinetics of catalytic carbon monoxide hydrogenation. *J. Mol. Catal.* **1992**, *71* (3), 357–364.

(99) J.A.S. Bett, K.W. Hall The microcatalytic technique applied to a zero order reaction: the dehydration of 2-butanol over hydroxyapatite catalysts, *J. Catal.* **1968**, 10, 105-*113*.

(100) Verma, A. Kaliaguine Estimation of rate coefficients from pulsed microcatalytic reactors: oxidation of ethylene over silver catalyst *J.Catal*. **1973**, 30, *430-437*.

(101) Hickman, D. A.; Degenstein, J. C.; Ribeiro, F. H. Fundamental principles of laboratory fixed bed reactor design. *Curr. Opin. Chem. Eng.* **2016**, *13*, 1–9.

(102) Nauman, E. B. Residence time theory. *Ind. Eng. Chem. Res.* **2008**, *47* (10), 3752–3766.

(103) Abdelrahman, O.; Vinter, K. P.; Ren, L.; Xu, D.; Gorte, R. J.; Tsapatsis, M.; Dauenhauer, P. J. Simple Quantification of Zeolite Acid Site Density by Reactive Gas Chromatography. *Catal. Sci. Technol.* **2017,** 7, 3831-3841.

(104) Li, S.; Kumar, G.; Abdelrahman, O. A.; Tsapatsis, M.; Dionisios, G.; Caratzoulas, S.; Dauenhauer, P. J. Mechanisms and Pathways of Dehydra-Decyclization of Tetrahydrofuran on H-ZSM5 *ACS Catal.* **2019**, 9, 11, 10279–10293

(105) F. Froment, G. K.B. Bischoff *Chemical Reaction Engineering*, Wiley (1974) 10.1021/ba-1972-0109

(106) Levenspiel, O.*Chemical Reaction Engineering,* Wiley (1998) .

(107) Gounder, R.; Iglesia, E. The Roles of Entropy and Enthalpy in Stabilizing Ion-Pairs at Transition States in Zeolite Acid Catalysis. *Acc. Chem. Res.* **2012**, *45* (2), 229–238.

(108) Chiang, H.; Bhan, A. Catalytic consequences of hydroxyl group location on the rate and mechanism of parallel dehydration reactions of ethanol over acidic zeolites. *J. Catal.* **2010**, *271* (2), 251–261.

(109) Williams, C.; Makarova, M. A.; Malysheva, L. V.; Paukshtis, E. A.; Zamaraev, K. I.; Thomas, J. M. Mechanistic studies of the catalytic dehydration of isobutyl alcohol on NaH-ZSM-5. *J. Chem. Soc. Faraday Trans.* **1990**, *86* (20), 3473–3485.

(110) Liu, D.; Bhan, A.; Tsapatsis, M.; Al Hashimi, S. Catalytic behavior of Brønsted acid sites in MWW and MFI zeolites with dual meso- and microporosity. *ACS Catal.* **2011**, *1* (1), 7–17.

(111) Kumar, G.; Liu, D.; Xu, D.; Ren, L; Tsapatsis, M.; Dauenhauer, P. J.; Dehydra-Decyclization of 2-Methyltetrahydrofuran to Pentadienes on Boron- Containing Zeolites. *Green Chem.*, **2020**, 22, 4147-4160.

(112) Gounder, R.; Iglesia, E. The catalytic diversity of zeolites: confinement and solvation effects within voids of molecular dimensions. *Chem. Commun.* **2013**, *49* (34), 3491.

(113) Scott, S. L. A Matter of Life(time) and Death. *ACS Catal.* **2018**, *8*, 8597–8599.

(114) Alexopoulos, K.; John, M.; Van Der Borght, K.; Galvita, V.; Reyniers, M. F.; Marin, G. B. DFT-based microkinetic modeling of ethanol dehydration in H-ZSM-5. *J. Catal.* **2016**, *339*, 173–185.

(115) M.S. Reisch, Coping with the helium shortage C&EN, 91 (2013), pp. 18-19 (https://cen.acs.org/articles/91/i5/Coping-Helium-Shortage.html)

(116) Mark Hillmyer. The promise of plastics from plants. *Science* **2016**, *358* (6365), 868–870.

(117) Schneiderman, D. K.; Hillmyer, M. A. 50th Anniversary Perspective: There Is a

Great Future in Sustainable Polymers. *Macromolecules* **2017**, *50* (10), 3733–3749.

(118) D. Cespi , F. Passarini , I. Vassura and F. Cavani, Butadiene from biomass, a life cycle perspective to address sustainability in the chemical industry. *Green Chem.* **2016**, *18* (6), 1625–1638.

(119) Rabnawaz, M.; Wyman, I.; Auras, R.; Cheng, S. A roadmap towards green packaging: The current status and future outlook for polyesters in the packaging industry. *Green Chem.* **2017**, *19* (20), 4737–4753.

(120) Behr, A.; Neubert, P. Piperylene - A versatile basic chemical in catalysis. *ChemCatChem* **2014**, *6* (2), 412–428.

(121) Neubert, P.; Fuchs, S.; Behr, A. Hydroformylation of piperylene and efficient catalyst recycling in propylene carbonate. *Green Chem.* **2015**, *17* (7), 4045–4052.

(122) Neubert, P.; Steffen, M.; Behr, A. Three step auto-tandem catalysed hydroesterification: Access to linear fruity esters from piperylene. *J. Mol. Catal. A Chem.* **2015**, *407*, 122–127.

(123) Neubert, P.; Meier, I.; Gaide, T.; Kuhlmann, R.; Behr, A. First telomerisation of piperylene with morpholine using palladium-carbene catalysts. *Catal. Commun.* **2016**, *77*, 70–74.

(124) Kakiuchi, Y.; Tanigawa, T.; Tsunoji, N.; Takamitsu, Y.; Sadakane, M.; Sano, T. Phosphorus modified small-pore zeolites and their catalytic performances in ethanol conversion and NH 3 -SCR reactions. *Appl. Catal. A Gen.* **2019**, *575* (November 2018), 204–213.

(125) Wang, C.; Li, S.; Mao, X.; Caratzoulas, S.; Gorte, R. J. H-D Exchange of Simple Aromatics as a Measure of Brønsted-Acid Site Strengths in Solids. *Catal. Letters* **2018**, *148* (11), 3548–3556.

(126) Lok, B. M.; Messina, C. A.; Patton, R. L.; Gajek, R. T.; Cannan, T. R.; Flanigen, E. M. Silicoaluminophosphate Molecular Sieves: Another New Class of Microporous Crystalline Inorganic Solids. *J. Am. Chem. Soc.* **1984**, *106* (20), 6092–6093.

(127) Dai, W.; Wang, X.; Wu, G.; Guan, N.; Hunger, M.; Li, L. Methanol-to-olefin conversion on silicoaluminophosphate catalysts: Effect of brønsted acid sites and framework structures. *ACS Catal.* **2011**, *1* (4), 292–299.

(128) Martens, J. A.; Grobet, P. J.; Jacobs, P. A. Catalytic activity and Si, Al, P ordering in microporous silicoaluminophosphates of the SAPO-5, SAPO-11, and SAPO-37 type. *J. Catal.* **1990**, *126* (1), 299–305.

(129) Chu, Cynthia T. W.; Kuehl, Guenther H.; Lago, Rudolph M.; Chang, Clarence D. lsomorphous Substitution in Zeolite Frameworks . II. Catalytic properties of [B]ZSM-5. *J. Catal.* **1985**, *458*, 451–458.

(130) Parrillo, D. J.; Lee, C.; Gorte, R. J.; White, D.; Farneth, W. E. Comparison of the Acidic Properties of H-[Al]ZSM-5, H-[Fe]ZSM-5, and H-[Ga]ZSM-5 Using Microcalorimetry, Hexane Cracking, and Propene Oligomerization. *J. Phys. Chem.*

1995, *99* (21), 8745–8749.

(131) Agarwal, V.; Metiu, H. Hydrogen Abstraction Energies and Ammonia Binding to BEA, ZSM-5, and α-Quartz Doped with Al, Sc, B, or Ga. *J. Phys. Chem. C* **2015**, *119* (28), 16106–16114.

(132) Yuan, S. P.; Wang, J. G.; Li, Y. W.; Jiao, H. Brønsted acidity of isomorphously substituted ZSM-5 by B, Al, Ga, and Fe. Density functional investigations. *J. Phys. Chem. A* **2002**, *106* (35), 8167–8172.

(133) Jones, A. J.; Iglesia, E. The Strength of Bronsted Acid Sites in Microporous Aluminosilicates. *ACS Catal.* **2015**, *5* (10), 5741–5755.

(134) Jones, A. J.; Carr, R. T.; Zones, S. I.; Iglesia, E. Acid strength and solvation in catalysis by MFI zeolites and effects of the identity, concentration and location of framework heteroatoms. *J. Catal.* **2014**, *312*, 58–68.

(135) Patet, R. E.; Koehle, M.; Lobo, R. F.; Caratzoulas, S.; Vlachos, D. G. General Acid-Type Catalysis in the Dehydrative Aromatization of Furans to Aromatics in H- [Al] -BEA , H- [Fe] -BEA , H- [Ga] -BEA , and H- [B] -BEA Zeolites. *J. Phys. Chem. C* **2017,** 121 , 13666 - 13679.

(136) Ren, L.; Guo, Q.; Orazov, M.; Xu, D.; Politi, D.; Kumar, P.; Alhassan, S. M.; Mkhoyan, K. A.; Sidiras, D. Pillared Sn-MWW Prepared by a Solid-State-Exchange Method and its Use as a Lewis Acid Catalyst. *ChemCatChem* **2016**, 1274–1278.

(137) Dapsens, P. Y.; Mondelli, C.; Pérez-Ramírez, J. Design of Lewis-acid centres in zeolitic matrices for the conversion of renewables. *Chem. Soc. Rev.* **2015**, *44* (20), 7025–7043.

(138) Ouyang, X.; Hwang, S. J.; Runnebaum, R. C.; Xie, D.; Wanglee, Y. J.; Rea, T.; Zones, S. I.; Katz, A. Single-step delamination of a MWW borosilicate layered zeolite precursor under mild conditions without surfactant and sonication. *J. Am. Chem. Soc.* **2014**, *136* (4), 1449–1461.

(139) Chen, J.; Liang, T.; Li, J.; Wang, S.; Qin, Z.; Wang, P.; Huang, L.; Fan, W.; Wang, J. Regulation of Framework Aluminum Siting and Acid Distribution in H-MCM-22 by Boron Incorporation and Its Effect on the Catalytic Performance in Methanol to Hydrocarbons. *ACS Catal.* **2016**, *6* (4), 2299–2313.

(140) Kester, P. M.; Miller, T.; Gounder, R. Ammonia Titration Methods to Quantify Brønsted Acid Sites in Zeolites Substituted with Aluminum and Boron *Ind. Eng. Chem.*, 2018, **57** , 6673 —6683.

(141) Zhu, Q.; Kondo, J. N.; Yokoi, T.; Setoyama, T.; Yamaguchi, M.; Takewaki, T.; Domen, K.; Tatsumi, T. The influence of acidities of boron- and aluminium-containing MFI zeolites on co-reaction of methanol and ethene. *Phys. Chem. Chem. Phys.* **2011**, *13* (32), 14598–14605.

(142) Li, C.; Vidal-Moya, A.; Miguel, P. J.; Dedecek, J.; Boronat, M.; Corma, A. Selective Introduction of Acid Sites in Different Confined Positions in ZSM-5 and Its Catalytic Implications. *ACS Catal.* **2018**, *8* (8), 7688–7697.

(143) Zhu, Q.; Kondo, J. N.; Setoyama, T.; Yamaguchi, M.; Domen, K.; Tatsumi, T. Activation of hydrocarbons on acidic zeolites: Superior selectivity of methylation of ethene with methanol to propene on weakly acidic catalysts. *Chem. Commun.* **2008**, No. 41, 5164–5166.

(144) Korányi, T. I.; Nagy, J. B. Distribution of aluminum and boron in the periodical building units of boron-containing β zeolites. *J. Phys. Chem. B* **2006**, *110* (30), 14728–14735.

(145) Li, S.; Abdelrahman, O. A.; Kumar, G.; Tsapatsis, M.; Vlachos, D. G.; Caratzoulas, S.; Dauenhauer, P. J. Dehydra-Decyclization of Tetrahydrofuran on H-ZSM5: Mechanisms, Pathways, and Transition State Entropy. *ACS Catal.* **2019**, *9* (11), 10279–10293.

(146) Bui, P.; Takagaki, A.; Kikuchi, R.; Oyama, S. T. Kinetic and Infrared Spectroscopy Study of Hydrodeoxygenation of 2-Methyltetrahydrofuran on a Nickel Phosphide Catalyst at Atmospheric Pressure. *ACS Catal.* **2016**, *6* (11), 7701–7709.

(147) Cho, A.; Kim, H.; Iino, A.; Takagaki, A.; Ted Oyama, S. Kinetic and FTIR studies of 2-methyltetrahydrofuran hydrodeoxygenation on Ni2P/SiO2. *J. Catal.* **2014**, *318*, 151–161.

(148) Witzke, M. E.; Almithn, A.; Coonrod, C. L.; Hibbitts, D. D.; Flaherty, D. W. Mechanisms and Active Sites for C-O Bond Rupture within 2-Methyltetrahydrofuran over Ni, Ni12P5, and Ni2P Catalysts. *ACS Catal.* **2018**, *8* (8), 7141–7157.

(149) Corma, A.; Corell, C.; Perez-Pariente, J. Synthesis and characterization of the MCM-22 zeolite, Zeolites (**1995**), 15(1), 2-8 CODEN: ZEOLD3; ISSN: 0144-2449. English.

(150) Maheshwari, S.; Jordan, E.; Kumar, S.; Bates, F. S.; Penn, R. L.; Shantz, D. F.; Tsapatsis, M. Layer structure preservation during swelling, pillaring, and exfoliation of a zeolite precursor. *J. Am. Chem. Soc.* **2008**, *130* (4), 1507–1516.

(151) Koller, H.; Senapati, S.; Ren, J.; Uesbeck, T.; Siozios, V.; Hunger, M.; Lobo, R. F. Post-Synthesis Conversion of Borosilicate Zeolite Beta to an Aluminosilicate with Isolated Acid Sites : A Quantitative Distance Analysis by Solid-State NMR. *J. Phys. Chem. C*, 2016, **120** , 9811 —9820 .

(152) Tong, H. T. T.; Koller, H. Control of Al for B framework substitution in zeolite Beta by counterions. *Microporous Mesoporous Mater.* **2012**, *148* (1), 80–87.

(153) Lin, F.; Yang, Y.; Chin, Y. H. Kinetic requirements of aldehyde transfer hydrogenation catalyzed by microporous solid Brønsted acid catalysts. *ACS Catal.* **2017**, *7* (10), 6909–6914.

(154) Lin, F.; Chin, Y. H. Alkanal transfer hydrogenation catalyzed by solid Brønsted acid sites. *J. Catal.* **2016**, *341*, 136–148.

(155) H. S. Fogler Elements of Chemical Reaction Engineering , Pearson Education Inc, Upper Saddle River, NJ, 2006.

(156) Kofke, T. J. G.; Gorte, R. J.; Kokotailo, G. T. Stoichiometric adsorption complexes in [B]- and [Fe]-ZSM-5 zeolites. *J. Catal.* **1989**, *116* (1), 252–262.

(157) Hwang, S. J.; Chen, C. Y.; Zones, S. I. Boron sites in borosilicate zeolites at various stages of hydration studied by solid state NMR spectroscopy. *J. Phys. Chem. B* **2004**, *108* (48), 18535–18546.

(158) Góra-Marek, K.; Tarach, K.; Choi, M. 2,6-Di-tert-butylpyridine sorption approach to quantify the external acidity in hierarchical zeolites. *J. Phys. Chem. C* **2014**, *118* (23), 12266–12274.

(159) A. Corma L. Forni, F. Márquez, J. Martínez-Triguero, D. Moscotti, V. F.; Mart, J.; Corma, A.; Forn, V.; Forni, L.; M, F. 2,6-Di-Tert-Butyl-Pyridine As a Probe Molecule To Measure External Acidity of Zeolites. *J. Catal.* **1998**, *179*, 451–458.

(160) Hwang, A.; Bhan, A. Bifunctional Strategy Coupling Y2O3-Catalyzed Alkanal Decomposition with Methanol-to-Olefins Catalysis for Enhanced Lifetime. *ACS Catal.* **2017**, *7* (7), 4417–4422.

(161) Chu, C. T. W.; Kuehl, G. H.; Lago, R. M.; Chang, C. D. Isomorphous substitution in zeolite frameworks. II. Catalytic properties of [B]ZSM-5. *J. Catal.* **1985**, *93* (2), 451–458.

(162) Yuen, L. T.; Zones, S. I.; Harris, T. V.; Gallegos, E. J.; Auroux, A. Product selectivity in methanol to hydrocarbon conversion for isostructural compositions of AFI and CHA molecular sieves. *Microporous Mater.* **1994**, *2* (2), 105–117.

(163) Hunter, E. P. L.; Lias, S. G. Evaluated gas phase basicities and proton affinities of molecules: An update. *J. Phys. Chem. Ref. Data* **1998**, *27* (3), 413–656.

(164) Lias, S. G.; Liebman, J. F.; Levin, R. D. Evaluated Gas Phase Basicities and Proton Affinities of Molecules; Heats of Formation of Protonated Molecules. *J. Phys. Chem. Ref. Data* **1984**, *13* (3), 695–808.

(165) Fois, E.; Gamba, A.; Tabacchi, G.; Trudu, F. *First principles studies on boron sites*; Elsevier B.V., 2008; Vol. 174.

(166) Zhang, W.-G.; Yu, D.-H.; Ji, X.-J.; Huang, H. Efficient Dehydration of Bio-based 2,3-Butanediol to Butanone over Boric Acid Modified HZSM-5 Zeolites. *Green Chem.* **2012**, 3441–3450.

(167) Röseler, J.; Heitmann, G.; Hölderich, W. F. Vapour-phase Beckmann rearrangement using B-MFI zeolites. *Appl. Catal. A Gen.* **1996**, *144* (1–2), 319–333.

(168) Forni, L.; Fornasari, G.; Trifirò, F.; Aloise, A.; Katovic, A.; Giordano, G.; Nagy, J. B. Calcination and deboronation of B-MFI applied to the vapour phase Beckmann rearrangement. *Microporous Mesoporous Mater.* **2007***, 101* ,161–168.

(169) Heitmann, G. P.; Dahlhoff, G.; Niederer, J. P. M.; Hölderich, W. F. Active Sites of a [B]-ZSM-5 Zeolite Catalyst for the Beckmann Rearrangement of Cyclohexanone Oxime to Caprolactam. *J. Catal.* **2000**, *194* (1), 122–129.

(170) A. Nau , H. W. Zanthoff , F. Geilen , D. Maschmeyer , M. Winterberg , S. Peitz , R. Bukohl and C. Boeing , *US Patent* , 2015/0258535A1, **2015**.

(171) Ranoux, A.; Djanashvili, K.; Arends, I. W. C. E.; Hanefeld, U. B-TUD-1: a versatile mesoporous catalyst. *RSC Adv.* **2013**, *3* (44), 21524.

(172) Sundaramurthy, V.; Eswaramoorthi, I.; Lingappan, N. The catalytic effect of boron substitution in MCM-41-type molecular sieves. *Can. J. Chem.* **2004**, *82* (5), 631–640.

(173) W. Hoelderich , F. Merger , W. F. Mross and G. Fouquet , *US Patent* , 4560822, **1985.**

(174) Kondo, J. N.; Shao, L.; Wakabayashi, F.; Domen, K. Doublebond migration of an olefin without protonated species on H(D) form zeolites. *J. Phys. Chem. B* **1997**, *101* (45), 9314–9320.

(175) Boronat, M.; Viruela, P.; Corma, A. Theoretical study of the mechanism of zeolite-catalyzed isomerization reactions of linear butenes. *J. Phys. Chem. A* **1998**, *102* (6), 982–989.

(176) Yu, L.; Karton, A. Assessment of theoretical procedures for a diverse set of isomerization reactions involving double-bond migration in conjugated dienes. *Chem. Phys.* **2014**, *441*, 166–177.

(177) Noh, G.; Zones, S. I.; Iglesia, E. Consequences of Acid Strength and Diffusional Constraints for Alkane Isomerization and β-Scission Turnover Rates and Selectivities on Bifunctional Metal-Acid Catalysts. *J. Phys. Chem. C* **2018**, *122*, 25475–25497.

(178) Noh, G.; Shi, Z.; Zones, S. I.; Iglesia, E. Isomerization and β-scission reactions of alkanes on bifunctional metal-acid catalysts: Consequences of confinement and diffusional constraints on reactivity and selectivity. *J. Catal.* **2018,** 368 , 389 —410.

(179) Sarazen, M. L.; Doskocil, E.; Iglesia, E. Effects of Void Environment and Acid Strength on Alkene Oligomerization Selectivity. *ACS Catal.* **2016**, *6* (10), 7059–7070.

(180) Tsapatsis, M.; Maheshwari, S. Pores by pillaring: Not always a maze. *Angew. Chemie - Int. Ed.* **2008**, *47* (23), 4262–4263.

(181) Wang, S.; Wei, Z.; Chen, Y.; Qin, Z.; Ma, H.; Dong, M.; Fan, W.; Wang, J. Methanol to olefins over H-MCM-22 zeolite: Theoretical study on the catalytic roles of various pores. *ACS Catal.* **2015**, *5* (2), 1131–1144.

(182) Laforge, S.; Martin, D.; Guisnet, M. Xylene transformation over H-MCM-22 zeolites: 3. Role of the three pore systems in o-, m- and p-xylene transformations. *Appl. Catal. A Gen.* **2004**, *268* (1–2), 33–41.

(183) Matias, P.; Lopes, J. M.; Laforge, S.; Magnoux, P.; Russo, P. A.; Ribeiro Carrott, M. M. L.; Guisnet, M.; Ramôa Ribeiro, F. Methylcyclohexane transformation over HMCM22 zeolite: Mechanism and location of the reactions. *J. Catal.* **2008**, *259* (2),

190–202.

(184) Matias, P.; Lopes, J. M.; Laforge, S.; Magnoux, P.; Guisnet, M.; Ramôa Ribeiro, F. n-Heptane transformation over a HMCM-22 zeolite: Catalytic role of the pore systems. *Appl. Catal. A Gen.* **2008**, *351* (2), 174–183.

(185) Wu, Y.; Emdadi, L.; Qin, D.; Zhang, J.; Liu, D. Quantification of external surface and pore mouth acid sites in unit-cell thick pillared MFI and pillared MWW zeolites. *Microporous Mesoporous Mater.* **2017**, *241*, 43–51.

(186) Qiao, Q.; Wang, R.; Gou, M.; Yang, X. Catalytic performance of boron and aluminium incorporated ZSM-5 zeolites for isomerization of styrene oxide to phenylacetaldehyde. *Microporous Mesoporous Mater.* **2014**, *195*, 250–257.

(187) Hu, Z.; Zhang, H.; Wang, L.; Zhang, H.; Zhang, Y.; Xu, H.; Shen, W.; Tang, Y. Highly stable boron-modified hierarchical nanocrystalline ZSM-5 zeolite for the methanol to propylene reaction. *Catal. Sci. Technol.* **2014**, *4* (9), 2891–2895.

(188) Yang, Y.; Sun, C.; Du, J.; Yue, Y.; Hua, W.; Zhang, C.; Shen, W.; Xu, H. The synthesis of endurable B-Al-ZSM-5 catalysts with tunable acidity for methanol to propylene reaction. *Catal. Commun.* **2012**, *24*, 44–47.

(189) Hwang, A.; Kumar, M.; Rimer, J. D.; Bhan, A. Implications of methanol disproportionation on catalyst lifetime for methanol-to-olefins conversion by HSSZ-13. *J. Catal.* **2017**, *346*, 154–160.

(190) Bligaard, T.; Bullock, R. M.; Campbell, C. T.; Chen, J. G.; Gates, B. C.; Gorte, R. J.; Jones, C. W.; Jones, W. D.; Kitchin, J. R.; Scott, S. L. Toward Benchmarking in Catalysis Science: Best Practices, Challenges, and Opportunities. *ACS Catal.* **2016**, *6* (4), 2590–2602.

(191) Sun, R.; Zheng, M.; Li, X.; Pang, J.; Wang, A.; Wang, X.; Zhang, T. Production of renewable 1,3-pentadiene from xylitol via formic acid-mediated deoxydehydration and palladium-catalyzed deoxygenation reactions. *Green Chem.* **2017**, *19* (3), 638–642.

(192) D. W. Norman *U.S. Patent* , 8981172B2, **2015**.

(193) Walker, T. W.; Motagamwala, A. H.; Dumesic, J. A.; Huber, G. W. Fundamental catalytic challenges to design improved biomass conversion technologies. *J. Catal.* **2019**, *369*, 518–525.

(194) Climent, M. J.; Corma, A.; Iborra, S. Conversion of biomass platform molecules into fuel additives and liquid hydrocarbon fuels. *Green Chem.* **2014**, *16* (2), 516–547.

(195) Serrano, D. P.; Melero, J. A.; Morales, G.; Iglesias, J.; Pizarro, P. Progress in the design of zeolite catalysts for biomass conversion into biofuels and bio-based chemicals. *Catal. Rev. - Sci. Eng.* **2018**, *60* (1), 1–70.

(196) Simonetti, D. A.; Dumesic, J. Catalytic production of liquid fuels from biomass-derived oxygenated hydrocarbons: Catalytic coupling at multiple length scales.

Catal. Rev. - Sci. Eng. **2009**, *51* (3), 441–484.

(197) Kumar, G.; Liu, D.; Xu, D.; Tsapatsis, M.; Dauenhauer, P. J.; Dehydra-Decyclization of 2-Methyltetrahydrofuran to Pentadienes on Boron- Containing Zeolites. *Green Chem.***, 2020,** ***22***, 4147-4160.

(198) Jones, A. J.; Carr, R. T.; Zones, S. I.; Iglesia, E. Acid strength and solvation in catalysis by MFI zeolites and effects of the identity, concentration and location of framework heteroatoms. *J. Catal.* **2014**, *312*, 58–68.

(199) Cho, H. J.; Ren, L.; Vattipailli, V.; Yeh, Y.-H.; Gould, N. G.; Xu, B.; Gorte, R. J.; Lobo, R.; Dauenhauer, P. J.; et al. Renewable p-Xylene from 2,5-Dimethylfuran and Ethylene Using Phosphorus-containing Zeolite Catalysts. *ChemCatChem* **2017**, 9, 398-402.

(200) Zhang, X.; Liu, D.; Xu, D.; Asahina, S.; Cychosz, K. A.; Agrawal, K. V.; Al Wahedi, Y.; Bhan, A.; Al Hashimi, S.; Terasaki, O.; et al. Synthesis of Self-Pillared Zeolite Nanosheets by Repetitive Branching. *Science* **2012**, *336* (6089), 1684–1687.

(201) Gulbinski, J.; Ren, L.; Vattipalli, V.; Chen, H.; Delaney, J.; Bai, P.; Dauenhauer, P.; Tsapatsis, M.; Abdelrahman, O. A.; Fan, W. Role of silica support in phosphoric acid catalyzed production of p-xylene from 2,5-dimethylfuran and ethylene. *Ind. Eng. Chem. Res.* **2020**, *59* (51), 22049–22056.

(202) Ipatieff, V.; Corson, B. B.; Egloff, G. Polymerization, a New Source of Gasoline. *Ind. Eng. Chem.* **1935**, *27* (9), 1077–1081.

(203) De Klerk, A.; Engelbrecht, D. J.; Boikanyo, H. Oligomerization of fischer-tropsch olefins: Effect of feed and operating conditions on hydrogenated motor-gasoline quality. *Ind. Eng. Chem. Res.* **2004**, *43* (23), 7449–7455.

(204) De Klerk, A.; Leckel, D. O.; Prinsloo, N. M. Butene oligomerization by phosphoric acid catalysis: Separating the effects of temperature and catalyst hydration on product selectivity. *Ind. Eng. Chem. Res.* **2006**, *45* (18), 6127–6136.

(205) Schwarzer, R.; du Toit, E.; Nicol, W. Solid phosphoric acid catalysts: The effect of free acid composition on selectivity and activity for 1-hexene dimerisation. *Appl. Catal. A Gen.* **2009**, *369* (1–2), 83–89.

(206) Krawietz, T. R.; Lin, P.; Lotterhos, K. E.; Torres, P. D.; Barich, D. H.; Clearfield, A.; Haw, J. F. Solid phosphoric acid catalyst: A multinuclear NMR and theoretical study. *J. Am. Chem. Soc.* **1998**, *120* (33), 8502–8511.

(207) Jain, S. K.; Tabassum, T.; Li, L.; Ren, L.; Fan, W.; Tsapatsis, M.; Caratzoulas, S.; Han, S.; Scott, S. L. P-Site Structural Diversity and Evolution in a Zeosil Catalyst. *J. Am. Chem. Soc.* **2021** 143, 1968-1983.

(208) Prinsloo, N. M. Preparation of a solid phosphoric acid catalyst from low-quality kieselguhr - Parameters controlling catalyst quality and Performance. *Ind. Eng. Chem. Res.* **2007**, *46* (23), 7838–7843.

(209) Ramis, G.; Rossi, P. F.; Busca, G.; Lorenzelli, V.; Ginestra, A. La; Patrono, P.

Phosphoric Acid on Oxide Carriers: 2: Surface Acidity and Reactivity toward Olefins. *Langmuir* **1989**, *5* (4), 917–923.

(210) Cerruti, M.; Morterra, C.; Ugliengo, P. Surface features of P-doped silica: A comparison between IR spectroscopy and theoretical modelling. *J. Mater. Chem.* **2004**, *14* (22), 3364–3369.

(211) Sastre, G.; Lewis, D. W.; Catlow, C. R. A. Structure and stability of silica species in SAPO molecular sieves. *J. Phys. Chem.* **1996**, *100* (16), 6722–6730.

(212) Suib, S. L.; Winiecki, A. M.; Kostapapas, A. Surface Chemical States of Aluminophosphate and Silicoaluminophosphate Molecular Sieves. *Langmuir* **1987**, *3* (4), 483–488.

(213) Xu, D.; Abdelrahman, O.; Ahn, S. H.; Guefrachi, Y.; Kuznetsov, A.; Ren, L.; Hwang, S.; Khaleel, M.; Al Hassan, S.; Liu, D.; et al. A quantitative study of the structure–activity relationship in hierarchical zeolites using liquid-phase reactions. *AIChE J.* **2019**, *65* (3), 1067–1075.

(214) Kresse, G.; Furthmüller, J. Efficient iterative schemes for ab initio total-energy calculations using a plane-wave basis set. *Phys. Rev. B - Condens. Matter Mater. Phys.* **1996**, *54*, 11169–11186.

(215) Perdew, J. P.; Burke, K.; Ernzerhof, M. Generalized Gradient Approximation Made Simple. *Phys. Rev. Lett.* **1996**, *77*, 3865–3868.

(216) Blochl, P. E.; Clemens, J. F.; Johannes Schimpl. The Projector Augmented Wave Method : ab-initio molecular dynamics with full wave functions. *Bull. Mater. Sci.* **2003**, *26*, 33–41.

(217) Kresse, G.; Furthmüller, J. Efficient iterative schemes for ab initio total-energy calculations using a plane-wave basis set. *Phys. Rev. B - Condens. Matter Mater. Phys.* **1996**, 54, 11169–11186.

(218) Grimme, S.; Antony, J.; Ehrlich, S.; Krieg, H.; Grimme, S.; Antony, J.; Ehrlich, S.; Krieg, H. A Consistent and Accurate Ab Initio Parametrization of Density Functional Dispersion Correction (DFT-D) for the 94 Elements H-Pu. *J. Chem. Phys.* **2010**, *132*, 154104-1–29.

(219) Grimme, S.; Ehrlich, S.; Goerigk, L. Effect of the Damping Function in Dispersion Corrected Density Functional Theory. *J. Comput. Chem.* **2011**, *32*, 1456–1465.

(220) Hanwell, M. D.; Curtis, D. E.; Lonie, D. C.; Vandermeersch, T.; Zurek, E.; Hurchison, G. R. Capillary surfaces with free boundary in a wedge. *Adv. Math. (N. Y).* **2014**, *262*, 476–483.

(221) Avogadro: an open-source molecular builder and visualization tool. Version 1.2.0. http://avogadro.cc/.

(222) Brändle, M.; Sauer, J. Acidity differences between inorganic solids induced by their framework structure. A combined quantum mechanics/molecular mechanics ab initio study on zeolites. *J. Am. Chem. Soc.* **1998**, *120*, 1556–1570.

(223) Tranca, D. C.; Zimmerman, P. M.; Gomes, J.; Lambrecht, D.; Keil, F. J.; Head-Gordon, M.; Bell, A. T. Hexane Cracking on ZSM-5 and Faujasite Zeolites: A QM/MM/QCT Study. *J. Phys. Chem. C* **2015**, *119*, 28836–28853.

(224) Zimmerman, P. M.; Tranca, D. C.; Gomes, J.; Lambrecht, D. S.; Head-Gordon, M.; Bell, A. T. Ab initio simulations reveal that reaction dynamics strongly affect product selectivity for the cracking of alkanes over H-MFI. *J. Am. Chem. Soc.* **2012**, *134*, 19468–19476.

(225) Ghorbanpour, A.; Rimer, J. D.; Grabow, L. C. Periodic, vdW-corrected density functional theory investigation of the effect of Al siting in H-ZSM-5 on chemisorption properties and site-specific acidity. *Catal. Commun.* **2014**, *52*, 98–102.

(226) Nimlos, C. T.; Hoffman, A. J.; Hur, Y. G.; Lee, B. J.; Di Iorio, J. R. Hibbitts, D. D.; Gounder, R.; Experimental and theoretical assessments of aluminum proximity in MFI zeolites and its alteration by organic and inorganic structure-directing agents. *Chem. Mater.* **2020**, 32, 21, 9277-9298.

(227) Hernandez-Tamargo, C. E.; Roldan, A.; De Leeuw, N. H. DFT Modeling of the Adsorption of Trimethylphosphine Oxide at the Internal and External Surfaces of Zeolite MFI. *J. Phys. Chem. C* **2016**, *120* (34), 19097–19106.

(228) Kokotailo, G. T.; Lawton, S. L.; Olson, D. H.; Meier, W. M. Structure of synthetic zeolite ZSM-5. *Nature* **1978**, *272* (5652), 437–438.

(229) Hernandez-Tamargo, C. E.; Roldan, A.; De Leeuw, N. H. A density functional theory study of the structure of pure-silica and aluminium-substituted MFI nanosheets. *J. Solid State Chem.* **2016**, *237*, 192–203.

(230) Li, S.; Abdelrahman, O. A.; Kumar, G.; Tsapatsis, M.; Vlachos, D. G.; Caratzoulas, S.; Dauenhauer, P. J. Dehydra-Decyclization of Tetrahydrofuran on H - ZSM5 : Mechanisms , Pathways , and Transition State Entropy. **2019,** 9, 11, 10279–10293.

(231) Gorte, R. J. What do we know about the acidity of solid acids ? *Catal. Letters* **1999**, *62* (1), 1–13.

(232) Parrillo, D. J.; Adamo, A. T.; Kokotailo, G. T.; Gorte, R. J. Amine adsorption in H-ZSM-5. *Appl. Catal.* **1990**, *67* (1), 107–118.

(233) Kofke, T. J. G.; Gorte, R. J.; Farneth, W. E. Stoichiometric adsorption complexes in H-ZSM-5. *J. Catal.* **1988**, *114* (1), 34–45.

(234) Patet, R. E.; Koehle, M.; Lobo, R. F.; Caratzoulas, S.; Vlachos, D. G. General Acid-Type Catalysis in the Dehydrative Aromatization of Furans to Aromatics in H-[Al]-BEA, H-[Fe]-BEA, H-[Ga]-BEA, and H-[B]-BEA Zeolites. *J. Phys. Chem. C* **2017**, *121* (25), 13666–13679.

(235) Chen, H.; Abdelrahman, O. A. Solvating Alkylamine Hofmann Elimination in Zeolites Through Cooperative Adsorption. ChemrXiv Preprint DOI: 10.26434/chemrxiv.14174024.v1.

(236) Malysheva, L. V.; Paukshtis, E. A.; Kotsarenko, N. S. Deamination of butylamines on the surface of acidic oxide catalysts. *React. Kinet. Catal. Lett.* **1984**, *24* (1–2), 91–95.

(237) Malysheva L.V.; Paukshtis, E.A.; Kotsarenko, N.S.; Interaction of butylamines with protonic centers of H-NaY zeolite. *React. Kinet. Catal. Letter*.**1984**, 24, 97–101.

(238) Jones, A. J.; Iglesia, E. Kinetic, Spectroscopic, and Theoretical Assessment of Associative and Dissociative Methanol Dehydration Routes in Zeolites. *Angew. Chemie - Int. Ed.* **2014**, *53* (45), 12177–12181.

(239) Macht, J.; Janik, M. J.; Neurock, M.; Iglesia, E. Mechanistic consequences of composition in acid catalysis by polyoxometalate keggin clusters. *J. Am. Chem. Soc.* **2008**, *130* (31), 10369–10379.

(240) Zhi, Y.; Shi, H.; Mu, L.; Liu, Y.; Mei, D.; Camaioni, D. M.; Lercher, J. A. Dehydration Pathways of 1-Propanol on HZSM-5 in the Presence and Absence of Water. *J. Am. Chem. Soc.* **2015**, *137* (50), 15781–15794.

(241) Prestianni, A.; Cortese, R.; Duca, D. Propan-2-ol dehydration on H-ZSM-5 and H-Y zeolite: A DFT study. *React. Kinet. Mech. Catal.* **2013**, *108* (2), 565–582.

(242) Alsalme, A. M.; Wiper, P. V.; Khimyak, Y. Z.; Kozhevnikova, E. F.; Kozhevnikov, I. V. Solid acid catalysts based on H3PW12O40 heteropoly acid: Acid and catalytic properties at a gas-solid interface. *J. Catal.* **2010**, *276* (1), 181–189.

(243) John, M.; Alexopoulos, K.; Reyniers, M. F.; Marin, G. B. Effect of zeolite confinement on the conversion of 1-butanol to butene isomers: Mechanistic insights from DFT based microkinetic modelling. *Catal. Sci. Technol.* **2017**, *7* (14), 2978–2997.

(244) John, M.; Alexopoulos, K.; Reyniers, M.; Marin, G. B. Reaction path analysis for 1-butanol dehydration in H-ZSM-5 zeolite : Ab initio and microkinetic modeling. *J. Catal.* **2015**, *330*, 28–45.

(245) John, M.; Alexopoulos, K.; Reyniers, M. F.; Marin, G. B. First-Principles Kinetic Study on the Effect of the Zeolite Framework on 1-Butanol Dehydration. *ACS Catal.* **2016**, *6* (7), 4081–4094.

(246) Konda, S. S. M.; Caratzoulas, S.; Vlachos, D. G. Computational Insights into the Role of Metal and Acid Sites in Bifunctional Metal/Zeolite Catalysts: A Case Study of Acetone Hydrogenation to 2-Propanol and Subsequent Dehydration to Propene. *ACS Catal.* **2016**, *6* (1), 123–133.

(247) Liu, Y.; Vjunov, A.; Shi, H.; Eckstein, S.; Camaioni, D. M.; Mei, D.; Baráth, E.; Lercher, J. A. Enhancing the catalytic activity of hydronium ions through constrained environments. *Nat. Commun.* **2017**, *8* (March), 2–9.

(248) Shetty, M.; Wang, H.; Chen, F.; Jaegers, N.; Liu, Y.; Camaioni, D. M.; Gutiérrez, O. Y.; Lercher, J. A. Directing the Rate-Enhancement for Hydronium Ion Catalyzed Dehydration via Organization of Alkanols in Nanoscopic Confinements. *Angew. Chemie* **2021,** 60, 2304 –2311.

(249) Gao, X.; Heyden, A.; Abdelrahman, O. A.; Bond, J. Q. Microkinetic analysis of acetone hydrogenation over Pt/SiO2. *J. Catal.* **2019**, *374*, 183–198.

(250) Abdelrahman, O. A.; Heyden, A.; Bond, J. Q. Microkinetic analysis of C3–C5 ketone hydrogenation over supported Ru catalysts. *J. Catal.* **2017**, *348*, 59–74.

(251) Ensing, B.; Laio, A.; Gervasio, F. L.; Parrinello, M.; Klein, M. L. A minimum free energy reaction path for the E2 reaction between fluoro ethane and a fluoride ion. *J. Am. Chem. Soc.* **2004**, *126* (31), 9492–9493.

(252) Chen, B. W. J.; Mavrikakis, M. How coverage influences thermodynamic and kinetic isotope effects for H2/D2 dissociative adsorption on transition metals. *Catal. Sci. Technol.* **2020**, *10* (3), 671–689.

(253) Zhi, Y.; Shi, H.; Mu, L.; Liu, Y.; Mei, D.; Camaioni, D. M.; Lercher, J. A. Dehydration Pathways of 1-Propanol on HZSM-5 in the Presence and Absence of Water. *J. Am. Chem. Soc.* **2015**, *137* (50), 15781–15794.

(254) Kozuch, S.; Martin, J. M. L. "Turning over" definitions in catalytic cycles. *ACS Catal.* **2012**, *2* (12), 2787–2794.

(255) Gounder, R.; Jones, A. J.; Carr, R. T.; Iglesia, E. Solvation and acid strength effects on catalysis by faujasite zeolites. *J. Catal.* **2012**, *286*, 214–223.

(256) Knaeble, W.; Carr, R. T.; Iglesia, E. Mechanistic interpretation of the effects of acid strength on alkane isomerization turnover rates and selectivity. *J. Catal.* **2014**, *319*, 283–296.

(257) Macht, J.; Carr, R. T.; Iglesia, E. Elimination Catalysis on Solid Acids. *J. Am. Chem. Soc.* **2009**, *131* (2), 6554–6565.

(258) Zhu, Y.; Romain, C.; Williams, C. K. Sustainable polymers from renewable resources. *Nature* **2016**, *540* (7633), 354–362.

(259) Hillmyer, M. A. The promise of plastics from plants. *Science* **2016**, 358, 868−870.

(260) Lundberg, D. J.; Lundberg, D. J.; Hillmyer, M. A.; Dauenhauer, P. J. Techno-economic Analysis of a Chemical Process to Manufacture Methyl-Îμ -caprolactone from Cresols. *ACS Sustain. Chem. Eng.* **2018**, *6* (11), 15316–15324.

(261) Patet, R. E.; Nikbin, N.; Williams, C. L.; Green, S. K.; Chang, C. C.; Fan, W.; Caratzoulas, S.; Dauenhauer, P. J.; Vlachos, D. G. Kinetic Regime Change in the Tandem Dehydrative Aromatization of Furan Diels-Alder Products. *ACS Catal.* **2015**, *5* (4), 2367–2375.

(262) Wijaya, Y. P.; Winoto, H. P.; Park, Y. K.; Suh, D. J.; Lee, H.; Ha, J. M.; Jae, J. Heteropolyacid catalysts for Diels-Alder cycloaddition of 2,5-dimethylfuran and ethylene to renewable p-xylene. *Catal. Today* **2017**, *293–294*, 167–175.

(263) Lundberg, D. J.; Lundberg, D. J.; Zhang, K.; Dauenhauer, P. J. Process Design and Economic Analysis of Renewable Isoprene from Biomass via Mesaconic Acid. *ACS Sustain. Chem. Eng.* **2019**, *7* (5), 5576–5586.

(264) Athaley, A.; Annam, P.; Saha, B.; Ierapetritou, M. Techno-economic and life cycle analysis of different types of hydrolysis process for the production of p-Xylene. *Comput. Chem. Eng.* **2019**, *121*, 685–695.

(265) Langenthal, W. V; Schnetger, J. *Processing of Natural and Synthetic Rubber*; Wiley-VCH, 2005.

(266) Furukawa, S.; Endo, M.; Komatsu, T. Bifunctional catalytic system effective for oxidative dehydrogenation of 1-butene and n -butane using Pd-based intermetallic compounds. *ACS Catal.* **2014**, *4* (10), 3533–3542.

(267) Makshina, E. V.; Dusselier, M.; Janssens, W.; Degrève, J.; Jacobs, P. A.; Sels, B. F. Review of old chemistry and new catalytic advances in the on-purpose synthesis of butadiene. *Chem. Soc. Rev.* **2014**, *43* (22), 7917–7953.

(268) Ho, C. R.; Shylesh, S.; Bell, A. T. Mechanism and Kinetics of Ethanol Coupling to Butanol over Hydroxyapatite. *ACS Catal.* **2016**, *6* (2), 939–948.

(269) Ipatieff, V. To the question of the decomposition of ethyl alcohol due to various catalysts. *J. Russ. Phys. Chem. Soc.* **1903**, *35*, 449–452.

(270) Lebedev, S. V. British Patent GB331,402, **1929**.

(271) Kyriienko, P. I.; Larina, O. V.; Soloviev, S. O.; Orlyk, S. M.; Calers, C.; Dzwigaj, S. Ethanol Conversion into 1,3-Butadiene by the Lebedev Method over MTaSiBEA Zeolites (M = Ag, Cu, Zn). *ACS Sustain. Chem. Eng.* **2017**, *5* (3), 2075–2083.

(272) Sato, S.; Sato, F.; Gotoh, H.; Yamada, Y. Selective dehydration of alkanediols into unsaturated alcohols over rare earth oxide catalysts. *ACS Catal.* **2013**, *3* (4), 721–734.

(273) Fang, L.; Jing, F.; Lu, J.; Hu, B.; Pera-Titus, M. Nano-flowered Ce@MOR hybrids with modulated acid properties for the vapor-phase dehydration of 1,3-butanediol into butadiene. *Green Chem.* **2017**, *19* (19), 4610–4621.

(274) Zeng, F.; Tenn, W. J.; Aki, S. N. V. K.; Xu, J.; Liu, B.; Hohn, K. L. Influence of basicity on 1,3-butadiene formation from catalytic 2,3-butanediol dehydration over γ-alumina. *J. Catal.* **2016**, *344*, 77–89.

(275) Lanzafame, P.; Centi, G.; Perathoner, S. Catalysis for biomass and CO2use through solar energy: Opening new scenarios for a sustainable and low-carbon chemical production. *Chem. Soc. Rev.* **2014**, *43* (22), 7562–7580.

(276) Ji, X. J.; Huang, H.; Ouyang, P. K. Microbial 2,3-butanediol production: A state-of-the-art review. *Biotechnol. Adv.* **2011**, *29* (3), 351–364.

(277) Liu, X.; Fabos, V.; Taylor, S.; Knight, D. W.; Whiston, K.; Hutchings, G. J. One-Step Production of 1,3-Butadiene from 2,3-Butanediol Dehydration. *Chem. - A Eur. J.* **2016**, *22* (35), 12290–12294.

(278) Yim, H.; Haselbeck, R.; Niu, W.; Pujol-Baxley, C.; Burgard, A.; Boldt, J.; Khandurina, J.; Trawick, J. D.; Osterhout, R. E.; Stephen, R.; et al. Metabolic

engineering of Escherichia coli for direct production of 1,4-butanediol. *Nat. Chem. Biol.* **2011**, *7* (7), 445–452.

(279) Chheda, J. N.; Román-Leshkov, Y.; Dumesic, J. A. Production of 5-hydroxymethylfurfural and furfural by dehydration of biomass-derived mono- and poly-saccharides. *Green Chem.* **2007**, *9* (4), 342–350.

(280) Song, D.; Yoon, Y. G.; Lee, C. J. Conceptual design for the recovery of 1,3-Butadiene and methyl ethyl ketone via a 2,3-Butanediol-dehydration process. *Chem. Eng. Res. Des.* **2017**, *123*, 268–276.

(281) Song, D.; Yoon, Y. G.; Lee, C. J. Techno-economic evaluation of the 2,3-butanediol dehydration process using a hydroxyapatite-alumina catalyst. *Korean J. Chem. Eng.* **2018**, *35* (12), 2348–2354.

(282) Chambers, J. M. Extractive distillation. *World Pet. Congr. Proc.* **1951**, *1951-May*, 90–106.

(283) Athaley, A.; Saha, B.; Ierapetritou, M. Biomass-based chemical production using techno-economic and life cycle analysis. *AIChE J.* **2019**, *65* (9), 1-15.

(284) Dutta, S.; De, S.; Saha, B.; Alam, M. I. Advances in conversion of hemicellulosic biomass to furfural and upgrading to biofuels. *Catal. Sci. Technol.* **2012**, *2* (10), 2025–2036.

(285) Cai, C. M.; Zhang, T.; Kumar, R.; Wyman, C. E. Integrated furfural production as a renewable fuel and chemical platform from lignocellulosic biomass. *J. Chem. Technol. Biotechnol.* **2014**, *89* (1), 2–10.

(286) Mettler, M. S.; Paulsen, A. D.; Vlachos, D. G.; Dauenhauer, P. J. Tuning cellulose pyrolysis chemistry: Selective decarbonylation via catalyst-impregnated pyrolysis. *Catal. Sci. Technol.* **2014**, *4* (11), 3822–3825.

(287) Mettler, M. S.; Mushrif, S. H.; Paulsen, A. D.; Javadekar, A. D.; Vlachos, D. G.; Dauenhauer, P. J. Revealing pyrolysis chemistry for biofuels production: Conversion of cellulose to furans and small oxygenates. *Energy Environ. Sci.* **2012**, *5* (1), 5414–5424.

(288) Biddy, M. J.; Scarlata, C.; Kinchin, C. Chemicals from Biomass: A Market Assessment of Bioproducts with Near-Term Potential, NREL Technical Report, NREL/TP-5100-65509; NREL, 2016. Available at: www.nrel.gov/publications (retrieved Dec 15, 2020).

(289) Gürbüz, E. I.; Wettstein, S. G.; Dumesic, J. A. Conversion of hemicellulose to furfural and levulinic acid using biphasic reactors with alkylphenol solvents. *ChemSusChem* **2012**, *5* (2), 383–387.

(290) Alonso, D. M.; Wettstein, S. G.; Mellmer, M. A.; Gurbuz, E. I.; Dumesic, J. A. Integrated conversion of hemicellulose and cellulose from lignocellulosic biomass. *Energy Environ. Sci.* **2013**, *6* (1), 76–80.

(291) Engler, R. E. Green Chemistry. Encyclopedia of Toxicology; Academic Press, **2005**;

pp 471−472.

(292) Paulino-Flores, M.; Martínez-Campos, Á. R.; Martínez-Castañeda, F. E.; López-Orona, C. A.; Vizcarra-Bordi, I.; Munguía, N. Evaluation of the sustainability of hybrid and native maize production systems. *J. Clean. Prod.* **2017**, *150*, 287–293.

(293) Bozell, J. J.; Petersen, G. R. Technology development for the production of biobased products from biorefinery carbohydrates—the US Department of Energy's "Top 10" revisited. *Green Chem.* **2010**, *12* (4), 539.

(294) Furfural Market Expected to Reach $1,434 Million, Globally by 2022 https://www.alliedmarketresearch.com/press-release/furfural-market.html. (Accessed 21 December 2020).

(295) Furfural: A renewable and versatile platform molecule for the synthesis of chemicals and fuels. *Energy Environ. Sci.* **2016**, *9* (4), 1144–1189.

(296) Lee, J.; Kr, D.; Chan, H.; Kr, J.; Koh, J. S. et al. US Patent 9,527,826 B2. **2016**.

(297) Sitthisa, S.; Resasco, D. E. Hydrodeoxygenation of furfural over supported metal catalysts: A comparative study of Cu, Pd and Ni. *Catal. Letters* **2011**, *141* (6), 784–791.

(298) García-Suárez, E. J.; Balu, A. M.; Tristany, M.; García, A. B.; Philippot, K.; Luque, R. Versatile dual hydrogenation-oxidation nanocatalysts for the aqueous transformation of biomass-derived platform molecules. *Green Chem.* **2012**, *14* (5), 1434–1439.

(299) Sitthisa, S.; Pham, T.; Prasomsri, T.; Sooknoi, T.; Mallinson, R. G.; Resasco, D. E. Conversion of furfural and 2-methylpentanal on Pd/SiO2 and Pd-Cu/SiO2 catalysts. *J. Catal.* **2011**, *280* (1), 17–27.

(300) Zhang, W.; Zhu, Y.; Niu, S.; Li, Y. A study of furfural decarbonylation on K-doped Pd/Al2O 3 catalysts. *J. Mol. Catal. A Chem.* **2011**, *335* (1–2), 71–81.

(301) Jung, K. J.; Gaset, A.; Molinier, J. Furfural decarbonylation catalyzed by charcoal supported palladium: Part II — A continuous process. *Biomass* **1988**, *16*, 89–96.

(302) Li, K.; Ozer, R. Vapor-Phase Decarbonylation Process. US Patent 8,404,871B2, **2013.**

(303) Wambach, L.; Irgang, M.; Fischer, M.; Raymond, P. E. L. Preparation of Furan by Decarbonylation of Furfural. US Patent 4,780,552, **1988**.

(304) An, K.; Musselwhite, N.; Kennedy, G.; Pushkarev, V. V.; Robert Baker, L.; Somorjai, G. A. Preparation of mesoporous oxides and their support effects on Pt nanoparticle catalysts in catalytic hydrogenation of furfural. *J. Colloid Interface Sci.* **2013**, *392* (1), 122–128.

(305) Smith, H. A.; Fuzek, J. F. Catalytic Hydrogenation of Furan and Substituted Furans on Platinum. *J Am. Chem. Soc.* **1949**, 71, 415−419.

(306) Mironenko, A. V.; Gilkey, M. J.; Panagiotopoulou, P.; Facas, G.; Vlachos, D. G.;

Xu, B. Ring activation of furanic compounds on ruthenium-based catalysts. *J. Phys. Chem. C* **2015**, *119* (11), 6075–6085.

(307) Godawa, C.; Rigal, L.; Gaset, A. Palladium catalyzed hydrogenation of furan: optimization of production conditions for tetrahydrofuran. *Resour. Conserv. Recycl.* **1990**, *3* (4), 201–216.

(308) Heisig, G. B. 1,4-Diiodobutane from Tetrahydrofuran. J. Am. Chem. Soc. 1939, 61, 525−526.

(309) Feb, P. United states patent office 2,310,383. **1943**, No. 2, 2–3.

(310) Li, S.; Abdelrahman, O. A.; Kumar, G.; Tsapatsis, M.; Vlachos, D.; Caratzoulas, S.; Dauenhauer, P. J. Dehydra-Decyclization of Tetrahydrofuran on H-ZSM5: Mechanisms, Pathways, and Role of Transition State Entropy. *ACS Catal.* **2019**, 9, 10279−10293.

(311) Butadiene – C4s prices, markets & analysis https://www.icis.com/explore/commodities/chemicals/butadiene-c4s/. (Accessed 20 Jan 2021)

(312) Global pressure pulls down US butadiene https://www.icis.com/explore/resources/news/2018/11/01/10276397/global-pressure-pulls-down-us-butadiene/.(Accessed 20 Jan 2021)

(313) C5 and hydrocarbon resins prices, forecasts, and analysis https://www.argusmedia.com/en/petrochemicals/argus-c-5-and-hydrocarbon-resins-services.(Accessed 21 Jan 2021)

(314) Goulas, K. A.; Mironenko, A. V; Jenness, G. R.; Mazal, T.; Vlachos, D. G. Fundamentals of C–O bond activation on metal oxide catalysts. *Nat. Catal.* **2019** (2), 269-276.

(315) Xu, Y. Decomposition of furan on Pd(111). *Top. Catal.* **2012**, *55* (5–6), 290–299.

Appendix

A1 Introduction

The following appendices provide detailed synthesis procedures, materials characterization, experimental methods, raw experimental data, and more detailed explanations to supplement the discussions in Chapters 2-6. They are ordered in correspondence to the preceding and reference previous chapters, as necessary.

A2 Mechanisms and pathways of THF dehydra-decyclization on H-ZSM-5

A2.1 Methods to correct for deactivation

A first order deactivation model (S1) was fitted to the experimentally observed rates and extrapolated to t=0 to estimate initial rates.

$$\frac{dr_i}{dt} = -kr_i; \text{ BCs: } r_i(t=0) = r_{i,o} \; and \; r_i(t \to \infty) = 0 \quad \text{(A2.1)}$$

$$r_i(t) = r_{i,0} \; exp^{-kt} \; [=][\text{mol product } i/g \; catalyst/\text{h}]$$

where $r_{i,0}$ is the initial rate of formation of product i (mol/g catalyst/h), and k is the deactivation rate constant (h^{-1}). This method ensured the estimation of rates under conditions where the catalyst existed in a relatively well-characterized state. The temporal resolution required to regress decay parameters was achieved by online GC injection through a six-port gas sampling valve (Vici Valco) periodically every 18 minutes. At least 8 injections were used to fit the experimental data with the first order deactivation profile to extract initial rates and deactivation rate constants.

A2.2 Additional computational and experimental results

Table A2.1 *Degree of rate control (X_{RC}) and selectivity control (X_{SC}) for each elementary reaction. Sensitivity analysis was done at 250 °C, 10 torr partial pressure of THF and WHSV of 1.83 g THF/ g cat/hr; 0.8% THF conversion is achieved at this condition.*

	X_{RC} butadiene formation	X_{RC} propene formation	X_{SC} butadiene formation
TS1	0.96	0.20	0.44
TS2	0.17	-0.10	0.15
TS3	0.00	0.00	0.00
TS4	0.00	0.00	0.00
TS5	0.00	0.00	0.00
TS6	0.00	0.00	0.00
TS7	0.00	0.00	0.00
TS8	0.00	0.00	0.00
TS9	0.10	-0.06	0.10
TS10	0.00	0.00	0.00
TS11	0.00	0.79	-0.46
TS12	-0.22	0.16	-0.22
TS13	-0.01	0.01	-0.01
TS14	0.00	0.00	0.00
TS15	0.00	0.00	0.00

Table A2.2 *Packed bed reactor summary of dehydration and Retro-Prins product distribution of 2-buten-1-ol (2BOL) and 3-buten-1-ol (3BOL).*

Feed	T(°C)	P_{THF} (torr)	WHSV (g feed/g cat/h)	Conversion (%)	Selectivity (%C basis)	
					Butadiene	Propene
2BOL	100	10.5	2.99	10.2	14.9	0
2BOL	110	10.5	2.99	14.60	15.05	0
2BOL	120	10.5	6.74	23.50	15.09	0
2BOL	130	10.5	6.36	24.40	21.75	0
2BOL	140	10.5	6.61	25.20	41.50	0
3BOL	100	10.5	3.25	0.30	2.70	7.43
3BOL	110	10.5	3.25	0.61	3.30	8.38
3BOL	120	10.5	3.01	0.99	8.10	14.71
3BOL	130	10.5	3.29	2.22	9.01	13.80
3BOL	140	10.5	3.01	6.28	13.70	16.73

Table A2.3 *Packed bed reactor summary of dehydration and Retro-Prins product distribution of 2-penten-1-ol (2POL), 3-penten-1-ol (3POL), 4-penten-1-ol (4POL) and 4-penten-2-ol (4P2OL) with fixed partial pressure of 10.5 torr*

Feed	T(°C)	WHSV (g feed/g cat/h)	Conversion (%)	Selectivity (%C basis) *		
				(1,3+1,4) PD^i + Isoprene	Butenes	Propene
4P2OL	150	3.8	10.1	15.7	0.79	20.17
4P2OL	140	4.1	7.56	7.25	0.40	12.18
4P2OL	130	3.98	6.3	9.34	0.64	32.19
4P2OL	120	3.98	5.98	12.44	0.32	18.91
4P2OL	110	3.88	5.27	4.1	0.28	12.93
4POL	140	3.62	9.51	2	0.38	0.00
4POL	130	3.88	9.3	1.2	0.14	0.00
4POL	150	3.75	10.5	2.05	0.40	0.00
4POL	120	3.75	6.67	1.04	0.42	0.00
4POL	110	3.73	5.1	1.3	0.54	0.00
3POL	130	3.71	9.74	11.4	0.52	0.00
3POL	120	3.71	10.4	29.4	1.46	0.00
3POL	100	3.7	4.47	23.4	1.11	0.00
3POL	140	3.61	10.2	18.7	0.82	0.00
3POL	150	3.61	10.4	15.2	0.74	0.00
2POL	140	3.82	24.2	58.4	0	0.00
2POL	130	3.82	22.9	61.5	0	0.00
2POL	120	3.82	24.7	45.5	0	0.00
2POL	110	3.72	18.3	60.1	0	0.00
2POL	100	3.72	12.5	58.5	0	0.00

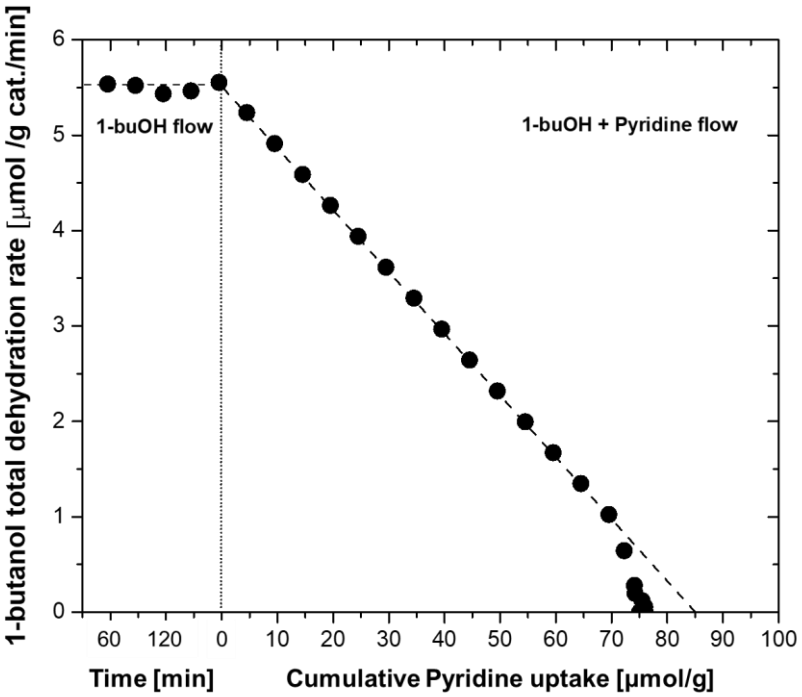

Figure A2.1 *1-butanol dehydration rates normalized by the mass of catalyst at 403 K as a function of cumulative pyridine uptake (Reaction conditions: 10.5 torr 1-butanol, 0.015 torr Pyridine (molar ratio of 1-butanol: Pyridine ~705). Dashed line indicates the linear regression fit to experimental data, which is extrapolated to the x-axis to calculate the number of Bronsted acid sites.*

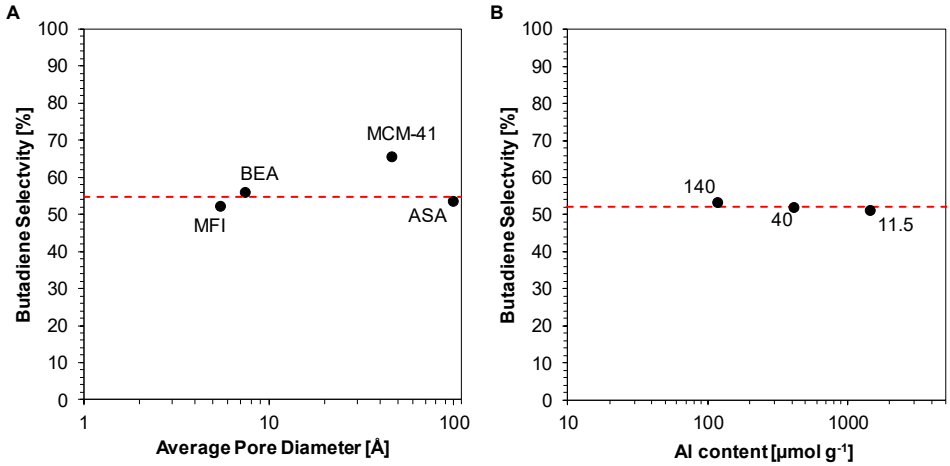

Figure A2.2 ***(A)*** *Butadiene selectivity as a function of average pore diameters for different aluminosilicates (microporous MFI and BEA (Zeolyst), mesoporous MCM-41 (Sigma Aldrich), and macroporous amorphous silica-alumina (grade 135, Sigma Aldrich))* ***(B)*** *Butadiene selectivity as a function of aluminum content over three different ZSM-5 catalysts (Zeolyst) (Reaction conditions: T= 503 K, WHSVs in the range of 1.8-17.9 g THF/g cat./h, and* P_{THF} *= 10 torr)*

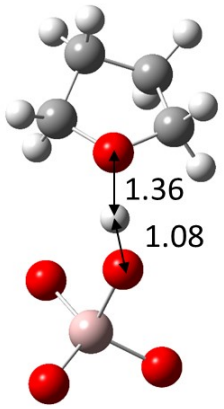

Figure A2.3 *Binding geometry of THF to H-ZSM5. Only the THF molecule and the active sites are shown. Indicated bond distances in Å. Color code: pink, Al; red, O; gray, Si; and white, H.*

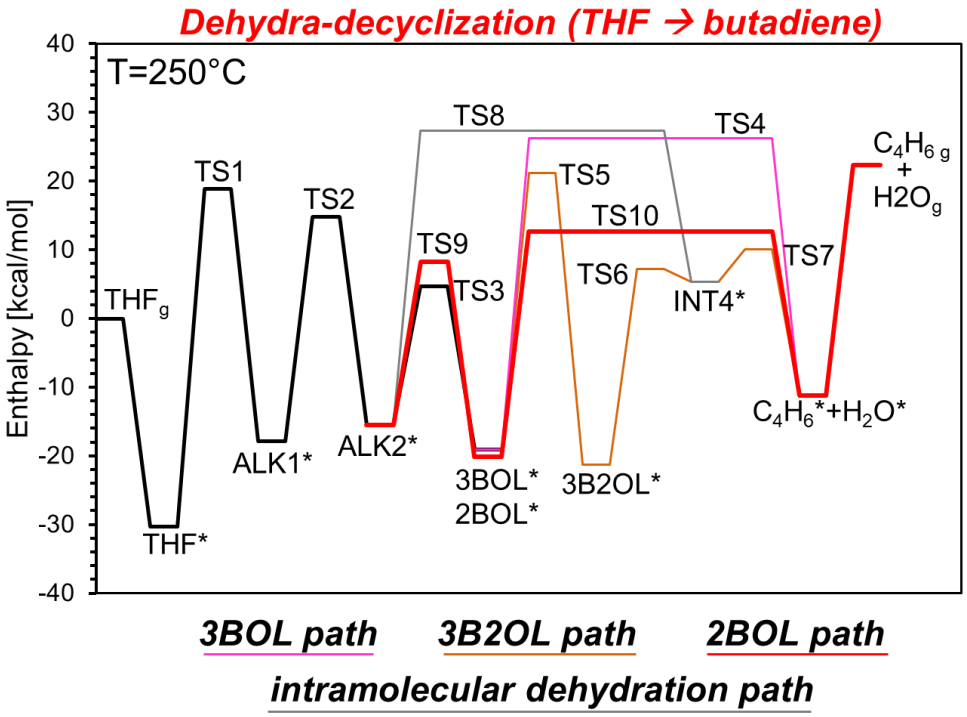

Figure A2.4 *Enthalpy profile of THF dehydra-decyclization to butadiene (C_4H_6) and water in H-ZSM5. Subscript 'g' indicates gas-phase species, and '*' marks surface species.*

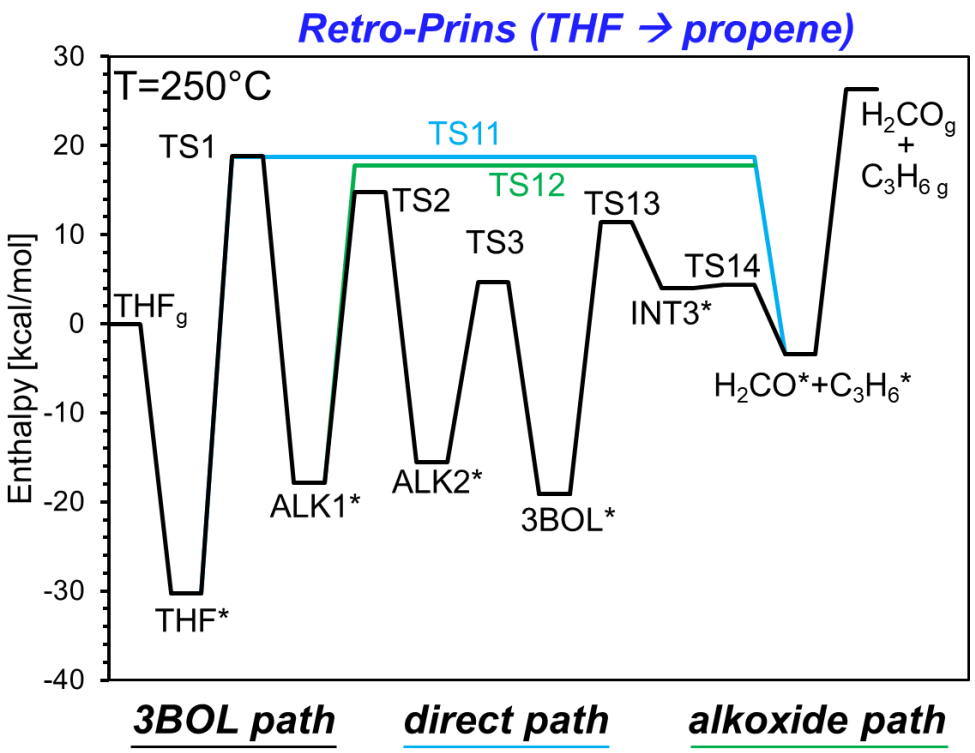

Figure A2.5 *Enthalpy profile of the retro-Prins fragmentation of THF to propene (C_3H_6) and formaldehyde (H_2CO) in H-ZSM5. Subscript 'g' indicates gas-phase species, '*' marks surface species*

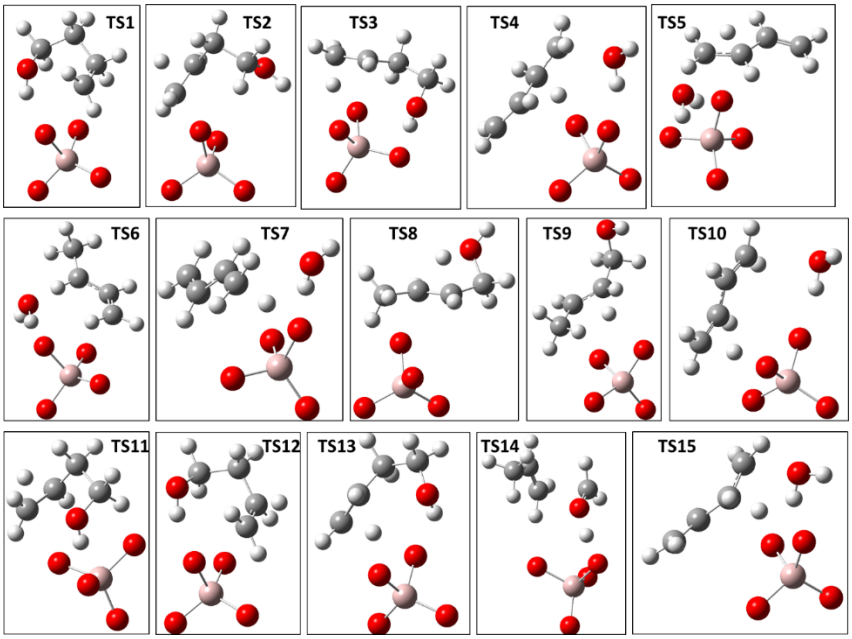

Figure A2.6 *Transition state structures for all fifteen elementary reactions proposed in the reaction network.*

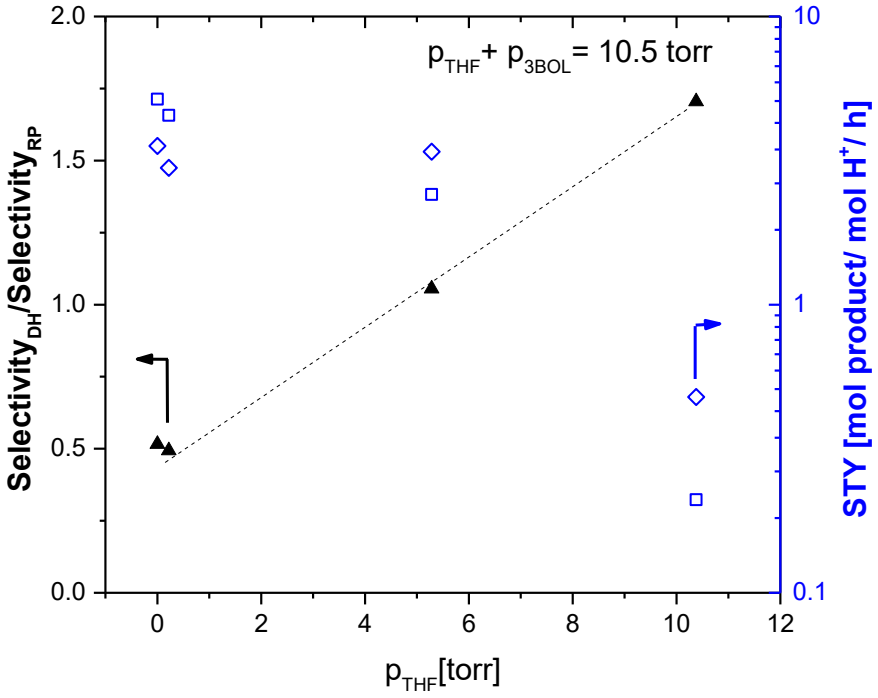

Figure A2.7 *The variation of the rate of dehydration and Retro-Prins condensation of 3-BOL as a function of the cofed THF partial pressure at 413 K. (□) represents the STYs yield for propene, and (◇) represents the STYs for butadiene. The reported rates and selectivity ratios are initial values (t=0). The dashed line is drawn to aid the eye.*

A3 Adapted Gas Chromatograph for Automated Catalytic Evaluation for Vapor-Phase Flow Chemistries

A3.1 Instrumentation of the micro-flow reactor setup

A3.1.1 Step-by step procedure for hardware modifications

i) All major part names and numbers of hardware to be added to an existing GC is included in **Table A3.1**. Smaller parts like Valco and Swagelok fittings will also need to be bought (not included in **Table A3.1**). Once all parts are available, proceed to the next step.

ii) If the GC comes with an installed front inlet, uninstall it, and re-install it as Auxiliary heater (Aux Temp 3).* Since this inlet is going to be used to house the reactor, this modification will allow for dosing more than one gas stream to the reactor bed by using different Aux EPC channels; installing it as front inlet does not allow this flexibility. Install and configure the back-inlet if the GC does not have it pre-installed.

iii) Uninstall and the ALS and use a capping nut to cap-off the front inlet (See **Figure A3.1**). Install the heated valve box kit.* If using an online detector like TCD, configure and install it.* Note that the TCD will come with its own pressure control module for supplying gases required for its operation (See **Figure A3.4**).

iv) Plug-in and configure the Auxiliary EPC* allowing for three separate channels for dosing gas streams. Aux EPC is going to be used to route gas flows to the reactor (See **Figure A3.4** and the next steps listed here). If using a QCD (POLYARC), install it as Auxiliary heater (Aux Temp 2). The instructions to do this can be found on Activated Research company's POLYARC manual here: (http://www.activatedresearch.com/Public_Documents/Polyarc%20Installation%20Manual.pdf). It is important to note that if using an online detector in addition to the FID, POLYARC will be installed on the MS opening located on the left side of the GC. If not using an online detector, it can be mounted vertically into either front or back detector opening.

This completes all the electronic configurations of additional hardware required.

Note: *The directions to implement * steps can be found in Agilent 7890 Operation manual available free of charge on Agilent's website:* https://www.agilent.com/cs/library/usermanuals/Public/7890B_Operation.pdf

Following steps illustrate the process tubing routing and other non-electronic modifications.

v) Mount the two six-port valves as shown in **Figure A3.1**.

vi) Follow **Figure A3.4** to use an upstream referenced mass-flow controller (Valco model 100) , and 1/16" tubing to route the gas flow from EPC channels 1, and 2 through valve V-2 (**Scheme 3.2** in main text) such that it allows either Helium or Air to be dosed to the reactor. Use another upstream referenced MFC (Valco model 100) for EPC channel 3 to dose small amount of diluent gas to avoid backflush related issues in tubing labeled T1 in **Figure A3.4**. A pressure gauge can be installed upstream of the reactor (either on the channel 3 like we have done, or downstream from the union of channels 1 and 2 in **Figure A3.4**).

vii) Similarly, follow **Figure A3.4** to route helium flow to the back-inlet through its own EPC via valve V-1 (**Scheme 3.2** in the main text). This inlet should then be connected to the GC column. The column is connected to the QCD (POLYARC), while the outlet of POLYARC is connected to FID **(as shown in Figure A3.3).** In short, use **Figure A3.4** as a guide to ensure the correct implementation of supply of gases to both the reactor (front) and the chromatography (back) part of the setup.

viii) Make other process tubing connections by following **Scheme 3.2** in the main text, and **Figures A3.1** and **Figure A3.3** here. When making the connections, ensure that the rotors of both 6-port-valves are in identical position (See **Figure A3.1** for illustration). After completing this step, leak test all individual lines after switching on the gas supply. Ensure that the system is leak-free before proceeding to next steps. Note that the connection from the reactor to the valve V-2 (**Scheme 3.2** in main text) requires an 1/16" inlet adapter nut, and that the vaporizer is just a ¼" tubing filled with a dispersant (as noted in the main text) which tees into the liquid flow from the syringe pump. We encountered problems of

unstable online signal without filling the vaporizer with quartz chips, and recommend using them to allow for effective vaporization.

ix) Use glass-wool insulation to completely insulate process tubing inside the valve box before closing it. During this process, ensure that the actuators sit exactly over the valves (details on how to do this can be found on Agilent's actuator kit manual: https://www.agilent.com/cs/library/usermanuals/Public/G2745-90107.pdf

x) As shown in **Scheme 3.2** in main text, under all configurations, the gas-flows exiting the reactor outlet necessarily exit the setup through the outlet of the TCD (if the online detector is not used, the exit process tubing will be directly from one of the outlets of valve V-1). In either case, it is possible to calibrate the metered gas flowrate (downstream of the MFCs) measured at reactor exit as a function of GC-set EPC pressure for the different EPC channels separately. Important note in doing this step is to ensure that all other flows except the specific channel being calibrated should be switched off. For example, in our case, when calibrating EPC 1 pressure with diluent gas flowrate, we ensured EPC 2 and EPC 3 were off. Additionally, since our measurements were on the outlet of TCD, all TCD flows (reference and make-up) were also switched off. Given the gas delivery mode **(Figure A3.4)**, EPC 1 and EPC 2 will have identical calibration curve as gas flows are metered using a single MFC. Once EPC 1 is calibrated, switch it off and repeat this procedure to calibrate EPC 3 following the same procedure.

This completes the hardware modifications to an existing GC to convert it to the reported micro-flow reactor.

A3.1.2 Step-by step procedure for software modifications. Using an example case, we now illustrate the method development on ChemStation which leads to the control of all major process parameters directly from the GC. This specific example is method development under configuration 2/3 in **Scheme 3.2**, and we highlight how the method can be modified to operate the setup in bypass-mode (Configuration-1).

i) Check that all configured hardware components show up in the online mode of ChemStation (Aux EPC channel 1/2/3, Aux Temp 2,3, valve box, TCD, FID, Back inlet, valves). If they do not, go back to hardware modification guide to correctly install and

configure all additional hardware. If all these show up on the online mode of ChemStation, it is straightforward to add them in the configurations window during method development (see **Figure A3.5**). Importantly, note that valve V-1 is to be configured as gas-sampling valve and valve V-2 as switching valve (**Figure A3.5 B**). For the gas sampling valve, it is possible to change the injection period, which will determine total amount of reactor effluent that gets injected. Depending on the split ratios for the back inlet as well as injection times, ensure that enough reactor effluent is being sampled for accurate quantification.

ii) Provided that the valves are correctly configured, the injection source can be set to the gas sampling valve when making a new method **(Figure A3.6 A).** Note that ALS does not show up as it has been uninstalled and unplugged **(Figure A3.6 B**). Since V-1 is installed as a gas-sampling valve, it switches (for a duration corresponding to the inject time), and then returns to its original position. This happens regardless of whether we operate in reactor mode or bypass mode. In bypass mode, this injection from sampling valve enables quantification of total carbon fed (for carbon balance calculations later), while in reactor mode, this injection allows for the quantification of products of reaction (**Scheme 3.2** in the main text).

iii) The control over these modes (Bypass vs. reactor) is decided simply by the switching valve. If the switching valve is ON as in **Figure A3.6 C**, it means that the feed contacts the reactor (the scenario where the reactor is downstream from the vaporizing section as described in the main text). In short, if the switching valve in ON (the tick box is checked), the setup operates in reactor mode. For creating methods involving operation in bypass mode, one can simply uncheck this box such that the reactor then switches to being upstream of the vaporizer such that the vaporized feed goes directly to the online detector (**Scheme 3.2** in the main text).

iv) As shown in **Figure A3.6 D**, back inlet is used for chromatography, and inlet parameters can be tuned from this window.

v) In the columns window tab (**Figure A3.6 E-G**), the EPC channel pressures can be input. Depending on the diluent gas flowrate required through the reactor which has already been calibrated previously with the EPC pressure set-points, enter appropriate values

corresponding to the gas flowrates required. Important point to note is that the total flow through the reactor will be the sum of flowrates through EPC 1 and EPC 3. The flowrate of the liquid feed along with the gas flowrates dictate the partial pressure of the feed in the reactor.

vi) **Figure A3.6 H-J** are routine steps for setting oven ramps and operation of detectors. It is important to note that there is a part of tubing from the reactor outlet to valve V-2 which goes through the oven, and another tubing connecting one of the outlets of V-1 to the TCD. Except these two, all other tubings are contained within the heated valve box. If high partial pressure of relatively heavy compounds is being used, we caution against starting the oven temperature from ambient to avoid condensation of any products of the reaction in these two tubings being routed through the oven. Separate calculations involving the comparison of vapor pressure of the liquid with partial pressure must be carried out to determine the minimum temperature to avoid any condensation of species.

vii) Since QCD (POLYARC) is installed as Aux Temp 2, it's temperature can be changed from the Aux Heaters window **(Figure A3.6 K).** More importantly, the reactor temperature can be controlled by changing the Thermal Aux 3 temperature in this window **(Figure A3.6 K).** One can decide the parameters required for the method to start in the readiness window **(Figure A3.6 L).**

Once a host of different methods are created (e.g., with different reaction temperatures, different diluent flowrates, bypass vs. reactor mode), they can be loaded into a sequence table on ChemStation. Once the catalyst bed is loaded **(Figure A3.2)**, sequence table is initiated, and feed is switched on (not coupled to the GC, and has to be done separately), the setup can operate without manual intervention.

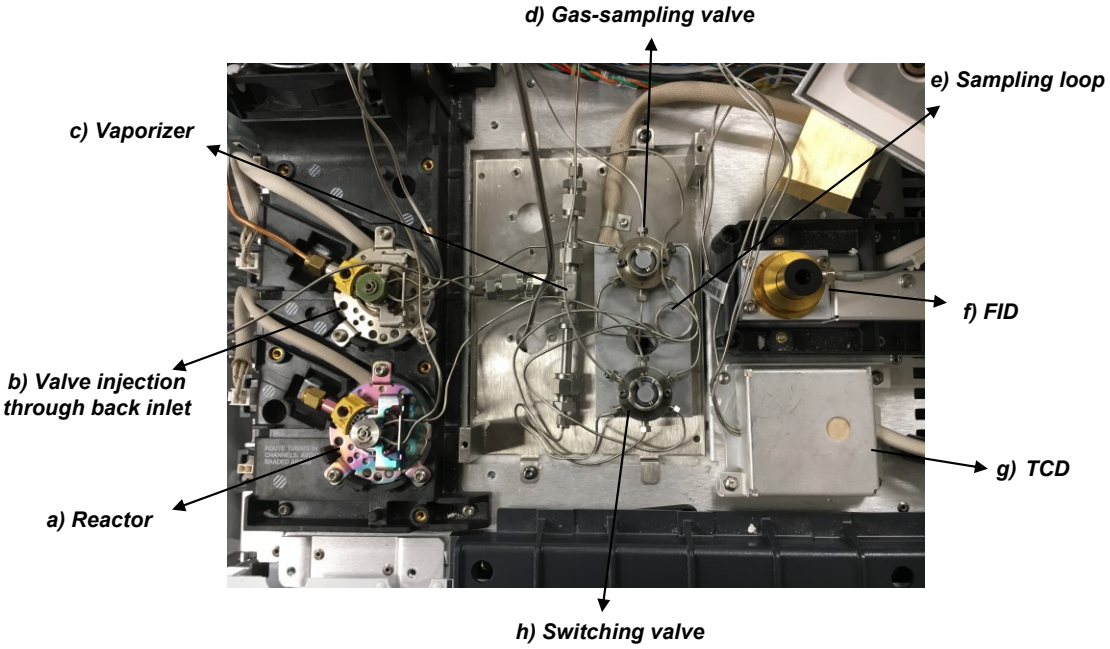

Figure A3.1 *Top view of the setup to illustrate the major components including (a) Reactor - front inlet was used for placing the packed bed and acted as the reactor vessel, (b) Back inlet was connected to the column and FID, and as such, was used for chromatography of the reactor effluent purging the sampling loop. Both the inlets were insulated using fiberglass insulation during operation, (c) Vaporizer provided dispersant surface to vaporize liquid feeds, (d) Gas sampling valve injected the contents of the sampling loop periodically into the back inlet, (e) Sampling loop, (f) FID, (g) TCD was installed as an online detector, (h) Switching valve configuration was used to operate the setup in bypass or reactor mode of operation.*

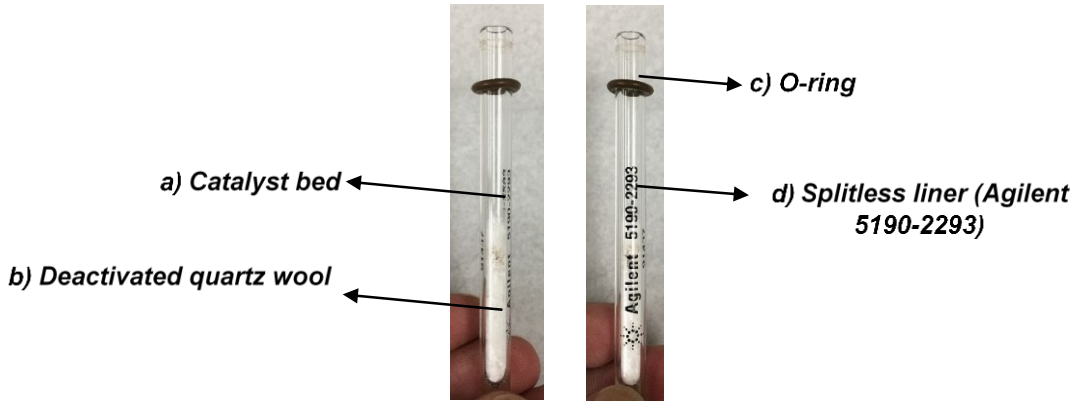

Figure A3.2 *(left) Illustrative picture of the reactor bed (a) packed between layers of deactivated quartz wool (b) (Catalyst HZSM-5 with Si/Al 140 in 500-1000 µm aggregates; (right) Illustrative picture of the inlet liner and the corresponding part number (d) with the O-ring (c)*

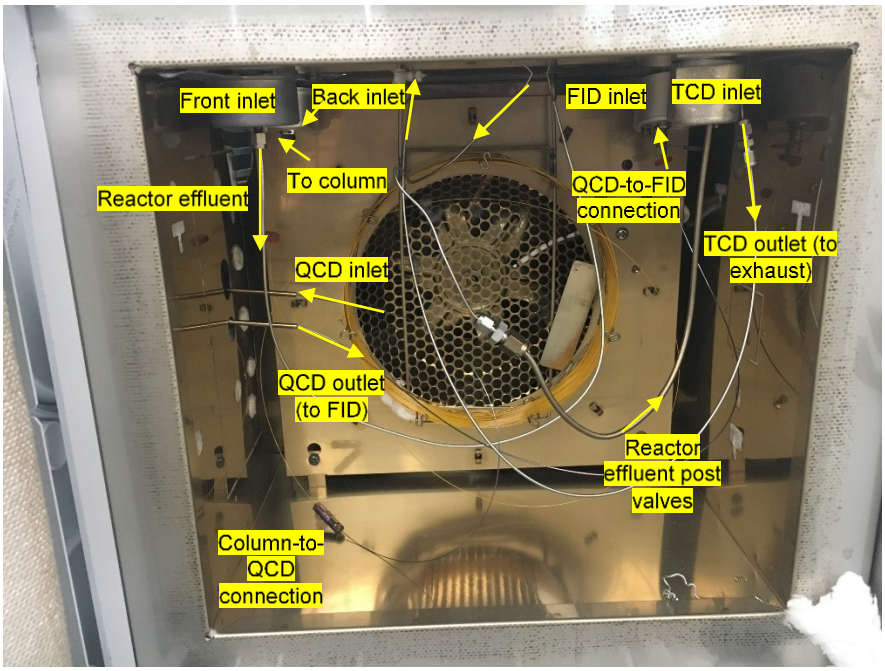

Figure A3.3 *Illustrative picture of the automated microflow reactor setup with all the connections and the process tubing marked.*

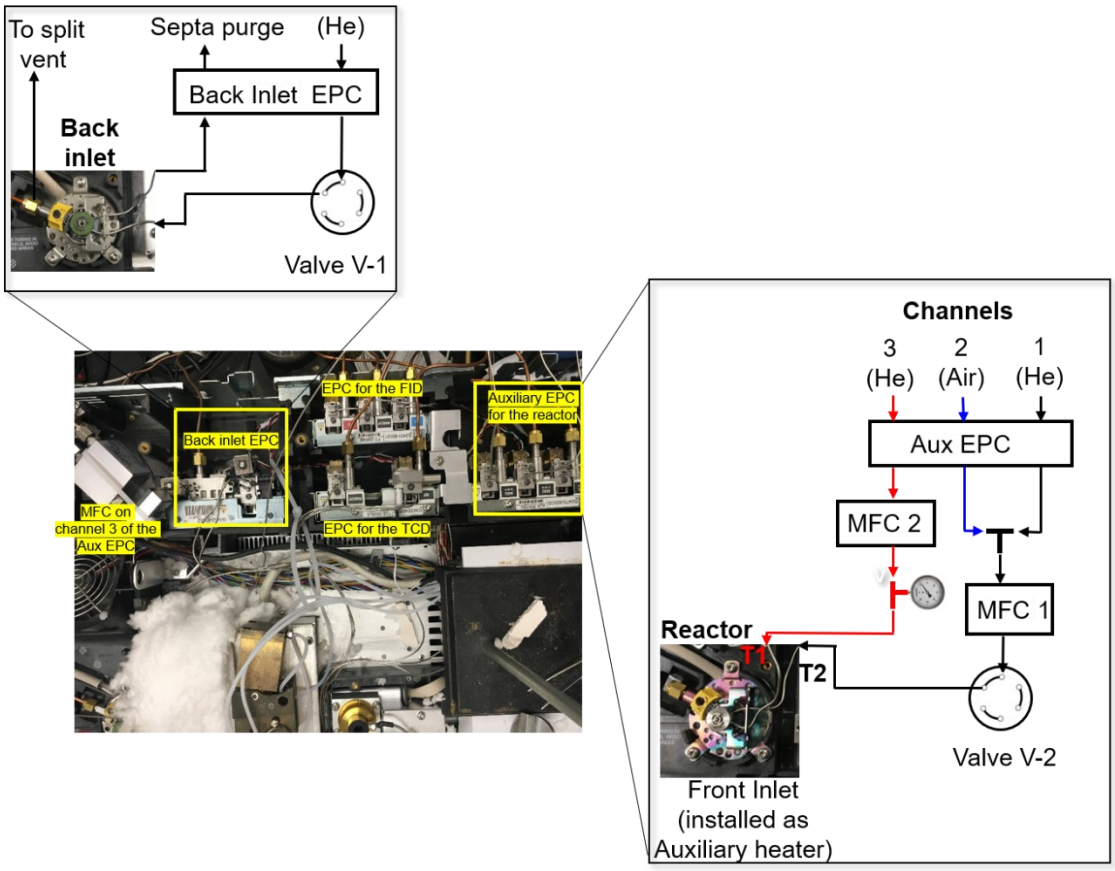

Figure A3.4 *Illustrative picture of all the pressure control modules installed on the microflow reactor setup. EPCs for different instrument parts are identified in the picture. The inset on the right shows the gas delivery mechanism to the reactor. Three channels from the auxiliary EPC were used to dose either helium (channels 1, and 3) or air (channel 2). While the required helium flows can be supplied through one channel alone (through tubing T2), it would require plugging off tubing (marked as T1) which can potentially cause backflush of compounds from the reactor. To avoid this, channel 3 was used to dose small helium flows (2-3 sccm) in conjunction with channel 1. Installing the reactor housing as a front inlet does not allow dosing multiple gases; therefore, the front inlet was installed as an auxiliary heater. The inset on the top shows the gas delivery to the back inlet employed for reactor effluent quantification.*

Table A3.1 *List of parts required to convert a typical Gas Chromatograph into a microflow reactor setup*.*

Item	Manufacturer	Part number	Description
Gas Chromatograph	Agilent	7890	Gas chromatograph equipped with two split/splitless inlets, and an FID detector
Deactivated quartz wool	Restek	24324	
GC-Column	Agilent	19091P-Q04	HP-PLOT/Q column, 30 m long, 0.32 mm ID, 20 um film
Inlet Adapter	Restek	27184	1/16” capillary inlet adapter fitting
Heated Valve Box kit	Agilent	G1581A	Heated valve enclosure, containing two pneumatic actuators
6 port valve x (2)	Vici Valco	DC6UWE	1/16”, 0.70 mm bore 6 port valve, medium temperature
Auxiliary EPC	Agilent	G3452-60509	Split/Splitless EPC module, 0 psi - 150 psi, used with series 7890 gas chromatography systems
Mass flow controller	Vici Valco	Model 100	Upstream-referenced gas flow controllers
Splitless inlet liner	Agilent	5190-2293	Quartz, splitless liner
Pressure gauge	McMaster	4089K61	Pressure gauge, single scale with bottom connection
Syring pump	Cole Parmer	74905-04	Cole-Parmer Syringe Pump, Infuse / Withdraw Programmable, Touchscreen Control
Sampling loop	Vici Valco	SL1KCW	stainless steel 1/16” sampling loop

*****The optional parts including an online detector and a quantitative carbon detector are not included. Additionally, the part numbers of process tubing and fittings are not listed for brevity**.**

A.

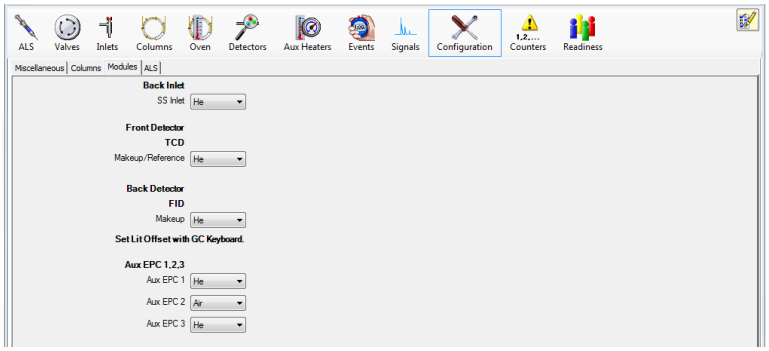

B.

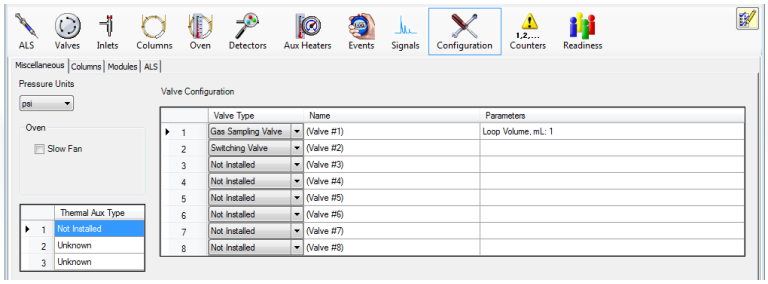

C.

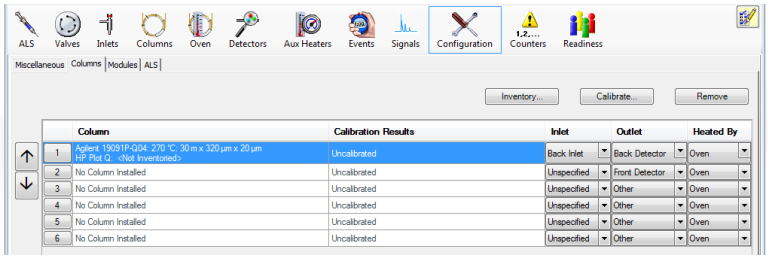

Figure A3.5 *Configuration of all the added hardware parts required for method development and control of reaction parameters directly from ChemStation method files (Steps for method development included in* ***Section A3.1.2)***

A.

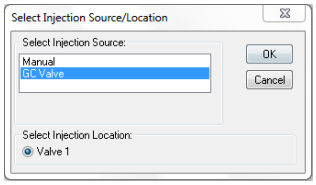
Select Injection Source/Location
Select Injection Source:
Manual
GC Valve
OK
Cancel
Select Injection Location:
Valve 1

B.

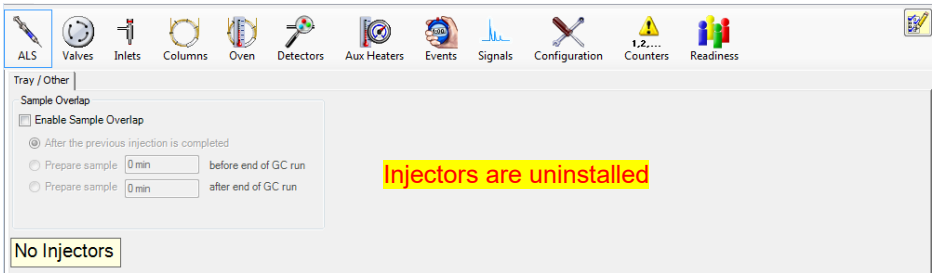
ALS
Valves
Inlets
Columns
Oven
Detectors
Aux Heaters
Events
Signals
Configuration
Counters
Readiness
Tray / Other
Sample Overlap
Enable Sample Overlap
After the previous injection is completed
Prepare sample 0 min before end of GC run
Prepare sample 0 min after end of GC run
Injectors are uninstalled
No Injectors

C.

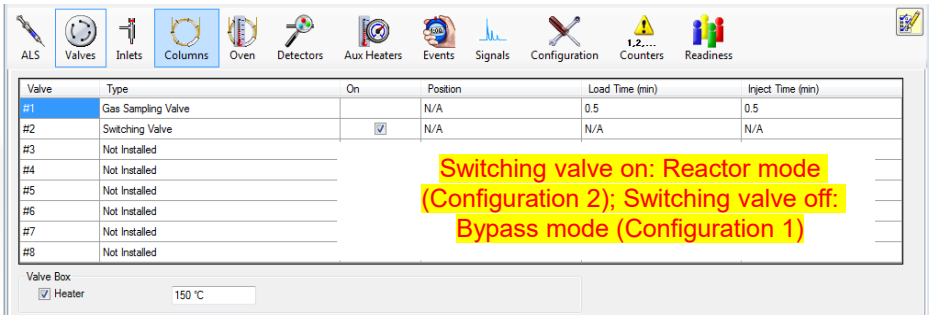
ALS
Valves
Inlets
Columns
Oven
Detectors
Aux Heaters
Events
Signals
Configuration
Counters
Readiness
Valve | Type | On | Position | Load Time (min) | Inject Time (min)
#1 | Gas Sampling Valve | | N/A | 0.5 | 0.5
#2 | Switching Valve | ☑ | N/A | N/A | N/A
#3 | Not Installed
#4 | Not Installed
#5 | Not Installed
#6 | Not Installed
#7 | Not Installed
#8 | Not Installed
Switching valve on: Reactor mode (Configuration 2); Switching valve off: Bypass mode (Configuration 1)
Valve Box
Heater 150 °C

D.

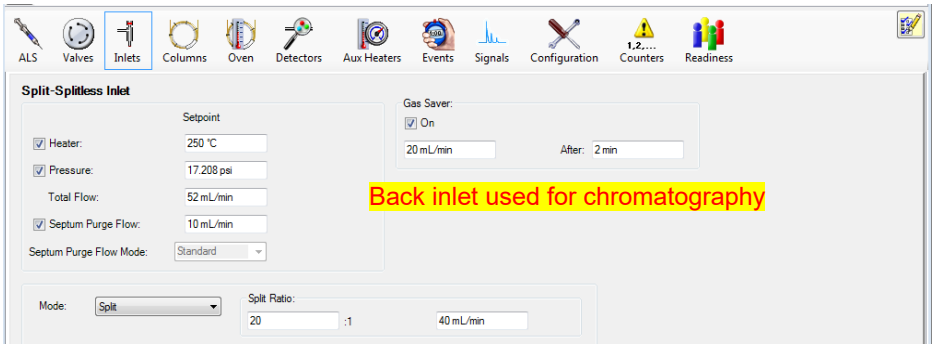
ALS
Valves
Inlets
Columns
Oven
Detectors
Aux Heaters
Events
Signals
Configuration
Counters
Readiness
Split-Splitless Inlet
Setpoint
Heater: 250 °C
Pressure: 17.208 psi
Total Flow: 52 mL/min
Septum Purge Flow: 10 mL/min
Septum Purge Flow Mode: Standard
Gas Saver:
On
20 mL/min
After: 2 min
Back inlet used for chromatography
Mode: Split
Split Ratio: 20 :1 40 mL/min

E.

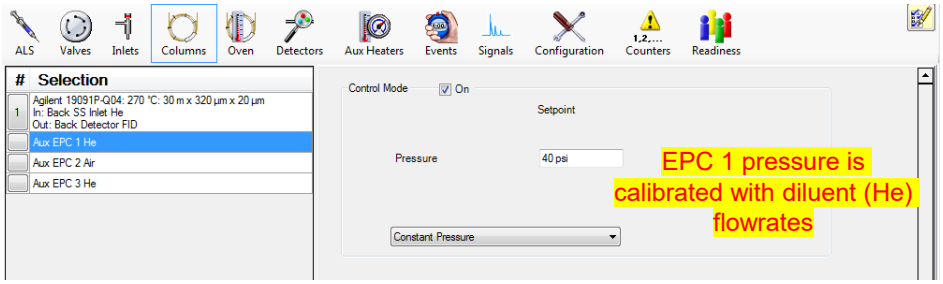
ALS
Valves
Inlets
Columns
Oven
Detectors
Aux Heaters
Events
Signals
Configuration
Counters
Readiness
Selection
1 Agilent 19091P-Q04: 270 °C: 30 m x 320 µm x 20 µm
In: Back SS Inlet He
Out: Back Detector FID
Aux EPC 1 He
Aux EPC 2 Air
Aux EPC 3 He
Control Mode On
Setpoint
Pressure 40 psi
Constant Pressure
EPC 1 pressure is calibrated with diluent (He) flowrates

F.

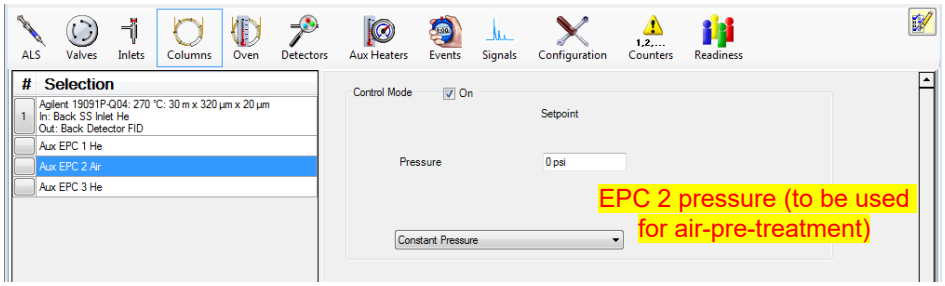
ALS
Valves
Inlets
Columns
Oven
Detectors
Aux Heaters
Events
Signals
Configuration
Counters
Readiness
Selection
1 Agilent 19091P-Q04: 270 °C: 30 m x 320 µm x 20 µm
In: Back SS Inlet He
Out: Back Detector FID
Aux EPC 1 He
Aux EPC 2 Air
Aux EPC 3 He
Control Mode On
Setpoint
Pressure 0 psi
Constant Pressure
EPC 2 pressure (to be used for air-pre-treatment)

G.

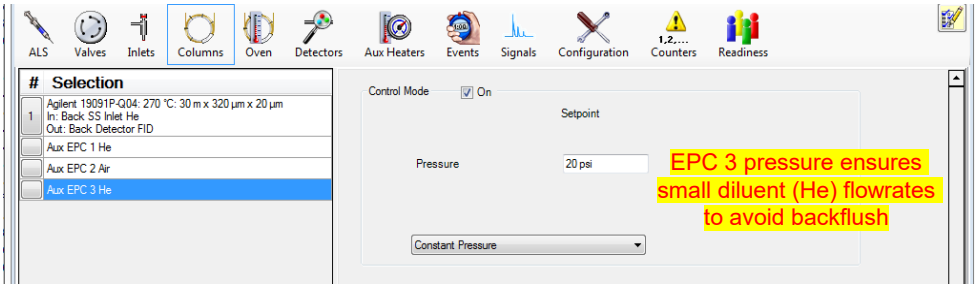
ALS
Valves
Inlets
Columns
Oven
Detectors
Aux Heaters
Events
Signals
Configuration
Counters
Readiness
Selection
1
Agilent 19091P-Q04: 270 °C: 30 m x 320 µm x 20 µm
In: Back SS Inlet He
Out: Back Detector FID
Aux EPC 1 He
Aux EPC 2 Air
Aux EPC 3 He
Control Mode
On
Setpoint
Pressure
20 psi
Constant Pressure
EPC 3 pressure ensures small diluent (He) flowrates to avoid backflush

H.

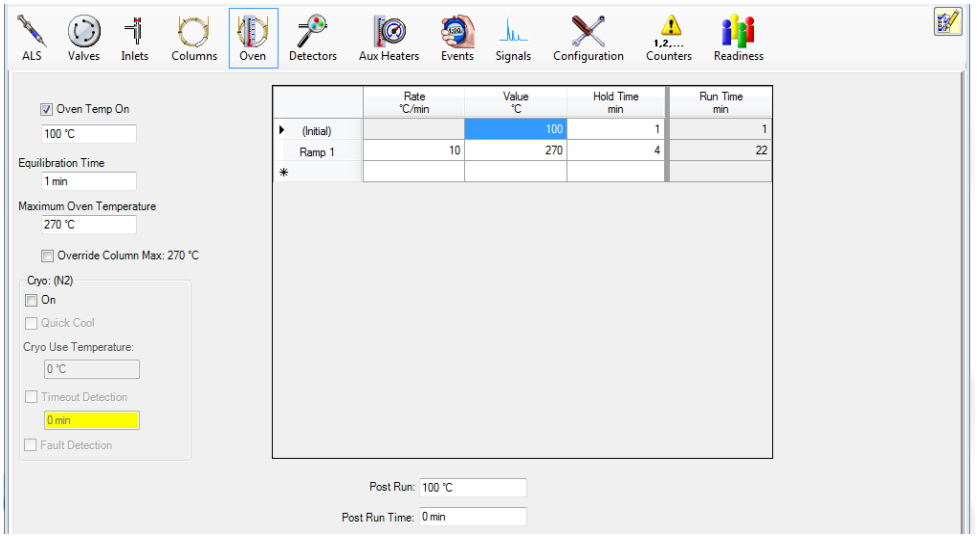
ALS
Valves
Inlets
Columns
Oven
Detectors
Aux Heaters
Events
Signals
Configuration
Counters
Readiness
Oven Temp On
100 °C
Equilibration Time
1 min
Maximum Oven Temperature
270 °C
Override Column Max: 270 °C
Cryo: (N2)
On
Quick Cool
Cryo Use Temperature:
0 °C
Timeout Detection
0 min
Fault Detection
Rate °C/min
Value °C
Hold Time min
Run Time min
(Initial)
100
1
1
Ramp 1
10
270
4
22
Post Run: 100 °C
Post Run Time: 0 min

I.

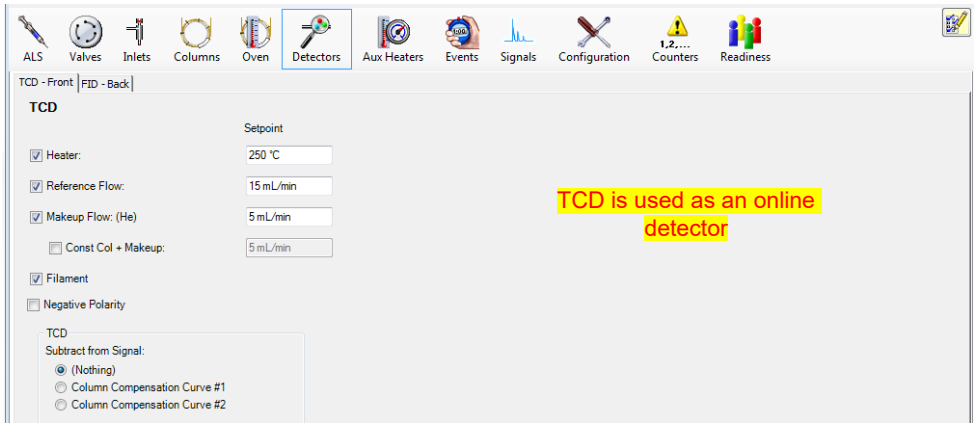
ALS
Valves
Inlets
Columns
Oven
Detectors
Aux Heaters
Events
Signals
Configuration
Counters
Readiness
TCD - Front
FID - Back
TCD
Setpoint
Heater:
250 °C
Reference Flow:
15 mL/min
Makeup Flow: (He)
5 mL/min
Const Col + Makeup:
5 mL/min
Filament
Negative Polarity
TCD
Subtract from Signal:
(Nothing)
Column Compensation Curve #1
Column Compensation Curve #2
TCD is used as an online detector

J.

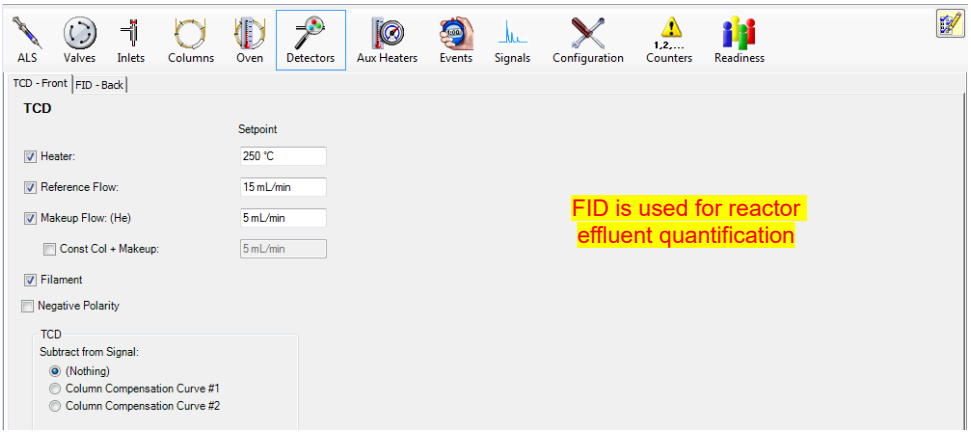
ALS
Valves
Inlets
Columns
Oven
Detectors
Aux Heaters
Events
Signals
Configuration
Counters
Readiness
TCD - Front
FID - Back
TCD
Setpoint
Heater:
250 °C
Reference Flow:
15 mL/min
Makeup Flow: (He)
5 mL/min
Const Col + Makeup:
5 mL/min
Filament
Negative Polarity
TCD
Subtract from Signal:
(Nothing)
Column Compensation Curve #1
Column Compensation Curve #2
FID is used for reactor effluent quantification

K.

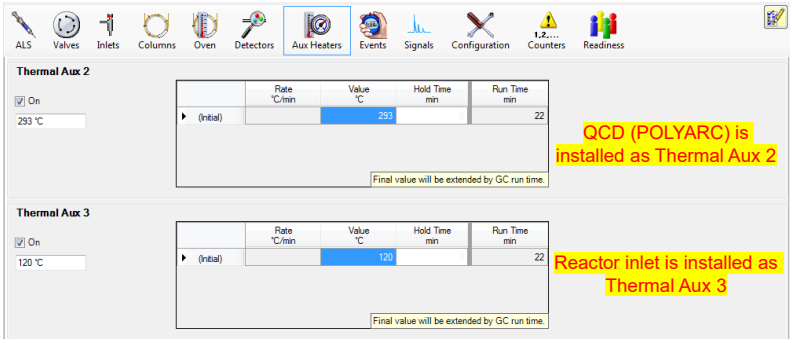

L.

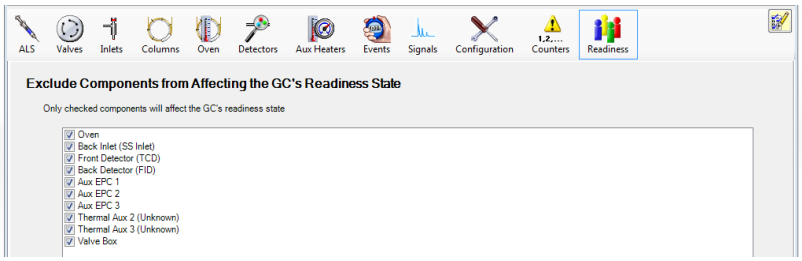

Figure A3.6 *A step-by-step guide for method development to control reaction parameters on the micro-flow reactor using ChemStation software connected to the GC (Agilent 7890B). Instructions corresponding to each of the windows shown here are included in* ***Section A3.1.2*** *(A) Injection source (B) ALS window; (C) Valves window; (D) Inlet window; (E) Columns window showing EPC 1 pressure; (F) Columns window showing EPC 2 pressure; (G) Columns window showing EPC 3 pressure; (H) Oven window; (I) Detectors window showing TCD; (J) Detectors window showing FID; (K) Auxiliary heaters window; and (L) Readiness window.*

A3.2 Brønsted acid site measurements

The Brønsted acid site measurement of HZSM-5 (Si/Al 140) was performed by the Hofmann elimination of tert-butylamine in the Reactive Gas Chromatography (RGC) setup, as described elsewhere.[1] The BAS count from these measurements was found to be ~94 (± 1.2) μmol/g, and all site time yields were calculated by normalizing mass-based rates by this count. **Figure A3.7** indicates the reproducibility of BAS counts in independent measurements.

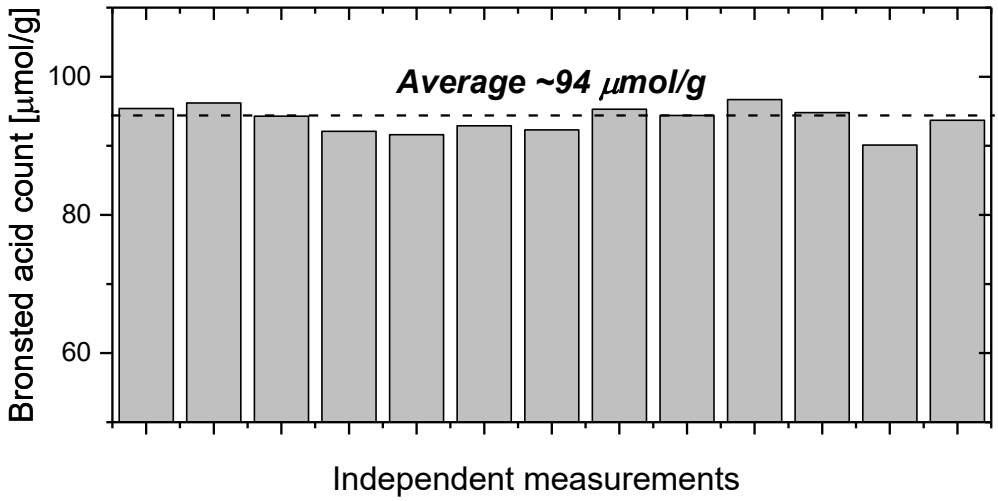

Figure A3.7 *Independent measurements of Brønsted acid site density of HZSM-5 (Si/Al 140). ~20-30 mg of 500-1000 μm aggregates were used to ensure minimal pressure drop across the catalyst bed (as these measurements were done at ~100 sccm He to avoid re-adsorption related artifacts). The bed was loaded into a GC inlet liner sandwiched between two plugs of quartz wool to perform the RGC experiment as described by Abdelrahman et al.*[1]

A3.3 Calculation of initial rates in 2-methyltetrahydrofuran (2-MTHF) dehydra-decyclization

To account for intervening deactivation in 2-MTHF dehydra-decyclization, the measured reaction rates were corrected back to a reference temperature of 503 K by repeatedly subjecting the bed to this condition in-between altering reaction temperatures. The initial rate at 503 K, when compared with the values obtained subsequently at the same condition, allows correction for the rate loss due to deactivation in the time elapsed between the two measurements. Rates were calculated maintaining a temporal resolution of ~22 minutes, and data from at least five online gas-sampling injections at the reference temperature (503 K) were taken to extract initial rates (t=0) by using a first order deactivation model

$$\frac{dr_i}{dt} = -kr_i; \text{ BCs: } r_i(t=0) = r_{i,o} \; and \; r_i(t \to \infty) = 0 \qquad \text{(A3.1)}$$

$$r_i(t) = r_{i,0} \; exp^{-kt} \; [=][\text{mol product } i/g \; catalyst/\text{h}]$$

where $r_{i,0}$ is the initial rate of formation of product i (mol/g catalyst/h), and k is the deactivation rate constant (h^{-1}). The temporal resolution required to regress decay parameters was achieved by online GC injection through a six-port gas sampling valve (Vici Valco) periodically at the start of each method.

A3.4 Tests for diffusion artifacts in kinetic measurements

GradientCheck© (www.gradientcheck.com) is a recent open-source tool developed by researchers at Dow Chemical Company /Purdue Catalysis Center, and it's use in transport calculations has been recently highlighted by Ribeiro/Hickman and co-workers.[2] The tool was used in this work for all heat/mass transfer calculations, which were performed at the highest reaction temperature at a fixed (5% conversion) for a given feed. All major parameters were calculated using this tool except Thiele modulus and the resulting effectiveness factor. It was found that the radius of the catalyst aggregate (R_{agg}) after pressing and sieving the catalyst was used by the tool for the calculation of Thiele modulus. As these calculations pertain to the gradients inside the individual zeolite crystallite, a more representative length scale is the average size of zeolite crystallite.[3–5] As $R_{agg} >> R_p$, the tool consistently overestimated Thiele moduli $\left(\varphi = \frac{R}{3}\sqrt{\frac{k}{D_e}}\right)$ and underestimated effectiveness factor values $(\eta = \tanh\varphi/\varphi)$. Therefore, these two parameters were calculated manually. All the raw input files (.json) used in this analysis are included with this submission. The catalyst properties used in the calculations are listed in **Table A3.2**, and the major transport parameters for each of the four chemistries are discussed in **sections A3.4.1, A3.4.2, A3.4.3, and A3.4.4**, respectively.

Table A3.2 *Catalyst properties used in the estimation of concentration/temperature gradients*

Catalyst pore tortuosity (τ) [a]	4
Catalyst void fraction (ε) [a]	0.4
Catalyst thermal conductivity (k_p) (W/m/K)[b]	0.15
Catalyst bulk density (ρ_{bulk}) (kg/m^3)[c]	1000
Catalyst particle shape	spheres
Catalyst total pore volume (V_{pore}) (cm^3/g)[d]	0.27
Catalyst surface area (S_{int}) (m^2/g) [d]	447
Bed length (L_b) (mm)	15
Reactor radius (R_r) (mm)	2
Particle aggregate diameter (R_{agg}) (μm)	750
Average crystallite size (R_p) (μm)	2.5[e]

[a] Assumed (Typical τ of 3-7 for porous catalysts; typical ε of 0.35-0.45)[6] ; [b] As reported[7]; [c] Zeolyst CBV28014 datasheet; [d] Calculated from Ar-adsorption; [e] Particle sizes of 250 nm-2 μm have been reported,[8–10] and highest value of 2.5 μm was chosen as a conservative estimate

A3.4.1 Dehydration of ethanol to di-ethyl ether

	Ethanol	DEE	Carrier gas (He)
Inlet mole fraction	0.033	0.0028	0.9642
Fluid viscosity (μ_f) (kg/m/s)	1.48×10^{-5} [a]	1.51×10^{-4} [b]	1.87×10^{-5} [a]
Heat capacity (C_p) (J/kg/K)	2077.7[c]	2237.11[c]	5190[d]
Thermal conductivity (k_f) (W/m/K)	0.171[a]	0.038[e]	0.156[f]

[a] As reported [11]; [b] approximated using values reported in[12]; [c] NIST database (@500 K) [d] calculated using Shomate equation at 503 K (NIST) [e] As reported [13]; [f] As reported in [14];

T (K)	503
Activation energy (E_a) (J/mol)	82424.8
Enthalpy of reaction (ΔH_{rxn}^o) (J/mol)	-24000[a]
Order of reaction	1 (assumed)
Rate of reaction (r_{obs}) (mol EtOH consumed/kg cat./s)	0.002872
Bulk concentration (C_b) (mol/m^3)	0.789
Effective diffusivity (D_e) (m^2/g)	3.42×10^{-8}
Mass transfer coefficient (k_c) (m/s)	0.54
Particle-fluid heat transfer coefficient (h) (W/m^2/K)	587
External concentration gradient (%)	0.287
Axial temperature change (K)	0.617
External temperature gradient (K)	0.05
Internal temperature gradient (K)	0.004
Mears criteria $\frac{Volume\ normalized\ Rate.R_{agg.}}{C_b.k_c} < \frac{0.15}{n}$	*LHS* 0.018
Weisz-Prater criteria $\frac{Volume\ normalized\ Rate.R_p^2}{C_b.D_e} < 0.3$	*LHS* 2.4×10^{-3}
Thiele modulus	0.039
Effectiveness factor	~1

[a] As reported in Connett *et al.*[15]

A3.4.2 Dehydration of 2-propanol to propylene

	2-Propanol	Propylene	Carrier gas (He)
Inlet mole fraction	0.0255	0.008	0.9642
Fluid viscosity (μ_f) (kg/m/s)	8.97×10^{-4} [a]	1.20×10^{-5} [b]	1.87×10^{-5}
Heat capacity (C_p) (J/kg/K)	1871.9[c]	2137[c]	5190
Thermal conductivity (k_f) (W/m/K)	0.1395[a]	0.035[d]	0.156

[a] As reported[13]; [b] As reported[16]; [c] NIST database; [d] As reported[17]

T (K)	433
Activation energy (E_a) (J/mol)	144417
Enthalpy of reaction (ΔH_{rxn}^o) (J/mol)	51200[a]
Order of reaction	1 (assumed)
Rate of reaction (r_{obs}) (mol 2PrOH consumed/kg cat./s)	0.00705
Bulk concentration (C_b) (mol/m^3)	0.708
Effective diffusivity (D_e) (m^2/g)	3.52×10^{-8}
Mass transfer coefficient (k_c) (m/s)	0.548
Particle-fluid heat transfer coefficient (h) (W/m^2/K)	818
External concentration gradient (%)	0.776
Axial temperature change (K)	-2.44
External temperature gradient (K)	-0.184
Internal temperature gradient (K)	-0.007
Mears criteria $\frac{Volume\ normalized\ Rate.R_{agg.}}{C_b.k_c} < \frac{0.15}{n}$	*LHS* 0.0486
Weisz-Prater criteria $\frac{Volume\ normalized\ Rate.R_p^2}{C_b.D_e} < 0.3$	*LHS* 6.5×10^{-3}
Thiele modulus	0.11
Effectiveness factor	~0.99

[a] As reported in the SI of Sullivan et al. [18]

A3.4.3 Dehydration of 1-butanol to di-butyl ether

	1-butanol	di-butyl ether	Carrier gas (He)
Inlet mole fraction	0.0249	0.002	0.9731
Fluid viscosity (μ_f) (kg/m/s)	1.64×10^{-4} [a]	2.9×10^{-4} [d]	1.87×10^{-5}
Heat capacity (C_p) (J/kg/K)	2024	2135.9 [b]	5190
Thermal conductivity (k_f) (W/m/K)	0.135 [a]	0.138 [e]	0.156

[a] As reported [13] [d]As reported [19]; [e]As reported [20];

T (K)	473
Activation energy (E_a) (J/mol)	73673.6
Enthalpy of reaction (ΔH_{rxn}^o) (J/mol)	-23000 [a]
Order of reaction	1 (assumed)
Rate of reaction (r_{obs}) (mol 1buOH consumed/kg cat./s)	3.63×10^{-3}
Bulk concentration (C_b) (mol/m^3)	0.633
Effective diffusivity (D_e) (m^2/g)	2.51×10^{-8}
Mass transfer coefficient (k_c) (m/s)	0.478
Particle-fluid heat transfer coefficient (h) (W/m^2/K)	700
External concentration gradient (%)	0.513
Axial temperature change (K)	0.651
External temperature gradient (K)	0.05
Internal temperature gradient (K)	0.002
Mears criteria $\frac{Volume\ normalized\ Rate.R_{agg.}}{C_b.k_c} < \frac{0.15}{n}$	*LHS* 0.032
Weisz-Prater criteria $\frac{Volume\ normalized\ Rate.R_p^2}{C_b.D_e} < 0.3$	*LHS* 5.1×10^{-3}
Thiele modulus	0.083
Effectiveness factor	~1

[a] Calculated from the enthalpy of elementary steps tabulated in John et al. [21]

A3.4.4 Dehydration of 2-MTHF to (1,3+1,4)-Pentadiene

	2-MTHF	1,3-Pentadiene	1,4-Pentadiene	Carrier gas (He)
Inlet mole fraction	0.0138	0.0002	$4x10^{-5}$	0.9861
Fluid viscosity (μ_f) (kg/m/s)	2×10^{-4} [a]	7.37×10^{-5} [b]	7.37×10^{-5} [b]	1.87×10^{-5}
Heat capacity (C_p) (J/kg/K)	1973[d]	1471.5[e]	1494.9[e]	5190
Thermal conductivity (k_f) (W/m/K)	0.15[f]	0.056[b]	0.056[b]	0.156

a As reported in [22]; [b] viscosity and thermal conductivity data for pentadienes was not found; approximated as 1,3-butadiene from Dortmund data bank[13]; [d] As reported in [23]; [e] Joback method as reported in [24]; [f] approximated as the thermal conductivity of THF reported in [13]

T (K)	543
Activation energy (E_a) (J/mol)	72836.4
Enthalpy of reaction (ΔH_{rxn}^o) (J/mol)	45800[a]
Order of reaction	1 (assumed)
Rate of reaction (r_{obs}) (mol 2MTHF consumed/kg cat./s)	9.27×10^{-4}
Bulk concentration (C_b) (mol/m^3)	0.306
Effective diffusivity (D_e) (m^2/g)	3.3×10^{-8}
Mass transfer coefficient (k_c) (m/s)	0.41
Particle-fluid heat transfer coefficient (h) (W/m^2/K)	501
External concentration gradient (%)	0.317
Axial temperature change (K)	-0.42
External temperature gradient (K)	-0.04
Internal temperature gradient (K)	-0.003
Mears criteria $\frac{Volume\ normalized\ Rate.R_{agg.}}{C_b.k_c} < \frac{0.15}{n}$	LHS 0.02
Weisz-Prater criteria $\frac{Volume\ normalized\ Rate.R_p^2}{C_b.D_e} < 0.3$	*LHS* 0.002
Thiele modulus	0.034
Effectiveness factor	~1

[a] As reported in Kumbhalkar et al.[25]

A3.5 Details of the use of the microflow reactor setup for the catalytic evaluation of HZSM-5

Table A3.3 *Product selectivities obtained during the catalytic evaluation of 2-propanol and 1-butanol dehydration on HZSM-5 (Si/Al 140) on the microflow reactor. Carbon balances close to within ±7%.*

Feed	Temperature (K)	Conversion (%)	WHSV (h^{-1})	Dehydration Selectivity (%C basis)	
				Unimolecular	Bimolecular
2-PrOH	393	0.46	7.32	57.5	42.5
2-PrOH	403	1.21	7.32	54.1	45.9
2-PrOH	423	5.8	7.32	78.7	21.3
2-PrOH	433	7.8	7.32	88.7	11.3
2-PrOH	443	13.9	7.32	94.7	5.3
1-BuOH	403	2.01	7.55	2	98
1-BuOH	423	3.5	7.55	8.2	91.8
1-BuOH	443	4.17	7.55	17.8	86.2
1-BuOH	463	11.55	7.55	25.6	74.4
1-BuOH	473	13.66	7.55	36.3	63.7

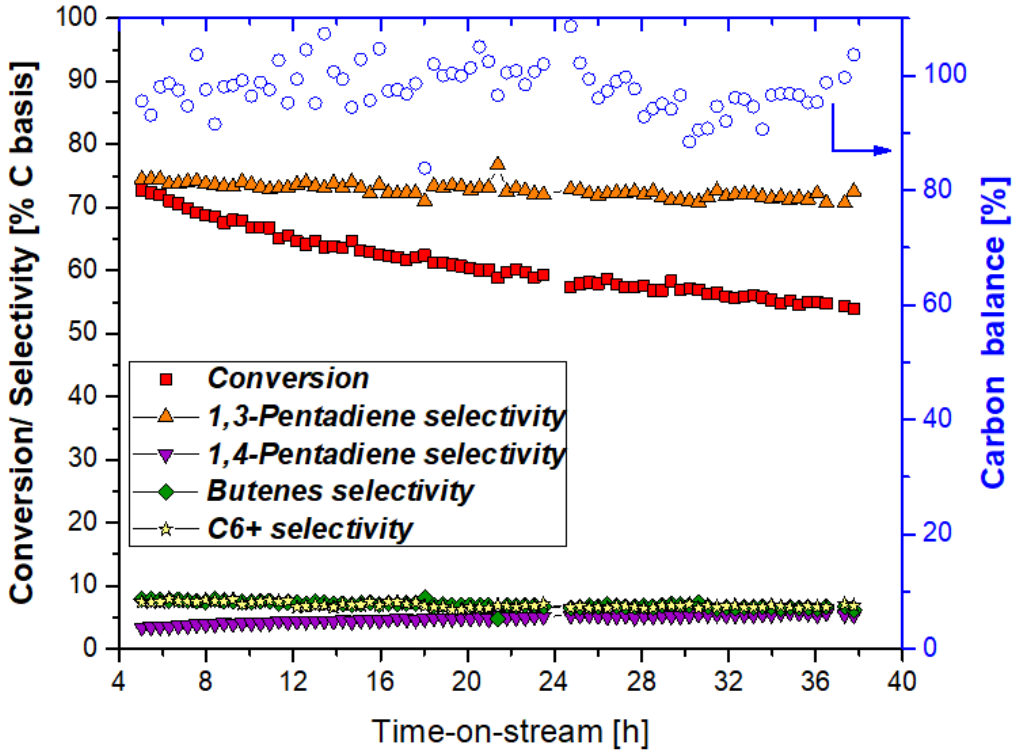

Figure A3.8 Stability analysis for HZSM-5 (Si/Al 11.5, Zeolyst 2314) in the dehydra-decyclization of 2-MTHF. *(primary axis) 2-MTHF conversion, and product selectivities to 1,3-pentadiene, 1,4-pentadiene, butenes, and C6+ fraction; (secondary axis) carbon balances (Reaction conditions: T= 608 K, $p_{2\text{-MTHF, inlet}}$= 3.5 torr, WHSV = 0.84 g 2-MTHF/ g cat./h, Carrier gas flowrate =35 sccm).*

A4 Catalytic consequences of acid-site strength and diffusional hurdles in the dehydra-decyclization of 2-methyltetrahydrofuran to pentadienes

A4.1 Synthesis and characterization results for all synthesized samples

A4.1.1 Synthesis of zeolites

MCM-22

Briefly, 1.32 g NaOH pellets were dissolved in 233.06 g deionized water (18.2 MΩ). Thereafter 1.37 g $NaAlO_2$ was added till full dissolution, followed by the addition of 14.34 g hexamethyleneimine(HMI). 17.68 g of fumed silica (Cab-o-sil M5) was added under stirring conditions, and mixture was stirred till a homogeneous gel was obtained. This gel with the chemical composition SiO_2: 0.112 NaOH: 0.493 HMI: 0.057 $NaAlO_2$: 44.04 H_2O was treated hydrothermally at 408 K for eleven days under rotation. Upon removal, ion exchange was performed by preparing 5% w/w mixture of Na-form of the prepared sample with 1.0 M NH_4NO_3 solution and keeping the solution under stirring conditions at 343 K for 12 hours. This material is the Al-MWW precursor (denoted as Al-MWW(P)). Calcination of this precursor lead to MCM-22.

MCM-36

For the synthesis of MCM-36, a wet cake of Al-MWW (P) (20 wt% solids) was swollen at room temperature under high pH conditions (pH~14) followed by pillaring of the swollen materials with TEOS. In the swelling process, typically, 9 g of wet cake of Al-MWW(P) was mixed with 35 g of an aqueous solution of 29 wt% CTAB and 11 g of an aqueous solution of 40 wt% TPAOH. The mixture was allowed to stir for 16 h at ambient temperature, and then the particles were recovered by repeated cycles of centrifugation and water washing (600 s centrifugation at 10000 rpm, and re-dispersion in fresh water). The swollen material was then dried at 343 K overnight. The pillaring process was conducted by mixing 5 g of swollen Al-MWW(P) powder with 25 g of TEOS, stirring for 24 h at 351 K under argon atmosphere, then filtering and drying at ambient temperature. A 1.0 g sample of the resulting solid was hydrolyzed with 10 g of water (pH ~ 8, controlled with NaOH) for 6 h at 313 K, then filtered, dried at 300 K to produce pillared MWW (MCM-36). After calcination (as described in the main text), successful swelling and pillaring of Al-MWW (P) was confirmed by the presence of (001) peak in the XRD patterns **(Figure A4.1B)**, as well the visible stacking of layers in the scanning TEM micrographs (**Figure A4.1H**).

B-MWW

8.04 g of boric acid was dissolved into 68.4 g deionized water (18.2 MΩ). After complete dissolution, 23.84 g of piperidine was added, and the mixture was stirred for 30 minutes. 12.0 g of fumed silica (Cab-o-sil M5) was then added to the above solution. A vortex shaker was used to mix the gel for at least 20 minutes prior to setting up magnetic stirring overnight, and the gel appeared translucent milky after vortex mixing. After stirring overnight, this gel with chemical composition SiO_2: 1.4 PI: 19 H_2O:0.65 H_3BO_3 was transferred to autoclaves and hydrothermally treated in a rotation oven at 443 K for seven days.

B-MFI

1.13 g of anhydrous borax was dissolved into 29.0 g of deionized water (18.2 MΩ). 4.5 g TPAOH and 4.5 g solid NaOH were added, and the solution was stirred for 30 minutes. Then, 2.71 g of fumed silica (Cab-o-Sil M5) was added to the solution, and the gel was stirred overnight. The gel with a chemical composition SiO_2: 0.49 TPAOH: 2.5 NaOH: 36 H_2O: 0.13 $Na_2B_4O_7$ was then transferred to autoclaves and hydrothermally treated in a static oven at 453 K for five days. Upon removal, ion exchange was performed by preparing 5% w/w mixture of Na-form of the prepared sample with 1.0 M NH_4NO_3 solution and keeping the solution under stirring conditions at 343 K for 12 hours.

B-BEA

0.54 g of boric acid was dissolved into 68.5 g deionized water (18.2 MΩ) and 22.83 g of TEAOH. The solution was stirred for 30 minutes. Then 24.03 g of fumed silica (Cab-o-sil M5) and 1.17 Si-BEA seeds (synthesized using procedures listed elsewhere[26]) were added to the above solution. After stirring for two hours, the gel with chemical composition SiO_2: 0.385 TEAOH: 14 H_2O: 0.067 H_3BO_3 was transferred to autoclaves and hydrothermally treated in a static oven at 423 K for four days.

Following hydrothermal treatment for B-BEA and B-MWW, and ion-exchange for B-MFI and MCM-22, all samples were separated and fully washed and centrifuged to pH ~ 9.0 followed by drying at 343 K overnight. These were then calcined using procedures reported in the main text.

A4.1.2 Characterization results for all zeolites with MWW topology

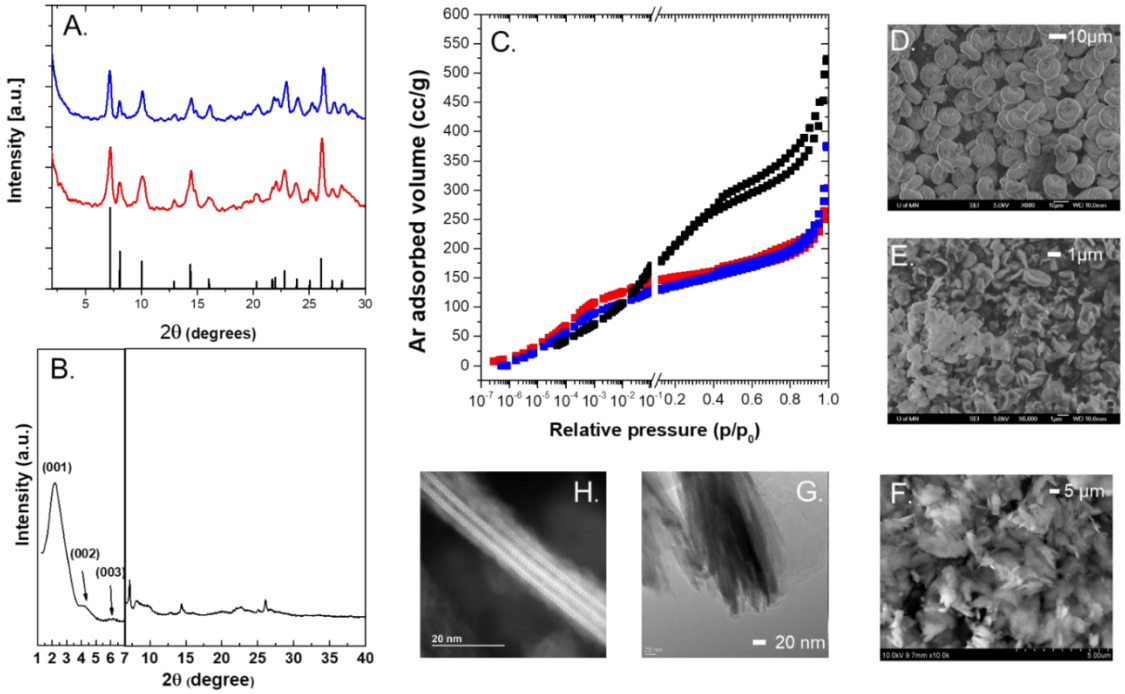

Figure A4.1 (A) *PXRD patterns for B-MWW (red), and MCM-22 (blue) compared with (bottom) MWW XRD pattern from International Zeolite Association (IZA)*[27] *;* ***(B)*** *PXRD pattern for MCM-36;* ***(C)*** *Ar adsorption-desorption isotherms for B-MWW(red, ■), MCM-22 (blue, ■) and MCM-36 (black,■);* ***(D)*** *SEM micrograph for B-MWW;* ***(E)*** *SEM micrograph for MCM-22;* ***(F)*** *SEM micrograph of MCM-36;* ***(G)*** *TEM micrograph of MCM-22 and* ***(H)*** *STEM image of MCM-36. Note that the presence of 001 peak* ***(Figure A4.1B)*** *indicates successful pillaring of MCM-22 to MCM-36 (long range order is preserved, and stacked layers are also visible in STEM image in* ***Figure A4.1H***

A4.1.3 Characterization results for all zeolites with MFI topology

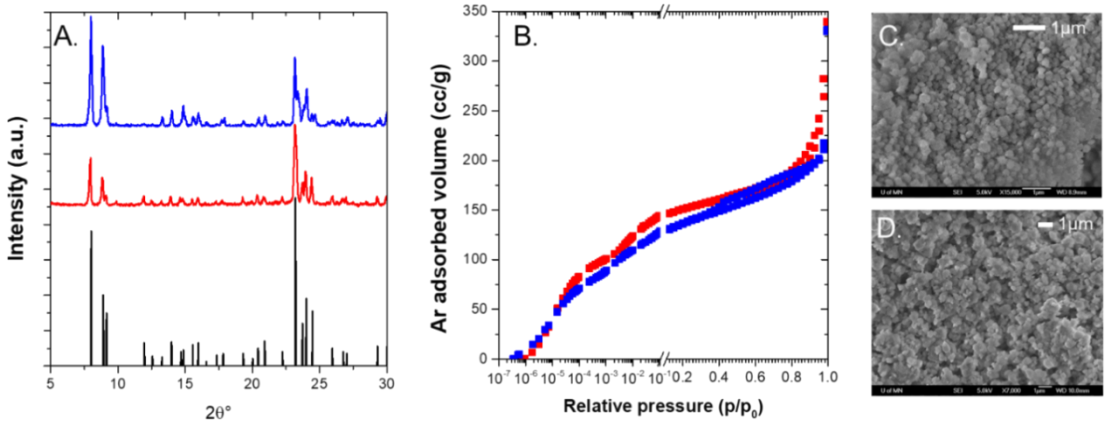

Figure A4.2. (A) *PXRD patterns for B-MFI (red), and ZSM-5 (blue) compared with (bottom) MFI XRD pattern from International Zeolite Association (IZA);*[27] ***(B)*** *Ar adsorption-desorption isotherms for B-MFI (red,■) and ZSM-5 (blue, ■); **(C)** SEM micrograph for B-MFI; **(D)** SEM micrograph for ZSM-5.*

A4.1.4 Characterization results for all zeolites with BEA topology

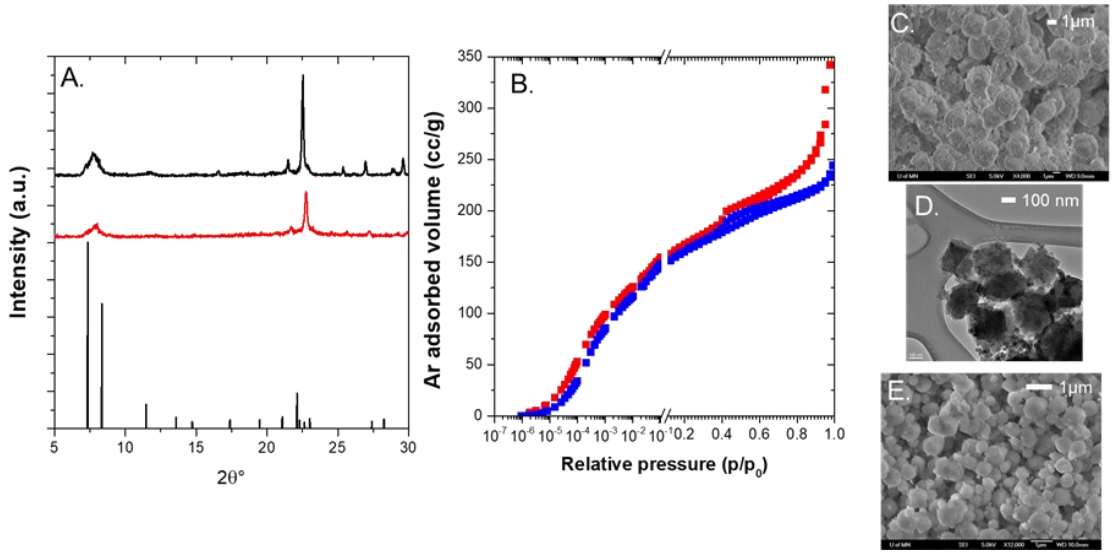

Figure A4.3 (A) *PXRD patterns for B-BEA (red), and Al-BEA (black) compared with (bottom) BEA XRD pattern from International Zeolite Association (IZA);*[27] ***(B)*** *Ar adsorption-desorption isotherms for B-BEA (red ■) and Al-BEA (blue ■); **(C)** SEM micrograph for B-BEA; **(D)** TEM micrograph for B-BEA; **(E)** SEM micrograph of Al-BEA.*

A4.1.5 Ex-situ characterization of boron and silicon environments in borosilicates

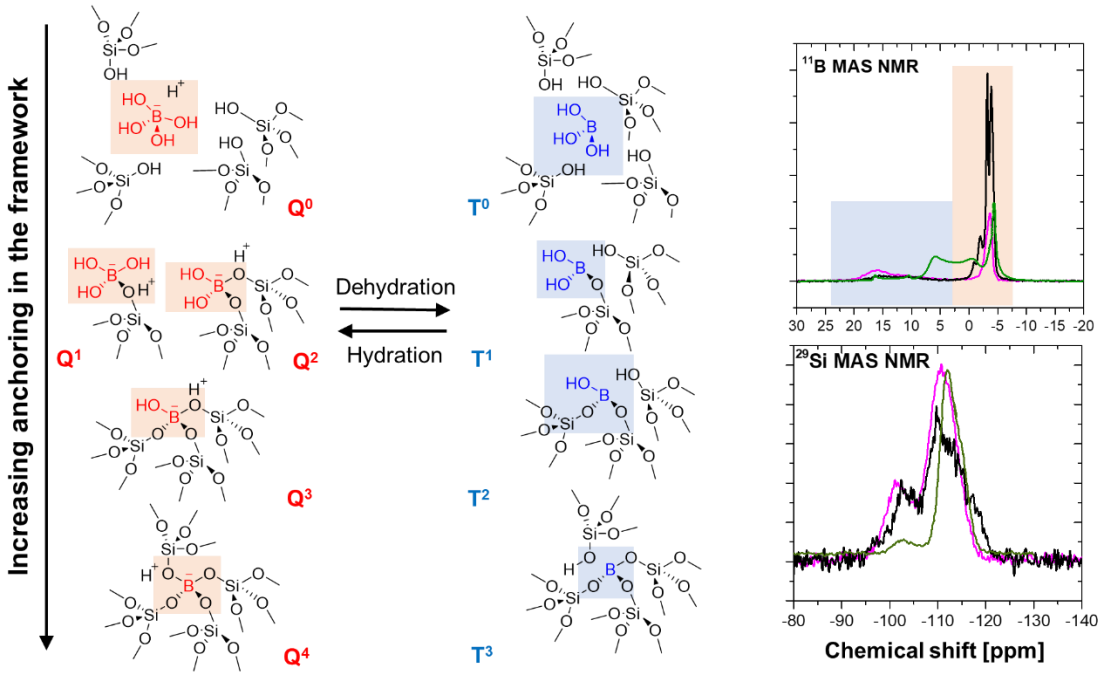

Figure A4.4 (A) *Trigonal and tetrahedral boron environments in borosilicates;* ***(B)*** *^{11}B MAS NMR spectra; and* ***(C)*** *^{29}Si MAS NMR spectra of B-MWW, B-BEA, and B-MFI.*

Numerous reports on the silicon states in aluminosilicates as well as borosilicates exist and are not discussed in detail here for brevity. Briefly, the occupancy of Si in these frameworks is either in form of $Si(OSi)_4$ linkages (represented as Q^4 by ^{29}Si-NMR), or as defect silanol nests $Si(OSi)_3OH$ (represented as Q^3). Q^4 shows a chemical shift of ~ -110 ppm whereas Q^3 shows a shift of ~ -100 ppm in ^{29}Si MAS NMR spectra. Both signals were found present in all the synthesized borosilicate samples **(Figure A4.4C)**. As hydrolysis of B-O-Si bonds leads to the formation of silanol nests, a relatively weak Q^3 signal in all samples indicated that most B-O-Si bonds were intact.[28,29] Previous reports have further highlighted that boron coordination is mostly trigonal in dehydrated samples, and it undergoes a change to tetrahedral state upon rehydration.[30,31] However, it is also possible that upon addition of excess water, trigonal (three-coordinated) B is hydrolyzed to a defect terminal B-OH linkage which can be completely extracted from the framework.[32] The broad range for tetrahedral B chemical shifts are in the range of -5 to 0 ppm, while different trigonal sites show a chemical shift in the range ~ 3 to 18 ppm in ^{11}B

MAS NMR spectra, depending on the anchoring of B in the framework.[30,31,33,34] **Figure A4.4A** depicts an exhaustive list of boron environments in borosilicates. It can be seen that trigonal sites T^0, T^2, T^3, can transform into tetrahedral sites (Q^0, Q^3, Q^4), respectively, on the addition of water, and this change is reversible upon dehydration. Such transformations can also take place upon interaction of trigonal B sites with bases like pyridine and ammonia.[33,35] Signals corresponding to both trigonal and tetrahedral B environments were present in the ^{11}B MAS NMR spectra of all three borosilicates considered in this work **(Figure A4.4B)**. Interestingly, B-MWW showed a multiplet for tetrahedral B. Generally, the different chemical environments of boron atoms at *T*-positions in zeolite frameworks only have a minor influence on chemical shifts in ^{11}B MAS NMR spectra,[30] and multiplets in this region are attributed to the presence of non-identical crystallographic distinct *T*-sites in frameworks including B-MWW,[36] B-RUB-1[37] and B-FER.[34] MWW has eight distinct *T*-sites, and the result indicates that B-MWW preserves long-range order of B in these distinct tetrahedral sites resolvable by ^{11}B NMR. It is also possible that B-MWW has higher B content than the other two borosilicates, and hence the distinct local environments are resolved in it. An accurate siting of B at these distinct sites, while possible using site multiplicities and previously reported relative stability of B in these distinct sites,[36] is challenging using 1-D NMR experiments alone. At each crystallographically distinct *T*-position, B can be sited in any of Q^0-Q^4 environments, making it difficult to accurately predict their NMR shifts, and hence an accurate assignment of the multiplet lies outside the scope of this work.

A4.2 Assessment of transport limitation during kinetic measurements

Mears' Criterion was used to estimate the existence of any external mass transfer calculations when measuring reaction rates. This was done for the catalyst exhibiting the highest mass-normalized rates (Al-BEA) at the highest temperature (513 K). It can be safely assumed that the less active catalysts (per mass basis) will not be external transport-limited provided this limiting case does not show these artifacts at identical reaction conditions. External mass transfer limitations can be neglected if the following inequality is satisfied

$$\frac{r_{obs}\rho_b Rn}{k_c C_b} < 0.15 \qquad \text{(A4.1)}$$

Where r_{obs} is the observed rate of reaction in mol $kgcat^{-1}$ s^{-1}, ρ_b is the catalyst bed density in kg m^{-3} ($\rho_b = (1-\phi)\rho_c$ where ϕ is the bed void fraction and ρ_c is the density of the catalyst, reported as 1000 kg m^{-3}), R is the catalyst aggregate size in m, n is the reactant reaction rate order, k_c is the external mass transfer coefficient in m s^{-1}, and C_b is the reactant bulk concentration in mol m^{-3}.

Table A4.1 *Tabulation of parameters for the calculation of Mears' Criteria for 2-MTHF dehydra-decyclization on Al-BEA (Si/Al 12.5) at 513 K*

Parameter	Value
r_{obs} (mol $kgcat^{-1}$ s^{-1})	4.34 x 10^{-3}
ρ_b (kg_{cat} m^{-3})	700 (ρ_c = 1000, assumed ϕ = 0.3)
R (m)	3.75x10^{-4} (average mesh size of 250-500 μm)
k_c (m s^{-1})[a]	0.102
C_b (mol m^{-3})	0.31 (10.5 torr 2-MTHF; total pressure 787.6 torr)
n	0
Mears' Criterion (Mass)	**0 (3.6 x 10^{-2} if assumed n = 1)**

[a] Estimated assuming Sh (Sherwood Number) = $k_c(2R)/D = 2 + 0.6\ Re^{1/2}Sc^{1/3}$; Re (Reynolds Number) = $\rho U(2R)/\mu$ and Sc (Schmidt number) = $\mu/\rho D$, where ρ = bulk gas density (Assumed to be He at 513 K, ρ = 0.15 kg m^{-3}), U = superficial velocity (total volumetric flow rate (1 cm^3 s^{-1}); tube diameter (2R) = 4 x10^{-3} m: U = 7.95x10^{-2} m s^{-1}), and μ = gas viscosity (estimated as He viscosity at 513 K = 2.85 x 10^{-5} Pa s). D is gas phase diffusivity, estimated using Chapman-Enskog theory of diffusivity for 2-MTHF in He at 513 K =2.47 x 10^{-4} m^2 s^{-1}).

The Mears criterion parameter show the reported rates are not corrupted by external mass transfer limitations.

Internal mass transfer limitations were evaluated by using the Weisz-Prater criterion **(Eq A4.2)** for the highest temperature on all the six catalysts.

$$C_{WP} = \eta\phi^2 = \frac{r_{obs}\rho_c R^2}{D_e C_{As}} \quad \text{(A4.2)}$$

where η is the dimensionless effectiveness factor, ϕ^2 is the dimensionless Thiele modulus, D_e is the effective diffusivity in m^2s^{-1} ($D_e = D\varepsilon\delta/\tau$, where ε is the porosity, δ is the constrictivity, and τ is the tortuosity, assumed to be average values of 0.35, 0.8, and 6, respectively), ρ_c is the particle density of the catalyst (assumed 1000 kg/m^3) and C_{As} is the reactant surface concentration in mol m^{-3} (Mears' criterion showed that there were no external mass transfer limitations, and hence we assume $C_{As} = C_b$). The upper limit of $\eta\varphi^2$ to safely assume that reaction is not diffusion limited is typically taken to be ~0.3.

The evaluation of D_e requires sorption experiments with framework dependent probe molecules, and we instead adopted an alternative method for these internal transport calculations. A prior study by Ruthven and co-workers has measured the effective diffusivity of 2-methyl cyclopentane (2-MCP) in silicalite-1,[38] which was assumed to be a surrogate for 2-MTHF given their similar sizes and chemical structures. Setting the value of Weisz-Prater parameter to 0.3 at the experimentally observed rates, the lower limit of D_e ($D_{e,min}$) which would still ensure the rates to be in kinetic regime was calculated for each catalyst, and compared with the effective diffusivity of 2-MCP ($D_{e,2\text{-MCP, actual}}$) in MFI micropores at the same temperature. Conclusions drawn from these calculations were different for the different frameworks.

a) MFI: If $D_{e,min} < D_{e,2\text{-MCP, actual}}$, the rates are strictly in kinetic regime and internal transport limitations are absent. If $D_{e,min} > D_{e,2\text{-MCP, actual}}$, internal transport limitations exist.

b) MWW: If $D_{e,min} > D_{e,2\text{-MCP, actual}}$, we can conclude that we are diffusion limited in the sinusoidal 10-MR channels of MWW (as they are smaller than MFI). However, the result is inconclusive if the opposite is true ($D_{e,min} < D_{e,2\text{-MCP, actual}}$). In short, the criteria can only confirm if we are diffusion-limited but not sufficient to prove if we are reaction-limited or not.

c) BEA: If $D_{e,min} < D_{e,2\text{-MCP, actual}}$, we can certainly say that we are not diffusion-limited in BEA (given BEA has larger micropores than MFI). However, the test remains inconclusive

in the case $D_{e,min} > D_{e,2\text{-}MCP,\ actual}$. In short, the criteria can only confirm if we are reaction-limited but not sufficient to prove if we are diffusion-limited or not.

The results of this calculation for B-MFI and ZSM-5 are shown in **Figure A4.5 (A-B)**. Since $D_{e,min} < D_{e,2\text{-}MCP,\ actual}$ for both B-MFI and ZSM-5 at the three highest temperatures of kinetic investigation, these data are in kinetic regime. The rates (per mass) for Al-BEA are within ~2x of ZSM-5 while the difference in $D_{e,min}$ and $D_{e,2\text{-}MCP}$ were almost an order of magnitude, and a similar analysis shows absence of internal transport limitations in Al-BEA as well. Similarly, B-BEA is significantly less active than B-MFI, and one can safely assume that absence of internal transport limitations in B-MFI implies that the data for B-BEA are also in kinetic regime.

The situation changes, however, in the case of both MWW catalysts. We note that the correct length scale to be used in the Thiele modulus formalism should not be the thickness of the platelet-shaped crystallites **(Figure A4.1 D-F)** but rather their diameter; the transport through external surface pockets to the crystallite is inhibited by 6-MR constrictions, and only happens through the sinusoidal 10-MR channels (which are somewhat smaller than MFI). The results of the calculations for MWW catalysts are shown in **Figure A4.5 (C-D)**. On MCM-22, $D_{e,min} \approx D_{e,2\text{-}MCP,\ actual}$, and we cannot rule out the presence of diffusional limitations. While data for only the highest three reaction temperatures is shown, this was also found to be the case at low temperatures (453 K). Therefore, even under reaction conditions used for DTBP titration experiments, the measurements were not strictly in kinetic regime. Similarly, for B-MWW, $D_{e,min} > D_{e,2\text{-}MCP,\ actual}$ which means that the presence of internal transport artifacts certainly cannot be ruled out in the rate measurements. We therefore do not report activation barriers for the MWW catalysts as the rates are not strictly in the kinetic regime under the reaction conditions.

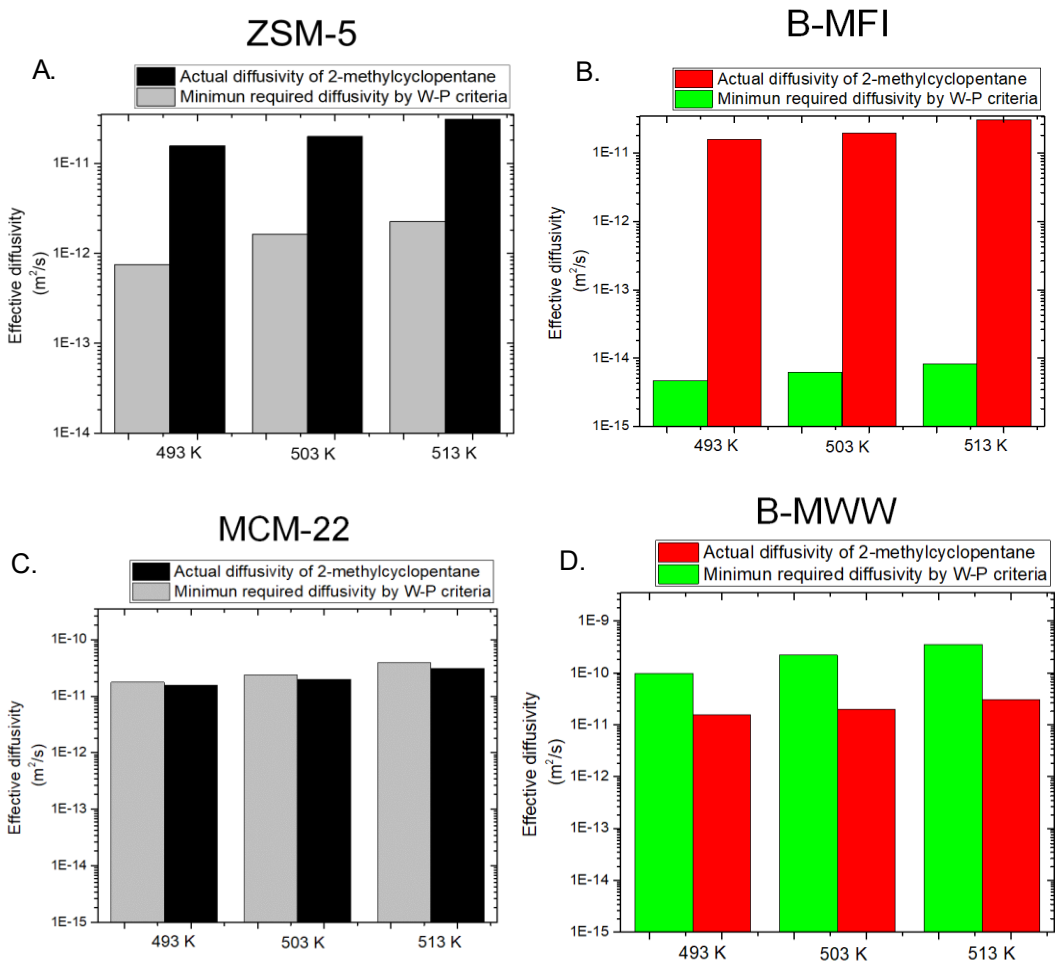

Figure A4.5 *Comparison of $D_{e,min}$, and $D_{e,2\text{-}MCP,\ actual}$ under 2-MTHF reaction conditions for* ***(A)*** *ZSM-5,* ***(B)*** *B-MFI,* ***(C)*** *MCM-22, and* ***(D)*** *B-MWW.*

A4.3 Catalytic performance of all zeolites for the dehydra-decyclization of 2-MTHF

While all mechanistic inquiries were sought under differential conditions, all zeolite samples were evaluated at different conversions to evaluate the product distributions and explore the range of 1,3-Pentadiene yields achievable. **Table A4.2** lists all the experiments conducted at relatively high temperatures, low 2-MTHF partial pressures, and low weight hourly space velocities to maximize conversions.

Table A4.2 *Reaction conditions and obtained product selectivities to major products*

Catalyst	T (K)	WHSV (h^{-1})	Conversion (%)	Carbon selectivity (%)			
				1,3-PD	(1,3+1,4)-PD	Butenes	C6+
B-MFI	608	0.89	35.2 (32.5)	63.5 (62.5)	89.3 (88.5)	3.5 (3.2)	1.5 (1.8)
	608	0.57	58.5	70.2	89.1	3.2	5.2
	658	0.21	93.3	83.2	91.2	3.5	5.6
	608	1.50	7.5	52.2	88.2	2.9	4.3
	608	0.45	47.7	71.1	89.9	3.1	5.1
ZSM-5	608	0.86	69.5	74.6	77.9	8.5	7.8
B-BEA	608	0.89	9.2 (8.1)	46.0 (45.2)	91.4 (90.5)	0.5 (0.4)	2.7 (2.4)
	658	0.16	44.9	53.3	87.8	1.5	5.2
	658	0.81	33.4	52.1	86.2	0.7	6.2
	658	0.09	50.7	53.9	91.7	1.5	4.3
Al-BEA	608	1.21	75.7	41.8	55.9	19.5	14.1
B-MWW	608	0.81	74.4	85.9	88.6	2.6	4.6
	658	0.85	98.6 (98.7)	86.1 (87.5)	87.6 (89.2)	3.5 (3.1)	6.6 (6.4)
	548	0.82	23.5 (23.8)	78.2 (78.8)	87.5 (87.1)	0.4 (0.5)	6.6 (8.6)
	608	0.29	39.5	79.1	91.6	1.2	4.6
	608	10.8	12.4	76.9	91.3	0.4	2.1
	608	0.31	57.5	82.6	88.3	1.6	5.3
MCM-22	608	1.20	88.1	67.7	73.9	10.4	9.4

Conversions and selectivity recorded at TOS ≈ 10h; bracketed conversions and selectivity reported at TOS≈ 48 h. Carbon balances close to within 10%. p_{2MTHF} = 3.6 torr. Carrier gas flowrate 35 sccm.

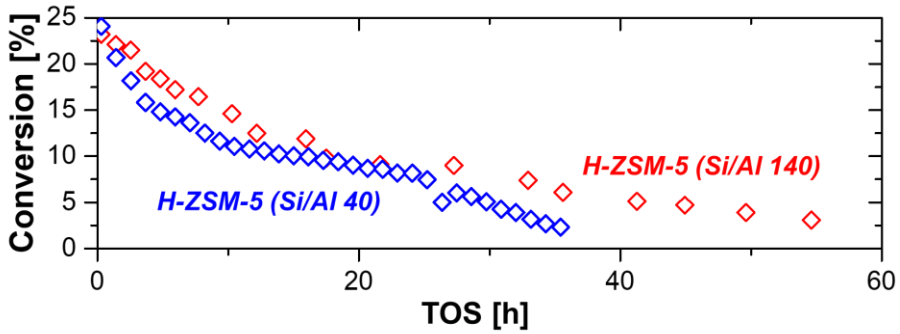

Figure A4.6 *2-MTHF conversion as a function of time-on-stream for aluminosilicate H-ZSM-5 with different aluminum contents (Reaction conditions: T= 658 K, p_{2-MTHF} =25 torr, WHSV = 6.8 h^{-1} for ZSM-5 (Si/Al 140), and 42.9 h^{-1} for ZSM-5 (Si/Al 40); Carrier gas flowrate= 123 sccm for ZSM-5 (Si/Al 40), and 30 sccm for ZSM-5 (Si/Al 140)).*

A4.4 Isomerization of 1,4-Pentadiene to 1,3-Pentadiene

A4.4.1 Equilibrium calculations for the inter-conversion of 1,3-, and 1,4-Pentadiene

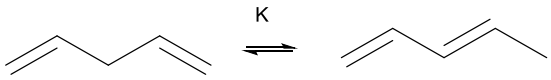

Table A4.3 *Enthalpy of formation, and gas phase entropies of 1,3-PD and 1,4-PD* (* NIST values)*

	$\Delta_f H^0$ (kJ/mol)	$S_{gas,0}$(J/mol)
1,3-Pentadiene (E)	75.77	315.6
1,3-Pentadiene (Z)	82.72	322.8
1,4-Pentadiene	106.3	334

Table A4.4 *Reaction enthalpies for the isomerization of 1,4-PD to 1,3-PD*

$\Delta_{rxn}H^0$ (kJ/mol)	-27.06
$\Delta_{rxn}S^0$ (kJ/mol)	-0.015
$\Delta_{rxn}G^0$(kJ/mol)	-9.143
K (298 K)	9352

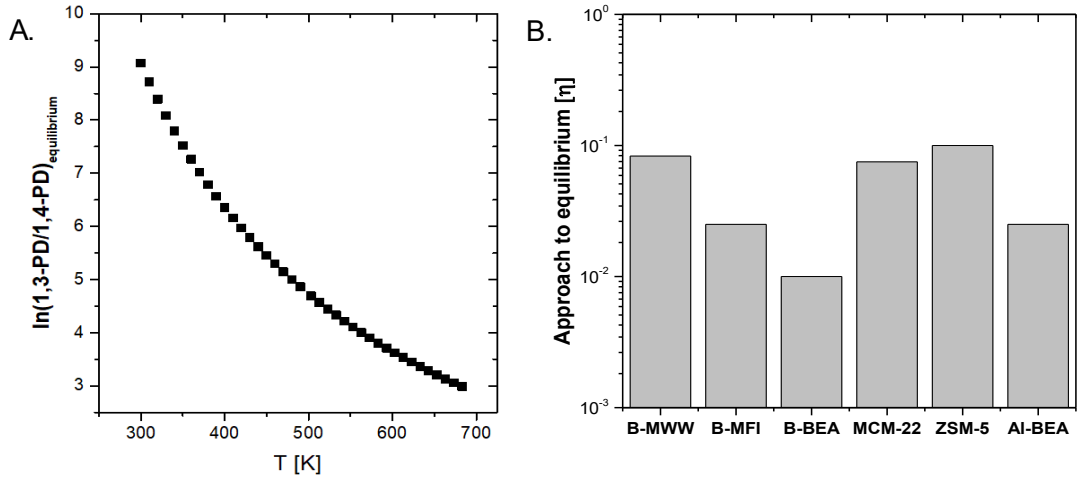

Figure A4.7 (A) *Variation of the equilibrium ratio of 1,3-Pentadiene to 1,4-Pentadiene with temperature (Van't Hoff Equation), and* ***(B)*** *The approach to equilibrium at 503 K* $\left(\eta = \frac{\left(\frac{P_{1,3-Pentadiene}}{P_{1,4-Pentadiene}}\right)}{K_{503\,K}}\right)$ *for all the zeolites at 503 K; the plot shows that the diene distribution remains far from equilibrium on all catalysts under investigated conditions*

A4.4.2 Equilibrium calculations for the inter-conversion of 1,3-, and 1,4-Pentadiene

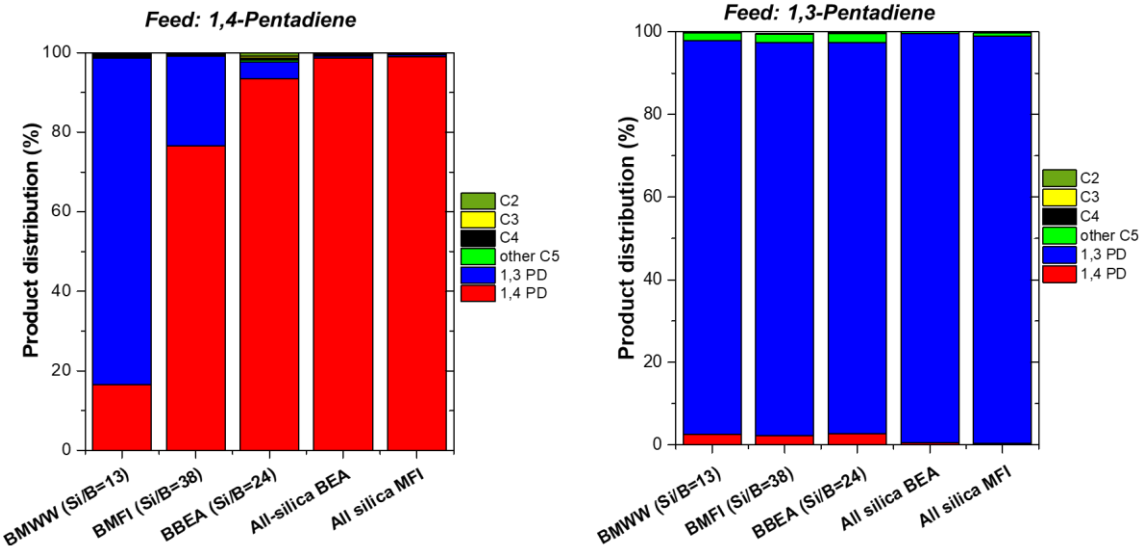

Figure A4.8 (left) *Product distribution obtained using pure 1,4-Pentadiene feed on different borosilicates;* ***(right)*** *Product distribution obtained using pure 1,3-Pentadiene feed on all borosilicates (all-silica materials are added for comparison). (Reaction conditions: T= 608 K,* p_{feed}*=3.5 torr, WHSV = 1.5* h^{-1}*, Carrier gas flowrate= 35 sccm, carbon balances close to ≈ 80-85%).*

A4.4.3 Diene distributions resulting from pure C5 alkenol feeds on ZSM-5 (Si/Al 140)

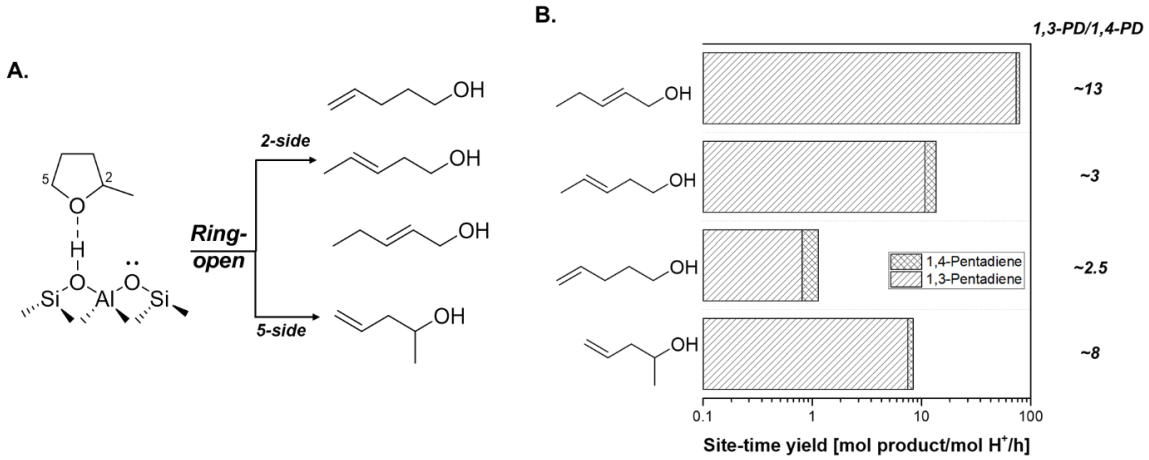

Figure A4.9 (A) *The alkenol intermediates resulting from the ring-opening of 2-MTHF**;** and **(B)** Site time yields for the production of 1,3-Pentadiene, and 1,4-Pentadiene and the corresponding 1,3-PD/1,4-PD ratios obtained from **(top to bottom)** 2-penten-1-ol, 3-penten-1-ol, 4-penten-1-ol, and 4-penten-2-ol (Reaction conditions: T= 413 K, p_{feed}= 10.5 torr, WHSV = 3.2-6.5 h^{-1}, Carrier gas flowrate= 60 sccm, Catalyst: ZSM-5 (Zeolyst) (Si/Al=140, with a BAS count of ≈ 85.3 µmol/g), all conversions kept in the range 2-5%).*

A5 On the Acid Sites of Phosphorous modified Zeosils

A5.1 Synthesis and characterization of P-zeosils

A5.1.1 Synthesis of P-zeosils.

All-silica zeolites used as supports for phosphoric acid were synthesized hydrothermally and the detailed procedures are listed below.

1- Si-SPP: The sample was synthesized with tetra(n-butyl)phosphonium hydroxide (TBPOH 40 wt%, TCI America) as the structure-directing agent and tetraethyl orthosilicate (TEOS, 98%, Sigma-Aldrich) as the silica source, and detailed recipe can be found in Zhang et al.[3] The products were collected by centrifuging and repeated washing with distilled water until pH < 8 and then dried at 70 ºC overnight. The as-synthesized sample was calcined at 550 ºC, and the removal of any remaining P-species from the decomposed SDA was removed by repeated washing with water. the calcined SPP was mixed with deionized water in a centrifuge tube and stirred in the oil bath (70 ºC) for 30 min, followed by centrifugation. This washing procedure was repeated 5 times, after which the sample was dried (at 70 ºC overnight) and calcined at 500 ºC for 4h in a box furnace.

2- Si-BEA: Sample was prepared under fluoride media with tetraethylammonium hydroxide (TEAOH, 40 wt % in water, Sigma Aldrich) as the SDA, and tetraethyl orthosilicate (TEOS, 98%, Sigma-Aldrich) as the silica source, and detailed recipe can be found in Camblor et al.[26] After hydrothermal synthesis, the products were collected by centrifuging and repeated washing with distilled water until pH<8 and then dried at 70 ºC overnight and calcined at 550 ºC for 4h in a box furnace.

3- Si-MFI: Sample was hydrothermally synthesized in fluoride media with Tetrapropylammonium bromide as SDA and Cab-o-Sil M5 as the silica source, and the detailed recipe can be found in Chézeau et al.[39] After hydrothermal synthesis, the products were collected by centrifuging and repeated washing with distilled water until pH<8 and then dried at 70 ºC overnight. The calcination for removal of surfactant was performed in a box furnace at 550 ºC for 10h.

4- Si-SBA-15: The sample was synthesized by modifying the recipe reported by Zhao et al.[40] First, 20 ml of 2M HCl was mixed with 104g deionized water and stirred for 10 min followed by adding

4g of PEO-PPO-PEO (P123, Sigma-Aldrich). The above mixture was stirred in a 40 °C oil bath for 30 min to dissolve the PEO-PPO-PEO. Then, 8.4g of tetraethyl orthosilicate (TEOS, Sigma-Aldrich) was added and stirred for 3h. The gel was then transferred to autoclaves and heated at 100°C for 24h. The products were collected by filtrating and repeated washing with deionized water and dried at 70 ºC overnight. The calcination for removal of surfactant was performed in a box furnace at 560 ºC for 10h without flowing any gas.

5- Si-MCM-41: The sample was synthesized by the following method: 1.1g of cetyltrimethylammonium bromide (CTAB) was mixed with 25ml of deionized water. Then 12 ml of ammonia water (20-25%, Aldrich) was added and stirred for 30 min. Then 5 ml of TEOS was added and stirred for 3h. The gel was then transferred to autoclaves and heated at 100°C for 24h. The products were collected by filtrating and repeated washing with distilled water and then dried at 70 ºC overnight. The calcination for removal of surfactant was performed in a box furnace at 550 ºC for 10h without flowing any gas.

6- Si-Stöber: This sample was synthesized using the exact recipe as reported by Stöber et al.[41] and is the same sample previously reported in Zhang et al.[42]

All P-containing zeosils except P-BEA were prepared using wet impregnation procedure as reported for preparation of P-BEA by Fan and co-workers.[43] In this procedure, the Si/P feeding was fixed at 25. Typically, first, 0.4 g of the mother all-silica sample, 18.2 µL of 85wt % phosphoric acid (H_3PO_4, Sigma-Aldrich), and 3.33 mL of deionized water were mixed. Then, the impregnated sample was dried at 90 °C overnight, followed by calcination at 600 °C for 25 min. For the synthesis of P-BEA, the impregnation procedure was modified by using ethanol and water as co-solvents. First, a phosphoric acid solution was prepared by mixing 182 µl of H_3PO_4 (85 wt %, Sigma-Aldrich) and 8.325 g of deionized water. Then, 1g of Si-BEA, 2.057g of above phosphoric acid solution and 6 ml of ethanol were mixed thoroughly. Then, the impregnated sample was dried at 90 °C overnight, followed by calcination at 600 °C for 25 min.

A5.1.2 Characterization results for P-zeosils.

i) P-BEA

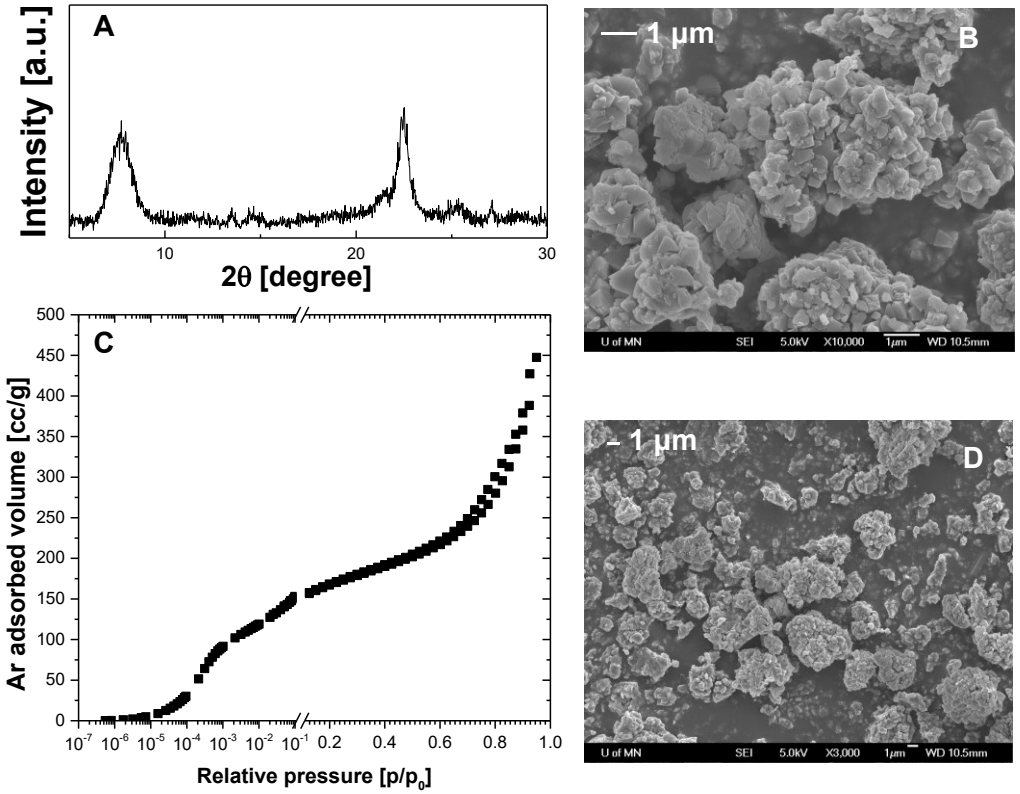

Figure A5.1 *(A) PXRD patterns for P-BEA; (B & D) SEM micrographs for P-BEA; (C) Ar adsorption-desorption isotherms for P-BEA (■).*

ii) P-SPP

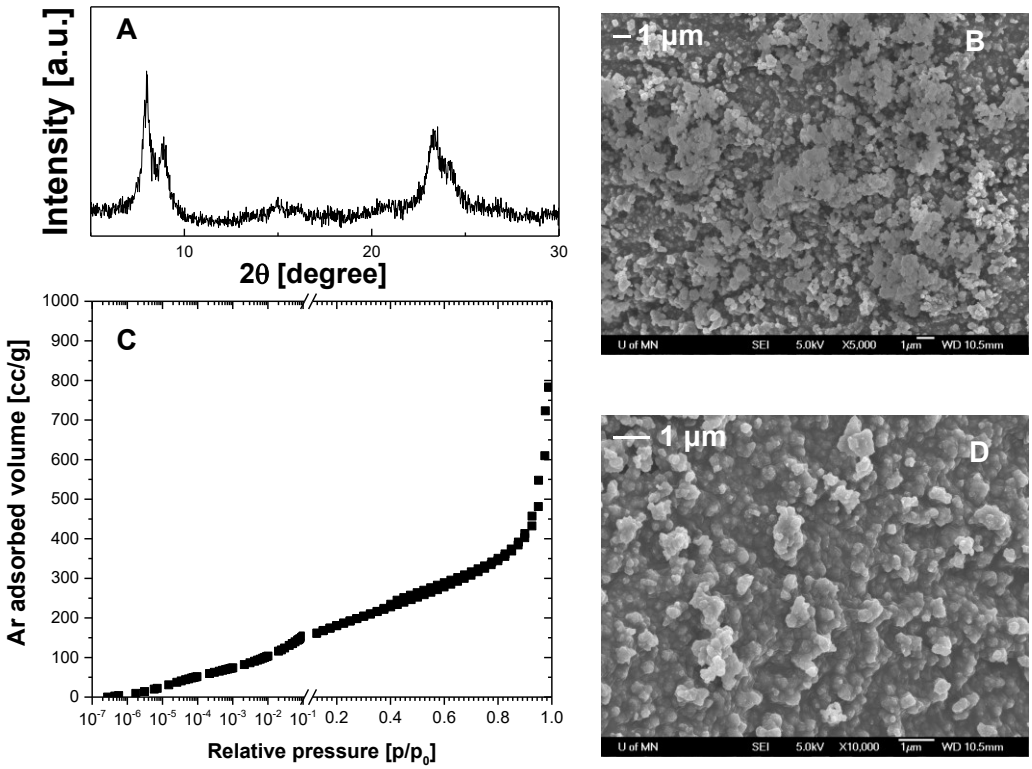

Figure A5.2 (A) *PXRD patterns for P-SPP;* ***(B & D)*** *SEM micrographs for P-SPP;* ***(C)*** *Ar adsorption-desorption isotherms for P-SPP (■).*

iii) P-SBA-15

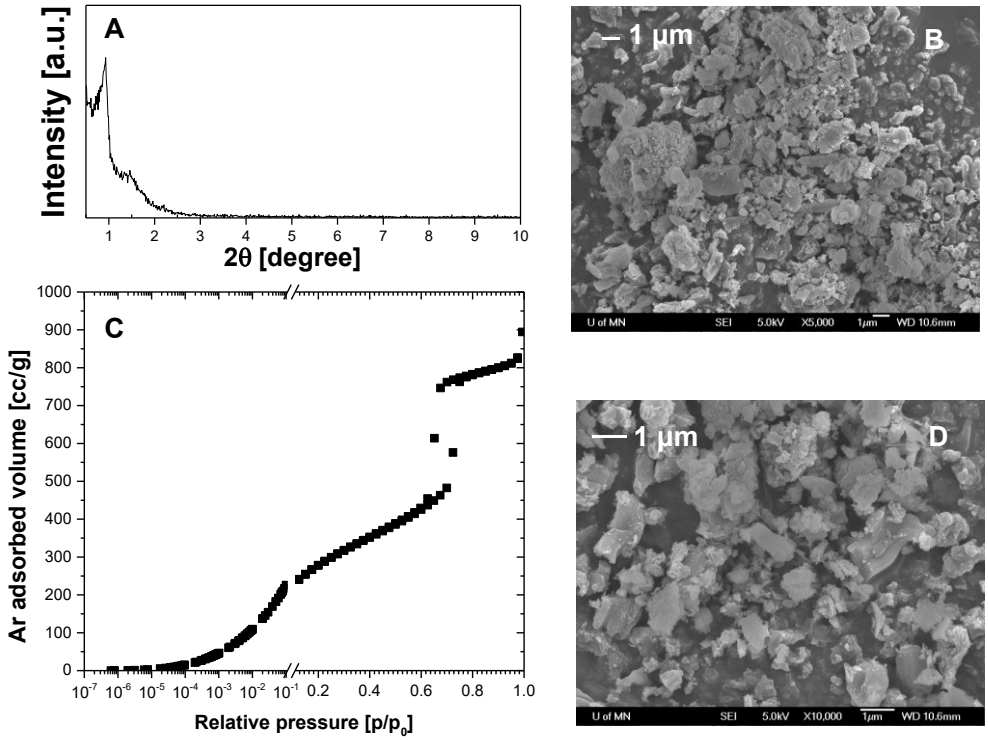

Figure A5.3 (A) *PXRD patterns for P-SBA-15;* ***(B & D)*** *SEM micrographs for P-SBA-15;* ***(C)*** *Ar adsorption-desorption isotherms for P-SBA-15 (■).*

iv) P-MFI

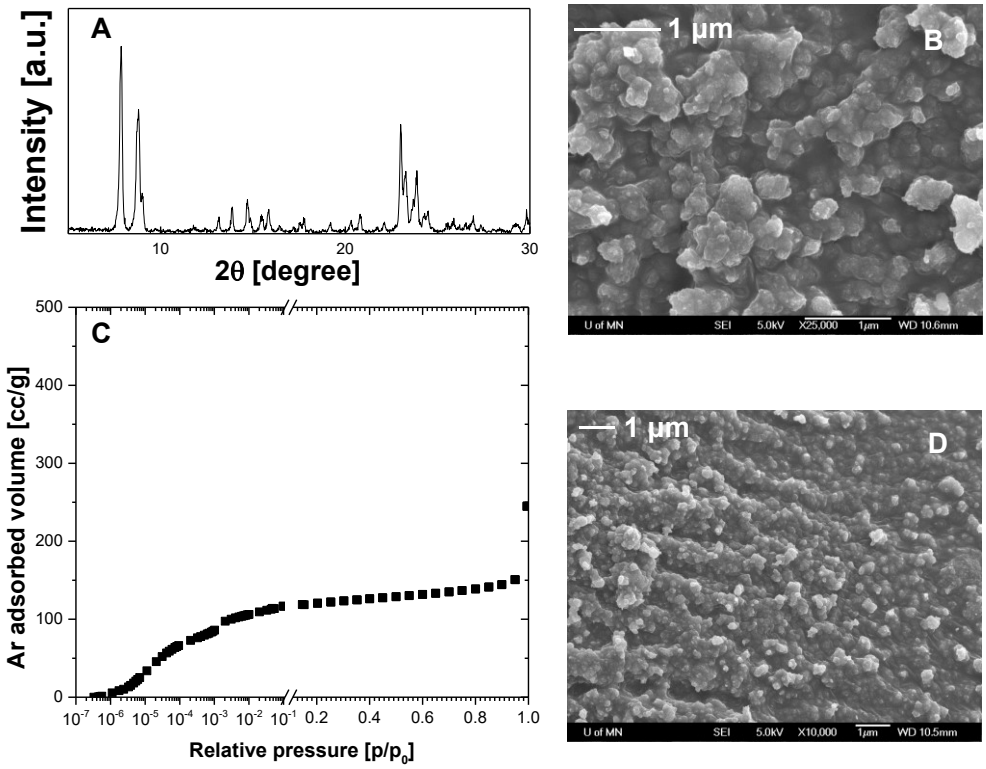

Figure A5.4 (A) *PXRD patterns for P-MFI;* ***(B & D)*** *SEM micrographs for P-MFI;* ***(C)*** *Ar adsorption-desorption isotherms for P-MFI (■).*

v) P-MCM-41

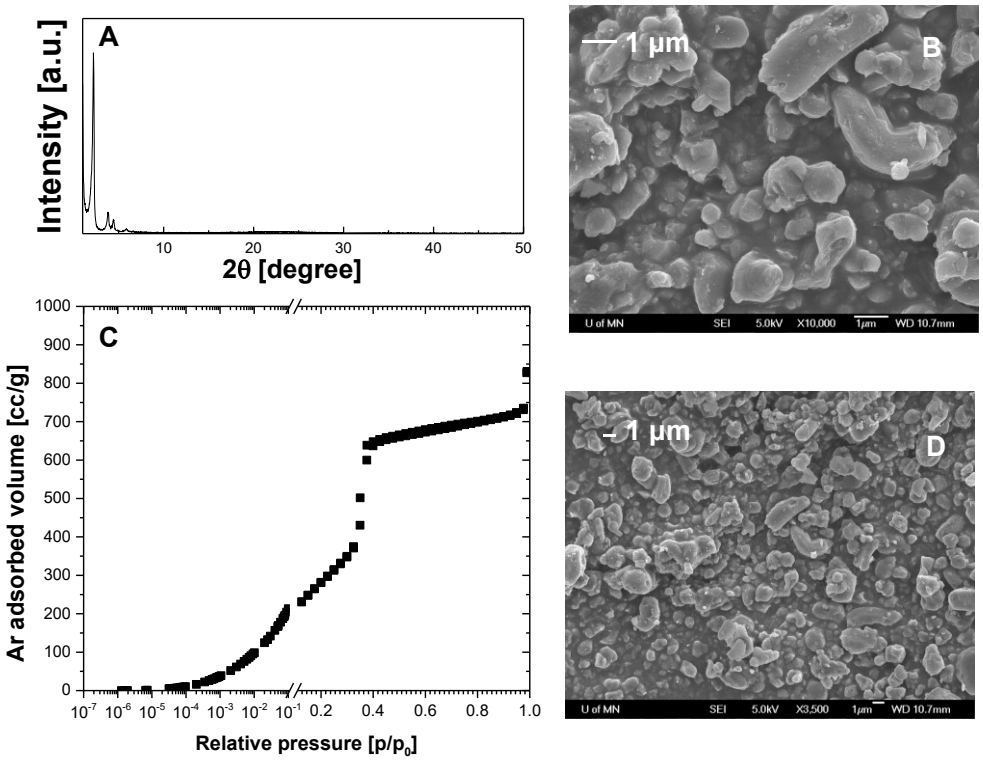

Figure A5.5 (A) *PXRD patterns for P-MCM-41;* ***(B & D)*** *SEM micrographs for P-MCM-41;* ***(C)*** *Ar adsorption-desorption isotherms for P-MCM-41 (■).*

vi) P- Stöber

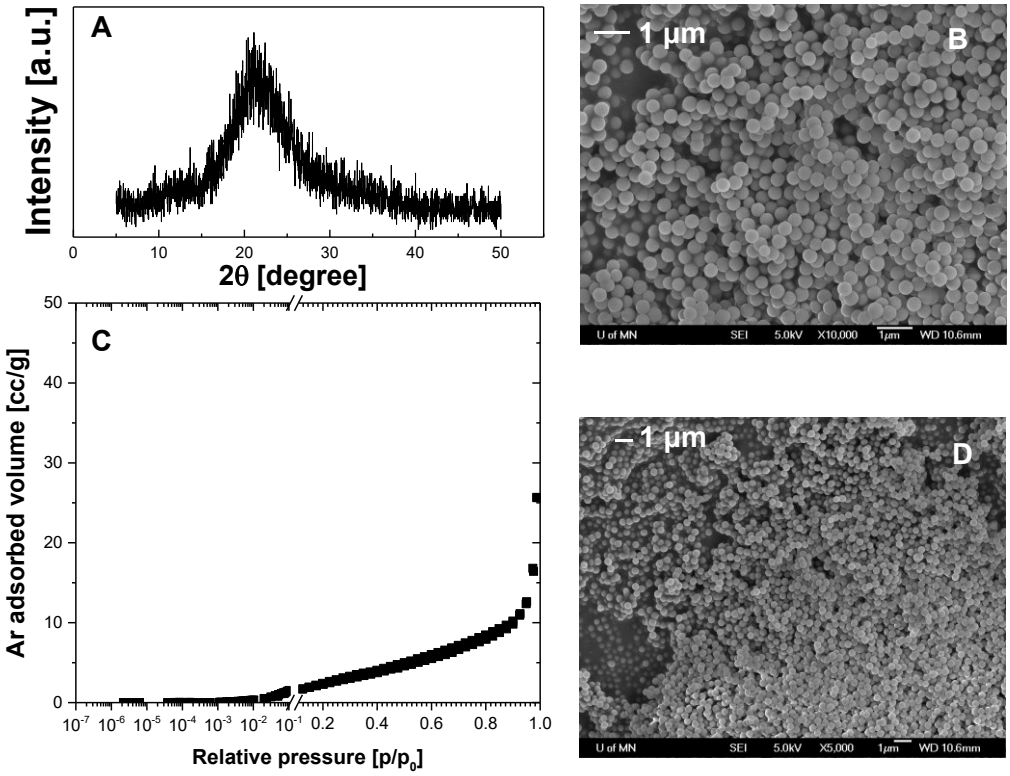

Figure A5.6 (A) *PXRD patterns for P-Stöber ;* ***(B & D)*** *SEM micrographs for P-Stöber ;* ***(C)*** *Ar adsorption-desorption isotherms for P-Stöber (■).*

Table A5.1 *Textural properties of all phosphorus-containing zeosils*

Catalyst	BET area [a] [$m^2\ g^{-1}$]	Total pore volume [b] [$cm^3\ g^{-1}$]
P-SPP	544.2	0.61
P-MFI	326.5	0.20
P-BEA	465.4	0.57
P-MCM-41	943.4	1.06
P-SBA-15	837.9	1.03
P-Stöber	8.2	0.03

[a] Determined from Ar adsorption–desorption isotherms; [b] Determined from Ar adsorption–desorption isotherms at $P/P_0 = 0.95$ for SPP, BEA, and MFI, and $P/P_0 = 0.99$ for SBA-15, Stöber, and MCM-41

A5.2 Optimized structures for all adsorption calculations

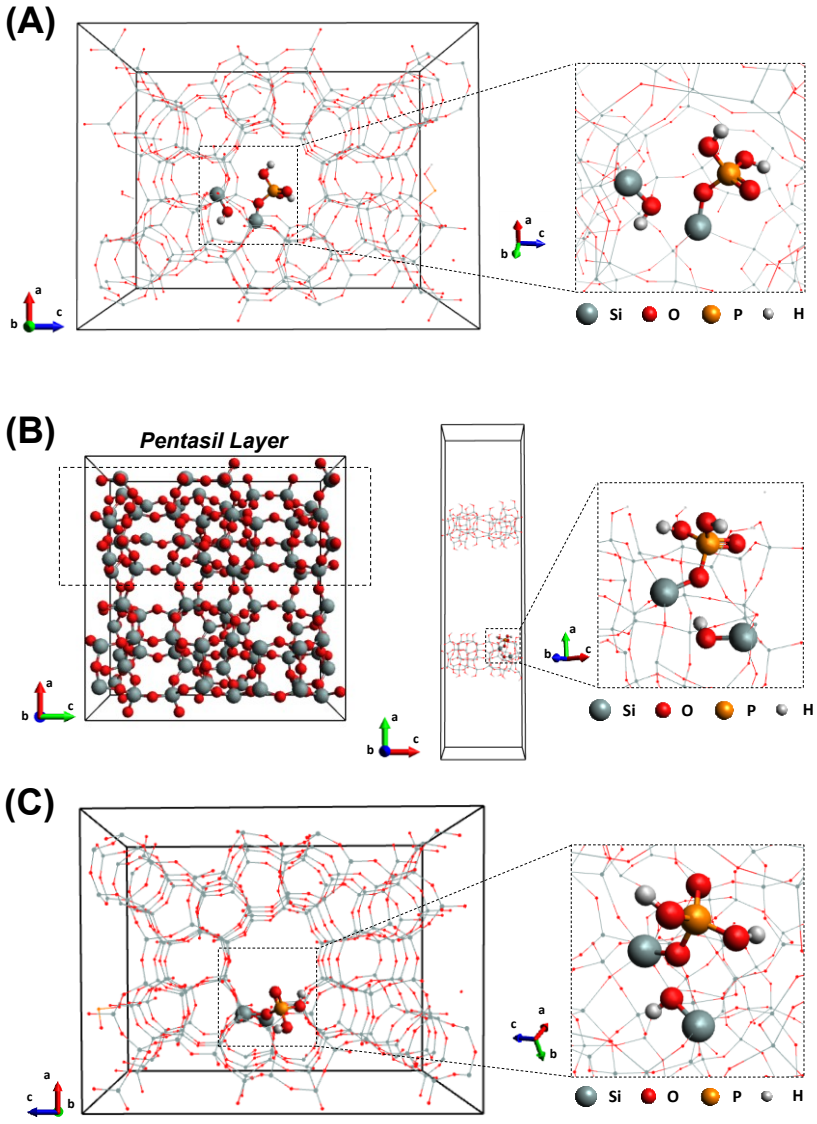

Figure A5.7 *The optimized structures of* ***(A)*** *an internal P-active site and* ***(B)*** *an external P-active site on T2-site in a P-MFI framework are presented. The structure containing the internal P-active site was optimized in a 1 × 1 × 1-unit cell, but shown in a 1 × 1 × 2 supercell for better visualization of the site and adsorption interactions.* ***(C)*** *Optimized structure of an internal P-site on T-12 position. Silicon, oxygen, phosphorus, and hydrogen atoms are represented by grey, red, orange, and white solid balls respectively.*

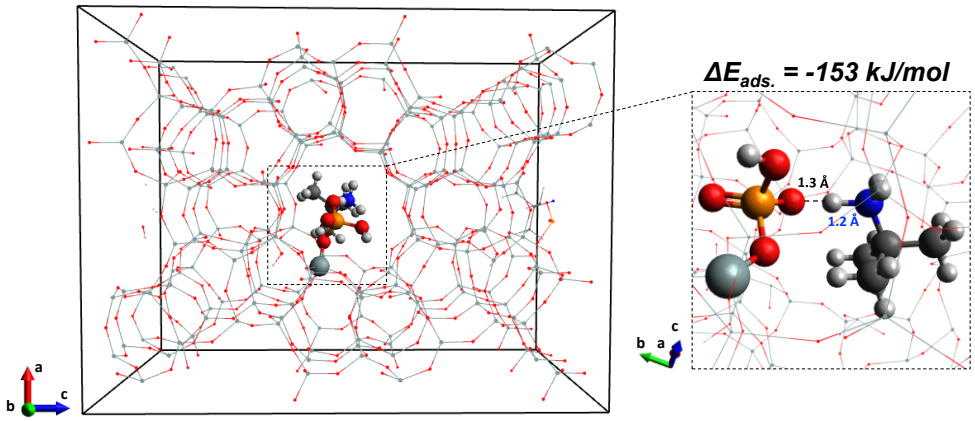

Figure A5.8 *The optimized structures of tBA adsorbed on an internal P-active site. The N-H atomic distances between the nitrogen of adsorbate and the proton of P-active site are shown in blue and the O-H distances between the oxygen and hydrogen of the P-active site are shown in black.*

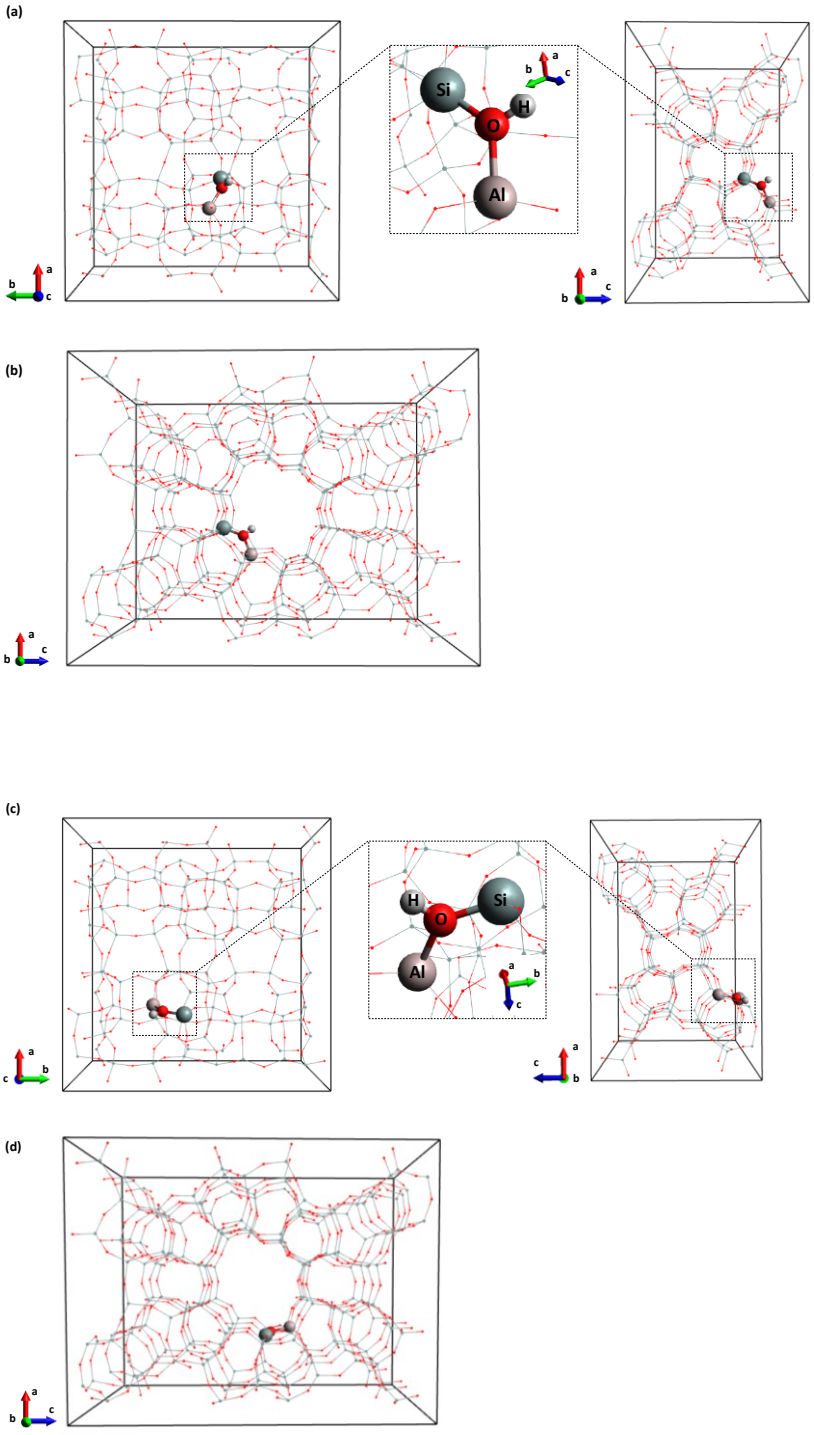

Figure A5.9 *Optimized structure of an Al-MFI framework containing a BAS on the T2 position is shown in* ***(a)*** *a 1 × 1 × 1-unit cell and* ***(b)*** *a 1 × 1 × 2 supercell and a BAS on the T12 position is shown in* ***(c)*** *a 1 × 1 × 1-unit cell and* ***(d)*** *a 1 × 1 × 2 supercell. The supercell was constructed for more clear visualization of the internal sites and adsorption on internal sites. Silicon, aluminum, oxygen, and hydrogen atoms are represented by grey, pink, red, and white solid balls, respectively.*

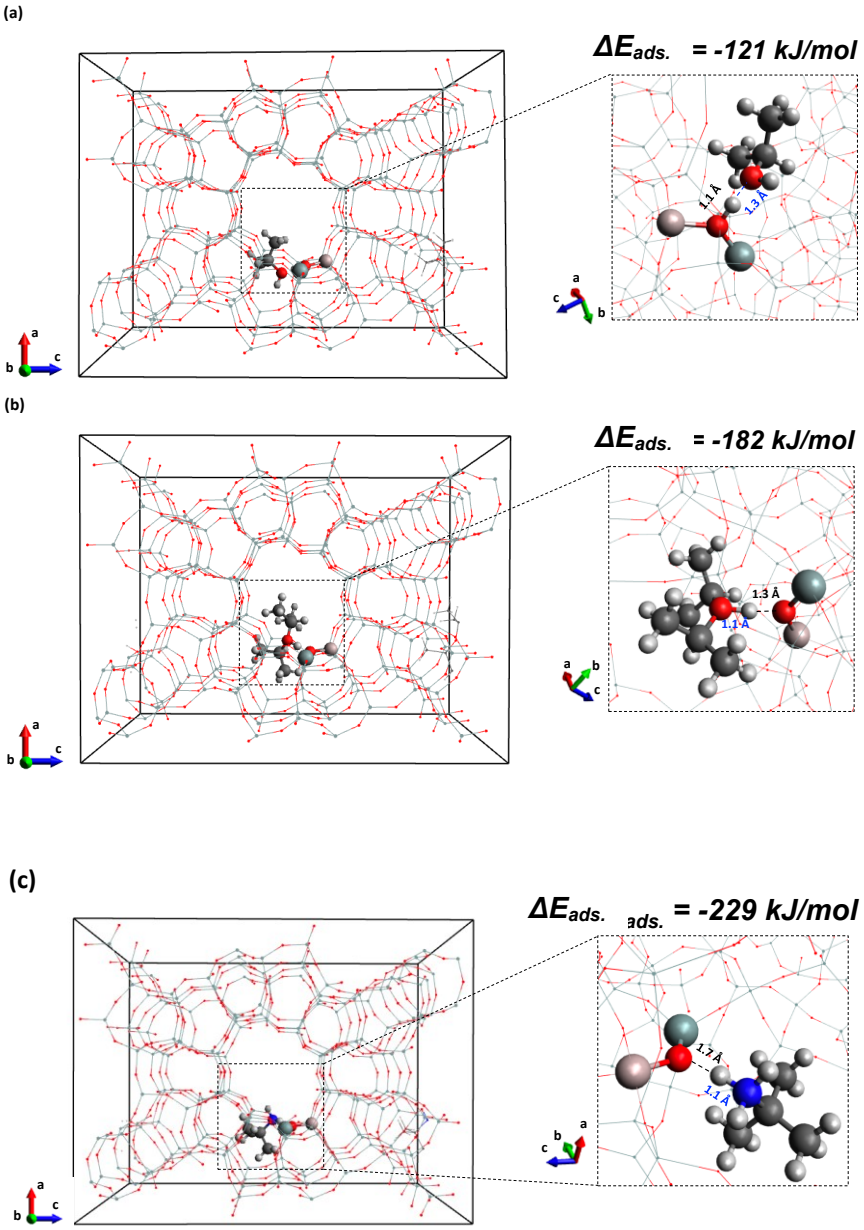

Figure A5.10 *The optimized structures of* ***(a)*** *IPA,* ***(b)*** *DIPE, and* ***(c)*** *tert-butylamine adsorbed on an internal BAS at the T12 in an Al-MFI framework are shown. The O-H or N-H distances between the oxygen/nitrogen and hydrogen of the BAS site are shown in black.*

A5.3 Catalytic evaluation of P-zeosils in IPA dehydration

A5.3.1 Regenerability of P-SPP for IPA dehydration

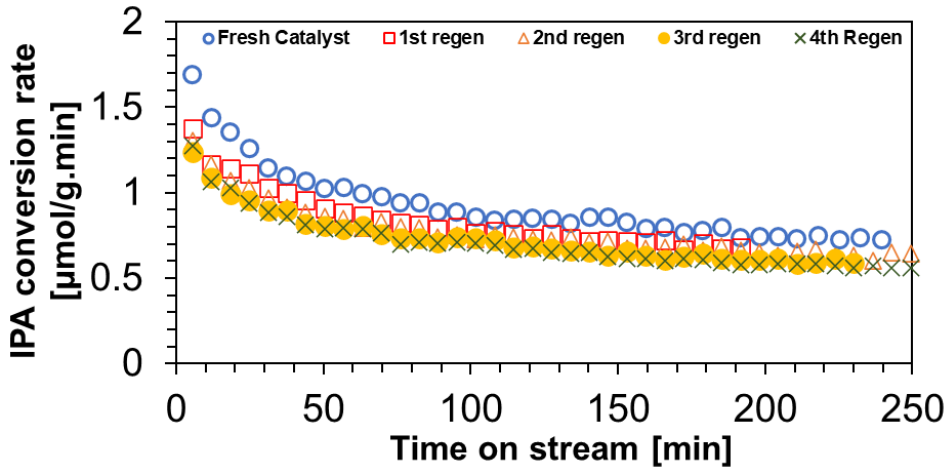

Figure A5.11 *Time-on-stream data for IPA conversion rates measured on P-SPP after cycles of regeneration by in-situ calcination at 823 K. (Reaction conditions p_{IPA} = 30 torr; T = 403 K; WHSV 2.69 g IPA/g cat./h; Diluent (He) flowrate 25 sccm).*

A.5.3.2 Uni-/bimolecular selectivity during in-situ pyridine titration experiments

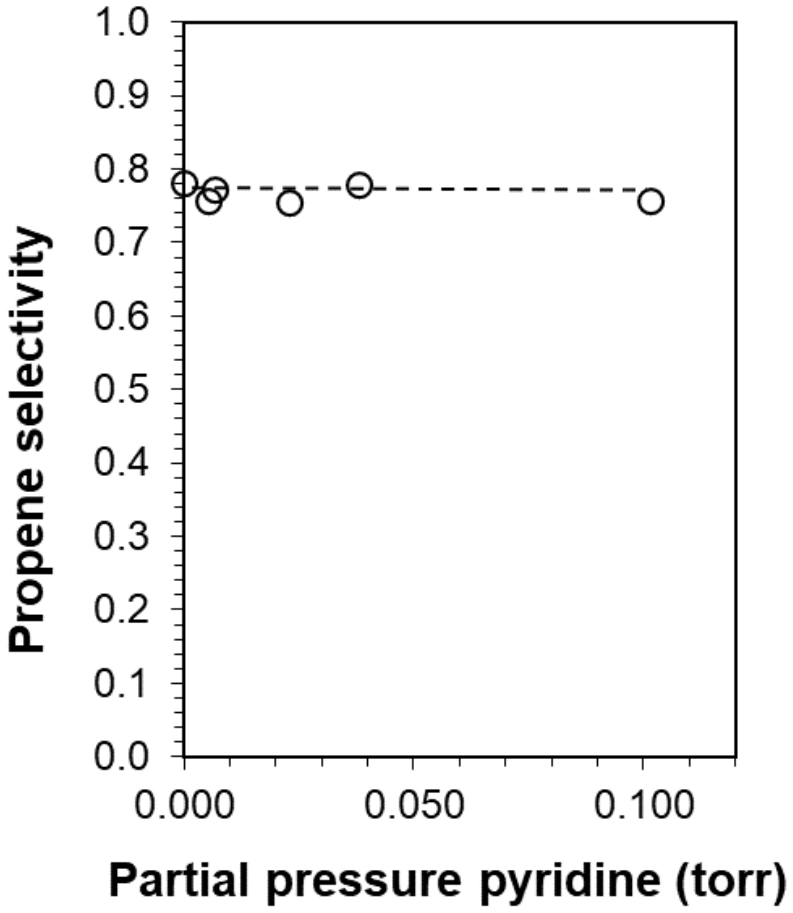

Figure A5.12 *Fractional propene selectivity as a function of pyridine partial pressure during in-situ pyridine titration experiments on P-SPP. The reported values correspond to the selectivities after pyridine saturation. Reaction conditions are the same as* ***Figure 5.9A*** *in the main text. The dashed line is the linear regression to the experimental data.*

A5.3.3 Calculation of KIE for unimolecular IPA dehydration on P-SPP

Investigation of isotopic labeling on rates are used to calculate kinetic isotope effects (KIE), defined as **Equation A5.1:**

$$\text{KIE} = \frac{k_H}{k_D} \qquad \text{(Eq A5.1)}$$

where k_H is the rate constant for the reaction with no deuterium atoms in the reactants, and k_D is the rate constant for reaction with deuterium atoms in the reactants. For a rate-limiting step involving the cleavage of C-H bonds, the KIE value can be estimated by the following equation[44]

$$\text{KIE} = \frac{k_H}{k_D} = exp\left(\frac{0.1865}{T}\upsilon_H\right) \qquad \text{(Eq A5.2)}$$

where T is the absolute temperature and υ_H is the vibrational frequency of the C-H in the units of cm^{-1}. The C-H bond stretching frequency is ~2985 cm^{-1},[44] implying the estimated KIE value involving the cleavage of a C-H bond is 3.98 at 403 K.

For a rate-limiting step involving the re-hybridization of α carbon from sp^3 to sp^2 hybridization in the transition state, the KIE value can be estimated by the following equation[44]

$$\text{KIE} = \frac{k_{2,H}}{k_{2,D}} = exp\left(-\frac{0.1865}{T}(\upsilon^{\#}_{C-H} - \upsilon^{R}_{C-H})\right) \qquad \text{(Eq. A5.3)}$$

where $\upsilon^{\#}$ is the vibrational frequncy of an C_α-H bond of the transition state and the υ^R is the vibrational frequncy of the corresponding C_α-H bond of the reactant molecules. For a transition state with sp^3 hybridization on the α carbon and a reactant with sp^2 hybridization on α carbon, the $\upsilon^{\#}$ is ~800cm^{-1} and the υ^R is ~1350 cm^{-1},[44] so the estimated KIE value is calculated to be 1.3 at 403 K.

A5.3.4 IPA dehydration kinetics on Al-BEA, Al-SPP and Al-MFI

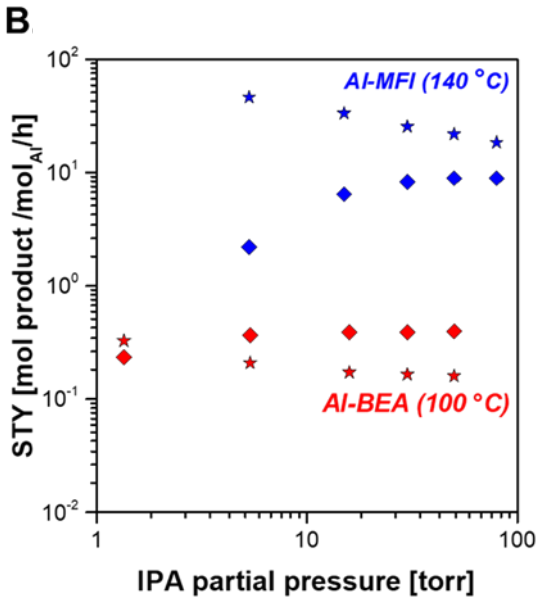

Figure A5.13 *Propylene (★) and di-isopropyl ether (◆) synthesis rates as a function of IPA partial pressures measured on Al-BEA (Si/Al 12.5) (red) and Al-MFI (Si/Al 40) (blue) (Reaction conditions: WHSV=2.5 g reactant/g cat./h; Carrier gas (He) flowrate =100 sccm; Conversions below 2.0%).*

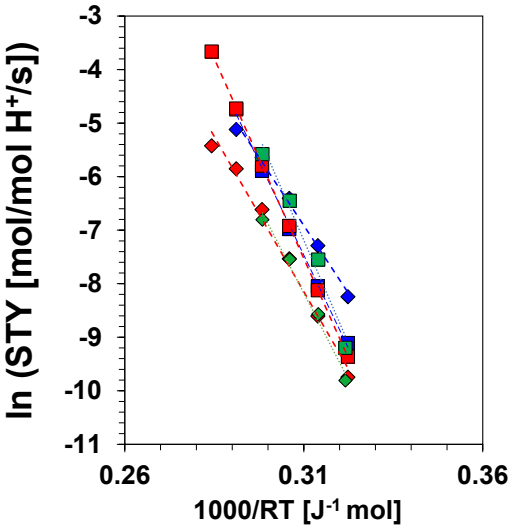

Figure A5.14 *Arrhenius plots of propylene (□) and di-isopropyl ether (◇) synthesis rates measured on Al-BEA (Si/Al 12.5) (blue), Al-SPP (Si/Al 62) (green) Al-MFI (Si/Al 40) (red) (Reaction conditions: p_{IPA} = 30 torr, WHSV=28.6-604 g reactant/g cat./h; Carrier gas (He) flowrate =100 sccm; Conversions below 8.5%).*

A5.3.5 External and internal transport limitations calculations

Mears' criterion was used to estimate the existence of any external mass transfer calculations when measuring reaction rates. This was done for the catalyst exhibiting the highest mass-normalized rates (P-MFI) at the highest temperature (443 K). It can be safely assumed that the less active catalysts (per mass basis) will not be external transport-limited provided this limiting case does not show these limitations at identical reaction conditions. External mass transfer limitations can be neglected if the Eq. A5.4 inequality is satisfied

$$\frac{r_{obs}\rho_b Rn}{k_c C_b} < 0.15 \qquad \text{(A5.4)}$$

Where r_{obs} is the observed rate of reaction in mol $kgcat^{-1}$ s^{-1}, ρ_b is the catalyst bed density in kg m^{-3} ($\rho_b = (1-\phi)\rho_c$ where ϕ is the bed void fraction and ρ_c is the density of the catalyst, reported as 1000 kg m^{-3}), R is the catalyst aggregate size in m, n is the reactant reaction rate order, k_c is the external mass transfer coefficient in m s^{-1}, and C_b is the reactant bulk concentration in mol m^{-3}.

Table A5.2 *Tabulation of parameters for the calculation of Mears' Criteria for IPA dehydration on P-MFI (Si/P 36) at 443 K*

Parameter	Value
r_{obs} (mol $kgcat^{-1}$ s^{-1})	6.85 x 10^{-3}
ρ_b (kg_{cat} m^{-3})	700 (ρ_c = 1000, assumed ϕ = 0.3)
R (m)	1.78x10^{-4} (average mesh size of 106-250 μm)
k_c (m s^{-1})[a]	0.055
C_b (mol m^{-3})	1.09 (30 torr IPA; total pressure 787.6 torr)
n	0
Mears' Criterion (Mass)	**0 (0.014 if assumed n = 1)**

[a] Estimated assuming Sh (Sherwood Number) = $k_c(2R)/D = 2 + 0.6\ Re^{1/2}Sc^{1/3}$; Re (Reynolds Number) = $\rho U(2R)/\mu$ and Sc (Schmidt number) = $\mu/\rho D$, where ρ = bulk gas density (Assumed to be He at 443 K, ρ = 0.13 kg m^{-3}), U = superficial velocity (total volumetric flow rate (0.42 cm^3 s^{-1}); tube diameter (2R) = 4 x10^{-3} m: U = 3.34 x10^{-2} m s^{-1}), and μ = gas viscosity (estimated as He viscosity at 443 K = 2.6 x 10^{-5} Pa s). D is gas phase diffusivity, estimated using Chapman-Enskog theory of diffusivity for IPA in He at 443 K =9.52 x 10^{-5} m^2 s^{-1}).

The Mears criterion parameter show the reported rates are not corrupted by external mass transfer limitations.

Internal mass transfer limitations were evaluated by using the Weisz-Prater criterion (Eq A5.5) for the highest temperature on all the six catalysts.

$$C_{WP} = \eta\phi^2 = \frac{r_{obs}\rho_c R^2}{D_e C_{As}} \qquad \text{(A5.5)}$$

where η is the dimensionless effectiveness factor, ϕ^2 is the dimensionless Thiele modulus, D_e is the effective diffusivity in m^2s^{-1} (D_e) ρ_c is the particle density of the catalyst (assumed 1000 kg/m^3) and C_{As} is the reactant surface concentration in mol m^{-3} (Mears' criterion showed that there were no external mass transfer limitations, and hence we assume $C_{As} = C_b$). The upper limit of $\eta\varphi^2$ to safely assume that reaction is not diffusion limited is typically taken to be ~0.3.

Table A5.3 *Tabulation of parameters for the calculation of the Weisz-Prater Criterion for IPA dehydration on P-MFI (Si/P 36) at 443 K*

Parameter	Value
r_{obs} (mol $kgcat^{-1}$ s^{-1})	6.85 x 10^{-3}
ρ_c (kg_{cat} m^{-3})	1000
R (m)	1 x10^{-6} (highest observed from SEM images in Figure **S4**)
C_{As} (mol m^{-3})	1.09 (30 torr IPA; total pressure 787.6 torr)
D_e (m^2 s^{-1})[a]	5.98 x 10^{-10} (assumed ε=0.35, δ=0.8, τ=6)
Calculated Weisz-Prater Criterion ($\eta\phi^2$)	**0.011**

[a] Calculated by the extending the Arrhenius plots reported for IPA diffusivity in the temperature range 285-343 K on silicalite-1 in Lin et al.[45] to 443 K.

The Weisz-Prater criterion parameter show the reported rates are not corrupted by internal mass transfer limitations.

A6 Concluding remarks and proposed future directions

A6.1 Details of process simulations for furfural-to-butadiene process

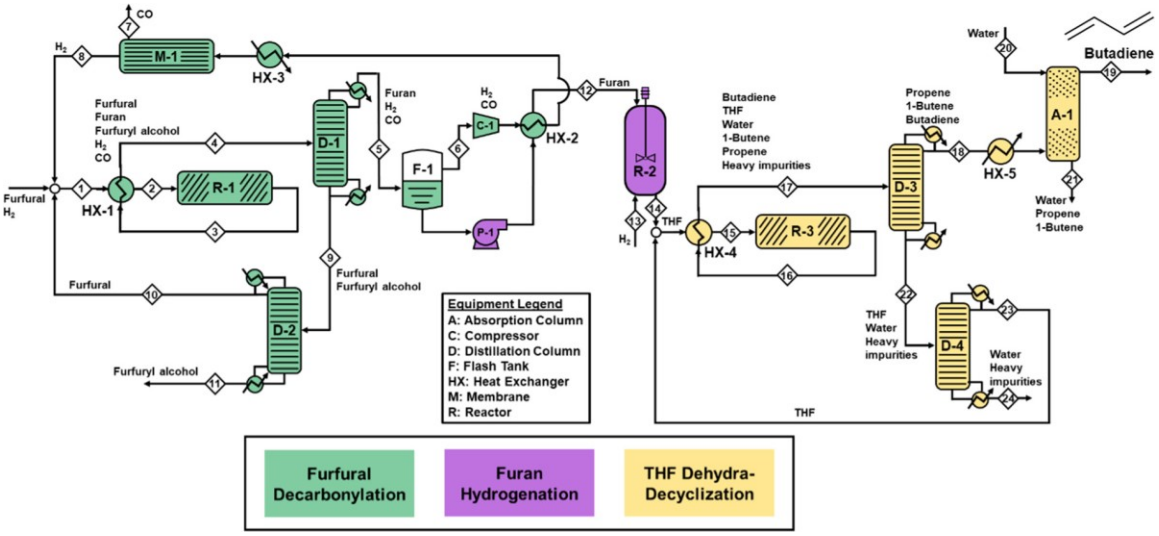

Figure A6.1 *Process flow diagram for the conversion of furfural to butadiene via furfural decarbonylation (R-1, D-1, D-2, F-1, C-1, M-1), furan hydrogenation (P-1, R-2), and tetrahydrofuran (THF) dehydra-decyclization (R-3, D-3, D-4, A-1).*

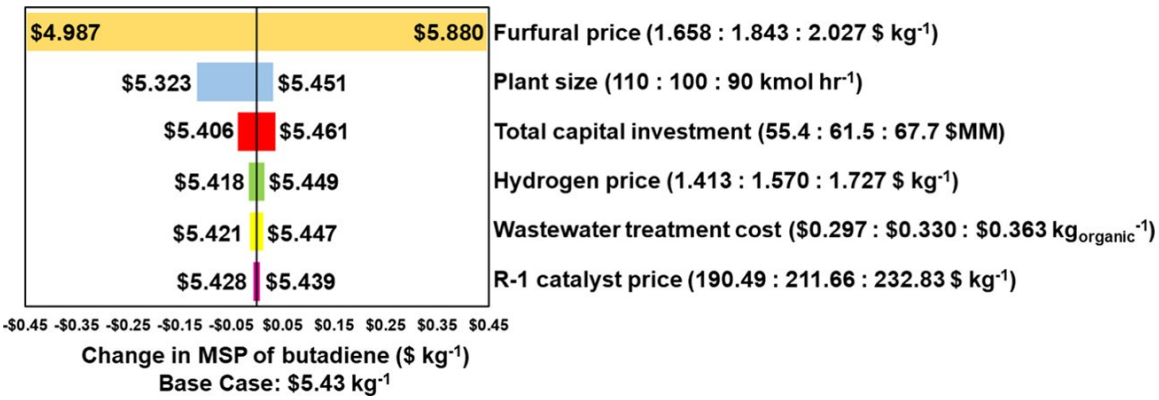

Figure A6.2 *Sensitivity of the minimum selling price (MSP) of butadiene to selected process parameters. Parameters were varied ±10% relative to the base case design of 100 kmol h^{-1} at furfural and hydrogen purchase prices of \$1.84 and \$1.57 kg^{-1} respectively.*

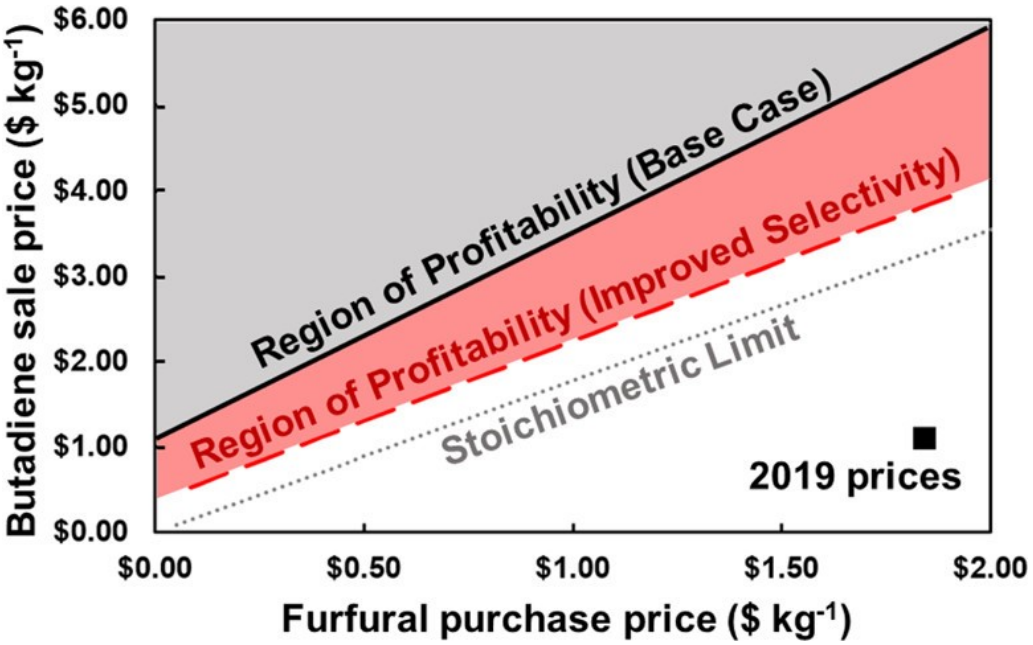

Figure A6.3 *Minimum selling price (MSP) of butadiene at varying furfural feedstock prices is shown for the base-case design (black solid line) and the hypothetical design with 95% selectivity in reactors R-1 and R-3 (red dashed line). The gray dotted line corresponds to the minimum profitable butadiene price assuming quantitative conversion and no processing costs. The hydrogen price is held constant at \$1.57 kg^{-1}. The base-case prices are shown for comparison.*

Appendix references

(1) Abdelrahman, O.; Vinter, K. P.; Ren, L.; Xu, D.; Gorte, R. J.; Tsapatsis, M.; Dauenhauer, P. J. Simple Quantification of Zeolite Acid Site Density by Reactive Gas Chromatography. *Catal. Sci. Technol.* **2017,** 7, 3831-3841.

(2) Hickman, D. A.; Degenstein, J. C.; Ribeiro, F. H. Fundamental principles of laboratory fixed bed reactor design. *Curr. Opin. Chem. Eng.* **2016**, *13*, 1–9.

(3) Zhang, X.; Liu, D.; Xu, D.; Asahina, S.; Cychosz, K. A.; Agrawal, K. V.; Al Wahedi, Y.; Bhan, A.; Al Hashimi, S.; Terasaki, O.; et al. Synthesis of Self-Pillared Zeolite Nanosheets by Repetitive Branching. *Science* **2012**, *336* (6089), 1684–1687.

(4) Konno, H.; Ohnaka, R.; Nishimura, J. I.; Tago, T.; Nakasaka, Y.; Masuda, T. Kinetics of the catalytic cracking of naphtha over ZSM-5 zeolite: Effect of reduced crystal size on the reaction of naphthenes. *Catal. Sci. Technol.* **2014**, *4* (12), 4265–4273.

(5) Konno, H.; Okamura, T.; Kawahara, T.; Nakasaka, Y.; Tago, T.; Masuda, T. Kinetics of n-hexane cracking over ZSM-5 zeolites - Effect of crystal size on effectiveness factor and catalyst lifetime. *Chem. Eng. J.* **2012**, *207–208*, 490–496.

(6) Holland, C. D.; Anthony, R. G. (1989) Fundamentals of Chemical Reaction Engineering; (Prentice Hall, ISBN 0133356396) .

(7) Murashov, V. V.; White, M. A. Thermal properties of zeolites: Effective thermal conductivity of dehydrated powdered zeolite 4A. *Mater. Chem. Phys.* **2002**, *75* (1–3), 178–180.

(8) Al-Dughaither, A. S.; De Lasa, H. HZSM-5 zeolites with different SiO2/Al2O3 ratios. Characterization and NH3 desorption kinetics. *Ind. Eng. Chem. Res.* **2014**, *53* (40), 15303–15316.

(9) Janda, A. L. Effects of Zeolite Structure and Si / Al Ratio on Adsorption Thermodynamics and Intrinsic Kinetics of Monomolecular Cracking and Dehydrogenation of Alkanes over Brønsted Acid Sites Ph.D. Dissertation, University of California, Berkeley **2015**.

(10) Shri Ramaswamy, Hua-Jiang Huang, B. V. R. (2013) Separation and Purification Technologies in Biorefineries. John Wiley & Sons Inc. Chichester, West Sussex, United Kingdom

(11) Engineering toolbox https://www.engineeringtoolbox.com/. (accessed 11/26/19)

(12) Meng, X.; Zheng, P.; Wu, J.; Liu, Z. Density and viscosity measurements of diethyl ether from 243 to 373 K and up to 20 MPa. *Fluid Phase Equilib.* **2008**, *271* (1–2), 1–5.

(13) Dortmund data bank http://www.ddbst.com/ddb.html. (accessed 11/26/19)

(14) Vargaftik, N. B.; Yakush, L. V. Temperature dependence of thermal conductivity of helium. *J. Eng. Phys.* **1977**, *32* (5), 530–532.

(15) Connett, J. E. Chemical equilibria 4. Enthalpy of dehydration of ethanol to diethyl ether by measurement of equilibrium constants in ethanol + ether + water by a vapour flow technique. *J. Chem. Thermodyn.* **1972**, *4* (1), 135–138.

(16) Iwasaki, H.; Tanishita, I.; Mural, Y.; Takahashi, M.; Makita, T. (1979) The Review of Physical Chemistry of Japan 49(1): 11-17.

(17) Assaela, M. J.; Koutian, A.; Huber, M. L.; Perkins, R. A. Reference correlations of the thermal conductivity of ethene and propene. *J. Phys. Chem. Ref. Data* **2016**, *45* (3).

(18) Sullivan, M. M.; Held, J. T.; Bhan, A. Structure and site evolution of molybdenum carbide catalysts upon exposure to oxygen. *J. Catal.* **2015**, *326*, 82–91.

(19) Meng, X.; Wu, J.; Liu, Z. J. (2009) Viscosity and Density Measurements of Diisopropyl Ether and Dibutyl Ether at Different Temperatures and Pressures Chem. Engg. data, 54 (9), 2353–2358.

(20) Li, X.; Wu, J.; Dang, Q. (2010) Thermal Conductivity of Liquid Diethyl Ether , Diisopropyl Ether , and Di- n -butyl Ether from 233 to 373 K at Pressures up to 30 MPa. *Chem. Eng. Data* 55, 3, 1241- 1246.

(21) John, M.; Alexopoulos, K.; Reyniers, M.; Marin, G. B. Reaction path analysis for 1-butanol dehydration in H-ZSM-5 zeolite : Ab initio and microkinetic modeling. *J Catal.* **2015**, *330*, 28–45.

(22) Engler, B. P.; Harrah, L. A. Viscosity and density of 2-methyltetrahydrofuran as a function of temperature. Sandia Labs. report, Albuquerque, NM (USA), (Reference number 10460457).**1978**.

(23) Comelli, F.; Francesconi, R.; Bigi, A.; Rubini, K. Molar heat capacities, densities, viscosities, and refractive indices of dimethyl sulfoxide + tetrahydropyran and + 2-methyltetrahydrofuran at (293.15, 303.15, and 313.15) K. *J. Chem. Eng. Data* **2007**, *52* (2), 639–644.

(24) Chemeo https://www.chemeo.com/. (accessed 11/26/19)

(25) Kumbhalkar, M. D.; Buchanan, J. S.; Huber, G. W.; Dumesic, J. A. **(2017)** Ring Opening of Biomass-derived Cyclic Ethers to Dienes over Silica/Alumina. *ACS Cat.* 8, 5248-5256..

(26) Camblor, M. a.; Corma, A.; Valencia, S. Spontaneous nucleation and growth of pure silica zeolite-B free of connectivity defects. *Chem. Commun.* **1996**, No. 20, 2365-2366.

(27) M.M.J. Treacy and; Higgins, J. B. *Collection of Simulated XRD Powder Patterns for Zeolites (5th) Revised Edition*; Elsevier Science 2007, Vol. 5.

(28) Zones, S. I.; Benin, A.; Hwang, S. J.; Xie, D.; Elomari, S.; Hsieh, M. F. Studies of aluminum reinsertion into borosilicate zeolites with intersecting channels of 10- and 12-ring channel systems. *J. Am. Chem. Soc.* **2014**, *136* (4), 1462–1471.

(29) Hwang, S. J.; Chen, C. Y.; Zones, S. I. Boron sites in borosilicate zeolites at various stages of hydration studied by solid state NMR spectroscopy. In *Journal of Physical Chemistry B*; 2004; Vol. 108, pp 18535–18546.

(30) Koller, H.; Fild, C.; Lobo, R. F. Variable anchoring of boron in zeolite beta. *Microporous Mesoporous Mater.* **2005**, *79* (1–3), 215–224.

(31) Koller, H.; Senapati, S.; Ren, J.; Uesbeck, T.; Siozios, V.; Hunger, M.; Lobo, R. F. Post-Synthesis Conversion of Borosilicate Zeolite Beta to an Aluminosilicate with Isolated Acid Sites : A Quantitative Distance Analysis by Solid-State NMR. *J. Phys. Chem. C*, 120 (18), 2016, 9811-9820.

(32) Tong, H. T. T.; Koller, H. Control of Al for B framework substitution in zeolite Beta by counterions. *Microporous Mesoporous Mater.* **2012**, *148* (1), 80–87.

(33) Mihályi, R. M.; Pál-Borbély, G.; Beyer, H. K.; Szegedi, Á.; Korányi, T. I. Characterization of aluminum and boron containing beta zeolites prepared by solid-state recrystallization of magadiite. *Microporous Mesoporous Mater.* **2007**, *98* (1–3), 132–142.

(34) Marthala, V. R. R.; Hunger, M.; Kettner, F.; Krautscheid, H.; Chmelik, C.; Kärger, J.; Weitkamp, J. Solvothermal synthesis and characterization of large-crystal all-silica, aluminum-, and boron-containing ferrierite zeolites. *Chem. Mater.* **2011**, *23* (10), 2521–2528.

(35) Trudu, F.; Tabacchi, G.; Gamba, A.; Fois, E. First Principles Studies on Boron Sites in Zeolites. *J. Phys. Chem. A* **2007**, *111* (45), 11626–11637.

(36) Chen, J.; Liang, T.; Li, J.; Wang, S.; Qin, Z.; Wang, P.; Huang, L.; Fan, W.; Wang, J. Regulation of Framework Aluminum Siting and Acid Distribution in H-MCM-22 by Boron Incorporation and Its Effect on the Catalytic Performance in Methanol to Hydrocarbons. *ACS Catal.* **2016**, *6* (4), 2299–2313.

(37) Grünewald-Lüke, A.; Marier, B.; Hochgräfe, M.; Gies, H. Quinuclidine derivates as structure directing agents for the synthesis of boron containing zeolites. *J. Mater. Chem.* **1999**, *9* (10), 2529–2536.

(38) Cavalcante, C. L.; Ruthven, D. M. Adsorption of Branched and Cyclic Paraffins in Silicalite. 2. Kinetics. *Ind. Eng. Chem. Res.* **1995**, *34* (1), 185–191.

(39) Chézeau, J. M.; Delmotte, L.; Guth, J. L.; Soulard, M. High-resolution solid-state 29Si and 13C n.m.r. on highly siliceous MFI-type zeolites synthesized in nonalkaline fluoride medium. *Zeolites* **1989**, *9* (1), 78–80.

(40) Zhao, D.; Feng, J.; Huo, Q.; Melosh, N.; Fredrickson, G. H.; Chmelka, B. F.; Stucky, G. D. Triblock Copolymer Syntheses of Mesoporous Silica with Periodic 50 to 300 Angstrom Pores. **1998**, *279* (January) 548-552.

(41) Werner Stober, A. F. Controlled Growth of Monodisperse Silica Spheres in the Micron Size Range. *J. Phys. Ther. Sci.* **2017**, *29* (1), 112–114.

(42) Zhang, H. Fabrication of Zeolite MFI Membranes on Low Cost Polymer Supports.

PhD thesis University of Minnesota **2017.**

(43) Cho, H. J.; Ren, L.; Vattipalli, V.; Yeh, Y. H.; Gould, N.; Xu, B.; Gorte, R. J.; Lobo, R.; Dauenhauer, P. J.; Tsapatsis, M.; et al. Renewable p-Xylene from 2,5-Dimethylfuran and Ethylene Using Phosphorus-Containing Zeolite Catalysts. *ChemCatChem* **2017**, *9* (3), 398–402.

(44) Chiang, H.; Bhan, A. Catalytic consequences of hydroxyl group location on the rate and mechanism of parallel dehydration reactions of ethanol over acidic zeolites. *J. Catal.* **2010**, *271* (2), 251–261.

(45) Lin, Y.S., Ma, Y.H., A comparative study of adsorption and diffusion of vapor-alcohols and alcohols from aqueous solutions in silicalite. Zeolites: Facts, Figures, Future, Elsevier Science Publishers Amsterdam, **1989,** 877-866.